Doctoral Dissertation
博士論文

On isospin symmetry breaking in nuclear density functional theory
(原子核密度汎関数理論におけるアイソスピン対称性の破れ)

A Dissertation Submitted for the Degree of Doctor of Philosophy
December 2021

令和3年12月 博士 (理学) 申請

Department of Physics, Graduate School of Science, The University of Tokyo
東京大学大学院理学系研究科物理学専攻

Tomoya Naito
内藤 智也

Abstract

The aim of this thesis is a detailed discussion of effects of the isospin symmetry breaking on ground-state properties, especially the total energy and the neutron-skin thickness, of atomic nuclei systematically.

A proton and a neutron have quite similar properties apart from their charge; hence, it is often convenient to regard these two particles as the two different *states* of a particle called "nucleon". An auxiliary spin-like quantum number to distinguish two *states* of a nucleon is called "isospin", and the fact that a proton and a neutron have quite similar properties is called isospin symmetry. It is also known that the nuclear interaction has also isospin symmetry: The proton-proton, neutron-neutron, and proton-neutron (the total isospin 1) nuclear interactions are almost the same. Accordingly, the isospin symmetry of atomic nuclei also holds almost perfectly. For instance, the mirror nuclei pair have quite similar properties. Here, the mirror nuclei pair is a pair of two atomic nuclei, one of which consists of Z protons and N neutrons and the other consists of N protons and Z neutrons.

Nevertheless, the electromagnetic interaction and the tiny contribution of the isospin symmetry breaking (ISB) terms of the nuclear interaction break the isospin symmetry of atomic nuclei: For example, the mass of an atomic nucleus is different from that of its mirror nucleus. Such isospin symmetry breaking of atomic nuclei have been highlighted, especially, these days. Despite the importance of the ISB terms of the nuclear interaction, it has been often neglected in the nuclear structure calculation. This is because the effective nuclear interaction, which is fitted to experimental data, is not accurate enough to discuss such small effects. Therefore, first, it is important to estimate the contribution of the electromagnetic interaction to nuclear properties, which, in principle, can be estimated exactly apart from the approximation introduced by many-body calculation methods since the interaction is exactly known from the quantum electrodynamics.

In this thesis, I shall discuss such isospin symmetry breaking in atomic nuclei theoretically. A quantum many-body method called mean-field calculation or density functional theory (DFT) is used since only this method can be applied to the whole nuclear chart at this moment.

The electromagnetic interaction has not been treated accurately and the ISB terms of the nuclear interaction have not been considered in nuclear DFT. Therefore, the electromagnetic interaction is treated as accurately as possible. By using the knowledge in condensed matter physics, the Coulomb exchange energy calculated with the Fock term is reproduced in a density functional framework. On top of it, the non-zero spatial charge distributions of protons and neutrons are taken into account for the Coulomb energy. The vacuum polarization for the Coulomb interaction and the electromagnetic spin-orbit interaction are also considered. The finite-light-speed correction to the Coulomb interaction is also discussed independently.

On top of such an accurate treatment of the electromagnetic interaction, effects of the ISB terms of the nuclear interaction are compared with those of the Coulomb interaction. Dependences of ground-state properties of doubly-magic nuclei on the strengths of the ISB terms of the nuclear interaction are discussed. Using these results, a novel method to pin down the strength of the charge symmetry breaking term of the nuclear energy density functional is also proposed.

Contents

Chapter 1

Introduction

It is known that atomic nuclei have almost the isospin symmetry, while its breaking is one of the important topics. In order to explain the isospin symmetry of atomic nuclei and its breaking, in this chapter, a brief introduction to the nuclear structure will be given.

1.1 Atomic Nuclei and Isospin

The atomic nuclei are composed of protons and neutrons, which interact with each other via the nuclear and the electromagnetic interactions. Since the protons and the neutrons have similar properties except for their charge, as shown in Table 1.1.1, both are called "nucleons" altogether and are regarded as two different *states* of nucleons. In order to distinguish two states, a new *auxiliary* quantum number called "isospin" is introduced. The isospin

$$\boldsymbol{t} = (t_x, t_y, t_z) = \frac{1}{2}\left(\begin{pmatrix} 0 & 1 \\ 1 & 0 \end{pmatrix}, \begin{pmatrix} 0 & -i \\ i & 0 \end{pmatrix}, \begin{pmatrix} 1 & 0 \\ 0 & -1 \end{pmatrix}\right) \tag{1.1.1}$$

is a spin-like $SU(2)$ variable and protons and neutrons are assigned to the eigenvalue of t_z as $t_z = -1/2$ and $+1/2$, respectively [1]. The concept of the isospin can be extended to the quark model [9], other hadrons, and atomic nuclei. Suppose an atomic nucleus is composed of Z protons and N neutrons. Using an algebra of the angular momentum, the z-projection of the isospin of the atomic nucleus, T_z, is $T_z = (N - Z)/2$.

The Hamiltonian of the atomic nuclei is written as

$$H = -\sum_{j=1}^{A} \frac{\hbar^2}{2m} \Delta_j + \sum_{1 \le j < k \le A} v_{\mathrm{nucl}}\left(\boldsymbol{r}_j, \sigma_j, \tau_j, \boldsymbol{r}_k, \sigma_k, \tau_k\right) + \sum_{1 \le j < k \le Z} v_{\mathrm{EM}}\left(\boldsymbol{r}_j, \boldsymbol{r}_k\right), \tag{1.1.2}$$

where $\boldsymbol{r}_j$, σ_j, and τ_j denote spatial, spin, and isospin coordinates of nucleon j, respectively [2], and v_{nucl} and v_{EM} denote the nuclear and the electromagnetic interactions, respectively. Only the Coulomb interaction $v_{\mathrm{Coul}} = e^2/|\boldsymbol{r}_j - \boldsymbol{r}_k|$ is considered in v_{EM} in most works. For simplicity, the nucleons are assumed to be point particles, and accordingly, the neutrons do not feel the Coulomb interaction. The mass difference between protons and neutrons are neglected. Therefore, the mass m in Eq. (1.1.2) is the average of nucleon mass $938.919\,\mathrm{MeV}/c^2$. In addition, for simplicity, the non-relativistic scheme, i.e., the Schrödinger equation, is used here.

As we shall discuss later, it is known that the nuclear interaction v_{nucl} approximately conserves the isospin, $[v_{\mathrm{nucl}}, \boldsymbol{T}] \simeq 0$, where $\boldsymbol{T}$ is the two-body total isospin operator $\boldsymbol{T} = \boldsymbol{t}_1 + \boldsymbol{t}_2$. Hence, if there were no Coulomb interaction, the atomic nuclei would have isospin symmetry. Due to the Coulomb interaction

[1] In particle or hadron physics, $t_z = +1/2$ and $-1/2$ are, respectively, assigned to protons and neutrons, which one can relate to their charge [1, 2] via the Nakano-Nishijima-Gell-Mann's formula [3–6]. The convention in low-energy nuclear physics was originally introduced by Heisenberg and Wigner [7, 8], in which the total isospins of $T_z = \sum_j t_{zj}$ of most stable nuclei become positive. The history of the convention of the isospin is summarized in Ref. [C1].

[2] The isospin satisfies $t_j = \frac{1}{2}\tau_j$, where τ_j refers to the Pauli matrices for the isospin space (isospace). Similarly, the spin satisfies $s_j = \frac{1}{2}\sigma_j$, where σ_j refers to the Pauli matrices for the spin space. Because of the convention, hereinafter, τ_j and σ_j are used, instead of t_j and s_j.

Table 1.1.1: Properties of protons and neutrons.

	Proton	Neutron
Charge (e)	$+1$	0
Spin J	$1/2$	$1/2$
Parity π	$+$	$+$
Isospin t	$1/2$	$1/2$
Isospin t_z	$-1/2$	$+1/2$
Internal quark structure	uud	udd
Mass (MeV/c^2) [10]	$938.2720813 \pm 0.0000058$	$939.5654133 \pm 0.0000058$

and tiny contribution of the isospin symmetry breaking (ISB) terms of the nuclear interaction, the isospin symmetry of the atomic nuclei are broken slightly, while T_z is still a good quantum number.

The Coulomb interaction between protons is repulsive, whereas the nuclear interaction is, in total, strongly attractive. If there were not the Coulomb interaction, due to the Pauli principle, $N = Z$ nuclei would be stable in the whole nuclear chart. However, as Z increases, the Coulomb repulsion between two protons contributes more significantly, and consequently, $N > Z$ nuclei become stable in the heavy-mass region.

1.2 Nuclear Interaction

The nuclear interaction microscopically originates from the strong interaction in particle physics, i.e., gluon exchanges between quarks of nucleons. The nuclear interaction in vacuum, which is determined with the two-body bound state or two-body scattering experiments, is known to be different from that in medium. Here, we focus on the two-body nuclear interaction in vacuum, while that in medium will be explained later.

The deuteron, which consists of a proton and a neutron, helps one to understand the two-body nuclear interaction in vacuum. The ground state of the deuteron, which is the unique bound state of the two nucleon systems, has the total spin 1, total isospin 0, and positive parity. Therefore, it is expected that the nuclear interaction has a spin-isospin dependence and $S = 1$, $T = 0$ channel is expected to be attractive strongly.

In addition, the nuclear binding energy per nucleon is, in general, almost constant ($\approx 8\,\mathrm{MeV}$) among the whole nuclear chart, which suggests that the nuclear interaction should be short-range [11].

The two-body nuclear interaction in vacuum is required to satisfy the following condition:

1. Invariance under interchange of particles;
2. Invariance under spatial rotation;
3. Invariance under spatial translation;
4. Invariance under charge-parity-time reversal transformation (CPT theorem).

The last one is required by the quantum field theory [12]. In addition, the two-body nuclear interaction satisfies the following condition almost perfectly:

5. Charge symmetry, i.e., two-body nuclear interaction between two protons and that between two neutrons are identical;
6. Charge independence, i.e., two-body nuclear interaction does not depend on the charges of nucleons.

Several forms of the two-body nuclear interaction in vacuum have been proposed, and one of the most popular forms, called Argonne V14 (AV14) interaction [13], is

$$
\begin{aligned}
&v_{\mathrm{nucl}}^{\mathrm{AV14}}\left(\boldsymbol{r}_j, \sigma_j, \tau_j, \boldsymbol{r}_k, \sigma_k, \tau_k\right) \\
&= v_1\left(r_{jk}\right) + v_2\left(r_{jk}\right)\left(\boldsymbol{\tau}_j \cdot \boldsymbol{\tau}_k\right) + v_3\left(r_{jk}\right)\left(\boldsymbol{\sigma}_j \cdot \boldsymbol{\sigma}_k\right) + v_4\left(r_{jk}\right)\left(\boldsymbol{\sigma}_j \cdot \boldsymbol{\sigma}_k\right)\left(\boldsymbol{\tau}_j \cdot \boldsymbol{\tau}_k\right) \\
&\quad + v_5\left(r_{jk}\right) S_{jk} + v_6\left(r_{jk}\right) S_{jk}\left(\boldsymbol{\tau}_j \cdot \boldsymbol{\tau}_k\right) + v_7\left(r_{jk}\right) \boldsymbol{L} \cdot \boldsymbol{S} + v_8\left(r_{jk}\right) \boldsymbol{L} \cdot \boldsymbol{S}\left(\boldsymbol{\tau}_j \cdot \boldsymbol{\tau}_k\right) \\
&\quad + v_9\left(r_{jk}\right) \boldsymbol{L}^2 + v_{10}\left(r_{jk}\right) \boldsymbol{L}^2\left(\boldsymbol{\tau}_j \cdot \boldsymbol{\tau}_k\right) + v_{11}\left(r_{jk}\right) \boldsymbol{L}^2\left(\boldsymbol{\sigma}_j \cdot \boldsymbol{\sigma}_k\right) + v_{12}\left(r_{jk}\right) \boldsymbol{L}^2\left(\boldsymbol{\sigma}_j \cdot \boldsymbol{\sigma}_k\right)\left(\boldsymbol{\tau}_j \cdot \boldsymbol{\tau}_k\right) \\
&\quad + v_{13}\left(r_{jk}\right)\left(\boldsymbol{L} \cdot \boldsymbol{S}\right)^2 + v_{14}\left(r_{jk}\right)\left(\boldsymbol{L} \cdot \boldsymbol{S}\right)^2\left(\boldsymbol{\tau}_j \cdot \boldsymbol{\tau}_k\right), \qquad (1.2.1)
\end{aligned}
$$

where $\boldsymbol{L}$ and $\boldsymbol{S}$ are, respectively, the two-body orbital and spin angular momentum operators,

$$S_{jk} = 3\frac{(\boldsymbol{\sigma}_j \cdot \boldsymbol{r}_{jk})(\boldsymbol{\sigma}_k \cdot \boldsymbol{r}_{jk})}{r_{jk}^2} - \boldsymbol{\sigma}_j \cdot \boldsymbol{\sigma}_k \tag{1.2.2}$$

is the tensor operator, $\boldsymbol{r}_{jk} = \boldsymbol{r}_j - \boldsymbol{r}_k$, and $r_{jk} = |\boldsymbol{r}_{jk}|$. The r_{jk} dependences of $v_j(r_{jk})$ are determined so that two-body scattering and deuteron properties are reproduced. Here, $\boldsymbol{\sigma}_j \cdot \boldsymbol{\sigma}_k$ and $\boldsymbol{\tau}_j \cdot \boldsymbol{\tau}_k$, respectively, become

$$\boldsymbol{\sigma}_j \cdot \boldsymbol{\sigma}_k = \begin{cases} -3 & \text{for } S = 0, \\ +1 & \text{for } S = 1, \end{cases} \tag{1.2.3}$$

$$\boldsymbol{\tau}_j \cdot \boldsymbol{\tau}_k = \begin{cases} -3 & \text{for } T = 0, \\ +1 & \text{for } T = 1. \end{cases} \tag{1.2.4}$$

The tensor interaction, which depends on S_{jk}, is specific to nuclear interaction and vanishes for the $S = 0$ state. Due to the existence of S_{jk}, the nuclear interaction does not conserve angular momentum. For example, the deuteron contains both S-wave ($L = 0$) and D-wave ($L = 2$) components [14–16]. This tensor interaction forms a spin-orbit mean field and plays crucial roles for nuclear structure, especially, the shell structure and its evolution [17–23, A16, A17].

To satisfy the CPT theorem, the following combinations of parity, spin, and isospin are allowed for the nuclear interaction:

- parity odd ($L = 1, 3, 5, \ldots$), spin singlet ($S = 0$), isospin singlet ($T = 0$),
- parity odd ($L = 1, 3, 5, \ldots$), spin triplet ($S = 1$), isospin triplet ($T = 1$),
- parity even ($L = 0, 2, 4, \ldots$), spin singlet ($S = 0$), isospin triplet ($T = 1$),
- parity even ($L = 0, 2, 4, \ldots$), spin triplet ($S = 1$), isospin singlet ($T = 0$).

The r_{jk} dependence of the central ($v_1, \ldots, v_4$), tensor (v_5 and v_6), spin-orbit (v_7 and v_8), $\boldsymbol{L}^2$ (v_9, v_{10}, v_{11}, and v_{12}), and $(\boldsymbol{L} \cdot \boldsymbol{S})^2$ (v_{13} and v_{14}) interactions in the AV14 interaction are shown in Fig. 1.2.1. In order to see the averaged total strength of each channel easily, the AV4' interaction [24], in which all the terms are projected *effectively* to the central force, is also shown. It is shown that the $S = 0$, $T = 1$ channel and $S = 1$, $T = 0$ channel give strong attractive interactions.

Historically, this nuclear interaction was termed "*exchange* force". The exchange force in this context does not mean the interaction with exchanging particles. Instead, it means the exchange of the coordinate. For example, the exchange force with respect to the spatial coordinate is $v_{\mathrm{H}}(r_{jk}) P_r$, where

$$P_r \varphi(\boldsymbol{r}_j, \sigma_j, \tau_j, \boldsymbol{r}_k, \sigma_k, \tau_k) = \varphi(\boldsymbol{r}_k, \sigma_j, \tau_j, \boldsymbol{r}_j, \sigma_k, \tau_k). \tag{1.2.5}$$

This exchange operator P_r is also extended to the spin and isospin, P_σ and P_τ, defined by

$$P_\sigma = \frac{1 + (\boldsymbol{\sigma}_1 \cdot \boldsymbol{\sigma}_2)}{2}, \tag{1.2.6}$$

$$P_\tau = \frac{1 + (\boldsymbol{\tau}_1 \cdot \boldsymbol{\tau}_2)}{2}, \tag{1.2.7}$$

respectively. The nuclear interaction was classified into four parts [1]: non-exchange force called Wigner force [25], spin-exchange force called Bartlett force [26], isospin-exchange force called Majorana force [27], and spatial-exchange force called Heisenberg force [7], as

$$\begin{aligned} v_{\mathrm{nucl}}(\boldsymbol{r}_j, \sigma_j, \tau_j, \boldsymbol{r}_k, \sigma_k, \tau_k) = {} & v_{\mathrm{W}}(\boldsymbol{r}_j, \sigma_j, \tau_j, \boldsymbol{r}_k, \sigma_k, \tau_k) \\ & + v_{\mathrm{B}}(\boldsymbol{r}_j, \sigma_j, \tau_j, \boldsymbol{r}_k, \sigma_k, \tau_k) P_\sigma \\ & + v_{\mathrm{M}}(\boldsymbol{r}_j, \sigma_j, \tau_j, \boldsymbol{r}_k, \sigma_k, \tau_k) P_\tau \\ & + v_{\mathrm{H}}(\boldsymbol{r}_j, \sigma_j, \tau_j, \boldsymbol{r}_k, \sigma_k, \tau_k) P_\sigma P_\tau, \end{aligned} \tag{1.2.8}$$

where due to the Fermi statistics, $P_r P_\sigma P_\tau = -1$ and accordingly $P_r = -P_\sigma P_\tau$ holds. This classification is rarely used recently to classify the nuclear interaction in vacuum, while this idea or even these names are used for the nuclear interaction in medium.

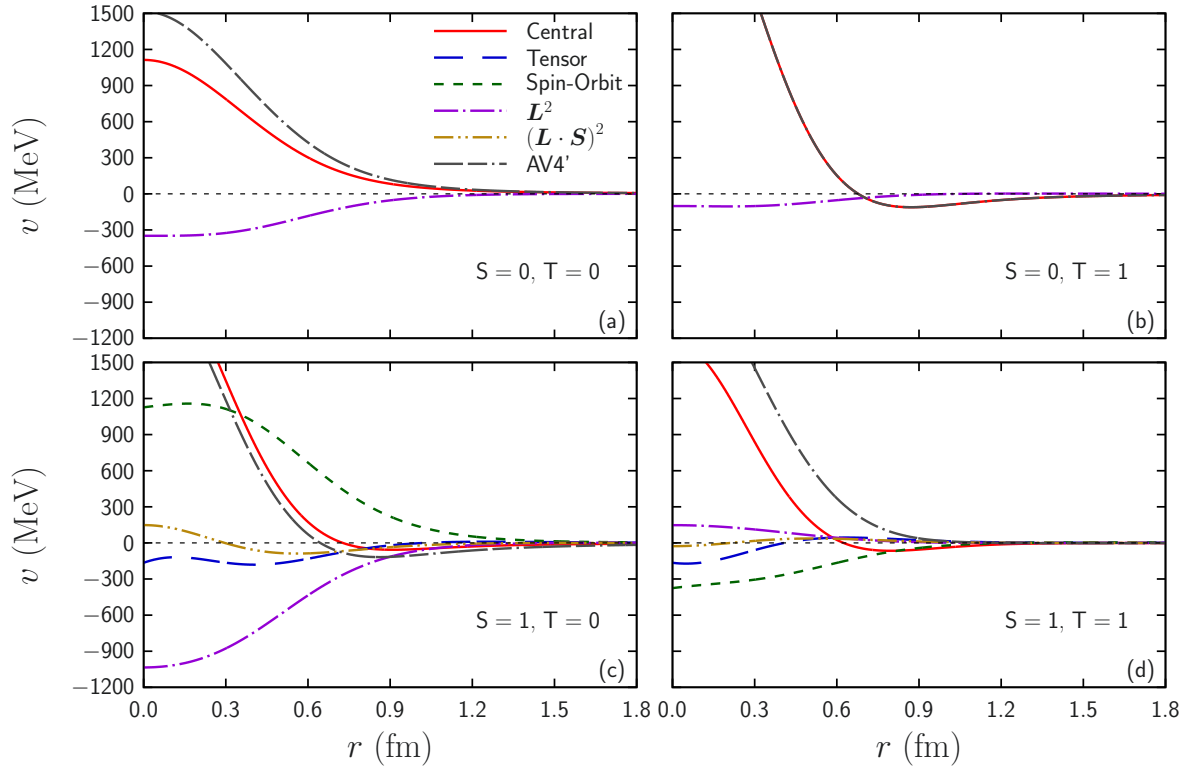

Figure 1.2.1: Radial dependence of central, tensor, spin-orbit, $\boldsymbol{L}^2$, and $(\boldsymbol{L}\cdot\boldsymbol{S})^2$ interactions in the AV14 interaction [13]. For comparison, the AV4' interaction [24] is also shown.

The nuclear interaction in vacuum can be described as the meson-exchange picture. Originally, Yukawa introduced the π-meson-exchange picture [28] as an analogy to the photon-exchange picture of the electromagnetic interaction in quantum electrodynamics. This idea has been extended to the exchange of other mesons lighter than nucleons, i.e., ρ, σ, and ω mesons, to explain the behaviour of the nuclear interaction. Note that the σ meson has not been observed yet, while it is included to describe scalar-isoscalar type coupling effectively, which originates, for instance, from the two-pion exchange process. These mesons have different spins, parities, and isospins, as shown in Table 1.2.1, and accordingly, the complicated nuclear interaction can be described. Microscopically, the nuclear interaction originates from the exchange of gluons between quarks inside nucleons, and these exchange processes can be, effectively, described as meson exchanges [29, 30]. Although this meson-exchange theory is just an effective theory, it helps us to understand the behaviour of the nuclear interaction [31]: The short-range repulsion ($r \lesssim 0.5\,\mathrm{fm}$) is due to the Pauli principle and the size of nucleons; the medium-range attraction ($0.5 \lesssim r \lesssim 1.0\,\mathrm{fm}$) is due to one-boson (except for pion) exchanges [32, 33] and two-pion exchange [34]; the long-range tail ($1.0 \lesssim r \lesssim 2.0\,\mathrm{fm}$) is due to the one-pion exchange [28].

It is also known that there exists interaction that can be described only by involving three nucleons but cannot by using two nucleons. This interaction is called three-body interaction. The microscopic origin of the three-body interaction has long been argued. One mechanism is called Fujita-Miyazawa type [35], where the nucleon A emits a pion and the nucleon B absorbs it; then the nucleon B excites to the resonance excited states called the Δ baryon; after that, the nucleon B deexcites with emitting a pion; the pion is absorbed by the nucleon C. This mechanism is shown schematically in Fig. 1.2.2. It is known that the three-body interaction is crucial to describe nuclear structure and neutron star properties [36–38].

Recently, two novel methods to determine nuclear interaction microscopically have been proposed: chiral effective field theory (ChEFT) [39, 40] and lattice quantum chromodynamics (LQCD) calculation [41–43]. In the former method, the nuclear interaction is described by using the pion exchange and point coupling, which describes the heavier-meson exchange. The nuclear interaction can be, then, expanded by the series of the order of meson-exchange processes, and finally, expressed by several coupling constants. The coupling

Table 1.2.1: Spin, parity, and isospin of mesons contributing to nuclear interaction.

Meson	Charge (e)	Spin	Parity	Isospin
$\pi^{\pm}$	± 1	0	$-$	1
π^0	0	0	$-$	1
σ	0	0	$+$	0
ρ	0, ± 1	1	$-$	1
ω	0	1	$-$	0

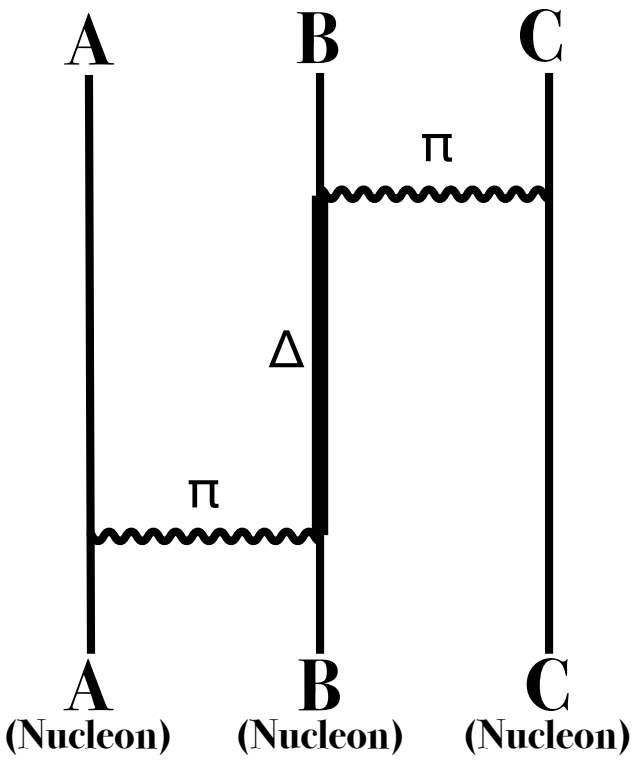

Figure 1.2.2: Schematic figure of the Fujita-Miyazawa type three-body nuclear interaction [35].

constants are determined to reproduce the experimental data [40]. In other words, the form, i.e., ansatz, of the nuclear interaction is based on the effective field theory, while the way to determine the parameters is the same as a conventional realistic one, like the AV14 bare interaction.

The latter, LQCD, is based on a totally different idea. To simulate nuclear interaction in vacuum, the four-dimensional space-time is discretized into a lattice. Two nucleons are put on the lattice, where the nucleon is represented as three quarks. Then, the quantum chromodynamics calculation is performed numerically.

The nuclear interaction derived by ChEFT has been applied to calculations for nuclear structure [44–47] and neutron star properties [48]. In contrast, nuclear interaction obtained by the LQCD calculation has still large numerical uncertainty and thus it has not been applied to the calculation of nuclear properties yet, while it helps one to understand other hadron-hadron interactions [49–52].

1.3 Nuclear Matter

One of the simplest nucleon systems is the homogeneous nucleon gas, called "nuclear matter". Similarly to electronic systems, this homogeneous matter helps one to understand the properties of nuclear interaction and provides a playground for testing many nuclear many-body calculation methods. In addition, as it is the simplest model of the neutron star, calculation of nuclear matter properties provides a relation between the mass and the radius of the neutron star [53], with combining the Tolman-Oppenheimer-Volkoff equation [54–56]. Note that the Coulomb interaction is usually neglected in nuclear matter in order to focus on properties of the nuclear interaction.

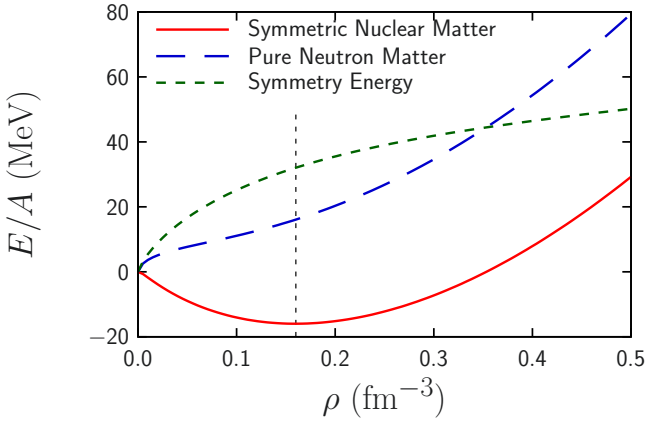

Figure 1.3.1: Equation of state of symmetric nuclear matter and pure neutron matter as functions of the density ρ. The symmetry energy is also shown as a function of the density ρ. The Skyrme interaction with the SLy4 parameter set [58] is used. The dashed vertical line represents the saturation density.

The equation of state (EoS) of nuclear matter, i.e., energy density as a function of the density of nuclear matter, is one of the most interesting topics. The EoS of symmetric nuclear matter ($\rho_p = \rho_n = \rho/2$) and pure neutron matter ($\rho_p = 0$, $\rho_n = \rho$) are plotted in Fig. 1.3.1. In general, the EoS is expanded as

$$\frac{E(\rho,\beta)}{A} = \frac{E(\rho,0)}{A} + E_{\rm sym}(\rho)\,\beta^2 + O\left(\beta^4\right), \tag{1.3.1}$$

where $\rho = \rho_n + \rho_p$ is the total density and $\beta = (\rho_n - \rho_p)/(\rho_n + \rho_p)$ is the isospin asymmetry. Due to the isospin symmetry, E/A must be an even function of β, where the tiny contribution of the ISB terms of the nuclear interaction introduces a term proportional to β [57, A6], which will be discussed later.

As seen in the figure, owing to the symmetry energy, symmetric nuclear matter is more stable than pure neutron matter. This difference ($E_{\rm sym}$ in Eq. (1.3.1)) is called the symmetry energy. This symmetry energy is due to the Pauli principle and the strong attractive nature of the proton-neutron interaction. It is also seen that the symmetric nuclear matter gives the minimum of $E/A \approx -16\,\mathrm{MeV}$ at $\rho_0 \approx 0.16\,\mathrm{fm}^{-3}$ called saturation density, while the pure neutron matter does not give a minimum. This is due to the balance of strong attractive interaction, the repulsive core, and the three-body repulsion.

Here, it is convenient to define several parameters related to EoS:

$$E_{\rm sym}(\rho) = J + L\left(\frac{\rho-\rho_0}{3\rho_0}\right) + \frac{1}{2}K_{\rm sym}\left(\frac{\rho-\rho_0}{3\rho_0}\right)^2 + \ldots, \tag{1.3.2}$$

$$\frac{E(\rho,0)}{A} = E_0 + \frac{1}{2}K_\infty\left(\frac{\rho-\rho_0}{3\rho_0}\right)^2 + \ldots, \tag{1.3.3}$$

where these two equations are the Taylor expansions around the saturation density. The saturation density is defined as the density which gives $P(\rho_0, 0) = 0$, where P is the pressure of nuclear matter defined by

$$\begin{aligned} P(\rho,\beta) &= \rho^2 \frac{\partial}{\partial\rho}\frac{E(\rho,\beta)}{A} \\ &\simeq \frac{K_\infty}{9\rho_0^2}(\rho-\rho_0)\rho^2 + \left[\frac{L}{3\rho_0}\rho^2 + \frac{K_{\rm sym}}{9\rho_0^2}(\rho-\rho_0)\rho^2\right]\beta^2. \end{aligned} \tag{1.3.4}$$

Accordingly, ρ_0 also satisfies

$$\frac{1}{A}\frac{dE(\rho,0)}{d\rho}\bigg|_{\rho=\rho_0} = 0, \tag{1.3.5}$$

i.e., it gives the minimum for $E(\rho,0)/A$. Hence, the first-order term does not appear in Eq. (1.3.3).

These parameters are not directly measured from any experiment. Nevertheless, these values are fundamental quantities of nuclear interaction; hence, they can be extracted by using experimental observables. For instance, the neutron-skin thickness, the difference between the neutron root-mean-square radius and the proton one [59], and some excitation spectra [60–63] are related to the L parameter, and thus measurements

of such parameters are devoted in many experimental facilities. Indeed, the L parameter is estimated by using several experiments as shown in Fig. 1.3.2. In addition, since such parameters represent the behaviour of EoS, neutron-star properties, especially, its mass-radius relation, is constrained by using such parameters obtained by experiments or theory. For example, Fig. 1.3.3 shows the neutron-star mass-radius relation.

1.4 Nuclear Structure and Nuclear Mean Field

The nuclear binding energy was, firstly, successfully described by Weizsäcker and Bethe quantitatively, concerning an atomic nucleus as a liquid drop with almost constant density ρ_0 [109, 110], in which no quantum effect is taken into account. In contrast, several atomic nuclei with specific proton or neutron numbers, such as Z or N = 8, 20, 28, 50, 82, and 126, called magic numbers, are known to be more stabilized. This is because protons and neutrons form "shell structure", and the shell is closed at magic numbers, for the same reason as to why the noble gas atoms are stable and significantly low reactivity, and at the magic numbers, there exist gaps called shell gaps.

The existence of this shell structure implies that atomic nuclei can be well described by using an independent particle model, similarly to the atoms, despite the strong attractive interaction. The magic numbers were also successfully described by the three-dimensional isotropic harmonic oscillator or square well potential with the strong spin-orbit interaction [111–113]. The spin-orbit interaction binds the $j = l + 1/2$ orbitals stronger, while $j = l - 1/2$ orbitals weaker in the atomic nuclei, whereas it behaves oppositely in the atoms.

The atomic nuclei whose proton and neutron numbers are both magic numbers, called doubly-magic nuclei, are known much more stable than the other nuclei. This is explained by the Cooper pair between two protons and that between two neutrons [114]. Protons or neutrons above the shell gap form pairs with the angular momentum 0^+. Accordingly, the ground states of all the nuclei with even Z and N, called even-even nuclei, are 0^+. In addition, the occupation probability of each orbital above the shell gap becomes a rational number. The atomic nuclei which are not even-even nuclei have remaining one proton and/or one neutron, which cannot form the like-particle Cooper pair. Eventually, such nuclei are less stable than the even-even nuclei. The existence of the Cooper pair between a proton and a neutron and its effect on nuclear properties have been argued but not yet settled [115–120].

At last, the shape of atomic nuclei is focused on. It is known that many atomic nuclei show "collective deformation" in which not only valence nucleons but also all the nucleons participate in the deformation. This collective deformation can be regarded as that the nuclear mean field itself is deformed.

Apart from the collective deformation, several different types of deformation are also known, such as core-plus-one-nucleon deformation and cluster states. The former is the deformation of an atomic nucleus whose configuration is the doubly-magic core plus one valence nucleon. The doubly-magic nuclei are spherical, which will be explained later, and thus, it is expected that the deformation of the nucleus is due to the valence nucleon. Nevertheless, the strong interaction between the core and the valence nucleon may induce the core deformation, and accordingly, the deformation may be larger than the one-valence nucleon level [121–125]. The latter is that the nucleons inside some atomic nuclei form α-particle clusters, and some neutrons sometimes behave as electrons in covalent bonds [126–134, A14, A19].

To describe the deformation, the angle-dependent radius of an atomic nucleus is denoted by $R(\theta, \varphi)$, which corresponds to the shape of the surface of the nucleus. The origin of the coordinate is the center of mass of the nucleus. This $R(\theta, \varphi)$ can be expanded as

$$R(\theta, \varphi) = R_0 \left[1 + \sum_{l=2}^{\infty} \sum_{m=-l}^{l} a_{lm} Y_{lm}^{*}(\theta, \varphi) \right], \tag{1.4.1}$$

where Y_{lm} is the spherical harmonics. Neither $l = 0$ nor $l = 1$ component is considered in Eq. (1.4.1) because $l = 0$ is absorbed in R_0 and $l = 1$ corresponds to the shift of the center of mass at the first order. If one focuses on the quadrupole deformation, Eq. (1.4.1) is reduced to

$$\begin{aligned} R(\theta, \varphi) &= R_0 \left[1 + \beta \cos\gamma Y_{2\,0}(\theta, \varphi) + \frac{\beta}{\sqrt{2}} \sin\gamma Y_{2\,+2}(\theta, \varphi) + \frac{\beta}{\sqrt{2}} \sin\gamma Y_{2\,-2}(\theta, \varphi) \right] \\ &= R_0 \left[1 + \sqrt{\frac{5}{16}} \beta \left\{ \cos\gamma \left(3\cos^2\theta - 1 \right) + \sqrt{3} \sin\gamma \sin^2\theta \cos 2\varphi \right\} \right] \end{aligned} \tag{1.4.2}$$

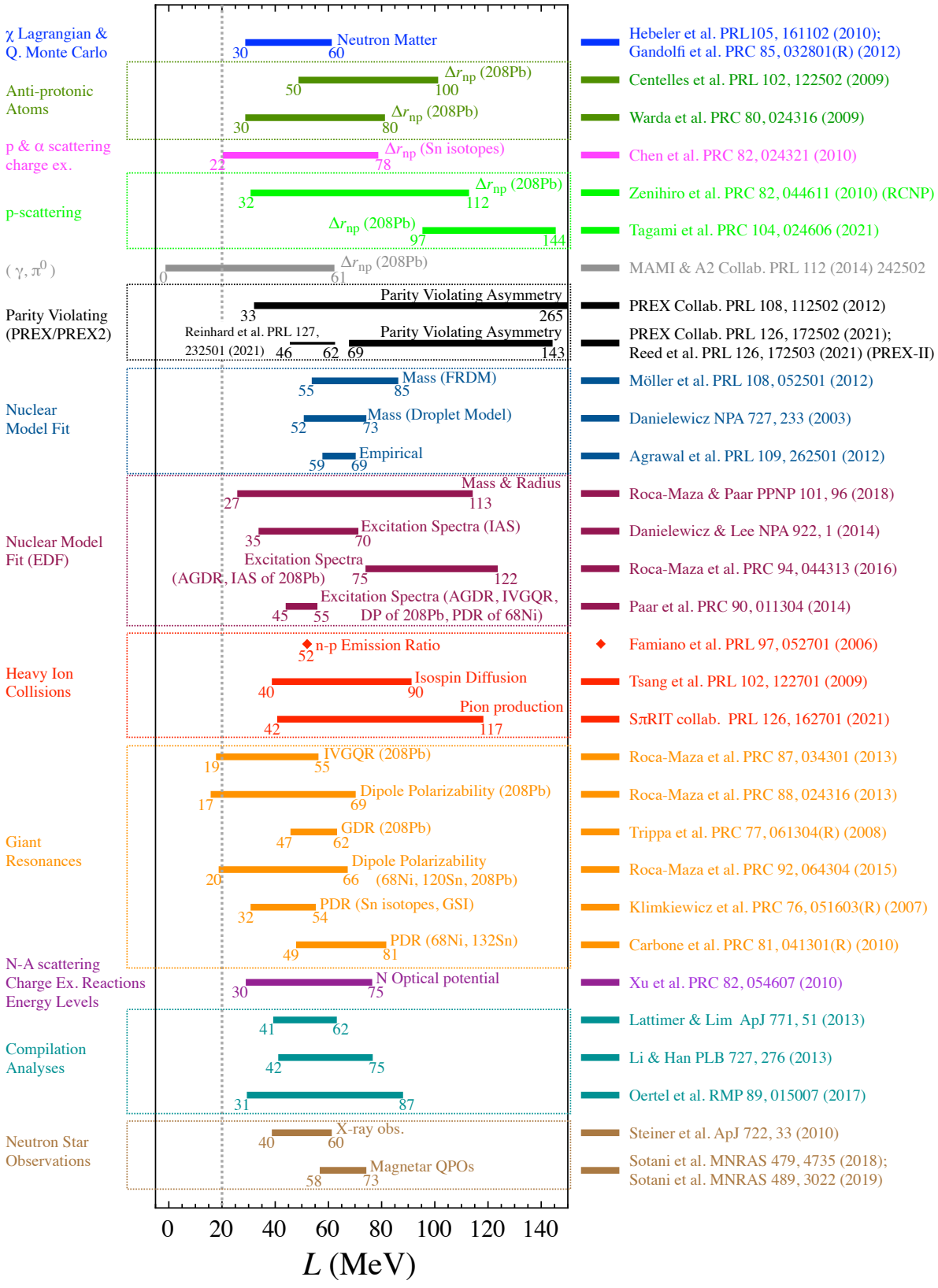

Figure 1.3.2: Estimation of the density dependence of the symmetry energy in the nuclear equation of state, L, by using several experiments combined with theoretical estimation [48, 61–94]. The vertical line is the lower limit of the L parameter obtained in Ref. [95]. This figure is taken from Ref. [A12].

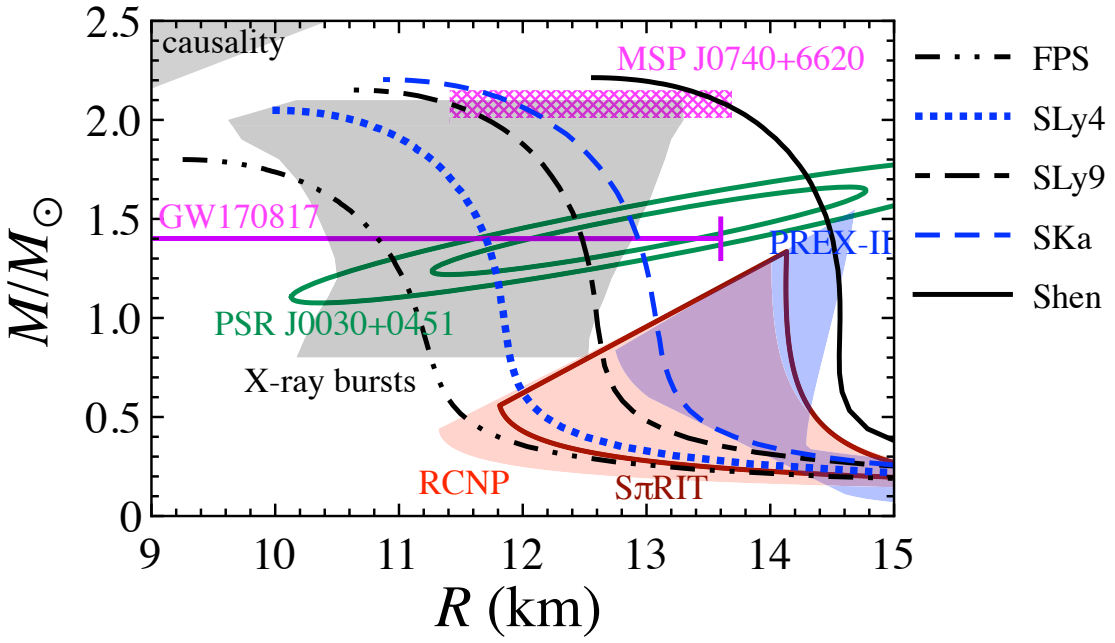

Figure 1.3.3: Neutron star mass (M) and radius (R) relation calculated from several nuclear equation of states [58,96–99]. The mass is normalized with the solar mass $M_\odot$. Constraints from maximum mass observation using the Shapiro delay (MSP J0740+6620) [100,101], gravitational wave observation (GW170817) [102], NICER (PSR J0030 + 0451) [103–105], X-ray burst [106], and causality [107] are shown. Constraint with an empirical formula [108] and L parameter obtained by several recent nuclear experiments [73, 91, 92] are also shown at the bottom right region. This figure is taken from Ref. [A12].

with $\beta > 0$ and $0 \leq \gamma < 2\pi$, where $\beta = 0$ corresponds to the spherical shape [3]. If one is only interested in the axial-deformed nuclei, possible values of γ are $n\pi/3$ ($n = 0, 1, \ldots, 5$). Then, $\beta > 0$ with $\gamma = (2n+1)\,\pi/3$ are identical to $\beta < 0$ with $\gamma = 2n\pi/3$. Hence, if one defines the symmetric axis of the axial deformation as z' axis, Eq. (1.4.2) is simplified to

$$R(\theta', \varphi') = R_0 \left[1 + \sqrt{\frac{5}{16\pi}} \beta \left(3\cos^2\theta - 1 \right) \right], \tag{1.4.3}$$

where both negative and positive numbers of β are allowed.

Figure 1.4.1 shows the schematic figure of axial quadrupole deformation. It is known that more nuclei show prolate deformation than oblate one, which may be due to the property of nuclear interaction, while it is not completely unrevealed yet [135–139]. It is also known that the doubly-magic nuclei are spherical, since all possible magnetic quantum numbers m for each orbital are occupied: $\sum_m |Y_{lm}(\theta, \varphi)|^2 = (2l+1)/4\pi$.

The origin of nuclear deformation has been discussed for a long time. It was shown that the proton-neutron strong isoscalar ($T = 0$) interaction induces nuclear deformation [140]. Recently, we proved both numerically and analytically in Ref. [A10] that even a neutron drop, a system in which neutrons are confined to isotropic harmonic oscillator potential, can also be deformed, and such collective deformation occurs due to the strong attractive interaction. Thus, it should also be noted that the central Coulomb potential is not sufficient to describe the reason why isolated atoms are spherical, and the repulsive nature of the Coulomb interaction is essential.

At last, a nucleon density distribution is revisited. Here, ρ_p and ρ_n denote the distributions of center-of-mass of protons and neutrons, respectively. They correspond to that one regards protons and neutrons as pointwise particles. Since the nuclear interaction is denoted as the interaction between pointwise nucleons, ρ_p and ρ_n can be measured by using hadron (nucleon) scattering.

The charge density distribution $\rho_{\rm ch}$ is also important, which can be measured by using the electron scattering [141–146]. Since protons and neutrons are composite particles, they have internal structures, and

[3] In the other sections, β denotes the isospin asymmetry. Only in this section, β denotes the deformation parameter.

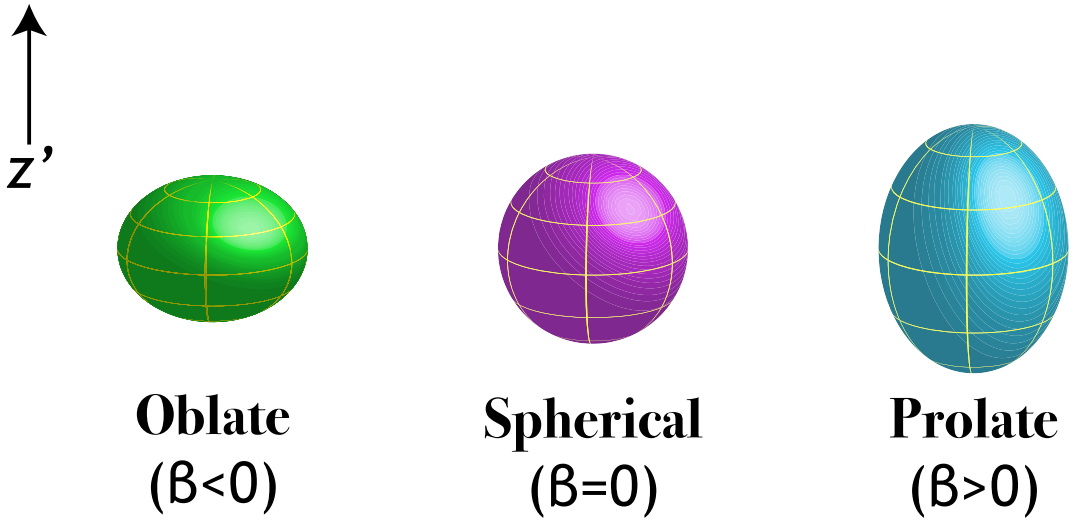

Figure 1.4.1: Schematic figure of axial quadrupole deformation. This figure is taken from Ref. [A10].

accordingly, finite charge density distributions, as shown in Fig. 1.4.2, whose spatial integral corresponds to the net charge. Therefore, these nucleon charge distributions must be taken into account for ρ_{ch}, and eventually, it can be calculated as [147, A18]

$$\tilde{\rho}_{\mathrm{ch}}(q) = \tilde{\rho}_p(q)\,\tilde{G}_{\mathrm{E}p}(q) + \tilde{\rho}_n(q)\,\tilde{G}_{\mathrm{E}n}(q) \tag{1.4.4}$$

in the lowest order, where $\tilde{\rho}$ is the Fourier transform of ρ defined by

$$\tilde{\rho}(q) = \int \rho(r)\, e^{-i\boldsymbol{q}\cdot\boldsymbol{r}}\, d\boldsymbol{r} = 4\pi \int_0^\infty \rho(r)\, \frac{\sin(qr)}{qr} r^2\, dr \tag{1.4.5}$$

and $\tilde{G}_{\mathrm{E}\tau}$ is the electric form factor of nucleon τ. The contribution of the magnetic form factor to $\tilde{\rho}_{\mathrm{ch}}$ is the higher-order with respect to the light speed c.

There are several definition of the Fourier transform. The electric form factor $\tilde{G}_{\mathrm{E}\tau}$ is usually normalized as $\tilde{G}_{\mathrm{E}p}(0) = 1$ and $\tilde{G}_{\mathrm{E}n}(0) = 0$. If the Fourier and the inverse Fourier transforms are, respectively, defined by

$$\tilde{f}(\boldsymbol{q}) = C \int f(\boldsymbol{r})\, e^{-i\boldsymbol{q}\cdot\boldsymbol{r}}\, d\boldsymbol{r}, \tag{1.4.6}$$

$$f(\boldsymbol{r}) = \frac{(2\pi)^{-3}}{C} \int \tilde{f}(\boldsymbol{q})\, e^{i\boldsymbol{q}\cdot\boldsymbol{r}}\, d\boldsymbol{q}, \tag{1.4.7}$$

where C may be 1, $(2\pi)^{-3/2}$, or $(2\pi)^{-3}$,

$$\tilde{G}_{\mathrm{E}\tau}(0) = C \int G_{\mathrm{E}\tau}(r)\, d\boldsymbol{r} \tag{1.4.8}$$

holds. Since $G_{\mathrm{E}\tau}$ corresponds to the charge distribution of a nucleon τ, the right-hand side of Eq. (1.4.8) should be C for $\tau = p$ and 0 for $\tau = n$. Therefore, $C = 1$ is used in this thesis.

1.5 Isospin Symmetry Breaking of Nuclear Interaction

Up to now, the nuclear interaction is assumed to have the isospin symmetry. Hence, the nuclear interaction between two protons, v_{pp}, that between two neutrons, v_{nn}, and that between a proton and a neutron with the total isospin $T = 1$ channel, $v_{pn}^{T=1}$, are assumed to be the same, while that between a proton and a neutron with the total isospin $T = 0$ channel, $v_{pn}^{T=0}$ is not; $v_{pp} \equiv v_{nn} \equiv v_{pn}^{T=1}$ and $v_{pn}^{T=1} \not\equiv v_{pn}^{T=0}$.

However, in fact, the isospin symmetry of the nuclear interaction is slightly broken. The isospin symmetry breaking (ISB) channel of the nuclear interaction is separated into two classes: the charge symmetry breaking (CSB) and the charge independence breaking (CIB). The charge symmetry and the charge independence

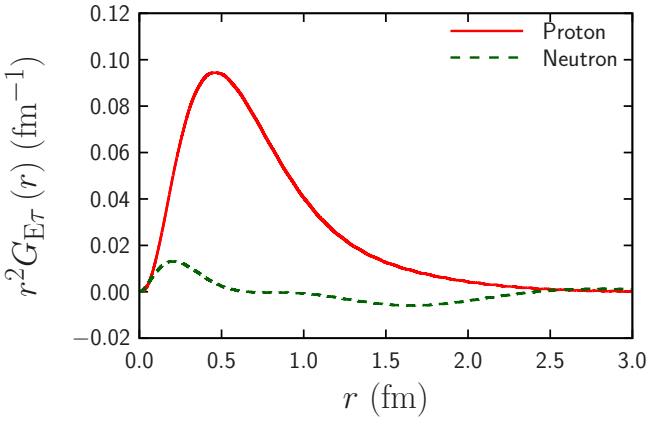

Figure 1.4.2: Nucleon charge density distributions $G_{\mathrm{E}\tau}(r)$ as functions of r. Electric form factors $\tilde{G}_{\mathrm{E}\tau}$ proposed in Ref. [148] are used.

correspond to symmetry under the $z \to -z$ transformation and arbitrary rotation in the isospace, respectively. The charge independence includes the charge symmetry, while the charge independence apart from the charge symmetry is simply referred to as the charge independence in this thesis. Therefore, the CSB corresponds to the fact that the proton-proton nuclear interaction is not the same as the neutron-neutron one, $v_{pp} \not\equiv v_{nn}$. The CIB corresponds to the fact that proton-neutron nuclear interaction in $T = 1$ channel is not identical to the nuclear interaction between the same particle. Due to the charge symmetry breaking, the CIB is defined by $v_{pn}^{T=1} \not\equiv (v_{pp} + v_{nn})/2$.

These CSB and CIB nuclear interactions can be defined more precisely in the context of the meson exchange. The two-body nuclear interaction, including the isospin symmetric part, is classified into four classes [149–153].

Class I Nuclear interaction with charge and isospin independence, i.e., which satisfies $\left[v_{jk}^{\mathrm{I}}, \boldsymbol{T}\right] = 0$, whose form is

$$v_{jk}^{\mathrm{I}} \sim a + b\boldsymbol{\tau}_j \cdot \boldsymbol{\tau}_k. \tag{1.5.1}$$

Class II Nuclear interaction with charge symmetry which breaks charge independence, whose form is

$$v_{jk}^{\mathrm{II}} \sim cT_{jk}. \tag{1.5.2}$$

Class III Nuclear interaction which breaks both charge independence and charge symmetry but is symmetric under the interchange between particles j and k, whose form is

$$v_{jk}^{\mathrm{III}} \sim d\left(\tau_{zj} + \tau_{zk}\right), \tag{1.5.3}$$

which satisfies $\left[v_{jk}^{\mathrm{III}}, \boldsymbol{T}^2\right] = 0$.

Class IV Nuclear interaction which breaks both charge independence and charge symmetry, and additionally, satisfies $\left[v_{jk}^{\mathrm{IV}}, \boldsymbol{T}^2\right] \neq 0$, whose form is

$$v_{jk}^{\mathrm{IV}} \sim e\left(\tau_{zj} - \tau_{zk}\right) + f\left(\boldsymbol{\tau}_j \times \boldsymbol{\tau}_k\right)_z. \tag{1.5.4}$$

Here, T_{jk} is the isotensor operator defined by

$$T_{jk} = 3\tau_{zj}\tau_{zk} - \boldsymbol{\tau}_j \cdot \boldsymbol{\tau}_k \tag{1.5.5}$$

and $\boldsymbol{T}$ is the two-body total isospin operator defined by $\boldsymbol{T} = (\boldsymbol{\tau}_j + \boldsymbol{\tau}_k)/2$. The CIB and CSB interactions discussed above correspond to class II and class III, respectively.

The CIB (class II) interaction originates from the mass difference between charged pions $\pi^{\pm}$ and neutral ones π^0 [154,155] in the one- and two-pion exchange potentials. In contrast, the CSB (class III) one originates

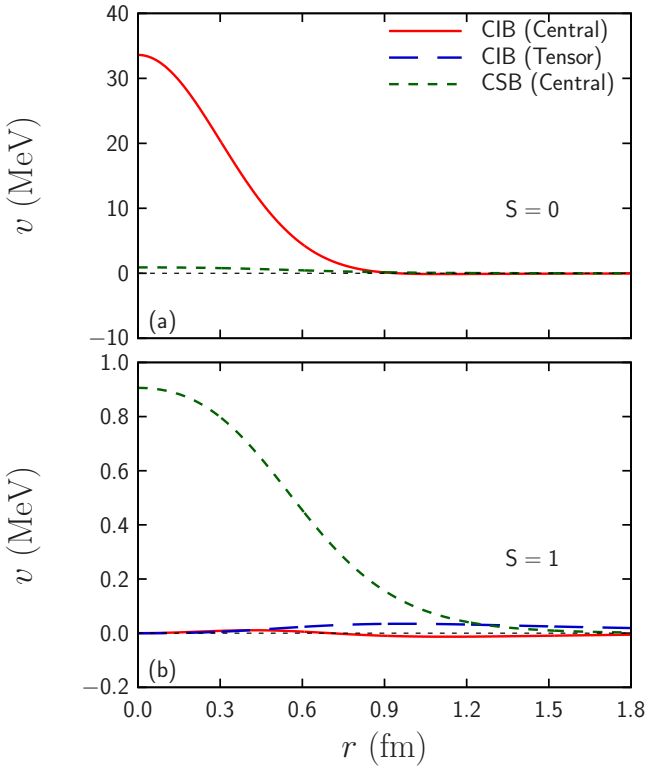

Figure 1.5.1: Radial dependence of the charge independence breaking (CIB) and charge symmetry breaking (CSB) interactions in the AV18 interaction [167].

from the mass difference between protons and neutrons in the two-pion exchange potential and π^0-η and ρ^0-ω mixings throughout the meson-exchange process which is mainly due to the electromagnetic interaction [156–161].

The ISB of nuclear interaction has also been studied by using the chiral EFT [152, 162–165] and boson-exchange picture [166]. Reference [162] proved by using the analysis of the QCD Lagrangian that the class I interaction is strongest and the strength of the class $(n+1)$ interaction is $O\left(m_\pi/m_\rho\right) \approx 1/5$ of the class n interaction, where $m_\pi \approx 140\,\mathrm{MeV}/c^2$ and $m_\rho \approx 770\,\mathrm{MeV}/c^2$ are, respectively, masses of π meson and ρ one and m_ρ is chosen as a typical scale of the QCD.

The Argonne V18 (AV18) interaction, one of the most used bare realistic interactions constructed phenomenologically to reproduce experimental data of nucleon scattering and the deuteron bound state, includes ISB terms on top of the AV14 interaction shown in Eq. (1.2.1) [167] as

$$\begin{aligned} v_{\mathrm{nucl}}^{\mathrm{AV18}}\left(\boldsymbol{r}_j,\sigma_j,\tau_j,\boldsymbol{r}_k,\sigma_k,\tau_k\right) = v_{\mathrm{nucl}}^{\mathrm{AV14}}\left(\boldsymbol{r}_j,\sigma_j,\tau_j,\boldsymbol{r}_k,\sigma_k,\tau_k\right) \\ + v_{15}\left(r_{jk}\right) T_{jk} + v_{16}\left(r_{jk}\right)\left(\boldsymbol{\sigma}_j\cdot\boldsymbol{\sigma}_k\right) T_{jk} + v_{17}\left(r_{jk}\right) S_{jk} T_{jk} \\ + v_{18}\left(r_{jk}\right)\left(\tau_{zj}+\tau_{zk}\right), \end{aligned} \tag{1.5.6}$$

where the second and third lines correspond to the CIB and CSB interactions, respectively, and are shown in Fig. 1.5.1. As seen in the figure, the CIB interaction for the spin-singlet channel is much weaker than the isospin symmetric channel, such as the AV14, and the CIB interaction for the spin-triplet channel is further weaker. The CSB interaction is around 30 % of the CIB interaction. These strengths are consistent with the analysis done by van Kolck [162]. Both the CIB and CSB central interactions are repulsive.

1.6 Work in This Thesis

The isospin symmetry breaking of the nuclear interaction is one of the fundamental topics toward understanding the nuclear interaction; hence, it has been studied theoretically for a long time [168–188]. If neither

the ISB terms of the nuclear interaction nor the electromagnetic interaction existed, the isospin symmetry of atomic nuclei would exactly hold. Consequently, the mirror nuclei pair have the same total energies and the excitation spectra, and the proton (neutron) radius of the former is the same as the neutron (proton) radius of the latter. Here, the mirror nuclei pair is a pair of two atomic nuclei, one of which consists of Z protons and N neutrons, and the other consists of N protons and Z neutrons. In $N = Z$ nuclei, the proton radius is identical to the neutron radius. Also, $T_\pm = T_x \pm iT_y$ commutes with the Hamiltonian. Hence, if the ground state of an atomic nucleus is denoted as $|\mathrm{GS},\, Z,\, N\rangle$, multiplets $|\mathrm{GS},\, Z,\, N\rangle$, $T_-\,|\mathrm{GS},\, Z,\, N\rangle$, $T_-^2\,|\mathrm{GS},\, Z,\, N\rangle$, ..., and $T_-^{(N-Z)}\,|\mathrm{GS},\, Z,\, N\rangle = |\mathrm{GS},\, N,\, Z\rangle$ have the same energy and the same total isospin T, while T_z is different. This multiplet is called isospin multiplet.

In reality, both the ISB terms of the nuclear interaction and the electromagnetic interaction exist, isospin symmetry of atomic nuclei is slightly broken. For instance, the mass difference of mirror nuclei and its Okamoto-Nolen-Schiffer anomaly [189,190] is one of the long-standing problems related to isospin symmetry breaking. If there are no ISB terms of the nuclear interaction, the mass difference of mirror nuclei originates from the Coulomb interaction. Nevertheless, it was pointed out in Refs. [189, 190] that the Coulomb interaction is not enough to describe the difference. In particular, the mass difference of mirror nuclei is not described well in the mean-field calculation with the electromagnetic interaction and the isospin symmetric nuclear interaction, which is referred to as the Okamoto-Nolen-Schiffer anomaly [189, 190]. Such topics have long been paid attention to [157–160, 168–172, 189–191].

Two recent experiments related to nuclear properties of mirror nuclei done at the National Superconducting Cyclotron Laboratory (NSCL), Michigan State University, the United States [192] and at the Radioactive Isotope Beam Factory (RIBF), RIKEN, Japan [193] should also be highlighted. In these experiments, it was revealed that the ground state of ^{73}Sr ($Z = 38$, $N = 35$) is revealed to be $J^\pi = 5/2^-$, while that of its mirror ^{73}Br ($Z = 35$, $N = 38$) is $J^\pi = 1/2^-$ [192], and ^{70}Kr ($Z = 36$, $N = 34$) has a different shape from ^{70}Se ($Z = 34$, $N = 36$) [193].

The proton-skin thickness, i.e., the difference between the proton radius and the neutron one, of $N = Z$ nuclei [194], the mass difference between the ground state of an atomic nucleus $|\mathrm{GS},\, N,\, Z\rangle$ and its analogue state $T_-\,|\mathrm{GS},\, N,\, Z\rangle$, called isobaric analogue energy [84, 183, 195], and masses of isospin multiplet called isospin multiplet mass equation [184,187,196–198] are also related to isospin symmetry breaking. It becomes a hot topic again because experimental techniques have been developed rapidly and accordingly exotic nuclei, especially, neutron-rich nuclei, have been synthesized and various properties have been measured precisely.

The isospin symmetry breaking of the nuclear interaction is also related to the flavour symmetry breaking of the quarks, i.e., the unitarity of the Cabibbo-Kobayashi-Maskawa (CKM) matrix [199, 200], which represents the flavour symmetry of the quarks. If the CKM matrix is not unitary, it indicates that there may be the fourth generation of quarks. The largest component of the CKM matrix, V_{ud}, can be estimated by using the half-lives of the superallowed β decay [174, 182, 201–205]. To extract V_{ud} from the half-lives of the superallowed β decay, the electromagnetic contribution and the ISB terms of the nuclear interaction must be estimated properly. Thus, the study of the isospin symmetry breaking of the nuclear interaction has indispensable to study not only for nuclear physics itself but also for particle physics.

The nuclear density functional theory (DFT) [206–209] is one of the strong methods toward discussion for such topics, where the nuclear DFT will be explained in detail in Sec. 2.3. At this moment, the nuclear DFT is only the method that can be applied to the whole nuclear chart [210]. The accuracy of the nuclear DFT is governed by the accuracy of the nuclear energy density functional (EDF), i.e., the effective interaction in medium. Improvement of the accuracy of the nuclear interaction in medium, in other words, the nuclear EDF, is also an important topic in nuclear physics. As will be discussed in Sec. 2.3, most nuclear EDFs have been derived with fitting to experimental data. The root-mean-square deviation between masses obtained theoretically using one of the most widely used EDFs, the SLy4 EDF [58], and experimental masses is 4.80 MeV [211] and that by the recent one, the UNEDF0, is 1.45 MeV [212]. In contrast, those of empirical mass formulae [213, 214] and the recent technique of machine learning [215, 216] predict masses of atomic nuclei within the order of 100 keV accuracy. In addition, to study nucleosynthesis in the universe, such as the r-process [217–219], masses and half-lives of atomic nuclei of the more exotic region, particularly more neutron-rich nuclei, than measured are required precisely. For example, masses with 100 keV accuracy is required to study the r-process path [220].

To improve the accuracy of a nuclear EDF, first, what is known should be estimated and subtracted precisely as much as possible, since the nuclear EDF is fitted to experimental data. Here, what is known is

the electromagnetic interaction. Estimation of the electromagnetic interaction will help one to evaluate the ISB terms of the nuclear EDF as well, since the isospin symmetry breaking of nuclear properties originates from both the Coulomb interaction and the ISB terms of the nuclear EDF; hence, to isolate effects originating from the ISB terms of the nuclear interaction from the experimental data, effects originating from the electromagnetic interaction is needed to be subtracted properly. Nevertheless, treatment of the Coulomb interaction in nuclear DFT has not been accurate enough, compared to the condensed matter DFT; the Coulomb LDA exchange EDF (the Hartree-Fock-Slater approximation) is used or the Coulomb exchange term is even neglected.

Motivated by the improvement of the nuclear EDF and by the study of the isospin symmetry breaking of atomic nuclei, we shall develop an accurate treatment of the Coulomb interaction in nuclear DFT in Chap. 3. First, by using knowledge of DFT in condensed matter physics—the generalized gradient approximation (GGA)—, the density gradient effect will be taken into account for the Coulomb exchange EDF in order to reproduce the Coulomb exact Fock energy. This is the first attempt of the GGA exchange EDF to the nuclear structure calculation. On top of it, higher-order correction to the electromagnetic interaction is discussed: the finite spatial charge distribution of nucleons, the vacuum polarization, the electromagnetic spin-orbit interaction, and the finite-light-speed correction to the Coulomb interaction. Since EDFs are written in terms of densities, instead of single-particle orbitals, the charge distribution of nucleons, which is implemented in form factors, can be easily considered. Some works have considered the charge distribution of nucleons, while it will be shown later that the effect is not taken into account properly. As will explain later, the vacuum polarization and the electromagnetic spin-orbit interaction have been introduced in Ref. [183], while we shall firstly show their systematic behaviours. It will also be shown that the mass difference of the mirror nuclei pair ^{48}Ca and ^{48}Ni can be reproduced by considering the density gradient in the Coulomb exchange EDF, the nuclear finite-size effect, the vacuum polarization, and the electromagnetic spin-orbit interaction, as well as the ISB terms of the nuclear interaction.

In Chap. 4, we shall compare the effect of the Coulomb interaction and the ISB terms of the nuclear interaction on nuclear properties related to the isospin symmetry breaking, the neutron-skin thickness and the mass difference of mirror nuclei. It will be shown that the CSB term of the nuclear interaction affects nuclear properties appreciably, while the CIB term affects only slightly or even does not affect. Since the accurate treatment of the electromagnetic interaction is achieved in this thesis, a comparative study between the electromagnetic interaction and the ISB terms of the nuclear interaction on nuclear properties is shown at the first time. It will also be shown that the ISB terms of the nuclear interaction affect the estimation of the L parameter of the nuclear EoS approximately in 10 MeV. We shall also show that the isospin symmetric terms of the nuclear EDF do not affect the dependence on the CSB strength on nuclear properties: This fact leads to a way to pin down the strength of the CSB term of the nuclear EDF using the *ab initio* calculation results.

In order to discuss such topics, Chap. 2 will provide the theoretical framework of this thesis: the density functional theory. At last, Chap. 5 is devoted to the conclusion of this thesis and perspectives.

Chapter 2

Theoretical Framework

The many-body systems of nucleons—the atomic nuclei—and the many-body systems of electrons—the atoms, molecules, and solids—share common properties, such as "magic numbers" and "noble gases" emerging from the shell closure [221,222]. Accordingly, similar calculation methods for electronic systems are also used for nuclear systems, although there is also a significant difference due to the difference of the interaction and the existence of external potential. Particularly, owing to the simpleness of the Coulomb interaction, many calculation methods have been developed accurately. Many properties of atoms, molecules, and solids can be approached experimentally; hence, the validity and the accuracy of many-body calculation methods have been understood well, and more calculation methods have been developed.

In this chapter, we shall explain the theoretical framework of this thesis, density functional theory. First, density functional theory for electronic systems are introduced, and then its application to nuclear physics is explained.

2.1 Quantum Many-Body Problems

All the things surrounding us are composed of atoms; an atom is composed of the atomic nucleus and many electrons; an atomic nucleus is composed of many protons and many neutrons. Electrons of atoms, molecules, and solids and protons and neutrons of atomic nuclei obey the Schrödinger or Dirac equation. Such systems, composed of many fermions, are referred to as "quantum many-body problems" altogether. Since properties of atoms, molecules, and solids are mainly determined by the "motion" of electrons, i.e., by the so-called electronic structure, and those of atomic nuclei are determined by the "motion" of nucleons—protons and neutrons—, it is indispensable to solve quantum many-body problems to understand such properties.

The Hamiltonian of the quantum many-body problems, in general, reads

$$H = -\sum_{j=1}^{N} \frac{\hbar^2}{2m_j} \Delta_j + \sum_{j=1}^{N} V_{\mathrm{ext}}\left(\boldsymbol{r}_j\right) + \sum_{1 \le j < k \le N} v_{\mathrm{int}}\left(\boldsymbol{r}_j, \boldsymbol{r}_k\right), \tag{2.1.1}$$

where m_j and $\boldsymbol{r}_j$ are the mass and the spatial coordinate of the particle j, Δ_j is the laplacian acting on $\boldsymbol{r}_j$, N is the total number of the particles, V_{ext} is the external field, and v_{int} is the two-body interaction. For simplicity, we consider the non-relativistic Schödinger equation and V_{ext} and v_{int} depend only on spatial coordinates. Furthermore, only the two-body interaction is considered here, while, in nuclear physics, it is known that the three-body interaction is indispensable to describe excitation spectra of the light nuclei [24, 35]. If one regards Eq. (2.1.1) as the Hamiltonian for the electronic systems, the motions of ions (atomic nuclei) are not considered in the Hamiltonian and are treated classically, which is called Born-Oppenheimer approximation [223]. Hereinafter, x_j abbreviates the combination of the spatial coordinate $\boldsymbol{r}_j$, the spin coordinate σ_j, and in some cases, the isospin τ_j.

In principle, once the ground-state wave function Ψ_{gs} of Eq. (2.1.1), which satisfies

$$H\Psi_{\mathrm{gs}}\left(\boldsymbol{r}_1, \boldsymbol{r}_2, \ldots, \boldsymbol{r}_N\right) = E_{\mathrm{gs}}\Psi_{\mathrm{gs}}\left(\boldsymbol{r}_1, \boldsymbol{r}_2, \ldots, \boldsymbol{r}_N\right), \tag{2.1.2}$$

is obtained, all the ground-state properties can be calculated. However, in practice, it is difficult to solve the eigenvalue problem [Eq. (2.1.2)] even numerically. Therefore, efficient methods are needed to obtain E_{gs} and

$\Psi_{\rm gs}$ or the ground-state density $\rho_{\rm gs}$ defined by

$$\begin{aligned}\rho_{\rm gs}(\boldsymbol{r}) &= \sum_j \int \Psi^*_{\rm gs}(\boldsymbol{r}_1, \boldsymbol{r}_2, \ldots, \boldsymbol{r}_N)\, \delta(\boldsymbol{r} - \boldsymbol{r}_j)\, \Psi_{\rm gs}(\boldsymbol{r}_1, \boldsymbol{r}_2, \ldots, \boldsymbol{r}_N)\, d\boldsymbol{r}_j \\ &= N \int \Psi^*_{\rm gs}(\boldsymbol{r}, \boldsymbol{r}_2, \ldots, \boldsymbol{r}_N)\, \Psi_{\rm gs}(\boldsymbol{r}, \boldsymbol{r}_2, \ldots, \boldsymbol{r}_N)\, d\boldsymbol{r}_2\, d\boldsymbol{r}_3\, \ldots d\boldsymbol{r}_N. \end{aligned} \tag{2.1.3}$$

Historically, just several years after the *discovery* of the Schrödinger equation in 1926 [224–228], efficient methods to solve quantum many-body problems, for instance the Thomas-Fermi model [229, 230] and the Hartree-Fock theory [231–236], were developed for the calculation of atomic structure. In the former approach, a many-body fermionic system is treated as an interacting Fermi gas without considering an equation of motion of each particle. Since in the homogeneous Fermi gas in an $L \times L \times L$ cubic with the periodic boundary condition, a single-particle orbital can be written as a plane wave $L^{-3/2} e^{i\boldsymbol{k}\cdot\boldsymbol{r}}$, the kinetic energy reads

$$\begin{aligned} T_0(n) &= -\frac{\hbar^2}{2m} 2L^{-3} \sum_j \int e^{-i\boldsymbol{k}\cdot\boldsymbol{r}}\, \Delta\, e^{i\boldsymbol{k}\cdot\boldsymbol{r}}\, d\boldsymbol{r} \\ &= \frac{\hbar^2}{2m} \frac{2}{V} \sum_j k^2 V \\ &= \frac{2\hbar^2}{2m} \left(\frac{L}{2\pi}\right)^3 \int_{k<k_{\rm F}} k^2\, d\boldsymbol{k} \\ &= \frac{2\hbar^2}{2m} \left(\frac{L}{2\pi}\right)^3 4\pi \int_0^{k_{\rm F}} k^4\, dk \\ &= \frac{2\hbar^2}{2m} \left(\frac{L}{2\pi}\right)^3 \frac{4\pi}{5} k_{\rm F}^5 \\ &= \frac{\hbar^2}{2m} \frac{k_{\rm F}^5}{5\pi^2} V, \end{aligned} \tag{2.1.4}$$

where $k_{\rm F}$ is the Fermi momentum and $V = L^3$ is the volume of the cubic. Here, n is the homogeneous density and satisfies

$$\begin{aligned} n &= \frac{2}{V} \sum_j e^{-i\boldsymbol{k}\cdot\boldsymbol{r}} e^{i\boldsymbol{k}\cdot\boldsymbol{r}} \\ &= \frac{2}{V} \sum_j 1 \\ &= \frac{2}{V} \left(\frac{L}{2\pi}\right)^3 \int_{k<k_{\rm F}} d\boldsymbol{k} \\ &= \frac{1}{3\pi^2} k_{\rm F}^3, \end{aligned} \tag{2.1.5}$$

where the factor 2 appeared in the first line is due to the spin degeneracy [1]. Accordingly, Eq. (2.1.4) reads

$$T_0(n) = \frac{\hbar^2}{2m} \frac{3^{5/3}\pi^{4/3}}{5} n^{5/3} V = \frac{3h^2}{10m} \left(\frac{3}{8\pi}\right)^{2/3} n^{5/3} V. \tag{2.1.6}$$

In the Thomas-Fermi approximation, the kinetic energy density is approximated as the same of the homogeneous system with the same local density, which reads

$$\begin{aligned} T_{\rm TF}[\rho] &= \int \frac{T_0(\rho(\boldsymbol{r}))}{V}\, d\boldsymbol{r} \\ &= \frac{3h^2}{10m} \left(\frac{3}{8\pi}\right)^{2/3} \int [\rho(\boldsymbol{r})]^{5/3}\, d\boldsymbol{r}, \end{aligned} \tag{2.1.7}$$

where ρ is the particle-number density of the system. The external potential energy simply reads

$$E_{\rm ext}[\rho] = \int V_{\rm ext}(\boldsymbol{r})\, \rho(\boldsymbol{r})\, d\boldsymbol{r}. \tag{2.1.8}$$

[1] Since n is a constant number in contrast to $\rho(\boldsymbol{r})$, the symbol n is used instead of ρ to distinguish two.

The interaction energy is treated classically within the Hartree approximation

$$E_{\mathrm{H}}[\rho] = \frac{1}{2}\iint v_{\mathrm{int}}(\boldsymbol{r},\boldsymbol{r}')\,\rho(\boldsymbol{r})\,\rho(\boldsymbol{r}')\;d\boldsymbol{r}\,d\boldsymbol{r}'. \tag{2.1.9}$$

This approach allows one to obtain the ground-state density distribution ρ_{gs} easily by minimizing the Thomas-Fermi total energy with respect to the density ρ. Owing to this simplicity, it has been widely used not only in condensed matter physics but also in nuclear physics [237–239] and astrophysics [240–242]. It is also used to study the stability of atoms or molecules mathematically [243, 244]. It was, however, claimed that the Thomas-Fermi approach cannot describe the shell structure of atoms and the molecular binding properly [245].

In the latter approach—the Hartree-Fock theory—, the ground-state wave function Ψ_{gs} is approximated to the Slater determinant Φ_0 to satisfy the Pauli exclusion principle. The Slater determinant Φ_0 gives the exact ground-state wave function if the interaction does not exist; $v_{\mathrm{int}} \equiv 0$. In the Hartree-Fock approximation, single-particle orbitals of the Slater determinant are determined from the variation of the expectation value of H; that is,

$$\delta\frac{\langle\Phi_0|H|\Phi_0\rangle}{\langle\Phi_0|\Phi_0\rangle} = 0. \tag{2.1.10}$$

This equation leads to the so-called Hartree-Fock equation for the single-particle orbitals φ_j in the Slater determinant;

$$\left[-\frac{\hbar^2}{2m_j}\,\Delta + V_{\mathrm{ext}}(\boldsymbol{r}) + V_{\mathrm{H}}(\boldsymbol{r})\right]\varphi_j(\boldsymbol{r}) - \int V_{\mathrm{F}}(\boldsymbol{r},\boldsymbol{r}')\,\varphi_j(\boldsymbol{r}')\;d\boldsymbol{r}' = \varepsilon_j\varphi_j(\boldsymbol{r}), \tag{2.1.11}$$

$$V_{\mathrm{H}}(\boldsymbol{r}) = \int v_{\mathrm{int}}(\boldsymbol{r},\boldsymbol{r}')\,\rho(\boldsymbol{r}')\;d\boldsymbol{r}', \tag{2.1.12}$$

$$V_{\mathrm{F}}(\boldsymbol{r},\boldsymbol{r}') = \sum_k v_{\mathrm{int}}(\boldsymbol{r},\boldsymbol{r}')\,\varphi_k^*(\boldsymbol{r}')\,\varphi_k(\boldsymbol{r}), \tag{2.1.13}$$

where V_{H} and V_{F} are, respectively, called Hartree and Fock potentials and ε_j is the single-particle energy. The ground-state energy in this approximation reads

$$E_{\mathrm{gs}} \simeq E_{\mathrm{gs}}^{\mathrm{HF}} = \sum_{j\in\mathrm{occ}}\varepsilon_j - \frac{1}{2}\left[\int V_{\mathrm{H}}(\boldsymbol{r})\,\rho(\boldsymbol{r})\;d\boldsymbol{r} - \sum_{j\in\mathrm{occ}}\iint V_{\mathrm{F}}(\boldsymbol{r},\boldsymbol{r}')\,\varphi_j^*(\boldsymbol{r})\,\varphi_j(\boldsymbol{r}')\;d\boldsymbol{r}\,d\boldsymbol{r}'\right]. \tag{2.1.14}$$

It had been applied to practical calculations for light atoms [246, 247]. Since the motion of particles is treated quantum mechanically, the shell structure of atoms can be reproduced, in contrast to the Thomas-Fermi approximation. Nevertheless, the Hartree-Fock approximation cannot reproduce chemical reactions accurately due to the lack of correlation effects [248–257]. For instance, motions of the other electrons may affect the electron, which is included only via the Fock term of the *effective* potential in the single-particle Hamiltonian [Eq. (2.1.11)]. The Fock term represents the interaction for the same spin; hence an effect of the other electrons with the opposite spin lacks.

To consider the many-body correlations in quantum many-body problems properly, numerous many-body methods have been proposed. Such methods are mainly classified into two: the wave function methods and density functional theory (DFT). The formers are, in short, methods providing the ground-state wave function Ψ_{gs} *directly* by diagonalizing the Hamiltonian with some approximations and truncations. In the configuration interaction method, one of the wave function methods, the ground-state wave function Ψ_{gs} is expanded by using Slater determinants with several-particle excitations [258–260]. The coupled-cluster method, which was originally developed in the context of nuclear physics, is a more sophisticated method to take into account Slater determinants with many-particle excitations [261, 262]. Other methods based on many-body perturbation theory [263] and the quantum Monte Carlo method [264, 265] are also of this group. It is known that the wave function methods, in general, provide accurate ground-state energy and wave function, while huge numerical cost is required and therefore it is difficult to apply to larger systems, such as solids and heavy atomic nuclei.

In contrast, the latter method—DFT—is based on a totally different idea than the wave function methods [266–268]. The ground-state energy can be written as a functional, called energy density functional (EDF), of the ground-state density, and one can obtain the ground-state energy and density by minimizing

the EDF. To take into account the effect of quantum mechanics, i.e., shell structure, the Slater determinant is used for the ground-state wave function. In short, owing to the introduction of the EDF and the Slater determinant, the numerical cost is much less than wave function methods, and consequently, DFT can be applied to larger systems; nonetheless, the Hohenberg-Kohn theorem [266], a key theorem of DFT, guarantees that DFT, in principle, provides the exact ground-state energy and density. The next section will be devoted to the introduction of DFT.

2.2 Density Functional Theory

In this section, key ideas of DFT will be explained. In principle, "DFT" refers to a theory in which the energy is described by a functional of the density, and thus the Thomas-Fermi approximation can also be classified as one of the DFTs. However, in practice, DFT mostly refers to the theory based on the Hohenberg-Kohn theorem [266], which is the key theorem of DFT, and the Kohn-Sham scheme [267], which is a practical implementation of DFT.

2.2.1 Hohenberg-Kohn Theorem

The Hohenberg-Kohn theorem is composed of two parts: Theorems 2.2.1 and 2.2.2.

Theorem 2.2.1 (Hohenberg and Kohn [266])**.** Assume the two-body interaction is given and the ground state is not degenerate. There is the one-to-one correspondence between the ground-state density $\rho_{\rm gs}$ and the external potential $V_{\rm ext}$.

The Schrödinger or Dirac equation guarantees that once the external potential $V_{\rm ext}$ is given, the ground-state wave function can be uniquely determined, and consequently, the ground-state density can also be uniquely determined unless the ground state is degenerate. Theorem 2.2.1 claims that, conversely, once the ground-state density $\rho_{\rm gs}$ is given, the external potential which gives the density can be uniquely determined.

Theorem 2.2.2 (Hohenberg and Kohn [266])**.** The ground-state energy $E_{\rm gs}$ can be expressed by using the "universal functional F", whose form is determined only by $v_{\rm int}$ but independent of $V_{\rm ext}$,

$$E_{\rm gs} = \inf_{\rho} \left[F\left[\rho\right] + \int V_{\rm ext}\left(\boldsymbol{r}\right) \rho\left(\boldsymbol{r}\right) \right]. \tag{2.2.1}$$

Proof. First, Theorem 2.2.1 will be proved. Let V_1 and V_2 be two external potentials which give the same ground-state density $\rho_{\rm gs}$. Here, V_1 and V_2 are assumed to be *intrinsically* different; that is, $V_1 - V_2$ is not a constant function and, accordingly, Ψ_1 and Ψ_2 differ from each other. The Hamiltonian corresponding to V_j is denoted by $H_j = T + V_j + v_{\rm int}$ and its ground-state energy and normalized wave function are denoted by E_j and Ψ_j;

$$E_j = \langle \Psi_j | H_j | \Psi_j \rangle .$$

The variational principle leads to an inequality

$$E_1 = \langle \Psi_1 | H_1 | \Psi_1 \rangle < \langle \Psi_2 | H_1 | \Psi_2 \rangle . \tag{2.2.2}$$

Since H_1 can be rewritten as $H_1 = H_2 - V_2 + V_1$, the right-hand side of Eq. (2.2.2) can be calculated as

$$\langle \Psi_2 | H_2 - V_2 + V_1 | \Psi_2 \rangle = E_2 + \int \left[V_1\left(\boldsymbol{r}\right) - V_2\left(\boldsymbol{r}\right) \right] \rho_{\rm gs}\left(\boldsymbol{r}\right) \, d\boldsymbol{r}. \tag{2.2.3}$$

Thus, one obtains

$$E_1 < E_2 + \int \left[V_1\left(\boldsymbol{r}\right) - V_2\left(\boldsymbol{r}\right) \right] \rho_{\rm gs}\left(\boldsymbol{r}\right) \, d\boldsymbol{r}. \tag{2.2.4}$$

Similarly, one also obtains

$$E_2 < E_1 + \int \left[V_2\left(\boldsymbol{r}\right) - V_1\left(\boldsymbol{r}\right) \right] \rho_{\rm gs}\left(\boldsymbol{r}\right) \, d\boldsymbol{r}. \tag{2.2.5}$$

The second term of the right-hand side of Eq. (2.2.4) is non-zero. Hence, comparing Eqs. (2.2.4) and (2.2.5), one obtains

$$E_1 + E_2 < E_1 + E_2, \tag{2.2.6}$$

which is a contradictory inequality. Thus, the assumption is wrong and there is the only one unique external potential which provides the given ground-state density.

The ground-state energy reads

$$\begin{aligned} E_{\mathrm{gs}} &= \inf_{\{\Psi\}} \langle \Psi | T + v_{\mathrm{int}} + V_{\mathrm{ext}} | \Psi \rangle \qquad (2.2.7) \\ &= \inf_{\{\Psi\}} \left[\langle \Psi | T + v_{\mathrm{int}} | \Psi \rangle + \langle \Psi | V_{\mathrm{ext}} | \Psi \rangle \right] \\ &= \inf_{\{\rho\}} \inf_{\{\Psi_\rho\}} \left[\langle \Psi_\rho | T + v_{\mathrm{int}} | \Psi_\rho \rangle + \langle \Psi_\rho | V_{\mathrm{ext}} | \Psi_\rho \rangle \right] \\ &= \inf_{\{\rho\}} \inf_{\{\Psi_\rho\}} \left[\langle \Psi_\rho | T + v_{\mathrm{int}} | \Psi_\rho \rangle + \int V_{\mathrm{ext}}(\boldsymbol{r}) \rho(\boldsymbol{r}) \, d\boldsymbol{r} \right] \\ &= \inf_{\{\rho\}} \left[\inf_{\{\Psi_\rho\}} \langle \Psi_\rho | T + v_{\mathrm{int}} | \Psi_\rho \rangle + \int V_{\mathrm{ext}}(\boldsymbol{r}) \rho(\boldsymbol{r}) \, d\boldsymbol{r} \right], \qquad (2.2.8) \end{aligned}$$

where Ψ_ρ is a trial wave function whose density is a given density ρ. In other words, the ground-state energy, which satisfies the variational principle, can be calculated by minimizing the total energy by changing the wave function which gives the density ρ first, and then minimizing it further by changing the density ρ, instead of changing the wave function Ψ directly [Eq. (2.2.7)]. Theorem 2.2.1 guarantees this two-step minimization. The universal functional F is defined by

$$F[\rho] = \inf_{\{\Psi_\rho\}} \langle \Psi_\rho | T + v_{\mathrm{int}} | \Psi_\rho \rangle . \qquad (2.2.9)$$

□

Note that these two theorems had been proposed in the original paper by Hohenberg and Kohn [266], while the proof shown above was proposed later by Levy [269, 270], and it was further given rigorously by Lieb [271]. Theorem 2.2.1 was also extended to degenerate ground states [272]: Let Ψ_{jk} be a ground-state wave function given by the external potential V_j and $\Psi_j = \sum_k c_{jk} \Psi_{jk}$. Then, one can apply the same proof of Theorems 2.2.1 and 2.2.2. Also, it should be noted that this proof has been rederived to using the Legendre transformation [273] in a more rigorous formalism.

Here, one question arises. Can an arbitrary function of the spatial coordinate $f(\boldsymbol{r})$ be a density? Can each $f(\boldsymbol{r})$ have a corresponding external potential? Such problems were already proposed in Ref. [266]. In the proof of Theorem 2.2.1, it is *implicitly* assumed that the density ρ is a solution of the Schrödinger equation. It is also obvious that there must be some conditions for a function f; for instance, $\int f(\boldsymbol{r}) \, d\boldsymbol{r}$ must be an integer number, otherwise the total particle number becomes a rational number.

The N-representability is a set of conditions in which a function f can be a density. The conditions are the following [274]:

1. A function f must be semi-positive definite,

$$f(\boldsymbol{r}) \geq 0 \qquad \text{for all } \boldsymbol{r}. \qquad (2.2.10)$$

2. The integral over the space of a function f must be an integer number,

$$\int f(\boldsymbol{r}) \, d\boldsymbol{r} = N \in \mathbb{N}. \qquad (2.2.11)$$

3. A function f must be smooth,

$$\int \left| \nabla \sqrt{f(\boldsymbol{r})} \right|^2 d\boldsymbol{r} < \infty. \qquad (2.2.12)$$

If one assumes that the ground-state wave function is described by the Slater determinant, the ground-state kinetic energy density reads $\sum_j |\nabla \varphi_j(\boldsymbol{r})|^2 = \left| \nabla \sum_j \varphi_j(\boldsymbol{r}) \right|^2$, while the ground-state density is $\sum_j |\varphi_j(\boldsymbol{r})|^2$. Therefore, the last point can be understood that the kinetic energy must be finite. Mathematically, the idea of Hohenberg-Kohn universal functionals has been extended for N-representable functionals rigorously called Levy-Lieb functional [269, 271].

The V-representability is whether an arbitrary function f can be a solution of the many-body Schrödinger equation. It was proved in Ref. [274] any N-representable function satisfies the V-representability; however, the exact condition for the V-representability is yet unknown. Meanwhile, by using the N- and V-representabilities, the Hohenberg-Kohn theorem claims that any N-representable function has a corresponding external potential. A schematic figure of these repreesntabilities is shown in Fig. 2.2.1.

2.2.2 Kohn-Sham Scheme

The Hohenberg-Kohn theorem guarantees that there is the exact universal functional F for a given interaction v_{int}. Nevertheless, it does not tell us how to determine F or how to derive ground-state properties using F. The simplest way to derive the ground-state density is just performing variation of Eq. (2.2.1):

$$0 = \frac{\delta}{\delta\rho}\left[F\left[\rho\right] + \int V_{\mathrm{ext}}\left(\boldsymbol{r}\right)\rho\left(\boldsymbol{r}\right)\,d\boldsymbol{r}\right] = \frac{\delta F\left[\rho\right]}{\delta\rho} + V_{\mathrm{ext}}\left(\boldsymbol{r}\right). \tag{2.2.13}$$

However, Eq. (2.2.13) does not provide any quantum mechanical properties, such as shell structure of atoms, similarly to the Thomas-Fermi approximation.

To overcome this problem, Kohn and Sham introduced an idea of orbitals, similarly to the Hartree-Fock approximation [267], and this method is referred to as the Kohn-Sham scheme. In this scheme, the ground-state wave function is assumed to be the Slater determinant,

$$\Phi_0^{\mathrm{gs}}\left(\boldsymbol{r}_1,\boldsymbol{r}_2,\ldots,\boldsymbol{r}_N\right) = \frac{1}{\sqrt{N!}}\begin{vmatrix}\varphi_1\left(\boldsymbol{r}_1\right) & \varphi_1\left(\boldsymbol{r}_2\right) & \cdots & \varphi_1\left(\boldsymbol{r}_N\right)\\ \varphi_2\left(\boldsymbol{r}_1\right) & \varphi_2\left(\boldsymbol{r}_2\right) & \cdots & \varphi_2\left(\boldsymbol{r}_N\right)\\ \vdots & \vdots & \ddots & \vdots\\ \varphi_N\left(\boldsymbol{r}_1\right) & \varphi_N\left(\boldsymbol{r}_2\right) & \cdots & \varphi_N\left(\boldsymbol{r}_N\right)\end{vmatrix}, \tag{2.2.14}$$

and accordingly, the ground-state density can be written as

$$\rho\left(\boldsymbol{r}\right) = \sum_{j=1}^{N}\left|\varphi_j\left(\boldsymbol{r}\right)\right|^2, \tag{2.2.15}$$

where the single-particle orbitals are assumed to be orthonormal,

$$\int \varphi_j^*\left(\boldsymbol{r}\right)\varphi_k\left(\boldsymbol{r}\right)\,d\boldsymbol{r} = \delta_{jk}. \tag{2.2.16}$$

Furthermore, the universal functional F is divided into three parts;

$$F\left[\rho\right] = T_{\mathrm{KS}} + E_{\mathrm{H}}\left[\rho\right] + E_{\mathrm{xc}}\left[\rho\right], \tag{2.2.17}$$

where T_{KS} is the Kohn-Sham kinetic energy defined by

$$T_{\mathrm{KS}} = -\sum_{j=1}^{N}\frac{\hbar^2}{2m_j}\int \varphi_j^*\left(\boldsymbol{r}\right)\Delta\,\varphi_j\left(\boldsymbol{r}\right)\,d\boldsymbol{r}, \tag{2.2.18}$$

E_{H} is the Hartree EDF defined by Eq. (2.1.9), and E_{xc} is just remaining part called the exchange-correlation EDF. Since the Kohn-Sham kinetic energy T_{KS} is not an explicit functional of ρ, it is not expressed as $T_{\mathrm{KS}}\left[\rho\right]$ here [2]. The exchange-correlation EDF is sometimes divided further into two parts: the exchange EDF E_{x} and the correlation one E_{c}. It should be noted that E_{H} is exactly known if the interaction is known, but E_{xc} is not. Approximations of E_{xc} will be discussed in the next section, and, in this section, it is assumed that E_{xc} is exactly known.

Then, the total EDF can be written as

$$E\left[\rho\right] = -\sum_{j=1}^{N}\frac{\hbar^2}{2m_j}\int \varphi_j^*\left(\boldsymbol{r}\right)\Delta\,\varphi_j\left(\boldsymbol{r}\right)\,d\boldsymbol{r} + \int V_{\mathrm{ext}}\left(\boldsymbol{r}\right)\rho\left(\boldsymbol{r}\right)\,d\boldsymbol{r} + \frac{1}{2}\iint v_{\mathrm{int}}\left(\boldsymbol{r},\boldsymbol{r}'\right)\rho\left(\boldsymbol{r}\right)\rho\left(\boldsymbol{r}'\right)\,d\boldsymbol{r}\,d\boldsymbol{r}' + E_{\mathrm{xc}}\left[\rho\right]. \tag{2.2.19}$$

[2] By using the inverse Kohn-Sham method, which will be explained later, ρ uniquely determines the Kohn-Sham effective potential V_{KS} and V_{KS} uniquely determines T_{KS}. Therefore, in principle, T_{KS} is a functional of ρ.

Performing variation of Eq. (2.2.19) with respect to a single-particle orbital φ_j^* with the constraint Eq. (2.2.16)

$$\frac{\delta}{\delta\varphi_j^*}\left[E\left[\rho\right]-\sum_{k=1}^{N}\varepsilon_{jk}\left(\int\varphi_j^*\left(\boldsymbol{r}\right)\varphi_k\left(\boldsymbol{r}\right)\,d\boldsymbol{r}-\delta_{jk}\right)\right]=0, \tag{2.2.20}$$

one obtains

$$-\frac{\hbar^2}{2m_j}\Delta\,\varphi_j\left(\boldsymbol{r}\right)+V_{\text{ext}}\left(\boldsymbol{r}\right)\varphi_j\left(\boldsymbol{r}\right)+\int v_{\text{int}}\left(\boldsymbol{r},\boldsymbol{r}'\right)\rho\left(\boldsymbol{r}'\right)\varphi_j\left(\boldsymbol{r}\right)\,d\boldsymbol{r}'+\left.\frac{\delta E_{\text{xc}}\left[\rho\right]}{\delta\varphi_j^*}\right|_{\rho=\rho(\boldsymbol{r})}=\varepsilon_{jk}\varphi_k\left(\boldsymbol{r}\right). \tag{2.2.21}$$

Using

$$\frac{\delta E_{\text{xc}}\left[\rho\right]}{\delta\varphi_j^*}=\frac{\delta E_{\text{xc}}\left[\rho\right]}{\delta\rho}\frac{\delta\rho}{\delta\varphi_j^*}=\frac{\delta E_{\text{xc}}\left[\rho\right]}{\delta\rho}\varphi_j \tag{2.2.22}$$

and the orthonormal condition [Eq. (2.2.16)], which leads to $\varepsilon_{jk}=0$ for $j\neq k$ and $\varepsilon_{jk}=\varepsilon_j$ for $j=k$, Eq. (2.2.21) becomes the Kohn-Sham equation

$$\left[-\frac{\hbar^2}{2m_j}\Delta+V_{\text{KS}}\left(\boldsymbol{r}\right)\right]\varphi_j\left(\boldsymbol{r}\right)=\varepsilon_j\varphi_j\left(\boldsymbol{r}\right), \tag{2.2.23}$$

where the Kohn-Sham *effective* potential V_{KS} reads

$$V_{\text{KS}}\left(\boldsymbol{r}\right)=V_{\text{ext}}\left(\boldsymbol{r}\right)+\int v_{\text{int}}\left(\boldsymbol{r},\boldsymbol{r}'\right)\rho_{\text{gs}}\left(\boldsymbol{r}'\right)\,d\boldsymbol{r}'+V_{\text{xc}}\left(\boldsymbol{r}\right), \tag{2.2.24}$$

$$V_{\text{xc}}\left(\boldsymbol{r}\right)=\left.\frac{\delta E_{\text{xc}}\left[\rho\right]}{\delta\rho}\right|_{\rho=\rho_{\text{gs}}(\boldsymbol{r})}, \tag{2.2.25}$$

and the effective Hamiltonian $h_{\text{KS}}=-\frac{\hbar^2}{2m_j}\Delta+V_{\text{KS}}\left(\boldsymbol{r}\right)$ is sometimes referred to as the Kohn-Sham effective Hamiltonian. If the Hartree and exchange-correlation EDFs are treated altogether as $E_{\text{Hxc}}\left[\rho\right]=E_{\text{H}}\left[\rho\right]+E_{\text{xc}}\left[\rho\right]$, Eq. (2.2.24) reads

$$V_{\text{KS}}\left(\boldsymbol{r}\right)=V_{\text{ext}}\left(\boldsymbol{r}\right)+V_{\text{Hxc}}\left(\boldsymbol{r}\right), \tag{2.2.26}$$

$$\begin{aligned}V_{\text{Hxc}}\left(\boldsymbol{r}\right)&=\left.\frac{\delta E_{\text{Hxc}}\left[\rho\right]}{\delta\rho}\right|_{\rho=\rho_{\text{gs}}(\boldsymbol{r})}\\&=\int v_{\text{int}}\left(\boldsymbol{r},\boldsymbol{r}'\right)\rho_{\text{gs}}\left(\boldsymbol{r}'\right)\,d\boldsymbol{r}'+\left.\frac{\delta E_{\text{xc}}\left[\rho\right]}{\delta\rho}\right|_{\rho=\rho_{\text{gs}}(\boldsymbol{r})}.\end{aligned} \tag{2.2.27}$$

The ground-state energy reads

$$\begin{aligned}E_{\text{gs}}&=E\left[\rho_{\text{gs}}\right]\\&=\sum_{j=1}^{N}\tau_j+\int V_{\text{ext}}\left(\boldsymbol{r}\right)\rho_{\text{gs}}\left(\boldsymbol{r}\right)\,d\boldsymbol{r}+\frac{1}{2}\iint v_{\text{int}}\left(\boldsymbol{r},\boldsymbol{r}'\right)\rho_{\text{gs}}\left(\boldsymbol{r}\right)\rho_{\text{gs}}\left(\boldsymbol{r}'\right)\,d\boldsymbol{r}\,d\boldsymbol{r}'+E_{\text{xc}}\left[\rho_{\text{gs}}\right] &(2.2.28)\\&=\sum_{j=1}^{N}\varepsilon_j-\frac{1}{2}\iint v_{\text{int}}\left(\boldsymbol{r},\boldsymbol{r}'\right)\rho_{\text{gs}}\left(\boldsymbol{r}\right)\rho_{\text{gs}}\left(\boldsymbol{r}'\right)\,d\boldsymbol{r}\,d\boldsymbol{r}'-\int V_{\text{xc}}\left(\boldsymbol{r}\right)\rho_{\text{gs}}\left(\boldsymbol{r}\right)\,d\boldsymbol{r}+E_{\text{xc}}\left[\rho_{\text{gs}}\right] &(2.2.29)\\&=\sum_{j=1}^{N}\varepsilon_j-\int V_{\text{Hxc}}\left(\boldsymbol{r}\right)\rho_{\text{gs}}\left(\boldsymbol{r}\right)\,d\boldsymbol{r}+E_{\text{Hxc}}\left[\rho_{\text{gs}}\right] &(2.2.30)\\&=\frac{1}{2}\sum_{j=1}^{N}\left(\varepsilon_j+\tau_j\right)+\frac{1}{2}\int V_{\text{ext}}\left(\boldsymbol{r}\right)\rho_{\text{gs}}\left(\boldsymbol{r}\right)\,d\boldsymbol{r}+E_{\text{rea}}, &(2.2.31)\end{aligned}$$

where τ_j and E_{rea} are the single-particle kinetic energy and the rearrangement term defined by

$$\tau_j=-\frac{\hbar^2}{2m_j}\int\varphi_j^{\text{gs}*}\left(\boldsymbol{r}\right)\Delta\,\varphi_j^{\text{gs}}\left(\boldsymbol{r}\right)\,d\boldsymbol{r}, \tag{2.2.32}$$

$$E_{\text{rea}}=E_{\text{Hxc}}\left[\rho_{\text{gs}}\right]-\frac{1}{2}\int V_{\text{Hxc}}\left(\boldsymbol{r}\right)\rho_{\text{gs}}\left(\boldsymbol{r}\right)\,d\boldsymbol{r}, \tag{2.2.33}$$

respectively. We have shown several expressions of the ground-state energy. Equations (2.2.28) and (2.2.29) are widely used in quantum chemistry and condensed matter physics. Equation (2.2.30) is the same as Eq. (2.2.29), but the Hartree and exchange-correlation terms are treated altogether to see how the interaction term behaves in the ground-state energy. Equation (2.2.31) is popular neither in quantum chemistry nor in condensed matter physics but in nuclear physics, where the second term of the right-hand side is zero in atomic nuclei, which are self-bound systems. The rearrangement term E_{rea} vanishes if E_{Hxc} is a quadratic function of ρ like the Hartree energy.

Solving Eqs. (2.2.15), (2.2.23), and (2.2.24) self-consistently, one obtains the exact solution of the ground-state energy and density. This procedure can qualitatively be understood as follows: The ground-state wave function of the non-interacting system with the effective external potential V_{KS} is exactly the Slater determinant, whose single-particle orbitals obey the Kohn-Sham equation [Eq. (2.2.23)]. Therefore, by using E_{xc} (or E_{Hxc}), the *real* system (interaction v_{int}, potential V_{ext}) is mapped into the *fictitious* system (interaction 0, potential V_{KS}), as shown in Fig. 2.2.1. Since the Kohn-Sham equation [Eq. (2.2.23)], at the same time, satisfies the variational principle with respect to ρ, and consequently, this ρ_{gs} is the minimizer of Eq. (2.2.1) [275]. Using the Schrödinger equation, V_{ext} determines ρ_{gs} uniquely; the Hohenberg-Kohn theorem guarantees that ρ_{gs} determines V_{KS} uniquely. Hence, the mapping from V_{ext} to V_{KS} is also unique.

It should also be emphasized that, up to now, there is no approximation, and thus, the ground-state energy and density are exact, as long as E_{xc} is exactly known. Indeed, this does not mean that the ground-state wave function obtained by the Kohn-Sham scheme is exact. Therefore, physical quantities obtained by the ground-state Kohn-Sham wave function, i.e., its expectation values, are not guaranteed to be exact. In addition, the physical meaning of the single-particle energies ε_j has not been known rather than the Lagrange multiplier, while it is also known that ε_j and φ_j often describe physical observables well [276]. Janak's theorem [277] claims that the partial derivative of $E[\rho]$ with respect to the occupation probability of the orbital j is equal to ε_j and the theorem is the counterpart of Koopman's theorem in the Hartree-Fock approximation [278].

2.2.3 Energy Density Functionals in Electronic Systems

In the previous section, it was assumed that E_{xc} is known exactly. However, practically, it is necessary to approximate E_{xc} even for the simple Coulomb interaction. In this section, several standard approximations are explained.

Following the idea of the Thomas-Fermi approximation, a plausible ansatz is that E_{xc} can be written as

$$E_{\mathrm{xc}}[\rho] \simeq \int \varepsilon_{\mathrm{xc}}(\rho(\boldsymbol{r}), |\nabla\rho(\boldsymbol{r})|, \ldots)\,\rho(\boldsymbol{r})\,d\boldsymbol{r}, \tag{2.2.34}$$

where the exchange-correlation energy density (energy par particle) $\varepsilon_{\mathrm{xc}}$ depends only on the density ρ and its derivatives at the local coordinate $\boldsymbol{r}$. This ansatz is also reasonable in view of the effective (Kohn-Sham) potential since the exchange-correlation potential only depends on the local coordinate $\boldsymbol{r}$;

$$V_{\mathrm{xc}}(\boldsymbol{r}) \simeq \varepsilon_{\mathrm{xc}}(\rho(\boldsymbol{r}), |\nabla\rho(\boldsymbol{r})|, \ldots) + \rho(\boldsymbol{r})\left.\frac{d\varepsilon_{\mathrm{xc}}(\rho, |\nabla\rho|, \ldots)}{d\rho}\right|_{\rho=\rho(\boldsymbol{r})}. \tag{2.2.35}$$

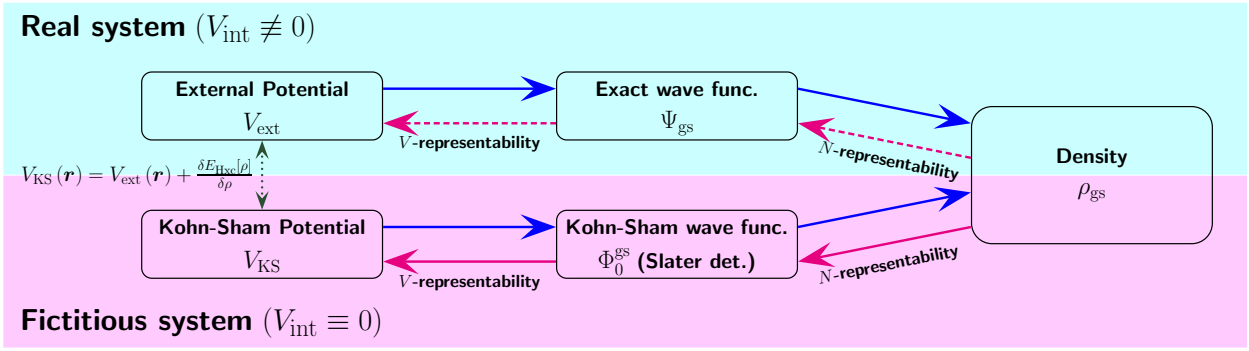

Figure 2.2.1: Schematic figure of the Kohn-Sham scheme. In the non-interacting fictitious system, N- and V-representabilities exactly hold.

Along this direction, the possible lowest-order approximation is that $\varepsilon_{\rm xc}$ only depends on the density ρ;

$$E_{\rm xc}\left[\rho\right] \simeq E_{\rm xc}^{\rm LDA}\left[\rho\right] = \int \varepsilon_{\rm xc}^{\rm LDA}\left(\rho\left(\boldsymbol{r}\right)\right)\rho\left(\boldsymbol{r}\right)\,d\boldsymbol{r}. \tag{2.2.36}$$

This approximation is called local density approximation (LDA). In the next level, $\varepsilon_{\rm xc}$ depends on the gradient density $|\nabla\rho|$ as well as the density ρ;

$$E_{\rm xc}\left[\rho\right] \simeq E_{\rm xc}^{\rm GGA}\left[\rho\right] = \int \varepsilon_{\rm xc}^{\rm GGA}\left(\rho\left(\boldsymbol{r}\right), |\nabla\rho\left(\boldsymbol{r}\right)|\right)\rho\left(\boldsymbol{r}\right)\,d\boldsymbol{r}. \tag{2.2.37}$$

This approximation is called generalized gradient approximation (GGA). Approximations beyond the GGA have also been discussed; Perdew and Schmidt summarized this idea as "Jacob's ladder", the original of which is a ladder an angel uses in Jacob's dream appeared in the Old Testament (a part of the bible) [279]. The Jacob's ladder in DFT is shown in Fig. 2.2.2, which shows that approximation should be improved step-by-step with considering higher-order terms step-by-step to achieve the chemical accuracy (accuracy of 0.1 eV level), where the LDA and the GGA are the first and second steps, respectively.

Hereinafter, in this subsection, the Hartree atomic unit $m_e = \hbar = e^2 = 4\pi\varepsilon_0 = 1$ is used, where m_e is the mass of electrons. In the electronic systems, the interaction is just the Coulomb interaction, and thus the Hartree EDF is known exactly as

$$E_{\rm H}\left[\rho\right] = \frac{1}{2}\iint \frac{\rho\left(\boldsymbol{r}\right)\rho\left(\boldsymbol{r}'\right)}{|\boldsymbol{r}-\boldsymbol{r}'|}\,d\boldsymbol{r}\,d\boldsymbol{r}'. \tag{2.2.38}$$

Here, we focus on the exchange and correlation EDF.

Local Density Approximation

First, we focus on the LDA $E_{\rm xc}$. It is known that the LDA $E_{\rm xc}$ gives the exact exchange-correlation energy for the homogeneous electron gas, since $|\nabla\rho|$ and differential of the higher orders of ρ vanish.

The exchange energy density in the LDA is formulated analytically. The exchange energy originates from the Fock term in the Hartree-Fock approximation;

$$E_{\rm F} = -\frac{1}{2}\sum_{j,\,k}^{\rm occ}\delta_{\sigma\sigma'}\iint \varphi_j^*\left(\boldsymbol{r}\right)\varphi_k^*\left(\boldsymbol{r}'\right)v_{\rm int}\left(\boldsymbol{r},\boldsymbol{r}'\right)\varphi_j\left(\boldsymbol{r}'\right)\varphi_k\left(\boldsymbol{r}\right)\,d\boldsymbol{r}\,d\boldsymbol{r}', \tag{2.2.39}$$

where $\sum_{j,\,k}^{\rm occ}$ is the summation over the occupied states and σ and σ' are the spin associated with the total coordinate x and x', respectively. Here, we assume the homogeneous electron gas in a cubic with the edge length L. A single-particle orbital of the homogeneous electron gas is a plane wave $L^{-3/2}e^{i\boldsymbol{k}\cdot\boldsymbol{r}}$, where the wave number $\boldsymbol{k}$ satisfies $\boldsymbol{k} = \frac{2\pi}{L}\left(n_1, n_2, n_3\right)$ with integer numbers n_1, n_2, and n_3. Substituting plane waves to Eq. (2.2.39), one obtains

$$E_{\rm F} = -\frac{2}{2}\frac{1}{L^6}\sum_{j,\,k}^{\rm occ}\sum_{\sigma\,\sigma'}\iint \frac{1}{|\boldsymbol{r}-\boldsymbol{r}'|}e^{-i\boldsymbol{k}'\cdot\boldsymbol{r}}e^{-i\boldsymbol{k}\cdot\boldsymbol{r}'}e^{i\boldsymbol{k}\cdot\boldsymbol{r}}e^{i\boldsymbol{k}'\cdot\boldsymbol{r}'}\,d\boldsymbol{r}\,d\boldsymbol{r}', \tag{2.2.40}$$

where the factor 2 comes from $\sum_{\sigma\,\sigma'}\delta_{\sigma\,\sigma'}$. Using

$$\begin{aligned}
\frac{2}{L^3}\sum_{j\in{\rm occ}} e^{-i\boldsymbol{k}\cdot\boldsymbol{r}'}e^{i\boldsymbol{k}\cdot\boldsymbol{r}} &\simeq \frac{2}{L^3}\left(\frac{L}{2\pi}\right)^3\int_{k<k_{\rm F}} e^{i\boldsymbol{k}\cdot\left(\boldsymbol{r}-\boldsymbol{r}'\right)}\,d\boldsymbol{k} \\
&= \frac{1}{4\pi^3}\int_0^{2\pi}\int_0^{\pi}\int_0^{k_{\rm F}} e^{ik|\boldsymbol{r}-\boldsymbol{r}'|\cos\theta}k^2\sin\theta\,dk\,d\theta\,d\varphi \\
&= \frac{2\pi}{4\pi^3}\int_0^{k_{\rm F}}\frac{2\sin\left(k\,|\boldsymbol{r}-\boldsymbol{r}'|\right)}{k\,|\boldsymbol{r}-\boldsymbol{r}'|}k^2\,dk \\
&= \frac{k_{\rm F}^3}{\pi^2}\frac{\sin\left(k_{\rm F}\,|\boldsymbol{r}-\boldsymbol{r}'|\right) - \left(k_{\rm F}\,|\boldsymbol{r}-\boldsymbol{r}'|\right)\cos\left(k_{\rm F}\,|\boldsymbol{r}-\boldsymbol{r}'|\right)}{\left(k_{\rm F}\,|\boldsymbol{r}-\boldsymbol{r}'|\right)^3}
\end{aligned} \tag{2.2.41}$$

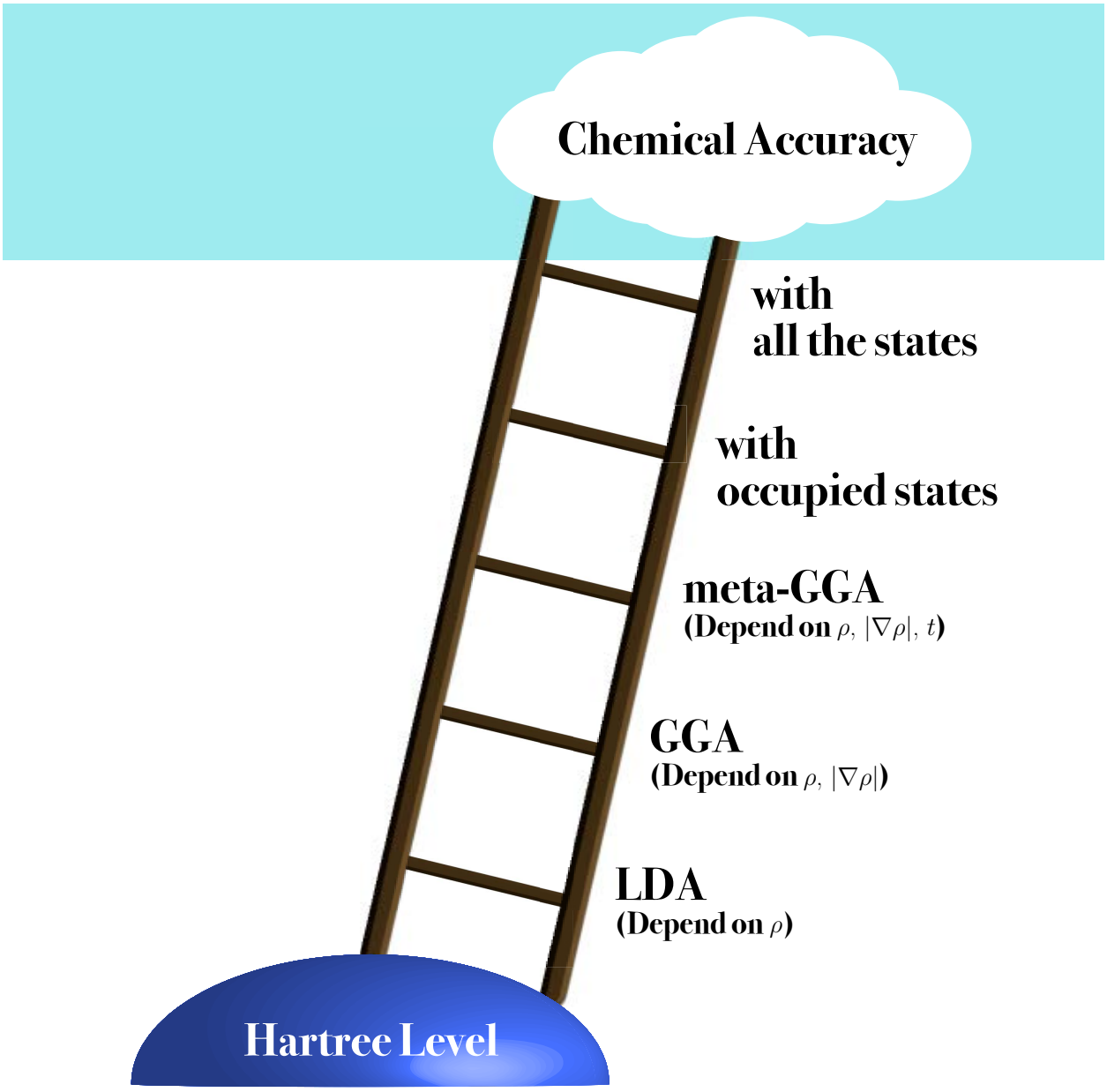

Figure 2.2.2: Jacob's ladder in density functional theory, which was originally proposed by Perdew and Schmidt [279].

and the following relation between the homogeneous density n and the Fermi momentum k_{F}, $n = k_{\mathrm{F}}^3/\left(3\pi^2\right)$ [Eq. (2.1.5)], one obtains Eq. (2.2.40) as

$$\begin{aligned}
E_{\mathrm{F}} &= -\frac{1}{L^6}\sum_{j,\,k}\iint \frac{1}{|\boldsymbol{r}-\boldsymbol{r}'|}e^{-i\boldsymbol{k}'\cdot\boldsymbol{r}}e^{-i\boldsymbol{k}\cdot\boldsymbol{r}'}e^{i\boldsymbol{k}\cdot\boldsymbol{r}}e^{i\boldsymbol{k}'\cdot\boldsymbol{r}'}\,d\boldsymbol{r}\,d\boldsymbol{r}' \\
&\simeq -\frac{1}{4}\iint \frac{1}{|\boldsymbol{r}-\boldsymbol{r}'|}\left[\frac{k_{\mathrm{F}}^3}{\pi^2}\frac{\sin\left(k_{\mathrm{F}}\left|\boldsymbol{r}-\boldsymbol{r}'\right|\right)-\left(k_{\mathrm{F}}\left|\boldsymbol{r}-\boldsymbol{r}'\right|\right)\cos\left(k_{\mathrm{F}}\left|\boldsymbol{r}-\boldsymbol{r}'\right|\right)}{\left(k_{\mathrm{F}}\left|\boldsymbol{r}-\boldsymbol{r}'\right|\right)^3}\right]^2 d\boldsymbol{r}\,d\boldsymbol{r}' \\
&= -\frac{1}{4}\iint \frac{k_{\mathrm{F}}^6}{\pi^4}\frac{1}{R}\left(\frac{\sin t - t\cos t}{t^3}\right)^2 d\boldsymbol{r}\,d\boldsymbol{r}' \\
&= -\frac{1}{4}\iint \frac{k_{\mathrm{F}}^6}{\pi^4}\frac{1}{R}\left(\frac{\sin t - t\cos t}{t^3}\right)^2 d\boldsymbol{r}\,d\boldsymbol{R}' \\
&= -\pi\iint \frac{k_{\mathrm{F}}^6}{\pi^4}\frac{1}{R}\left(\frac{\sin t - t\cos t}{t^3}\right)^2 R^2\,d\boldsymbol{r}\,dR \\
&= -\pi\iint \frac{k_{\mathrm{F}}^4}{\pi^4}\frac{\left(\sin t - t\cos t\right)^2}{t^5}\,d\boldsymbol{r}\,dt \\
&= -\frac{3}{4}\left(\frac{3}{\pi}\right)^{1/3} n^{4/3}V,
\end{aligned} \tag{2.2.42}$$

where $\boldsymbol{R} = \boldsymbol{r} - \boldsymbol{r}'$ and $t = k_{\mathrm{F}}\left|\boldsymbol{r}-\boldsymbol{r}'\right| = k_{\mathrm{F}}R$. Accordingly, the LDA exchange EDF reads

$$E_{\mathrm{x}}^{\mathrm{LDA}}\left[\rho\right] = -\frac{3}{4}\left(\frac{3}{\pi}\right)^{1/3}\int\left[\rho\left(\boldsymbol{r}\right)\right]^{4/3}\,d\boldsymbol{r}. \tag{2.2.43}$$

In contrast to the LDA exchange energy, the analytic form of the correlation energy is unknown even in the LDA. Only asymptotic behaviours of high-density and low-density limits are known. The high-density limit was obtained by Gell-Mann and Brueckner [280] using the technique of the Feynman diagram as

$$\varepsilon_{\mathrm{c}}^{\mathrm{LDA}}\left(r_{\mathrm{s}},\zeta=0\right) \to 0.0311\log r_{\mathrm{s}} - 0.0480 \qquad \left(r_{\mathrm{s}}\to 0\right), \tag{2.2.44}$$

where r_{s} and $\varepsilon_{\mathrm{c}}^{\mathrm{LDA}}$ are, respectively, the Wigner-Seitz radius and the correlation energy density in the LDA defined by

$$r_{\mathrm{s}} = \left(\frac{3}{4\pi\rho}\right)^{1/3} \tag{2.2.45}$$

and

$$E_{\mathrm{c}}^{\mathrm{LDA}}\left[\rho\right] = \int\varepsilon_{\mathrm{c}}^{\mathrm{LDA}}\left(r_{\mathrm{s}}\left(\boldsymbol{r}\right),\zeta=0\right)\rho\left(\boldsymbol{r}\right)\,d\boldsymbol{r}. \tag{2.2.46}$$

Here, ζ is the spin polarization, which will be discussed later, and $\zeta = 0$ means the spin-unpolarized system. In the low-density limit, the electron gas forms the body-centered cubic known as the Wigner crystal [281,282] and its correlation energy is proportional to $1/r_{\mathrm{s}}$.

Modern correlation energy densities in the LDA, $\varepsilon_{\mathrm{c}}^{\mathrm{LDA}}$, are based on the correlation energy for the homogeneous electron gas obtained numerically by Ceperley and Alder by using the diffusion Monte Carlo (DMC) calculation [283]. In this calculation, only ε_{c} for several r_{s} (usually $r_{\mathrm{s}} = 1$, 2, 5, 10, 20, 50, and 100 Bohr) were obtained, while to perform a practical DFT calculation, ε_{c} for arbitrary r_{s} is needed. Thus, interpolation functions were proposed. Parametrizations by Vosko, Wilk, Nusair (VWN) [284], Perdew and Zunger (PZ81) [285], and Perdew and Wang (PW92) [286] have been widely used. Their forms are, respectively,

$$\varepsilon_{\mathrm{c}}^{\mathrm{VWN}}\left(r_{\mathrm{s}},\zeta=0\right) = A\left\{\log\frac{x^2}{X\left(x\right)} + \frac{2b}{Q}\arctan\frac{Q}{2x+b} - \frac{bx_0}{X\left(x_0\right)}\left[\log\frac{\left(x-x_0\right)^2}{X\left(x\right)} + \frac{2\left(b+2x_0\right)}{Q}\arctan\frac{Q}{2x+b}\right]\right\} \tag{2.2.47}$$

with $x = \sqrt{r_{\mathrm{s}}}$, $X\left(x\right) = x^2 + bx + c$, $Q = \sqrt{4c-b^2}$ $A = 0.0310907$, $x_0 = -0.10498$, $b = 3.72744$, and $c = 12.9352$,

$$\varepsilon_{\mathrm{c}}^{\mathrm{PZ81}}\left(r_{\mathrm{s}},\zeta=0\right) = \begin{cases} A\log r_{\mathrm{s}} + B + Cr_{\mathrm{s}}\log r_{\mathrm{s}} + Dr_{\mathrm{s}} & \left(r_{\mathrm{s}} < 1\,\mathrm{Bohr}\right), \\ \gamma/\left(1+\beta_1\sqrt{r_{\mathrm{s}}}+\beta_2 r_{\mathrm{s}}\right) & \left(r_{\mathrm{s}} \geq 1\,\mathrm{Bohr}\right), \end{cases} \tag{2.2.48}$$

with $A = 0.0311$, $B = -0.0480$, $C = 0.0020$, $D = -0.0116$, $\gamma = -0.1423$, $\beta_1 = 1.0529$, and $\beta_2 = 0.3334$, and

$$\varepsilon_{\mathrm{c}}^{\mathrm{PW92}}\left(r_{\mathrm{s}}, \zeta = 0\right) = -2A\left(1 + \alpha_1 r_{\mathrm{s}}\right) \log\left[1 + \frac{1}{2A\left(\beta_1 r_{\mathrm{s}}^{1/2} + \beta_2 r_{\mathrm{s}} + \beta_3 r_{\mathrm{s}}^{3/2} + \beta_4 r_{\mathrm{s}}^2\right)}\right], \tag{2.2.49}$$

with $A = 0.031091$, $\alpha_1 = 0.21370$, $\beta_1 = 7.5957$, $\beta_2 = 3.5876$, $\beta_3 = 1.6382$, and $\beta_4 = 0.49294$. Here, A in these three parametrizations and B in PZ81 are determined to reproduce the behaviour of high-density limit [Eq. (2.2.44)].

Furthermore, recently, two other methods have been applied to obtain the correlation energy density: One is based on the second-order Møller-Plesset many-body perturbation theory (MP2) [263,287] and the other is based on the functional-renormalization-group aided density functional theory (FRG-DFT) [288,289,A7,A9]. The former provides the simple form of $\varepsilon_{\mathrm{c}}^{\mathrm{LDA}}$ as

$$\varepsilon_{\mathrm{c}}^{\mathrm{MP2}}\left(r_{\mathrm{s}}, \zeta = 0\right) = a \log\left(1 + \frac{b}{r_{\mathrm{s}}} + \frac{c}{r_{\mathrm{s}}^2}\right). \tag{2.2.50}$$

The parameters a, b, and c are obtained to reproduce the high-density limit as $a = \left(\log 2 - 1\right) / \left(2\pi^2\right)$ and $b = c = 27.4203609$ [290], or to reproduce both the high-density limit and DMC calculation obtained by Ceperely and Alder [283] as $a = \left(\log 2 - 1\right) / \left(4\pi^2\right)$, $b = 21.7392245$, and $c = 27.4203609$ [291]. The latter—FRG-DFT—provides $\varepsilon_{\mathrm{c}}^{\mathrm{LDA}}$ for numerous values of r_{s} thanks to the low numerical cost of the FRG-DFT, and accordingly, the DFT calculation without using interpolation function of ε_{c} is available [A9]. Reference [A9], nevertheless, provides the PZ81-like ε_{c} based on the correlation energy of the homogeneous electron gas obtained by the FRG-DFT, as with $A = 0.0311$, $B = -0.0480$, $C = 0.00173055$, $D = -0.0100569$, $\gamma = -0.175617$, $\beta_1 = 1.67669$, and $\beta_2 = 0.348219$. The detail of the FRG-DFT will be given in Sec. 2.2.4.

Figure 2.2.3(a) shows correlation energy densities discussed above as functions of the Wigner-Seitz radius r_{s} and Fig. 2.2.3(b) shows relative differences ε_{c} obtained by the PZ81. In principle, the VWN, PZ81, and PW92 functionals are expected to provide identical ε_{c} since these three functionals are fitted to the same data obtained by the DMC. Reference [A9] found that the error due to the fitting, i.e., difference among the VWN, PZ81, and PW92, is just a quarter of the error due to the original data, i.e., difference between DMC results and FRG-DFT ones, around $r_{\mathrm{s}} \lesssim 10$ a.u., relevant density region in many atoms and many solids.

At last of this part, the spin dependence of the exchange and correlation energy densities in the LDA is discussed. The extended version of the LDA is called local spin density approximation (LSDA). First, the spin polarization ζ is defined by

$$\zeta = \frac{\rho_\uparrow - \rho_\downarrow}{\rho_\uparrow + \rho_\downarrow} = \frac{\rho_\uparrow - \rho_\downarrow}{\rho}, \tag{2.2.51}$$

where $\rho = \rho_\uparrow + \rho_\downarrow$ is the total density. The exchange EDF in the LSDA can be calculated with the spin-scaling relation as

$$\begin{aligned} E_{\mathrm{x}}^{\mathrm{LSDA}}\left[\rho_\uparrow, \rho_\downarrow\right] &= -\frac{3}{8}\left(\frac{3}{\pi}\right)^{1/3} \int \left[2\rho_\uparrow\left(\boldsymbol{r}\right)\right]^{4/3} d\boldsymbol{r} - \frac{3}{8}\left(\frac{3}{\pi}\right)^{1/3} \int \left[2\rho_\downarrow\left(\boldsymbol{r}\right)\right]^{4/3} d\boldsymbol{r} \\ &= -\frac{3}{8}\left(\frac{3}{\pi}\right)^{1/3} \int \left\{\left(1+\zeta\right)^{4/3} + \left(1-\zeta\right)^{4/3}\right\} \left[\rho\left(\boldsymbol{r}\right)\right]^{4/3} d\boldsymbol{r}. \end{aligned} \tag{2.2.52}$$

Here, the spin-unpolarized and spin-polarized exchange energy densities are, respectively,

$$\varepsilon_{\mathrm{x}}^{\mathrm{LDA}}\left(r_{\mathrm{s}}, \zeta = 0\right) = -\frac{3}{4}\left(\frac{3}{\pi}\right)^{1/3} \left[\rho\left(\boldsymbol{r}\right)\right]^{1/3}, \tag{2.2.53}$$

$$\varepsilon_{\mathrm{x}}^{\mathrm{LDA}}\left(r_{\mathrm{s}}, \zeta = 1\right) = -\frac{3}{4}\left(\frac{3}{\pi}\right)^{1/3} \left[2\rho\left(\boldsymbol{r}\right)\right]^{1/3}, \tag{2.2.54}$$

and the LDA exchange energy density for arbitrary spin polarization reads

$$\varepsilon_{\mathrm{x}}^{\mathrm{LDA}}\left(r_{\mathrm{s}}, \zeta\right) = \varepsilon_{\mathrm{x}}^{\mathrm{LDA}}\left(r_{\mathrm{s}}, \zeta = 0\right) + f_{\mathrm{x}}\left(\zeta\right)\left[\varepsilon_{\mathrm{x}}^{\mathrm{LDA}}\left(r_{\mathrm{s}}, \zeta = 1\right) - \varepsilon_{\mathrm{x}}^{\mathrm{LDA}}\left(r_{\mathrm{s}}, \zeta = 0\right)\right], \tag{2.2.55}$$

where the spin-dependent function $f_{\mathrm{x}}\left(\zeta\right)$ is

$$f_{\mathrm{x}}\left(\zeta\right) = \frac{\left(1+\zeta\right)^{4/3} + \left(1-\zeta\right)^{4/3} - 2}{2\left(2^{1/3} - 1\right)}. \tag{2.2.56}$$

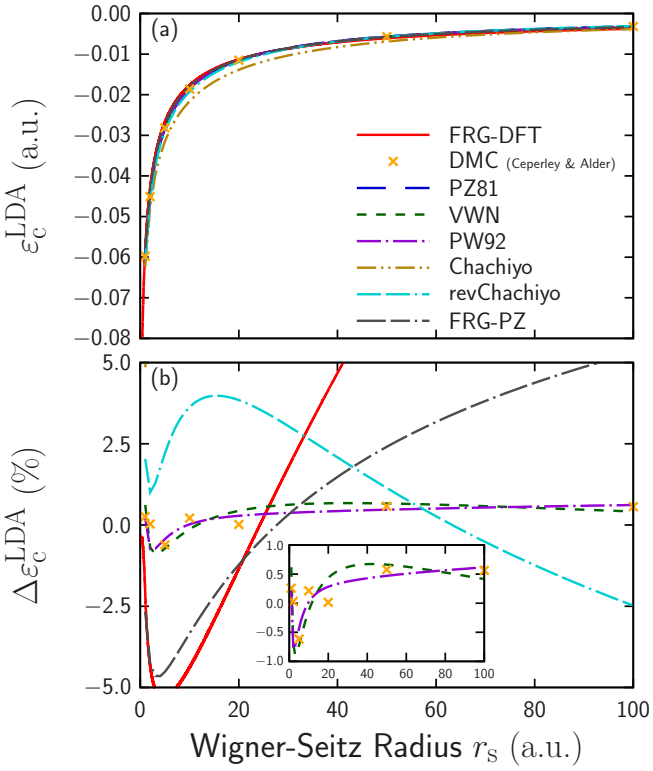

Figure 2.2.3: (a) Correlation energy density ε_c of PZ81 [285], VWN [284], PW92 [286], Chachiyo [290], rev-Chachiyo [291], and FRG-PZ [A9] parametrizations shown as functions of the Wigner-Seitz radius r_s. For comparison, correlation energy density calculated by using the diffusion Monte Carlo (DMC) [283] and the FRG-DFT [A9] are also shown. (b) Relative differences from ε_c obtained by the PZ81, $\Delta\varepsilon_c = \left(\varepsilon_c - \varepsilon_c^{PZ81}\right)/\varepsilon_c^{PZ81}$ are shown as functions of r_s. Results for the VWN, PW92, and DMC calculation are also shown in inset.

For the correlation energy density, $\varepsilon_c^{LDA}(r_s, \zeta = 1)$ can be obtained as the same way as $\varepsilon_c^{LDA}(r_s, \zeta = 0)$, while the interpolation function $f_c(\zeta)$ is still unknown. Hence, the interpolation function for the exchange energy density $f_x(\zeta)$ [Eq. (2.2.56)] is practically used for $f_c(\zeta)$ as well [292]. Recently, Yokota and I noticed by using the FGR-DFT that $f_c(\zeta)$ for the LDA correlation energy density may depend on the Wigner-Seitz radius r_s [A11].

Generalized Gradient Approximation

One-level higher approximation of the LDA is the GGA, in which the dependence on density gradient $|\nabla\rho|$ is taken into account for the exchange-correlation energy density ε_{xc}. It is known that the LDA E_{xc} cannot describe some stable structures of even simple crystals, such as iron (ferromagnetic phase with the body-centered cubic structure), whereas the GGA E_{xc} can [293, 294]. Owing to such success, the GGA E_{xc} is nowadays widely used in condensed matter physics. In contrast to the LDA, there is no obvious criterion which ε_{xc}^{GGA} must satisfy, except the trivial one; ε_{xc}^{GGA} must be identical to ε_{xc}^{LDA} in the case of $|\nabla\rho| = 0$. Thus, different GGA functional assumes different criteria, while many GGA functionals give similar results.

Most GGA exchange and correlation energy densities are written as

$$\varepsilon_x^{GGA}(\rho, |\nabla\rho|) = \varepsilon_x^{LDA}(\rho, \zeta)\, F(\rho, s, \zeta), \tag{2.2.57}$$
$$\varepsilon_c^{GGA}(\rho, |\nabla\rho|) = \varepsilon_c^{LDA}(\rho, \zeta) + H(\rho, t, \zeta), \tag{2.2.58}$$

where s and t are dimensionless density gradients

$$s = \frac{|\nabla\rho|}{2k_{\mathrm{F}}\rho} = \frac{|\nabla\rho|}{2\left(3\pi^2\right)^{1/3}\rho^{4/3}}, \tag{2.2.59}$$

$$t = \frac{|\nabla\rho|}{2\varphi\left(\zeta\right)k_{\mathrm{s}}\rho}, \tag{2.2.60}$$

Here, $k_{\mathrm{s}} = \sqrt{4k_{\mathrm{F}}/\left(\pi a_{\mathrm{B}}\right)}$ is the Thomas-Fermi wave number, $a_{\mathrm{B}} = 4\pi\varepsilon_0\hbar^2/\left(m_e e^2\right)$ is the Bohr radius, which is unity in the Hartree atomic unit, and $\varphi\left(\zeta\right) = \left[\left(1+\zeta\right)^{2/3} + \left(1-\zeta\right)^{2/3}\right]/2$ is the spin-scaling factor. The factor F is called enhancement factor.

Here, we introduce how F and H in GGA functionals are determined. The parametrization by Perdew, Burke, and Ernzerhof (PBE) [295] is taken as an example. The forms of F and H are, respectively,

$$F^{\mathrm{PBE}}\left(s\right) = 1 + \kappa - \frac{\kappa}{1+\mu s^2/\kappa}, \tag{2.2.61}$$

$$H^{\mathrm{PBE}}\left(\rho,t,\zeta\right) = \frac{e^2}{a_{\mathrm{B}}}\gamma\left[\varphi\left(\zeta\right)\right]^3\log\left[1+\frac{\beta}{\gamma}t^2\left(\frac{1+A\left(\rho,\zeta\right)t^2}{1+A\left(\rho,\zeta\right)t^2+\left[A\left(\rho,\zeta\right)\right]^2t^4}\right)\right], \tag{2.2.62}$$

where

$$A\left(\rho,\zeta\right) = \frac{\beta}{\gamma}\left[\exp\left(-\frac{a_{\mathrm{B}}\varepsilon_{\mathrm{c}}^{\mathrm{LDA}}\left(\rho\right)}{e^2\gamma\left[\varphi\left(\zeta\right)\right]^3}\right)-1\right]^{-1}, \tag{2.2.63}$$

$\beta \approx 0.066725$, $\gamma = \left(1-\log 2\right)/\pi^2$, $\kappa = 0.804$, and $\mu = \beta\left(\pi^2/3\right) \approx 0.21951$. These functional forms and parameters are determined to satisfy the following conditions [295, 296].

1. The trivial condition that $\varepsilon_{\mathrm{xc}}^{\mathrm{GGA}}$ must be identical to $\varepsilon_{\mathrm{xc}}^{\mathrm{LDA}}$ in the case of $|\nabla\rho| = 0$, i.e., $F\left(0\right) = 1$ and $H\left(\rho,0,\zeta\right) = 0$.

2. In the limit of $t \to 0$, H satisfies $H \to \frac{e^2}{a_{\mathrm{B}}}\beta\left[\varphi\left(\zeta\right)\right]^3t^2$, which comes from the sum rule of the correlation hole $\int h_{\uparrow\downarrow}\left(\boldsymbol{r},\boldsymbol{r}+\boldsymbol{u}\right)d\boldsymbol{u} = 0$ and was derived in Ref. [297].

3. In the limit of $t \to \infty$, H should satisfy $\varepsilon_{\mathrm{c}}^{\mathrm{GGA}} \to 0$, i.e., $H \to -\varepsilon_{\mathrm{c}}^{\mathrm{LDA}}$.

4. In the high-density limit with uniform scaling $\lambda \to \infty$ with $\rho\left(\boldsymbol{r}\right) \to \lambda^3\rho\left(\lambda\boldsymbol{r}\right)$, ε_{c} should satisfy $\varepsilon_{\mathrm{c}} \to$ const. [298].

5. In the uniform scaling $\rho\left(\boldsymbol{r}\right) \to \lambda^3\rho\left(\lambda\boldsymbol{r}\right)$, $E_{\mathrm{x}}^{\mathrm{GGA}}$ should satisfy $E_{\mathrm{x}}^{\mathrm{GGA}}\left[\lambda^3\rho\left(\lambda\boldsymbol{r}\right)\right] = \lambda E_{\mathrm{x}}^{\mathrm{GGA}}\left[\rho\left(\boldsymbol{r}\right)\right]$, which comes from the sum rule of the exchange hole $\int h_{\parallel}\left(\boldsymbol{r},\boldsymbol{r}+\boldsymbol{u}\right)d\boldsymbol{u} = -1$ and was derived in Ref. [299].

6. The spin-dependence of the exchange functional should obey $E_{\mathrm{x}}^{\mathrm{GGA}}\left[\rho_\uparrow,\rho_\downarrow\right] = \frac{1}{2}E_{\mathrm{x}}^{\mathrm{GGA}}\left[2\rho_\uparrow\right] + \frac{1}{2}E_{\mathrm{x}}^{\mathrm{GGA}}\left[2\rho_\downarrow\right]$.

7. The exchange functional should obey the Lieb-Oxford bound [300–302]

$$E_{\mathrm{x}}\left[\rho\right] \geq E_{\mathrm{xc}}\left[\rho\right] \geq -1.679e^2\int\left[\rho\left(\boldsymbol{r}\right)\right]^{4/3}d\boldsymbol{r}. \tag{2.2.64}$$

8. In the limit of $s \to 0$, the LDA linear response should be recovered, and thus $F_{\mathrm{x}}\left(s\right) \to 1 + \mu s^2$ ($\mu = \beta\pi^2/3$).

Combining conditions 2 and 8, one can find

$$\varepsilon_{\mathrm{xc}}^{\mathrm{GGA}}\left(\rho,|\nabla\rho|\right) \to \varepsilon_{\mathrm{xc}}^{\mathrm{LDA}}\left(\rho\right) + O\left(|\nabla\rho|^3\right) \tag{2.2.65}$$

at $|\nabla\rho| \to 0$ limit.

The exchange hole $h_{\parallel}\left(\boldsymbol{r}_1,\boldsymbol{r}_2\right)$ is defined by [272]

$$h_{\parallel}\left(\boldsymbol{r}_1,\boldsymbol{r}_2\right) = -\sum_{\sigma=\uparrow,\downarrow}\frac{\left|\sum_{j=1}^{N_\sigma}\varphi_{j\sigma}^*\left(\boldsymbol{r}_1\right)\varphi_{j\sigma}\left(\boldsymbol{r}_2\right)\right|^2}{\rho_\sigma\left(\boldsymbol{r}_1\right)}, \tag{2.2.66}$$

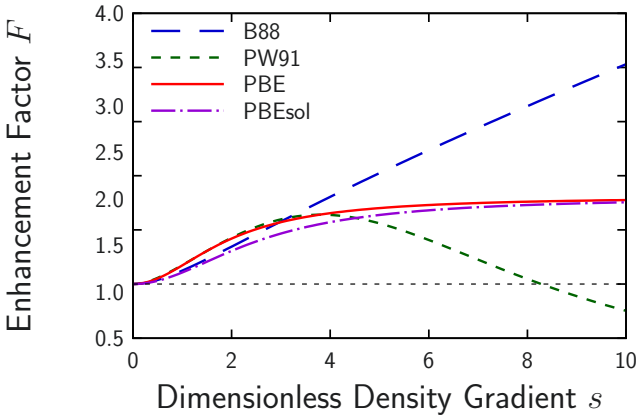

Figure 2.2.4: GGA enhancement factors F of the B88 [308], PW91 [309], PBE [295], and PBEsol [306] as functions of the dimensionless density gradient s.

where N_σ is the number of electrons with the spin σ, $N = N_\uparrow + N_\downarrow$, $\rho_\sigma(\boldsymbol{r}) = \sum_{j=1}^{N_\sigma} |\varphi_{j\sigma}(\boldsymbol{r})|^2$ is the density for the spin σ. The correlation hole $h_{\not\parallel}(\boldsymbol{r}_1, \boldsymbol{r}_2)$ is defined by the remaining part of the exchange-correlation hole $h(\boldsymbol{r}_1, \boldsymbol{r}_2)$ [303–305];

$$h_{\not\parallel}(\boldsymbol{r}_1, \boldsymbol{r}_2) = h(\boldsymbol{r}_1, \boldsymbol{r}_2) - h_{\parallel}(\boldsymbol{r}_1, \boldsymbol{r}_2), \tag{2.2.67}$$

where $h(\boldsymbol{r}_1, \boldsymbol{r}_2)$ is determined to satisfy

$$\varepsilon_{\mathrm{xc}}^{\mathrm{exact}}(\boldsymbol{r}) = \frac{1}{2}\int \frac{h(\boldsymbol{r}, \boldsymbol{r}')}{|\boldsymbol{r} - \boldsymbol{r}'|}\, d\boldsymbol{r}' \tag{2.2.68}$$

with the *exact* exchange-correlation energy density $\varepsilon_{\mathrm{xc}}^{\mathrm{exact}}$.

It is known that the PBE often overestimates the lattice constant of crystals. To overcome such problems, a modified version of the PBE functional named "PBEsol" was also proposed [306], in which $\mu = 10/81 \approx 0.1235$ [307] is used instead. For these two functionals, κ is determined to satisfy the mathematical Lieb-Oxford bound and thus robust, while μ is rather flexible.

There are also several widely used GGA EDFs. In this thesis, the detailed derivations of the other GGA EDFs are out of the scope; forms of two widely used ones, the B88 [308] and the PW91 [309], are, nonetheless, shown below to compare them with the PBE EDF, which will be used in this work. The B88 exchange enhancement factor is written as

$$F^{\mathrm{B88}}(s) = 1 + \frac{4\beta}{3}\left(\frac{\pi}{6}\right)^{1/3} \frac{\left[2\left(3\pi^2\right)^{1/3} s\right]^2}{1 + 6\beta\left[2\left(3\pi^2\right)^{1/3} s\right]\sinh^{-1}\left[2\left(3\pi^2\right)^{1/3} s\right]}, \tag{2.2.69}$$

while the gradient correction to the correlation EDF is not considered, i.e., $H \equiv 0$. Here, β is the fitting parameter, and in the original paper [308], $\beta = 0.0042$ was used to reproduce the Hartree-Fock calculation of the noble-gas atoms.

The PW91 exchange and correlation correction terms, F and H, are written, respectively, as

$$F^{\mathrm{PW91}}(s) = \frac{1 + 0.19645 s \sinh^{-1}(7.7956 s) + \left(0.2743 - 0.1508 e^{-100 s^2}\right) s^2}{1 + 0.19645 s \sinh^{-1}(7.7956 s) + 0.004 s^4}, \tag{2.2.70}$$

$$\begin{aligned} H^{\mathrm{PW91}}(\rho, t, \zeta) = {} & [\varphi(\zeta)]^3 \frac{\beta^2}{2\alpha} \log\left[1 + \frac{2\alpha}{\beta}\frac{t^2 + A(\rho,\zeta)\, t^4}{1 + A(\rho,\zeta)\, t^2 + [A(\rho,\zeta)]^2 t^4}\right] \\ & + \nu\left[C_{\mathrm{c}}(r_{\mathrm{s}}) - C_{\mathrm{c}}(0) - \frac{3}{7}C_{\mathrm{x}}\right][\varphi(\zeta)]^3 t^2 \exp\left[-100\,[\varphi(\zeta)]^4 \frac{k_{\mathrm{s}}^2}{k_{\mathrm{F}}^2} t^2\right], \end{aligned} \tag{2.2.71}$$

where $\alpha = 0.09$, $\beta = \nu C_{\mathrm{c}}(0)$, $\nu = (16/\pi)\left(3\pi^2\right)^{1/3}$, and

$$A(\rho, \zeta) = \frac{2\alpha}{\beta}\left[\exp\left(-\frac{2\alpha\varepsilon_{\mathrm{c}}^{\mathrm{LDA}}(\rho,\zeta)}{g^3\beta^2}\right) - 1\right]^{-1} \tag{2.2.72}$$

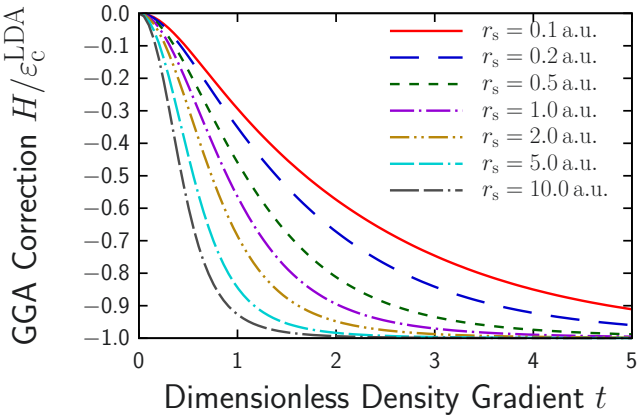

Figure 2.2.5: Ratio of the GGA correction to the correlation energy, H, to the LDA correlation energy, ε_c^{LDA}, of the PBE functional [295] as functions of the dimensionless density gradient t.

Here,

$$C_{xc}(r_s) = 10^{-3} \frac{2.568 + ar_s + br_s^2}{1 + cr_s + dr_s + 10br_s^3} \tag{2.2.73}$$

with $a = 23.266$, $b = 7.389 \times 10^{-3}$, $c = 8.723$, and $d = 0.472$ was derived by Rasolt and Geldart [310], $C_x = -0.001667$, and $C_c(r_s) = C_{xc}(r_s) - C_x$.

Figure 2.2.4 shows the B88, PW91, PBE, and PBEsol GGA exchange enhancement factors F as functions of the dimensionless density gradient s. Figure 2.2.5 shows ratios of the gradient corrections of the PBE GGA correlation energy density H to the LDA correlation energy, H/ε_c^{LDA}, as functions of the dimensionless density gradient t.

Although several approximation methods, such as the LDA and the GGA, have been proposed, even the way to estimate the systematic error of approximations has not been known yet. Moreover, the strategy to achieve accurate EDFs is still under discussion [311, 312]. Indeed, for example, it is known that, despite the success of the GGA EDF for the reproduction of the iron crystal structure, GGA EDFs often overestimate lattice constants of crystals and bond lengths of molecules, while the LDA EDF reproduces nicely [272]. Thus, using a GGA EDF is one of the standards in DFT calculations, while the LDA EDF is still used.

2.2.4 Novel Methods toward Energy Density Functional

In this section, two novel approaches to obtain EDFs, especially E_{xc}, are discussed. Thanks to the rapid development of machine learning (including neural network) techniques, there have been several attempts to obtain E_{xc} by using such techniques [313–320], which is out of the scope of this thesis. Instead, here, although they are not a central idea of this thesis, two different methods will be introduced: approaches based on functional renormalization group and based on an inverse problem. The former is based on a technique of quantum field theory, while the latter is based on one-to-one correspondence discussed in the Hohenberg-Kohn theorem with assuming that some ground-state densities ρ_{gs} are known.

Effective Action Formalism

One starts from the classical action of the system S in the imaginary-time formalism

$$\begin{aligned} S_\lambda[\varphi, \varphi^\dagger] = &\iint \varphi^\dagger(\tau + \varepsilon, \boldsymbol{r}) \left[\hbar \frac{\partial}{\partial \tau} - \frac{\hbar^2}{2m} \Delta\right] \varphi(\tau, \boldsymbol{r}) \, d\boldsymbol{r} \, d\tau \\ &+ \iiiint \varphi^\dagger(\tau + \varepsilon, \boldsymbol{r}) \varphi^\dagger(\tau' + \varepsilon', \boldsymbol{r}') v_\lambda(\tau, \tau', \boldsymbol{r}, \boldsymbol{r}') \varphi(\tau, \boldsymbol{r}) \varphi(\tau', \boldsymbol{r}') \, d\boldsymbol{r} \, d\tau \, d\boldsymbol{r}' \, d\tau', \end{aligned} \tag{2.2.74}$$

where v_λ is the scaled two-body interaction defined by

$$v_\lambda(\tau, \boldsymbol{r}, \tau', \boldsymbol{r}') = \lambda \delta(\tau - \tau') v_{int}(\boldsymbol{r}, \boldsymbol{r}') \tag{2.2.75}$$

and ε and ε' are positive infinitesimal numbers which satisfy $\varepsilon' > \varepsilon$. The partition function Z in the two-particle point irreducible formalism [321,322] can be calculated as

$$Z_\lambda [J] = \iint \exp\left(-S_\lambda \left[\varphi, \varphi^\dagger\right] + \iint J(\tau, \boldsymbol{r})\, \rho(\tau, \boldsymbol{r})\, d\tau\, d\boldsymbol{r}\right) \mathcal{D}\varphi\, \mathcal{D}\varphi^\dagger \tag{2.2.76}$$

under the path-integral formalism [12,323], where $\rho(\tau, \boldsymbol{r}) = \varphi^\dagger(\tau + \varepsilon, \boldsymbol{r})\, \varphi(\tau, \boldsymbol{r})$ is the density and J is the external potential. The effective action Γ, which includes quantum fluctuations, can be calculated with the Legendre transformation of $W_\lambda [J] = \log Z_\lambda [J]$ as

$$\Gamma_\lambda [\rho] = \iint J_{\mathrm{sup},\,\lambda} [\rho](\tau, \boldsymbol{r})\, \rho(\tau, \boldsymbol{r})\, d\tau\, d\boldsymbol{r} - W_\lambda \left[J_{\mathrm{sup},\,\lambda} [\rho]\right], \tag{2.2.77}$$

where $J_{\mathrm{sup},\,\lambda}$ satisfies

$$\left.\frac{\delta W_\lambda [J]}{\delta J(\tau, \boldsymbol{r})}\right|_{J = J_{\mathrm{sup},\,\lambda}} = \rho(\tau, \boldsymbol{r}). \tag{2.2.78}$$

There is an exact relation between the effective action $\Gamma_{\lambda=1} [\rho]$ and the total EDF $E[\rho]$ [322]

$$E[\rho] = \lim_{\beta \to \infty} \frac{\Gamma_{\lambda=1} [\rho]}{\beta}, \tag{2.2.79}$$

where β is the inverse temperature. Hence, once the effective action $\Gamma_{\lambda=1}$ is calculated, one can obtain the total EDF $E[\rho]$ accordingly. One of the techniques to calculate $\Gamma_{\lambda=1}$ is the functional renormalization group (FRG) [324]. The effective action of $\lambda = 0$ can be calculated easily since it corresponds to the non-interacting system. Once one finds λ dependence of Γ_λ, i.e., $\partial\Gamma_\lambda [\rho] / \partial\lambda$ called flow equation, solving the differential equation with respect to λ, one can obtain $\Gamma_{\lambda=1} [\rho]$. The differential equation of Γ_λ, i.e., the flow equation, is difficult to be solved since it is a functional differential equation and a closed form of Γ_λ. Hence, an approximation is, in practice, further introduced to solve it. The second-order vertex expansion, i.e., the Taylor expansion around the ground-state density, is usually adopted, which leads to hierarchical differential equations that can be solved numerically.

For instance, the flow equation for the homogeneous electron gas reads [A7, A9]

$$\begin{aligned}\frac{\partial \Gamma_\lambda [\rho]}{\partial \lambda} = \frac{1}{2} \iiiint \frac{\partial}{\partial \lambda} v_\lambda(\tau, \boldsymbol{r}, \tau', \boldsymbol{r}') \Big\{ &[\rho(\tau, \boldsymbol{r}) - n_{\mathrm{bg}}] [\rho(\tau', \boldsymbol{r}') - n_{\mathrm{bg}}] \\ &+ \Gamma_\lambda^{(2)-1} [\rho](\tau + \varepsilon', \boldsymbol{r}, \tau', \boldsymbol{r}') - \rho(\tau, \boldsymbol{r})\, \delta(\boldsymbol{r} - \boldsymbol{r}') \Big\}\, d\boldsymbol{r}\, d\tau\, d\boldsymbol{r}'\, d\tau',\end{aligned} \tag{2.2.80}$$

where $\Gamma_\lambda^{(2)-1} [\rho]$ is defined to satisfy

$$\iint \Gamma_\lambda^{(2)-1} [\rho](\tau + \varepsilon, \boldsymbol{r}, \tau'', \boldsymbol{r}'') \frac{\delta^2 \Gamma_\lambda [\rho]}{\delta\rho(\tau'', \boldsymbol{r}'')\, \delta\rho(\tau', \boldsymbol{r}')}\, d\boldsymbol{r}''\, d\tau'' = \delta(\tau - \tau')\, \delta(\boldsymbol{r} - \boldsymbol{r}'). \tag{2.2.81}$$

Here, $n_{\mathrm{bg}} = 3/\left(4\pi r_{\mathrm{s}}^3\right)$ is the density of the background (positive) ions to keep the system neutral and is the same as that of the homogeneous electron gas. With introducing the vertex expansion, $\Gamma_\lambda [\rho]$ is written as

$$\begin{aligned}\Gamma_\lambda [\rho] = \Gamma_\lambda [\rho_{\mathrm{gs},\,\lambda}] + \mu_\lambda \int [\rho(\tau, \boldsymbol{r}) - \rho_{\mathrm{gs},\,\lambda}(\tau, \boldsymbol{r})]\, d\tau\, d\boldsymbol{r} \\ + \sum_{n=2}^{\infty} \int \cdots \int \frac{\delta^n \Gamma_\lambda [\rho_{\mathrm{gs},\,\lambda}]}{\delta\rho(\tau_1, \boldsymbol{r}_1) \ldots \delta\rho(\tau_n, \boldsymbol{r}_n)} \left\{ \prod_{j=1}^{n} [\rho(\tau_j, \boldsymbol{r}_j) - \rho_{\mathrm{gs},\,\lambda}(\tau_j, \boldsymbol{r}_j)] \right\} d\boldsymbol{r}_1\, d\tau_1 \ldots d\boldsymbol{r}_n\, d\tau_n,\end{aligned} \tag{2.2.82}$$

where $\rho_{\mathrm{gs},\,\lambda}$ is the ground-state density at λ and μ_λ is the chemical potential chosen to satisfy $\rho_{\mathrm{gs},\,\lambda=0}(\tau, \boldsymbol{r}) \equiv n_{\mathrm{bg}}$ and $\partial\rho_{\mathrm{gs},\,\lambda}(\tau, \boldsymbol{r}) / \partial\lambda \equiv 0$.

This method had been proposed by Polonyi and Sailer [325] and was applied to several zero- and one-dimensional toy models of with finite number of particles with short-range interaction [326–328] and one-dimensional homogeneous nuclear matter [288]. It was also applied to calculate excited states of a one-dimensional system [329]. Recently, we applied this method to the two- and three-dimensional homogeneous electron gases to obtain LDA correlation EDFs [A7,A9], and extended to the spin-polarized systems to obtain $f_{\mathrm{c}}(\zeta)$ given in Eq. (2.2.56) for the LDA correlation EDF [A11].

Inverse Approach

Suppose that the ground-state densities of some systems are already known by using, for instance, experiments or wave function methods. The Hohenberg-Kohn theorem for the non-interacting system guarantees that once $\rho_{\rm gs}$ is known, the effective potential $V_{\rm KS}$ for the system can be, in principle, calculated exactly. Indeed, such an inverse method was proposed and tested in the 1990s [330–333]. However, after that, this method, called inverse Kohn-Sham (IKS) method, was adopted to discuss an accuracy of an exchange-correlation EDF or discussed to improve the numerical method [334]. It was also applied to nuclear system [335]. Recent progresses are summarized in Ref. [336].

Recently, we proposed in Ref. [A8] that this IKS method can be used to improve a known exchange-correlation EDF, which is assumed to have enough accuracy, combined with the density functional perturbation theory (DFPT) [337]. In this method, called "IKS-DFPT", the exact ground-state energy $E_{\rm gs}^{\rm exact}$ is expressed by using two ways as follows:

$$E_{\rm gs}^{\rm exact} = T_{\rm KS}^{\rm exact} + \int V_{\rm ext}\left(\boldsymbol{r}\right) \rho_{\rm gs}^{\rm exact}\left(\boldsymbol{r}\right)\, d\boldsymbol{r} + E_{\rm Hxc}^{\rm exact}\left[\rho_{\rm gs}^{\rm exact}\right], \tag{2.2.83}$$

$$E_{\rm gs}^{\rm exact} = \sum_{j\in{\rm occ}} \varepsilon_j^{\rm exact} + E_{\rm Hxc}^{\rm exact}\left[\rho_{\rm gs}^{\rm exact}\right] - \int \frac{\delta E_{\rm Hxc}^{\rm exact}\left[\rho_{\rm gs}^{\rm exact}\right]}{\delta\rho\left(\boldsymbol{r}\right)} \rho_{\rm gs}^{\rm exact}\left(\boldsymbol{r}\right)\, d\boldsymbol{r}, \tag{2.2.84}$$

where $\rho_{\rm gs}^{\rm exact}$ is the exact ground-state density, which is assumed to be known, and $E_{\rm Hxc}^{\rm exact}$ is the exact Hartree-exchange-correlation EDF, which we shall derive in this method. Here, it should be noted that $T_{\rm KS}^{\rm exact}$ and $\varepsilon_j^{\rm exact}$ can be derived from $\rho_{\rm gs}^{\rm exact}$ by using the IKS method. Since the known functional $\tilde{E}_{\rm Hxc}$ is assumed to be good enough and accordingly the density derived by using this functional, $\tilde{\rho}_{\rm gs}$, is also expected to be good enough, deviation from the exact ones is assumed to be small enough and treated perturbatively;

$$E_{\rm Hxc}^{\rm exact}\left[\rho\right] = \tilde{E}_{\rm Hxc}\left[\rho\right] + \lambda E_{\rm Hxc}^{(1)}\left[\rho\right] + O\left(\lambda^2\right), \tag{2.2.85}$$

$$\rho_{\rm gs}^{\rm exact}\left(\boldsymbol{r}\right) = \tilde{\rho}_{\rm gs}\left(\boldsymbol{r}\right) + \lambda\rho_{\rm gs}^{(1)}\left(\boldsymbol{r}\right) + O\left(\lambda^2\right), \tag{2.2.86}$$

$$\varphi_j^{\rm exact}\left(\boldsymbol{r}\right) = \tilde{\varphi}_j\left(\boldsymbol{r}\right) + \lambda\varphi_j^{(1)}\left(\boldsymbol{r}\right) + O\left(\lambda^2\right). \tag{2.2.87}$$

Here, $\tilde{\varphi}_j$ and $\varphi_j^{(1)}$ are assumed to be orthogonal. Equation (2.2.83) can be rearranged to

$$\begin{aligned}
E_{\rm gs}^{\rm exact} &= T_{\rm KS}^{\rm exact} + \int V_{\rm ext}\left(\boldsymbol{r}\right)\tilde{\rho}_{\rm gs}\left(\boldsymbol{r}\right)\, d\boldsymbol{r} + \tilde{E}_{\rm Hxc}\left[\tilde{\rho}_{\rm gs}\right] \\
&\quad + \lambda\int V_{\rm ext}\left(\boldsymbol{r}\right)\rho_{\rm gs}^{(1)}\left(\boldsymbol{r}\right)\, d\boldsymbol{r} + \lambda E_{\rm Hxc}^{(1)}\left[\tilde{\rho}_{\rm gs}\right] + \lambda\int \frac{\delta\tilde{E}_{\rm Hxc}\left[\tilde{\rho}_{\rm gs}\right]}{\delta\rho\left(\boldsymbol{r}\right)}\rho_{\rm gs}^{(1)}\left(\boldsymbol{r}\right)\, d\boldsymbol{r} + O\left(\lambda^2\right) \\
&= \tilde{T}_{\rm KS} + \int V_{\rm ext}\left(\boldsymbol{r}\right)\tilde{\rho}_{\rm gs}\left(\boldsymbol{r}\right)\, d\boldsymbol{r} + \tilde{E}_{\rm Hxc}\left[\tilde{\rho}_{\rm gs}\right] \\
&\quad + \lambda\int V_{\rm ext}\left(\boldsymbol{r}\right)\rho_{\rm gs}^{(1)}\left(\boldsymbol{r}\right)\, d\boldsymbol{r} + \lambda E_{\rm Hxc}^{(1)}\left[\tilde{\rho}_{\rm gs}\right] + \lambda\int \frac{\delta\tilde{E}_{\rm Hxc}\left[\tilde{\rho}_{\rm gs}\right]}{\delta\rho\left(\boldsymbol{r}\right)}\rho_{\rm gs}^{(1)}\left(\boldsymbol{r}\right)\, d\boldsymbol{r} \\
&\quad - \frac{\lambda\hbar^2}{2m}\int\left[\varphi_j^{(1)*}\left(\boldsymbol{r}\right)\Delta\,\tilde{\varphi}_j\left(\boldsymbol{r}\right) + \tilde{\varphi}_j^*\left(\boldsymbol{r}\right)\Delta\,\varphi_j^{(1)}\left(\boldsymbol{r}\right)\right] d\boldsymbol{r} + O\left(\lambda^2\right) \\
&= \tilde{E}_{\rm gs} + \lambda E_{\rm Hxc}^{(1)}\left[\tilde{\rho}_{\rm gs}\right] + O\left(\lambda^2\right)
\end{aligned} \tag{2.2.88}$$

since the kinetic energy satisfies

$$\begin{aligned}
T_{\rm KS}^{\rm exact} &= \sum_j \int \varphi_j^{\rm exact*}\left(\boldsymbol{r}\right)\left(-\frac{\hbar^2}{2m}\Delta\right)\varphi_j^{\rm exact}\left(\boldsymbol{r}\right)\, d\boldsymbol{r} \\
&= \sum_j \int \tilde{\varphi}_j^*\left(\boldsymbol{r}\right)\left(-\frac{\hbar^2}{2m}\Delta\right)\tilde{\varphi}_j\left(\boldsymbol{r}\right)\, d\boldsymbol{r} - \frac{\lambda\hbar^2}{2m}\int\left[\varphi_j^{(1)*}\left(\boldsymbol{r}\right)\Delta\,\tilde{\varphi}_j\left(\boldsymbol{r}\right) + \tilde{\varphi}_j^*\left(\boldsymbol{r}\right)\Delta\,\varphi_j^{(1)}\left(\boldsymbol{r}\right)\right] d\boldsymbol{r} + O\left(\lambda^2\right).
\end{aligned} \tag{2.2.89}$$

and

$$
\begin{aligned}
&-\frac{\hbar^2}{2m}\int\left[\varphi_j^{(1)*}(\boldsymbol{r})\,\Delta\,\tilde{\varphi}_j(\boldsymbol{r})+\tilde{\varphi}_j^{*}(\boldsymbol{r})\,\Delta\,\varphi_j^{(1)}(\boldsymbol{r})\right]d\boldsymbol{r}+\int V_{\mathrm{ext}}(\boldsymbol{r})\,\rho_{\mathrm{gs}}^{(1)}(\boldsymbol{r})\,d\boldsymbol{r}+\int\frac{\delta\tilde{E}_{\mathrm{Hxc}}\left[\tilde{\rho}_{\mathrm{gs}}\right]}{\delta\rho(\boldsymbol{r})}\rho_{\mathrm{gs}}^{(1)}(\boldsymbol{r})\,d\boldsymbol{r}\\
&=-\frac{\hbar^2}{2m}\int\left[\varphi_j^{(1)*}(\boldsymbol{r})\,\Delta\,\tilde{\varphi}_j(\boldsymbol{r})+\tilde{\varphi}_j^{*}(\boldsymbol{r})\,\Delta\,\varphi_j^{(1)}(\boldsymbol{r})\right]d\boldsymbol{r}\\
&\quad+\int V_{\mathrm{ext}}(\boldsymbol{r})\left[\varphi_j^{(1)*}(\boldsymbol{r})\,\tilde{\varphi}_j(\boldsymbol{r})+\tilde{\varphi}_j^{*}(\boldsymbol{r})\,\varphi_j^{(1)}(\boldsymbol{r})\right]d\boldsymbol{r}\\
&\quad+\int\frac{\delta\tilde{E}_{\mathrm{Hxc}}\left[\tilde{\rho}_{\mathrm{gs}}\right]}{\delta\rho(\boldsymbol{r})}\left[\varphi_j^{(1)*}(\boldsymbol{r})\,\tilde{\varphi}_j(\boldsymbol{r})+\tilde{\varphi}_j^{*}(\boldsymbol{r})\,\varphi_j^{(1)}(\boldsymbol{r})\right]d\boldsymbol{r}\\
&=\int\left[\varphi_j^{(1)*}(\boldsymbol{r})\,\tilde{h}_{\mathrm{KS}}\tilde{\varphi}_j(\boldsymbol{r})+\tilde{\varphi}_j^{*}(\boldsymbol{r})\,\tilde{h}_{\mathrm{KS}}\varphi_j^{(1)}(\boldsymbol{r})\right]d\boldsymbol{r}\\
&=\tilde{\varepsilon}_j\int\left[\varphi_j^{(1)*}(\boldsymbol{r})\,\tilde{\varphi}_j(\boldsymbol{r})+\tilde{\varphi}_j^{*}(\boldsymbol{r})\,\varphi_j^{(1)}(\boldsymbol{r})\right]d\boldsymbol{r}=0,
\end{aligned}
\tag{2.2.90}
$$

where $\tilde{h}_{\mathrm{KS}}=-\frac{\hbar^2}{2m}\Delta+\tilde{V}_{\mathrm{KS}}$ is the Kohn-Sham effective Hamiltonian for the known EDF. Equation (2.2.84) can be rearranged to

$$
\begin{aligned}
E_{\mathrm{gs}}^{\mathrm{exact}}=&\sum_j\varepsilon_j^{\mathrm{exact}}+\tilde{E}_{\mathrm{Hxc}}\left[\rho_{\mathrm{gs}}^{\mathrm{exact}}\right]-\int\frac{\delta\tilde{E}_{\mathrm{Hxc}}\left[\rho_{\mathrm{gs}}^{\mathrm{exact}}\right]}{\delta\rho(\boldsymbol{r})}\rho_{\mathrm{gs}}^{\mathrm{exact}}(\boldsymbol{r})\,d\boldsymbol{r}\\
&+\lambda E_{\mathrm{Hxc}}^{(1)}\left[\rho_{\mathrm{gs}}^{\mathrm{exact}}\right]-\lambda\int\frac{\delta E_{\mathrm{Hxc}}^{(1)}\left[\rho_{\mathrm{gs}}^{\mathrm{exact}}\right]}{\delta\rho(\boldsymbol{r})}\rho_{\mathrm{gs}}^{\mathrm{exact}}(\boldsymbol{r})\,d\boldsymbol{r}+O\left(\lambda^2\right).
\end{aligned}
\tag{2.2.91}
$$

Combining Eqs. (2.2.88) and (2.2.91), one obtains

$$
\begin{aligned}
&\sum_j\varepsilon_j^{\mathrm{exact}}+\tilde{E}_{\mathrm{Hxc}}\left[\rho_{\mathrm{gs}}^{\mathrm{exact}}\right]-\int\frac{\delta\tilde{E}_{\mathrm{Hxc}}\left[\rho_{\mathrm{gs}}^{\mathrm{exact}}\right]}{\delta\rho(\boldsymbol{r})}\rho_{\mathrm{gs}}^{\mathrm{exact}}(\boldsymbol{r})\,d\boldsymbol{r}-\tilde{E}_{\mathrm{gs}}\\
&=\lambda E_{\mathrm{Hxc}}^{(1)}\left[\tilde{\rho}_{\mathrm{gs}}\right]+\lambda\int\frac{\delta E_{\mathrm{Hxc}}^{(1)}\left[\rho_{\mathrm{gs}}^{\mathrm{exact}}\right]}{\delta\rho(\boldsymbol{r})}\rho_{\mathrm{gs}}^{\mathrm{exact}}(\boldsymbol{r})\,d\boldsymbol{r}-\lambda E_{\mathrm{Hxc}}^{(1)}\left[\rho_{\mathrm{gs}}^{\mathrm{exact}}\right],
\end{aligned}
\tag{2.2.92}
$$

where the left-hand side can be calculated, and thus, in principle, one can derive $\lambda E_{\mathrm{Hxc}}^{(1)}$. The master equation [Eq. (2.2.92)] is the functional equation and thus it is, in practice, difficult to solve. Hence, in Ref. [A8], the form of $\lambda E_{\mathrm{Hxc}}^{(1)}$ was assumed, and it was benchmarked that it reproduces less than 1 % error.

The IKS-DFPT was further applied to nuclear DFT [A15]. It is expected to work more efficiently, since the LDA part can be constrained to the homogeneous nucleon gas, called nuclear matter, while the other part can also be constrained with respect to the symmetry.

2.3 Nuclear Density Functional Theory

In this section, it is discussed how to obtain the ground state of the Hamiltonian [Eq. (1.1.2)]. There are several methods to solve this Hamiltonian, which can be divided into several classes: *ab initio* methods, shell model calculation, nuclear density functional theory, and others.

In short, the *ab initio* methods refer to the wave function methods with the bare nuclear interaction, such as the Green's function Monte Carlo calculation [338–343], the no-core shell model calculation [44, 344–348], the self-consistent Green's function calculation [349–354], the lattice effective field theory [355–360], and the Brueckner-Hartree-Fock calculation [176, 361–365]. Here, the bare nuclear interaction is the nuclear interaction in vacuum, which can be determined from nucleon scattering experiments and the bound state of deuterons. Since in these methods the bare interaction is explicitly treated, it is expected that there is no approximation for nuclear interaction. However, due to the numerical costs and the accuracy of the bare nuclear interaction, only light-mass atomic nuclei or doubly-magic nuclei can be calculated.

The nuclear shell model corresponds to the configuration interaction method with the frozen core approximation [366, 367]. In this calculation, nucleons in the doubly-magic core are not taken into account for the calculation, and only the valence nucleons are considered. The Hamiltonian for these valence nucleons is diagonalized by using the Slater determinants, where the particle-hole excitations of these valence nucleons

are also limited only to several major shells. Since the active space is limited, the effective nuclear interaction should be used, instead of the bare one. If one considers a different active space, one is supposed to use a different effective interaction, while effective interactions can be derived from the bare interaction [45, 47, 368]. The configuration interaction method, in general, requires huge numerical costs; thus, the number of nucleons one can consider in the active space is also limited. Therefore, this method can be applied up to medium-heavy or, at most, heavy nuclei.

In contrast to the above two methods, the mean-field approximation or density functional theory can be applied to all the atomic nuclei [87, 206–208, 369]. In the nuclear mean-field theory, the ground-state wave function is calculated by the Hartree-Fock approximation. Since the bare nuclear interaction is strongly attractive, the medium effect is so strong. Consequently, the Hartree-Fock calculation with the bare interaction does not give proper results. Instead, the effective nuclear interaction is used for v_{nucl} in the Hamiltonian. In order to incorporate the in-medium effect, it is assumed that the effective interaction has density dependence. As a result, the Hartree-Fock equation becomes the density-dependent Hartree-Fock equation or even the Kohn-Sham equation in DFT; thus, the Hartree-Fock or mean-field calculation in nuclear physics is now frequently called as DFT. Relation between the effective interaction in nuclear DFT and the bare nuclear interaction has not been clear yet. On top of nuclear DFT calculation, the pairing correlation can be considered for even-even nuclei, where such calculation is called Hartree-Fock plus BCS or Hartree-Fock-Bogoliubov calculation [209, 370].

Here, it should be noted that, in contrast to the condensed matter DFT, since the atomic nuclei are self-bound systems, there is no external potential. Therefore, in principle, the Hohenberg-Kohn theorem does not hold because the translation symmetry is not broken. Nevertheless, it is known that the nuclear DFT practically works well, and the extension of the Hohenberg-Kohn theorem to the self-bound systems, where the translation symmetry is broken, has been discussed in Refs. [371–373]: Thus, it is expected that the nuclear Hartree-Fock and density functional theories are applicable to nuclear structure calculation [3]. The remaining part of this section is devoted to the detailed discussion of the nuclear Hartree-Fock and density functional theories.

Effective Interaction

There are several kinds of effective interactions used in nuclear density functional theory: the Skyrme [374, 375], the Gogny [376], and the Michigan three-range Yukawa (M3Y) [377, 378] type interactions in non-relativistic schemes.

The Skyrme interaction, which will be used in this thesis and explained in detail below, is the most widely used effective interaction in nuclear DFT. As will be explained later, the Skyrme interaction directly leads to the corresponding EDF; hence, the Skyrme interaction itself is also frequently referred to as the Skyrme EDF. The form of the effective interaction is the delta-function type zero-range interaction, which was derived by using the low-momentum expansion of the nuclear interaction in medium [374]. Thanks to the form of the interaction, the Skyrme EDF only depends on the local density and its derivative; as a result, the calculation cost is quite low and thus systematic investigation on the whole nuclear chart can be done rather easily [211]. In contrast to the Skyrme type, the forms of the Gogny and the M3Y type effective interactions are the Gaussian and Yukawa type finite-range interactions, respectively. Consequently, the numerical cost is larger than the Skyrme type, while some long-range behaviours such as nuclear reaction and fission can be described well [379].

The relativistic version of the nuclear DFT, called covariant density functional theory (CDFT) [380, 381], is also a widely used but rather different idea. One starts from the Lagrangian with the meson exchange. To incorporate the in-medium effect, non-linear terms for meson fields is introduced or density dependence is introduced in the coupling constant between meson and nucleon. Then, the Hamiltonian for the systems is constructed by the Legendre transformation of the Lagrangian. The CDFT is divided into two classes further: relativistic mean-field (RMF) and relativistic Hartree-Fock (RHF) calculations. In the RMF calculation, only the Hartree term is considered; in the RHF calculation, both the Hartree and Fock terms are considered.

[3] If they were not applicable or their approximations were not enough, in practice, many properties could not be reproduced. As mentioned, modern nuclear EDFs reproduce experimental nuclear masses within several MeV root-mean-square deviations, which is evidence that the nuclear DFT works well. If one regards the following calculation method as the nuclear Hartree-Fock calculation, instead of the nuclear DFT, the Hohenberg-Kohn theorem is not needed, and thus, one need not pay attention to the collapse of this theorem.

All the EDFs contain several parameters, which are constrained by using experimental data of charge radii and binding energies of several nuclei, as well as the nuclear matter properties given theoretically. Since the available experimental data are limited to the stable nuclei or unstable nuclei not far from the stable nuclei, EDFs usually give similar results for stable nuclei, while different EDFs often give different results for exotic nuclei. In addition, nuclear properties are related to properties of nuclear EoS around the saturation density; thus, EoSs obtained by EDFs are quite similar around the saturation density, while they deviate above saturation density [382]. An *ab initio* EDF, i.e., an EDF whose parameters are determined without referring to any experimental data, is desired to overcome such problems [383–387].

Skyrme Interaction

The Skyrme interaction proposed in 1958 [374] is based on the low-momentum expansion up to the second order since the nuclear interaction is short-range and, consequently, it is expected that the momentum dependence is weak. This Skyrme interaction consists of two-body interaction and three-body interaction, where the three-body interaction is assumed to be the point coupling;

$$v_{\mathrm{Sky3}}\left(\boldsymbol{r}_1,\boldsymbol{r}_2,\boldsymbol{r}_3\right)=t_3\delta\left(\boldsymbol{r}_1-\boldsymbol{r}_2\right)\delta\left(\boldsymbol{r}_2-\boldsymbol{r}_3\right), \tag{2.3.1}$$

whose Hartree-Fock expectation value is identical to

$$\tilde{v}_{\mathrm{Sky3}}\left(\boldsymbol{r}_1,\boldsymbol{r}_2\right)=\frac{t_3}{6}\left(1+P_\sigma\right)\delta\left(\boldsymbol{r}_1-\boldsymbol{r}_2\right)\rho\left(\frac{\boldsymbol{r}_1+\boldsymbol{r}_2}{2}\right). \tag{2.3.2}$$

Accordingly, the modern Skyrme effective interaction is written as

$$\begin{aligned}v_{\mathrm{Sky}}\left(\boldsymbol{r}_1,\boldsymbol{r}_2\right)=&\,t_0\left(1+x_0P_\sigma\right)\delta\left(\boldsymbol{r}_1-\boldsymbol{r}_2\right)\\&+\frac{t_1}{2}\left(1+x_1P_\sigma\right)\left[\boldsymbol{k}^{\dagger 2}\delta\left(\boldsymbol{r}_1-\boldsymbol{r}_2\right)+\delta\left(\boldsymbol{r}_1-\boldsymbol{r}_2\right)\boldsymbol{k}^2\right]+t_2\left(1+x_2P_\sigma\right)\boldsymbol{k}^\dagger\cdot\delta\left(\boldsymbol{r}_1-\boldsymbol{r}_2\right)\boldsymbol{k}\\&+\frac{t_3}{6}\left(1+x_3P_\sigma\right)\delta\left(\boldsymbol{r}_1-\boldsymbol{r}_2\right)\left[\rho\left(\frac{\boldsymbol{r}_1+\boldsymbol{r}_2}{2}\right)\right]^\alpha+iW_0\boldsymbol{\sigma}\cdot\boldsymbol{k}^\dagger\times\delta\left(\boldsymbol{r}_1-\boldsymbol{r}_2\right)\boldsymbol{k},\end{aligned} \tag{2.3.3}$$

where the last term corresponds to the spin-orbit interaction and $\boldsymbol{k}=\nabla_1-\nabla_2$. The parameters α, t_j, x_j ($j=0$, 1, 2, and 3), W_0, and W_0' are determined to reproduce nuclear EoS obtained by other methods, especially, Ref. [388], and nuclear binding energies and charge radii for selected nuclei. In the original Skyrme interaction, α and x_3 were set to 1 and 0, respectively, while in the modern Skyrme interaction, α and x_3 are treated as fitting parameters as the other parameters.

The Hartree-Fock calculation was firstly performed in early 1970s [389,390], and its systematic application to both spherical and axially deformed nuclei was done in 1972 [375, 391]. The Hartree-Fock expectation value for the modern Skyrme interaction reads [392, 393]

$$\begin{aligned}\mathcal{E}^{\mathrm{H}}\left(\boldsymbol{r}\right)=&\frac{t_0}{2}\left(1+\frac{x_0}{2}\right)\left[\rho\left(\boldsymbol{r}\right)\right]^2+\frac{t_3}{12}\left(1+\frac{x_3}{2}\right)\left[\rho\left(\boldsymbol{r}\right)\right]^{\alpha+2}\\&+\frac{1}{4}\left[t_1\left(1+\frac{x_1}{2}\right)+t_2\left(1+\frac{x_2}{2}\right)\right]\rho\left(\boldsymbol{r}\right)t\left(\boldsymbol{r}\right)\\&-\frac{1}{16}\left[3t_1\left(1+\frac{x_1}{2}\right)-t_2\left(1+\frac{x_2}{2}\right)\right]\rho\left(\boldsymbol{r}\right)\Delta\rho\left(\boldsymbol{r}\right)\\&-\frac{1}{16}\left(t_1x_1+t_2x_2\right)\left[\boldsymbol{J}\left(\boldsymbol{r}\right)\right]^2+\frac{W_0}{2}\rho\left(\boldsymbol{r}\right)\nabla\cdot\boldsymbol{J}\left(\boldsymbol{r}\right),\end{aligned} \tag{2.3.4}$$

$$\begin{aligned}\mathcal{E}^{\mathrm{x}}\left(\boldsymbol{r}\right)=&-\frac{t_0}{2}\left(\frac{1}{2}+x_0\right)\left\{\left[\rho_n\left(\boldsymbol{r}\right)\right]^2+\left[\rho_p\left(\boldsymbol{r}\right)\right]^2\right\}-\frac{t_3}{12}\left(\frac{1}{2}+x_3\right)\left[\rho\left(\boldsymbol{r}\right)\right]^\alpha\left\{\left[\rho_n\left(\boldsymbol{r}\right)\right]^2+\left[\rho_p\left(\boldsymbol{r}\right)\right]^2\right\}\\&-\frac{1}{4}\left[t_1\left(\frac{1}{2}+x_1\right)-t_2\left(\frac{1}{2}+x_2\right)\right]\left[\rho_n\left(\boldsymbol{r}\right)t_n\left(\boldsymbol{r}\right)+\rho_p\left(\boldsymbol{r}\right)t_p\left(\boldsymbol{r}\right)\right]\\&+\frac{1}{16}\left[3t_1\left(\frac{1}{2}+x_1\right)+t_2\left(\frac{1}{2}+x_2\right)\right]\left[\rho_n\left(\boldsymbol{r}\right)\Delta\rho_n\left(\boldsymbol{r}\right)+\rho_p\left(\boldsymbol{r}\right)\Delta\rho_p\left(\boldsymbol{r}\right)\right]\\&+\frac{1}{16}\left(t_1-t_2\right)\left\{\left[\boldsymbol{J}_n\left(\boldsymbol{r}\right)\right]^2+\left[\boldsymbol{J}_p\left(\boldsymbol{r}\right)\right]^2\right\}+\frac{W_0'}{2}\left[\rho_n\left(\boldsymbol{r}\right)\nabla\cdot\boldsymbol{J}_n\left(\boldsymbol{r}\right)+\rho_p\left(\boldsymbol{r}\right)\nabla\cdot\boldsymbol{J}_p\left(\boldsymbol{r}\right)\right],\end{aligned} \tag{2.3.5}$$

$$E_{\mathrm{nucl}}\left[\{\rho\}\right]=\int\left[\mathcal{E}^{\mathrm{H}}\left(\boldsymbol{r}\right)+\mathcal{E}^{\mathrm{x}}\left(\boldsymbol{r}\right)\right]d\boldsymbol{r}, \tag{2.3.6}$$

where the particle density ρ_τ, the kinetic density t_τ, and the current density $\boldsymbol{J}_\tau$ for the nucleon τ ($\tau = p, n$) read

$$\rho_\tau(\boldsymbol{r}) = \sum_{j\in\mathrm{occ}} \left|\varphi_{j\tau}(\boldsymbol{r})\right|^2, \tag{2.3.7}$$

$$t_\tau(\boldsymbol{r}) = \sum_{j\in\mathrm{occ}} \left|\nabla\varphi_{j\tau}(\boldsymbol{r})\right|^2, \tag{2.3.8}$$

$$\boldsymbol{J}_\tau(\boldsymbol{r}) = \sum_{j\in\mathrm{occ}} \varphi^*_{j\tau}(\boldsymbol{r})\,\boldsymbol{\sigma}\times\nabla\varphi_{j\tau}(\boldsymbol{r}), \tag{2.3.9}$$

respectively, and $\varphi_{j\tau}(\boldsymbol{r})$ is the spatial part of a single-particle orbital of nucleon τ. The total densities are denoted as $\rho(\boldsymbol{r}) = \rho_p(\boldsymbol{r}) + \rho_n(\boldsymbol{r})$, $t(\boldsymbol{r}) = t_p(\boldsymbol{r}) + t_n(\boldsymbol{r})$, and $\boldsymbol{J}(\boldsymbol{r}) = \boldsymbol{J}_p(\boldsymbol{r}) + \boldsymbol{J}_n(\boldsymbol{r})$. Here, $\mathcal{E}^{\mathrm{H}}$ and $\mathcal{E}^{\mathrm{x}}$ correspond to Hartree and exchange Skyrme energy densities, respectively, and are functionals of ρ_τ, t_τ, and $\boldsymbol{J}_\tau$, which are simply referred to as $\{\rho\}$ altogether. It should be noted that, in condensed matter physics, an energy density refers to energy per particle, while in nuclear physics, an energy density refers to energy per volume. In the original Skyrme interaction given in Eq. (2.3.3), the isoscalar and isovector spin-orbit strengths, W_0 and W_0', are identical, i.e., $W_0 = W_0'$; however, to describe charge radii of isotopic chain better, $W_0 \neq W_0'$ was introduced in Ref. [394], and now this treatment is rather popular.

Combining with E_{nucl} shown in Eq. (2.3.6) and the EDF for the electromagnetic interaction E_{EM}, one obtains the total interaction functional

$$E_{\mathrm{int}}[\{\rho\}] = E_{\mathrm{nucl}}[\{\rho\}] + E_{\mathrm{EM}}[\{\rho\}], \tag{2.3.10}$$

which corresponds to E_{Hxc} in the Kohn-Sham equation [Eqs. (2.2.26) and (2.2.27)]. Hence, solving the Kohn-Sham equation with E_{int}, one can obtain the ground-state wave function and density.

In most works, only the Coulomb interaction is considered for the electromagnetic interaction, and accordingly, E_{EM} is composed of two parts: Coulomb Hartree [Eq. (2.2.38)] and exchange EDFs, $E_{\mathrm{CH}}[\rho_{\mathrm{ch}}]$ and $E_{\mathrm{Cx}}[\rho_{\mathrm{ch}}]$. Here, it should be noticed that the Coulomb interaction is interaction between *charge* of particles. Therefore, the arguments of E_{CH} and E_{Cx} are *charge* density distribution ρ_{ch}, instead of proton density distribution ρ_p. Since charge of protons and neutrons are +1 and 0, respectively, ρ_{ch} is almost identical to ρ_p, while there is still a difference as shown in Eq. (1.4.4). This difference will be focused on in Sec. 3.4.

The EoS obtained by the Skyrme interaction reads

$$\begin{aligned}
\frac{E_{\mathrm{Skyrme}}}{A}(\rho,\beta) = {}& \frac{3}{5}\frac{\hbar^2}{2m}\frac{(1+\beta)^{5/3}+(1-\beta)^{5/3}}{2}\left(\frac{3\pi^2}{2}\right)^{2/3}\rho^{2/3} \\
&+ \frac{t_0}{2}\left(1+\frac{x_0}{2}\right)\rho \\
&+ \frac{3}{20}\left[t_1\left(1+\frac{x_1}{2}\right)+t_2\left(1+\frac{x_2}{2}\right)\right]\frac{(1+\beta)^{5/3}+(1-\beta)^{5/3}}{2}\left(\frac{3\pi^2}{2}\right)^{2/3}\rho^{5/3} \\
&+ \frac{t_3}{12}\left(1+\frac{x_3}{2}\right)\rho^{\alpha+1} \\
&- \frac{t_0}{2}\left(\frac{1}{2}+x_0\right)\frac{(1+\beta)^2+(1-\beta)^2}{4}\rho \\
&- \frac{1}{4}\left[t_1\left(\frac{1}{2}+x_1\right)-t_2\left(\frac{1}{2}+x_2\right)\right]\frac{3}{5}\left(\frac{3\pi^2}{2}\right)^{2/3}\frac{(1+\beta)^{8/3}+(1-\beta)^{8/3}}{4}\rho^{5/3} \\
&- \frac{t_3}{12}\left(\frac{1}{2}+x_3\right)\frac{(1+\beta)^2+(1-\beta)^2}{4}\rho^{\alpha+1} \\
\simeq {}& \left\{\frac{3}{5}\frac{\hbar^2}{2m}\left(\frac{3\pi^2}{2}\right)^{2/3}\rho^{2/3} + \frac{3}{8}t_0\rho + \frac{3}{80}\left(\frac{3\pi^2}{2}\right)^{2/3}\left[3t_1+t_2(5+4x_2)\right]\rho^{5/3} + \frac{t_3}{16}\rho^{\alpha+1}\right\} \\
&+ \left\{\frac{1}{3}\frac{\hbar^2}{2m}\left(\frac{3\pi^2}{2}\right)^{2/3}\rho^{2/3} - \frac{1}{8}t_0(1+2x_0)\rho \right. \\
&\left. - \frac{1}{24}\left(\frac{3\pi^2}{2}\right)^{2/3}\left[3t_1x_1 - t_2(4+5x_2)\right]\rho^{5/3} - \frac{1}{48}t_3(1+2x_3)\rho^{\alpha+1}\right\}\beta^2,
\end{aligned} \tag{2.3.11}$$

where $\beta = (\rho_n - \rho_p)/\rho$, i.e., $\rho_n = (1+\beta)\rho/2$, $\rho_p = (1-\beta)\rho/2$, $t_n = 3\left(3\pi^2\right)^{2/3}\rho_n^{5/3}/5$, and $t_p = 3\left(3\pi^2\right)^{2/3}\rho_p^{5/3}/5$. Accordingly, EoS parameters J, L, $K_{\rm sym}$, and K_∞ read [395]

$$\begin{aligned}
J &= \frac{1}{3}\frac{\hbar^2}{2m}\left(\frac{3\pi^2}{2}\right)^{2/3}\rho_0^{2/3} - \frac{1}{8}t_0\left(1+2x_0\right)\rho_0 \\
&\quad - \frac{1}{24}\left(\frac{3\pi^2}{2}\right)^{2/3}\left[3t_1x_1 - t_2\left(4+5x_2\right)\right]\rho_0^{5/3} - \frac{1}{48}t_3\left(1+2x_3\right)\rho_0^{\alpha+1}, \qquad (2.3.12)\\
L &= \frac{2}{3}\frac{\hbar^2}{2m}\left(\frac{3\pi^2}{2}\right)^{2/3}\rho_0^{2/3} - \frac{3}{8}t_0\left(1+2x_0\right)\rho_0 \\
&\quad - \frac{5}{24}\left(\frac{3\pi^2}{2}\right)^{2/3}\left[3t_1x_1 - t_2\left(4+5x_2\right)\right]\rho_0^{5/3} - \frac{1}{16}t_3\left(1+2x_3\right)\left(\alpha+1\right)\rho_0^{\alpha+1}, \qquad (2.3.13)\\
K_{\rm sym} &= -\frac{2}{3}\frac{\hbar^2}{2m}\left(\frac{3\pi^2}{2}\right)^{2/3}\rho_0^{2/3} \\
&\quad - \frac{5}{12}\left(\frac{3\pi^2}{2}\right)^{2/3}\left[3t_1x_1 - t_2\left(4+5x_2\right)\right]\rho_0^{5/3} - \frac{3}{16}t_3\left(1+2x_3\right)\alpha\left(\alpha+1\right)\rho_0^{\alpha+1}, \qquad (2.3.14)\\
K_\infty &= -\frac{6}{5}\frac{\hbar^2}{2m}\left(\frac{3\pi}{2}\right)^{2/3}\rho_0^{2/3} \\
&\quad + \frac{3}{8}\left(\frac{3\pi^2}{2}\right)^{2/3}\left[3t_1 + t_2\left(5+4x_2\right)\right]\rho_0^{5/3} + \frac{9}{16}t_3\alpha\left(\alpha+1\right)\rho_0^{\alpha+1}, \qquad (2.3.15)
\end{aligned}$$

respectively. The pressure of nuclear matter is

$$\begin{aligned}
P\left(\rho,\beta\right) &= \rho^2\frac{\partial}{\partial\rho}\frac{E_{\rm Skyrme}}{A}\left(\rho,\beta\right) \\
&\simeq \left\{\frac{2}{5}\frac{\hbar^2}{2m}\left(\frac{3\pi^2}{2}\right)^{2/3}\rho^{5/3} + \frac{3}{8}t_0\rho^2 + \frac{1}{16}\left(\frac{3\pi^2}{2}\right)^{2/3}\left[3t_1 + t_2\left(5+4x_2\right)\right]\rho^{8/3} + \frac{t_3}{16}\left(\alpha+1\right)\rho^{\alpha+2}\right\} \\
&\quad + \left\{\frac{2}{9}\frac{\hbar^2}{2m}\left(\frac{3\pi^2}{2}\right)^{2/3}\rho^{5/3} - \frac{t_0}{8}\left(1+2x_0\right)\rho^2 \right.\\
&\quad \left. - \frac{5}{72}\left(\frac{3\pi^2}{2}\right)^{2/3}\left[3t_1x_1 - t_2\left(4+5x_2\right)\right]\rho^{8/3} - \frac{1}{48}\left(\alpha+1\right)t_3\left(1+2x_3\right)\rho^{\alpha+2}\right\}\beta^2. \qquad (2.3.16)
\end{aligned}$$

The saturation density ρ_0 satisfies

$$\frac{2}{5}\frac{\hbar^2}{2m}\left(\frac{3\pi^2}{2}\right)^{2/3}\rho_0^{5/3} + \frac{3}{8}t_0\rho_0^2 + \frac{1}{16}\left(\frac{3\pi^2}{2}\right)^{2/3}\left[3t_1 + t_2\left(5+4x_2\right)\right]\rho_0^{8/3} + \frac{t_3}{16}\left(\alpha+1\right)\rho_0^{\alpha+2} = 0. \qquad (2.3.17)$$

The Skyrme effective interaction or EDF was justified from the point of view of DFT. As in most EDFs for electron systems, it is assumed that the EDF only depends on local densities. It can be rather justified than the Coulomb systems since the nuclear interaction is short-range in contrast to the Coulomb interaction [396–398]. Here, several densities are defined as follows: the particle density ρ_τ, the kinetic energy density t_τ, the spin density $\boldsymbol{s}_\tau$, the momentum density $\boldsymbol{j}_\tau$, the spin-current tensor $J_{\mu\nu\tau}$, the vector density of the kinetic

energy $\boldsymbol{T}_\tau$ [396], respectively, defined by

$$\rho_\tau(\boldsymbol{r}) = \sum_{j\in\mathrm{occ}} \sum_{\sigma=\pm1} \left|\varphi_{j\tau}(\boldsymbol{r},\sigma)\right|^2, \tag{2.3.18}$$

$$t_\tau(\boldsymbol{r}) = \sum_{j\in\mathrm{occ}} \sum_{\sigma=\pm1} \left|\nabla\varphi_{j\tau}(\boldsymbol{r},\sigma)\right|^2, \tag{2.3.19}$$

$$\boldsymbol{s}_\tau(\boldsymbol{r}) = \sum_{j\in\mathrm{occ}} \sum_{\sigma,\,\sigma'=\pm1} \varphi^*_{j\tau}(\boldsymbol{r},\sigma')\,\varphi_{j\tau}(\boldsymbol{r},\sigma)\,\langle\sigma'|\hat{\boldsymbol{\sigma}}|\sigma\rangle, \tag{2.3.20}$$

$$\boldsymbol{j}_\tau(\boldsymbol{r}) = \sum_{j\in\mathrm{occ}} \sum_{\sigma=\pm1} \frac{1}{2i}\left[\varphi^*_{j\tau}(\boldsymbol{r},\sigma)\,\nabla\varphi_{j\tau}(\boldsymbol{r},\sigma) - \varphi_{j\tau}(\boldsymbol{r},\sigma)\,\nabla\varphi^*_{j\tau}(\boldsymbol{r},\sigma)\right], \tag{2.3.21}$$

$$J_{\mu\nu\tau}(\boldsymbol{r}) = \sum_{j\in\mathrm{occ}} \sum_{\sigma,\,\sigma'=\pm1} \frac{1}{2i}\left[\varphi^*_{j\tau}(\boldsymbol{r},\sigma')\,\nabla_\mu\varphi_{j\tau}(\boldsymbol{r},\sigma) - \varphi_{j\tau}(\boldsymbol{r},\sigma)\,\nabla_\mu\varphi^*_{j\tau}(\boldsymbol{r},\sigma')\right]\langle\sigma'|\hat{\sigma}_\nu|\sigma\rangle, \tag{2.3.22}$$

$$\boldsymbol{T}_\tau(\boldsymbol{r}) = \sum_{j\in\mathrm{occ}} \sum_{\sigma,\,\sigma'=\pm1} \left[\nabla\varphi^*_{j\tau}(\boldsymbol{r},\sigma')\cdot\nabla\varphi_{j\tau}(\boldsymbol{r},\sigma)\right]\langle\sigma'|\hat{\boldsymbol{\sigma}}|\sigma\rangle. \tag{2.3.23}$$

Here, ρ_τ, t_τ, and $J_{\mu\nu\tau}$ are symmetric under the time-reversal transformation, while $\boldsymbol{s}_\tau$, $\boldsymbol{j}_\tau$, and $\boldsymbol{T}_\tau$ are antisymmetric, and the spin-orbit density $\boldsymbol{J}$ is defined by $J_{\lambda\tau} = \sum_{\mu\nu}\varepsilon_{\lambda\mu\nu}J_{\mu\nu\tau}$, where $\varepsilon_{\lambda\mu\nu}$ is the Levi-Civita symbol. Because the Hamiltonian must have the time-reversal symmetry, the combination of these densities are limited. The following form comprises the Skyrme EDF;

$$\begin{aligned}
&\mathcal{E}^q_{\mathrm{nucl}}(\boldsymbol{r}) \\
&= C^{\mathrm{den}}_q\left[\rho_q(\boldsymbol{r})\right]^2 + C^{\mathrm{dden}}_q\rho_q(\boldsymbol{r})\,\Delta\,\rho_q(\boldsymbol{r}) + C^{\mathrm{kin}}_q\rho_q(\boldsymbol{r})\,t_q(\boldsymbol{r}) + C^{\mathrm{cur}}_q\left[\boldsymbol{J}_q(\boldsymbol{r})\right]^2 + C^{\mathrm{SO}}_q\rho_q(\boldsymbol{r})\,\nabla\cdot\boldsymbol{J}_q(\boldsymbol{r}) \\
&\quad + C^{\mathrm{spin}}_q\left[\boldsymbol{s}_q(\boldsymbol{r})\right]^2 + C^{\mathrm{dspin}}_q\boldsymbol{s}_q(\boldsymbol{r})\cdot\Delta\,\boldsymbol{s}_q(\boldsymbol{r}) + C^{\mathrm{vkin}}_q\boldsymbol{s}_q(\boldsymbol{r})\cdot\boldsymbol{T}_q(\boldsymbol{r})\,C^{\mathrm{mom}}_q\left[\boldsymbol{j}_q(\boldsymbol{r})\right]^2 + C^{\mathrm{dmom}}_q\boldsymbol{s}_q\cdot\left[\nabla\times\boldsymbol{j}_q(\boldsymbol{r})\right],
\end{aligned} \tag{2.3.24}$$

where the first and second lines consist of the time-even and time-odd densities, respectively, and $q = 0$ and 1, respectively, mean isoscalar and isovector, where these densities are defined by, for instance, $\rho_{q=0} = \rho_n + \rho_p$ and $\rho_{q=1} = \rho_n - \rho_p$. The coefficients C_q can also depend on densities with time-even combination, while the Skyrme EDF corresponds to that only C^{den}_q and C^{dden}_q have ρ dependences. The relation between C_q in Eq. (2.3.24) and the parameters of the Skyrme EDF is shown in Ref. [397].

Chapter 3

Accurate Treatment of Electromagnetic Interaction

In this chapter, the treatment of the electromagnetic interaction in the nuclear DFT is improved to estimate the electromagnetic contribution to total energies as accurately as possible. First, the generalized gradient approximation is applied to the nuclear DFT. Then, the higher-order contributions are considered.

3.1 Current Status of Coulomb Energy Density Functional in Nuclear Density Functional Theory

In the nuclear DFT, the ground-state energy can be written as

$$E_{\mathrm{gs}}\left[\rho_p, \rho_n\right] = T_{\mathrm{KS}} + E_{\mathrm{nucl}}\left[\rho_p, \rho_n\right] + E_{\mathrm{EM}}\left[\rho_{\mathrm{ch}}\right], \tag{3.1.1}$$

where T_{KS} is the Kohn-Sham kinetic energy defined by Eq. (2.2.18), E_{nucl} is the nuclear EDF, and E_{EM} is the electromagnetic EDF. In most works, only the Coulomb interaction is considered; $E_{\mathrm{EM}}\left[\rho_{\mathrm{ch}}\right] = E_{\mathrm{CH}}\left[\rho_{\mathrm{ch}}\right] + E_{\mathrm{Cx}}\left[\rho_{\mathrm{ch}}\right]$, where E_{CH} and E_{Cx} are, respectively, the Coulomb Hartree and exchange EDFs. The Coulomb Hartree EDF can be defined and calculated without any ambiguity by Eq. (2.2.38). The Coulomb exchange EDF is expected to reproduce the Coulomb exact-Fock energy defined by Eq. (2.2.39) if one neglects the size (charge distribution) of nucleons; nevertheless, the Coulomb LDA EDF [Eq. (2.2.43)] is usually used for E_{Cx} due to the numerical cost, or it is sometimes even neglected. For example, most Skyrme EDFs, such as the SLy4 and SLy5 EDFs [58], are fitted to the experimental data with the Coulomb LDA exchange energy, while the SKX EDF [175], one of the Skyrme EDFs, is fitted to the experimental data without considering the Coulomb exchange energy with an assertion that the Coulomb exchange energy is cancelled with the nuclear CSB energy by coincidence, and accordingly, the fitting error was reduced, although it is not a physically well-based treatment.

As discussed in Sec. 2.3, the nuclear EDF E_{nucl} is given by the fitting to the experimental data, where the ISB terms of the nuclear interaction are not considered. The difference between E_{Cx} calculated by the LDA and that by the exact-Fock energy is expected to be absorbed in E_{nucl}. Thus, in total, E_{gs} is expected to reproduce the experimental data within a relatively small difference. However, if one is interested in phenomena related to the isospin symmetry breaking, such differences may not be discussed appropriately, since most part, which is determined by E_{nucl}, is cancelled.

Therefore, in this section, the accuracy of the electromagnetic EDF in nuclear DFT is improved as much as possible, with borrowing the idea of DFT for electronic systems. Then, one will be able to discuss phenomena related to isospin symmetry breaking more precisely. In addition, the expression using the density, instead of single-particle orbitals, has an advantage for taking into account the effect of the nucleon form factors, which will be explained later.

Sections 3.2 and 3.3 are devoted to Coulomb GGA exchange EDFs. Since the Coulomb LDA exchange EDF depends only on the local density $\rho_p\left(\boldsymbol{r}\right)$, following the Jacob's ladder in DFT [Fig. 2.2.2], the density gradient $\left|\nabla\rho\left(\boldsymbol{r}\right)\right|$ should be taken into account as the next step in order to improve the accuracy. In Sec. 3.2, several Coulomb GGA exchange EDFs used in DFT for condensed matter physics are tested using

experimental charge density distribution to see how large the EDF dependence is. In Sec. 3.3, we attempt a Coulomb GGA exchange EDF to the self-consistent DFT calculation for atomic nuclei. We take the Perdew-Burke-Ernzerhof parametrization of the Coulomb GGA (GGA-PBE) exchange EDF [295] as an example. We adjust a parameter to reproduce the exact Coulomb Fock energy in nuclear DFT.

In Secs. 3.4 and 3.5, higher-order contributions than the Coulomb interaction with assuming protons as *point* particles are taken into account. Possible corrections are spatial charge distributions of nucleons and higher-order correction to the Coulomb interaction. In the former, contributions are divided into two parts: electric form factors and magnetic ones, where the contribution of the magnetic form factors correspond to the electromagnetic spin-orbit interaction. In the latter, the next-leading order corrections to the Coulomb interaction in terms of the coupling constant α are the finite-light-speed correction to the Coulomb interaction called Breit correction, the vacuum polarization, the self-energy, and the two-photon exchange interaction [167, 399] [1]. It is known that the self-energy gives a non-negligible contribution to the atomic spectra, i.e., electronic structures of atoms, while the mass of protons M_p is so heavy that it may be negligible in atomic nuclei. The two-photon exchange interaction is $1/M_p$ weaker than the vacuum polarization [167]; hence it is not considered. Therefore, the electric and magnetic form factors of nucleons, the vacuum polarization, and the Breit correction on nuclear properties will be taken into account. First, in Sec. 3.4, effects of the nucleon form factor on the Coulomb energy, which will be referred to as the finite-size effect, and the vacuum polarization of the Coulomb interaction will be considered in $E_{\rm EM}$ [2]. In Ref. [191], it was estimated how large the electric form factor of protons, vacuum polarization, and the electromagnetic spin-orbit interaction affect the isobaric analogue energy; hence, the corrections considered in Sec. 3.4 are the same as Ref. [191], apart from the electric form factor of neutrons.

In Sec. 3.5 the Breit correction will be considered independently on top of the Coulomb LDA EDF, while corrections considered in Sec. 3.4 is not considered. Since the GGA EDF of the Breit correction is, at this moment, impossible to apply to nuclear DFT calculation, as will be discussed, the Coulomb-Breit LDA exchange EDF will be used. The Coulomb interaction is the electromagnetic interaction in which the speed of light is assumed to be infinity, i.e., it is the instantaneous electromagnetic interaction. Therefore, once one considers the finite light speed, the correction to the Coulomb interaction appears, which is called Breit correction [402–404]. This correction is non-negligible in the electronic structure of super-heavy atoms [405, A13]. We shall test how large the Breit correction affects nuclear ground-state properties, which will be discussed at the LDA level.

Since parameters of nuclear EDFs are determined to reproduce the experimental data after subtracting the Coulomb contributions, which is usually estimated by the Coulomb LDA, the nuclear EDF implicitly includes the effect of the correction discussed in this chapter. However, throughout this chapter, the nuclear EDF is not refitted to experimental data. Instead, it will be discussed how large such corrections are without comparing them to experimental data. Only one exception is the comparison to the experimental value of the mass difference of a mirror nuclei pair because contributions of the nuclear EDF are cancelled with each other due to the isospin symmetry. Since it is still under discussion how to estimate the systematic uncertainty of nuclear EDF, the accuracy of nuclear EDF will not be discussed; the statistical uncertainty may be able to be discussed [63], while its contribution is expected to be smaller than the statistical uncertainty; hence it is not considered, either.

Note that Secs. 3.2, 3.3, 3.4, and 3.5 are based on Refs. [A1], [A2], [A3], and [A5], respectively.

3.2 Preliminary Test of Coulomb Exchange Energy Density Functional in Generalized Gradient Approximation

Before applying the Coulomb GGA exchange EDF to self-consistent nuclear DFT, we perform a simple survey on which GGA EDFs can be applied. Coulomb exchange energies of the selected nuclei are estimated by using the charge density distribution $\rho_{\rm ch}$ measured experimentally [144], where sum-of-Gaussian fittings are used for $\rho_{\rm ch}$. As discussed above, the Coulomb exchange EDF in nuclear DFT is expected to reproduce the Coulomb exact-Fock energy, if the nucleon finite size is neglected. Figure 3 of Ref. [406] showed the Z

[1] In the AV18 bare nuclear interaction, all these corrections including finite-size effects are considered when the electromagnetic contribution is removed from experimental data [167].

[2] The effect of the vacuum polarization is expected to be already subtracted in the nucleon form factors [400, 401]. Hence, it is also expected that there is no double counting.

dependence of the relative error of the Coulomb exchange energy calculated by using the Coulomb LDA to that by the exact-Fock term. Thus, if the Coulomb GGA exchange EDF can reproduce the curve, it indicates that the Coulomb GGA exchange EDF may be applicable to nuclear DFT.

In general, with all the physical constants shown explicitly, the Coulomb LDA and GGA exchange EDF is written as

$$E_{\mathrm{Cx}}[\rho] = -\frac{3}{4}\frac{e^2}{4\pi\varepsilon_0}\left(\frac{3}{\pi}\right)^{1/3}\int [\rho(\boldsymbol{r})]^{4/3} F(s(\boldsymbol{r}))\, d\boldsymbol{r}. \tag{3.2.1}$$

Here, the enhancement factor F and the density gradient s are dimensionless. Thus, enhancement factors F given in Eqs. (2.2.61), (2.2.69), and (2.2.70) are invariant with respect to units taken. Note that the enhancement factor F for the LDA is the constant function, $F^{\mathrm{LDA}} \equiv 1$. The B88, PW91, PBE, and PBEsol GGA exchange EDFs are tested as examples.

Calculated Coulomb direct and exchange energies for the selected nuclei are shown in Table 3.2.1. Panels (a) and (b) of Fig. 3.2.1 show the relative difference between the exchange energy calculated by using the Coulomb LDA and that by the Coulomb GGA,

$$\Delta E_{\mathrm{Cx}} = \frac{E_{\mathrm{Cx}}^{\mathrm{GGA}} - E_{\mathrm{Cx}}^{\mathrm{LDA}}}{E_{\mathrm{Cx}}^{\mathrm{GGA}}}, \tag{3.2.2}$$

as functions of Z and A, respectively. Panel (b) of Fig. 3.2.1 is quite similar to Fig. 3 of Ref. [406]. Hence, it can be concluded that the Coulomb GGA exchange EDF, in general, reproduces the Coulomb exact-Fock energy quite nicely. In addition, all the GGA EDFs give similar results and the deviation among these is less than 2 %, although the Coulomb GGA enhancement factors deviate from each other at $s \gtrsim 4$ as shown in Fig. 2.2.4.

In order to understand such behaviour, Fig. 3.2.2 shows the charge density ρ_{ch} and its dimensionless density gradient s for ^{208}Pb obtained in Ref. [144] are plotted as functions of r. In the central region ($0 \le r \lesssim 5\,\mathrm{fm}$), ρ_{ch} is almost constant, and accordingly $s \simeq 0$. Therefore, the LDA and the GGA give almost the same energy density $\varepsilon_{\mathrm{x}}F$ at this region. In the surface region ($5 \lesssim r \lesssim 8\,\mathrm{fm}$), ρ_{ch} rapidly decreases and accordingly s increases. Nonetheless, the value of s ranges $0 \le s \lesssim 4$, in which all the GGA enhancement factors give the similar value. Therefore, the LDA and the GGA give different energy densities, while these GGA EDFs give almost the same. In $r \gtrsim 8\,\mathrm{fm}$, s diverges, but ρ_{ch} is almost zero, and thus, this region does not contribute to the Coulomb exchange energy. As a result, the LDA and the GGA give different Coulomb exchange energy, while the GGA exchange EDFs give no significant difference and there is no criterion to choose. Hence, in this work, we shall use the GGA-PBE EDF for self-consistent calculation, since it is the most widely used EDF in condensed matter physics and its form is the simplest among them.

The reason why ΔE_{Cx} is a decreasing function with respect to Z (or A) is also related to this analysis. The ratio of the surface region to the whole density in light nuclei is larger than that in heavy nuclei. Since only the surface region gives a significant difference of the LDA and the GGA. The relative differences of the Coulomb exchange energy calculated by the LDA is larger in light nuclei, and decreases as Z (or A) increases.

3.3 Modification of Coulomb Exchange Energy Density Functional in Generalized Gradient Approximation for Nuclear Structure Calculation

The previous section shows that the Coulomb GGA exchange EDF may reproduce the Coulomb exact-Fock energy more accurately than the Coulomb LDA one. The numerical cost of the Coulomb exact-Fock energy [Eq. (2.2.39)] is proportional to N^4 with the number of particles N, while the numerical cost of the Coulomb GGA exchange energy is proportional to N^3 [272].

In the nuclear DFT calculation, finite-range interaction, such as the Gogny interaction, can be used, as well as zero-range interaction. However, due to the numerical cost, DFT calculation with the finite-range interaction can be performed only with the basis expansion so far. In principle, the basis expansion method with a complete orthonormal basis can reproduce any functions, while, in practice, due to the numerical cost, the number of bases is limited. As a result, the basis expansion is not enough to calculate properties of exotic nuclei, for instance, halo nuclei. In order to calculate such nuclei, the calculation with spatial mesh

Table 3.2.1: Coulomb exchange energies calculated by the B88, PW91, PBE, and PBEsol GGA exchange EDF and experimental charge density distribution. For comparison, Coulomb Hartree energies and the Coulomb exchange energies calculated by the LDA EDF are also shown. All the data are shown in MeV. This table is taken from Ref. [A1].

Nuclei	Coulomb Hartree	Coulomb Exchange				
		LDA	B88	PW91	PBE	PBEsol
^{4}He	1.5177	−0.6494	−0.7150	−0.7290	−0.7281	−0.7030
^{12}C	9.4807	−1.9615	−2.0770	−2.1088	−2.1048	−2.0562
^{16}O	15.4092	−2.6375	−2.7727	−2.8119	−2.8065	−2.7484
^{40}Ca	75.7443	−7.0874	−7.3189	−7.3947	−7.3814	−7.2774
^{48}Ca	75.6828	−7.1129	−7.3485	−7.4198	−7.4087	−7.3051
^{58}Ni	136.6040	−10.2823	−10.5706	−10.6623	−10.6471	−10.5167
^{116}Sn	356.4989	−18.4107	−18.8105	−18.9417	−18.9188	−18.7361
^{124}Sn	352.4883	−18.2437	−18.6441	−18.7726	−18.7506	−18.5691
^{206}Pb	810.3373	−30.3764	−30.9124	−31.0875	−31.0566	−30.8113
^{208}Pb	808.5319	−30.3080	−30.8436	−31.0223	−30.9904	−30.7439

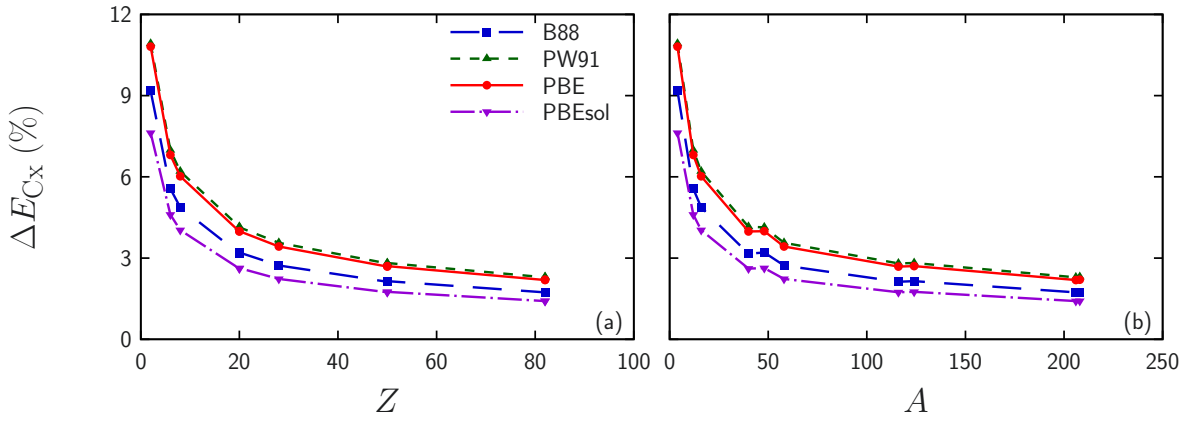

Figure 3.2.1: Relative difference between the exchange energy calculated by using the Coulomb LDA and that by the Coulomb GGA, $\Delta E_{\rm Cx}$, as functions of (a) Z and (b) A, respectively. This figure is taken from Ref. [A1].

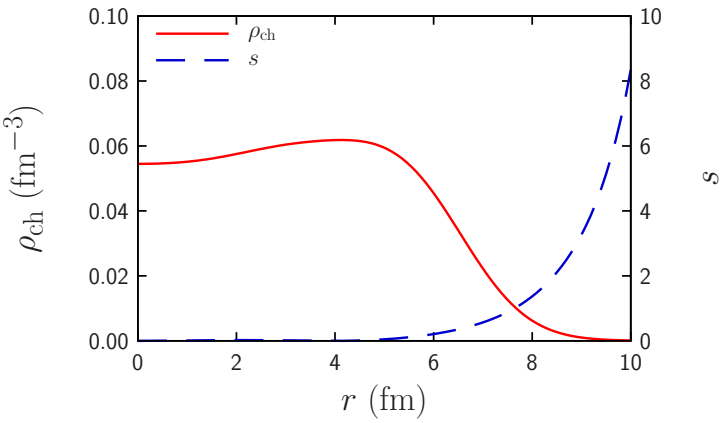

Figure 3.2.2: Charge density $\rho_{\rm ch}$ and its dimensionless density gradient s for ^{208}Pb obtained in Ref. [144] as functions of r.

is often performed [407], while the numerical cost increases as the number of meshes increases. Accordingly, the numerical cost is larger than the basis expansion method, and, in such calculation, it is still difficult to

use finite-range interactions. Therefore, numerically efficient and accurate methods to treat the Coulomb exchange energy are still demanded.

In the previous section, we have shown that all the selected Coulomb GGA exchange EDF give similar results. Hence, here, we apply the Coulomb GGA-PBE exchange EDF to nuclear DFT calculation. The enhancement factor of the Coulomb GGA-PBE exchange EDF is Eq. (2.2.61). It includes two parameters, κ and μ. As discussed in Sec. 2.2.3, κ is determined to satisfy the Lieb-Oxford bound and thus it must be kept in any system. On the contrary, μ is determined by using the linear response in the slowly-varying limit, while a criterion to fix μ is rather arbitrary. Indeed, it is known that the PBEsol EDF, whose μ is different from the original PBE one, reproduces properties of solids better. With considering these facts, in order to reproduce the Coulomb exchange energy calculated by using the exact-Fock term more precisely in nuclear DFT, μ is multiplied by λ as

$$F^{\lambda\text{-PBE}}(s) = 1 + \kappa - \frac{\kappa}{1 + \lambda\mu s^2/\kappa} \tag{3.3.1}$$

and we shall find the proper value of λ.

3.3.1 Numerical Setup

The self-consistent Skyrme Hartree-Fock calculation is performed by using the code SKYRME_RPA [408], where the Coulomb GGA-PBE exchange EDF is implemented in this work. The SAMi EDF [409] is used for the nuclear part E_{nucl} in Eq. (3.1.1), whose parameters are shown in Table 4.3.1 in Chap. 4.

The pairing interaction is not considered and the spherical symmetry is assumed since we shall calculate only doubly-magic nuclei. In order to calculate the radial wave function, a mesh with an interval 0.1 fm in $0 \leq r \leq 15$ fm is used. The difference between ρ_p and ρ_{ch} is not considered in the self-consistent calculations, i.e., $E_{\text{CH}}[\rho_{\text{ch}}] + E_{\text{Cx}}[\rho_{\text{ch}}]$ is approximated to $E_{\text{CH}}[\rho_p] + E_{\text{Cx}}[\rho_p]$, as usual.

For comparison, the Coulomb exchange energy calculated by the exact-Fock term [Eq. (2.2.39)] is also performed. Hereinafter, Eq. (2.2.39) is referred to as the exact-Fock term and the Coulomb exchange energy calculated with Eq. (2.2.39) is referred to as the exact-Fock energy. A perturbation method proposed in Ref. [85] is used to calculate it. In other words, the self-consistent calculation is performed within the Coulomb LDA EDF first, and the difference between the Coulomb LDA exchange energy and the Coulomb exact-Fock energy is taken into account perturbatively for the single-particle energies, and accordingly, the total energy, as

$$\begin{aligned}\tilde{\varepsilon}_j &= \varepsilon_j + \left[\iint \varphi_j^*(\boldsymbol{r}) V_{\text{F}}(\boldsymbol{r},\boldsymbol{r}') \varphi_j(\boldsymbol{r}')\, d\boldsymbol{r}\, d\boldsymbol{r}' - \int \varphi_j^*(\boldsymbol{r}) V_{\text{Cx}}^{\text{LDA}}(\boldsymbol{r}) \varphi_j(\boldsymbol{r})\, d\boldsymbol{r}\right] \\ &= \varepsilon_j - \frac{e^2}{2}\sum_k \iint \frac{\varphi_k^*(\boldsymbol{r}')\varphi_k(\boldsymbol{r})}{|\boldsymbol{r}-\boldsymbol{r}'|}\varphi_j(\boldsymbol{r}')\varphi_j^*(\boldsymbol{r})\, d\boldsymbol{r}\, d\boldsymbol{r}' + \frac{e^2}{2}\left(\frac{3}{\pi}\right)^{1/3}\int [\rho_p(\boldsymbol{r})]^{1/3}\varphi_j(\boldsymbol{r})\varphi_j^*(\boldsymbol{r})\, d\boldsymbol{r},\end{aligned} \tag{3.3.2}$$

$$\tilde{E}_{\text{tot}} = E_{\text{tot}} + \sum_j (\tilde{\varepsilon}_j - \varepsilon_j). \tag{3.3.3}$$

3.3.2 Systematic Analysis

Table 3.3.1 shows Coulomb exchange energies of doubly-magic nuclei calculated by using the Coulomb GGA-PBE exchange EDF with $\lambda = 1.00$ (original), 1.25, and 1.50. For comparison, Coulomb exchange energies calculated by using the Coulomb LDA and the exact-Fock term are also shown. Panels (a) and (b) of Fig. 3.3.1 show the relative difference between the exchange energy calculated by using the Coulomb LDA and that by the Coulomb GGA,

$$\Delta E_{\text{Cx}}^{\text{LDA}} = \frac{E_{\text{Cx}}^{\text{GGA}} - E_{\text{Cx}}^{\text{LDA}}}{E_{\text{Cx}}^{\text{GGA}}}, \tag{3.3.4}$$

as functions of Z and A, respectively. Panels (c) and (d) of Fig. 3.3.1 show the relative error of the exchange energy calculated by using the Coulomb LDA to that by the exact-Fock term,

$$\Delta E_{\text{Cx}}^{\text{exact}} = \frac{E_{\text{Cx}}^{\text{GGA}} - E_{\text{Cx}}^{\text{exact}}}{E_{\text{Cx}}^{\text{GGA}}}, \tag{3.3.5}$$

Table 3.3.1: Coulomb exchange energies $E_{\rm Cx}$ for the doubly-magic nuclei calculated with the LDA and Coulomb GGA-PBE exchange EDFs compared with exact-Fock energies. All the data are shown in MeV. This table is taken from Ref. [A2].

Nucleus	LDA	Exact-Fock	GGA-PBE		
			$\lambda = 1.00$	$\lambda = 1.25$	$\lambda = 1.50$
^{4}He	−0.627	−0.732	−0.701	−0.712	−0.722
^{16}O	−2.854	−3.088	−3.038	−3.067	−3.094
^{40}Ca	−7.558	−7.980	−7.879	−7.933	−7.982
^{48}Ca	−7.458	−7.812	−7.774	−7.826	−7.873
^{100}Sn	−19.768	−20.429	−20.347	−20.446	−20.537
^{132}Sn	−18.804	−19.446	−19.359	−19.452	−19.537
^{208}Pb	−31.265	−32.090	−32.013	−32.140	−32.256
^{310}126	−48.304	−49.305	−49.266	−49.432	−49.585

as functions of Z and A, respectively. It is seen that, in general, the Coulomb GGA-PBE exchange EDF reproduces the exact-Fock energy less than 5 % error, as expected in the previous section; the error of $|\Delta E_{\rm Cx}^{\rm exact}|$ obtained by the original ($\lambda = 1.00$) Coulomb GGA-PBE exchange EDF ranges between 0.5–4.5 %, which corresponds to 30–100 keV. As λ increases, the Coulomb GGA-PBE exchange EDF gives more closer results to the exact-Fock energy. Eventually, $\lambda = 1.25$ gives better results on the medium-heavy and heavy nuclei region, and $\lambda = 1.50$ gives better results on the light nuclei region.

As discussed in the previous section, the significant difference of the Coulomb GGA exchange energy is due to the surface region. If one assumes that all the nuclei have similar density distribution, the proton density is approximately Z/A of the total density. Figure 3.3.2 shows $\Delta E_{\rm Cx}^{\rm exact}$ as a function of Z/A. The calculation performed in this section is self-consistent, and thus, it is not simple as discussed just above. However, in the heavy nuclei, as Z/A increases, $\Delta E_{\rm Cx}^{\rm exact}$ increases slightly. Thus, a reason why $\lambda \geq 1.25$ reproduces the Coulomb exact-Fock energy in atomic nuclei may be that the parameter μ may have a density dependence.

Hereinafter, $\lambda = 1.25$ is used for all the calculation in nuclear DFT since we focus on systematic behaviour in especially, medium-heavy and heavy mass regions.

3.3.3 Detailed Analysis of ^{208}Pb

Next, we shall perform a detailed analysis of a specific nucleus. Here, ^{208}Pb is taken as an example. The proton single-particle energies are shown in Table 3.3.2. It is seen that the exact-Fock term gives single-particle orbitals bound deeper approximately by 100–500 keV, while the Coulomb GGA-PBE exchange EDF gives similar single-particle energies to the Coulomb LDA EDF.

In order to understand this difference, the Coulomb exchange potential $V_{\rm Cx}$ obtained by the Coulomb LDA and the Coulomb GGA are shown in Fig. 3.3.3(a). The relative difference between the exchange potential obtained by the Coulomb LDA and that by the Coulomb GGA,

$$\Delta V_{\rm Cx} = \frac{V_{\rm Cx}^{\rm GGA} - V_{\rm Cx}^{\rm LDA}}{V_{\rm Cx}^{\rm GGA}}, \tag{3.3.6}$$

is shown in Fig. 3.3.3(b). It is seen that $V_{\rm Cx}$ obtained by the Coulomb GGA-PBE EDF shows the significant difference at the surface region, while both the Coulomb LDA and GGA give the similar values of $V_{\rm Cx}$ at the central region. Because $V_{\rm Cx}$ is just a small part of the total potential, this difference is tiny compared to the total potential. Accordingly, single-particle energies do not change drastically. Indeed, Fig. 3.3.4(a) shows the proton and neutron density distributions, ρ_p and ρ_n. These densities obtained by the Coulomb GGA do not show any visible difference from those obtained by the Coulomb LDA. As seen in Fig. 3.3.4(b), in which

$$\Delta\rho_\tau = \frac{\rho_\tau^{\rm GGA} - \rho_\tau^{\rm LDA}}{\rho_\tau^{\rm GGA}} \qquad (\tau = p,\, n) \tag{3.3.7}$$

are plotted, there is a difference between ρ_p obtained by the Coulomb LDA and that by the Coulomb GGA EDF at the surface region, while it is just 0.2 %. Since the Coulomb interaction does not affect neutrons, ρ_n

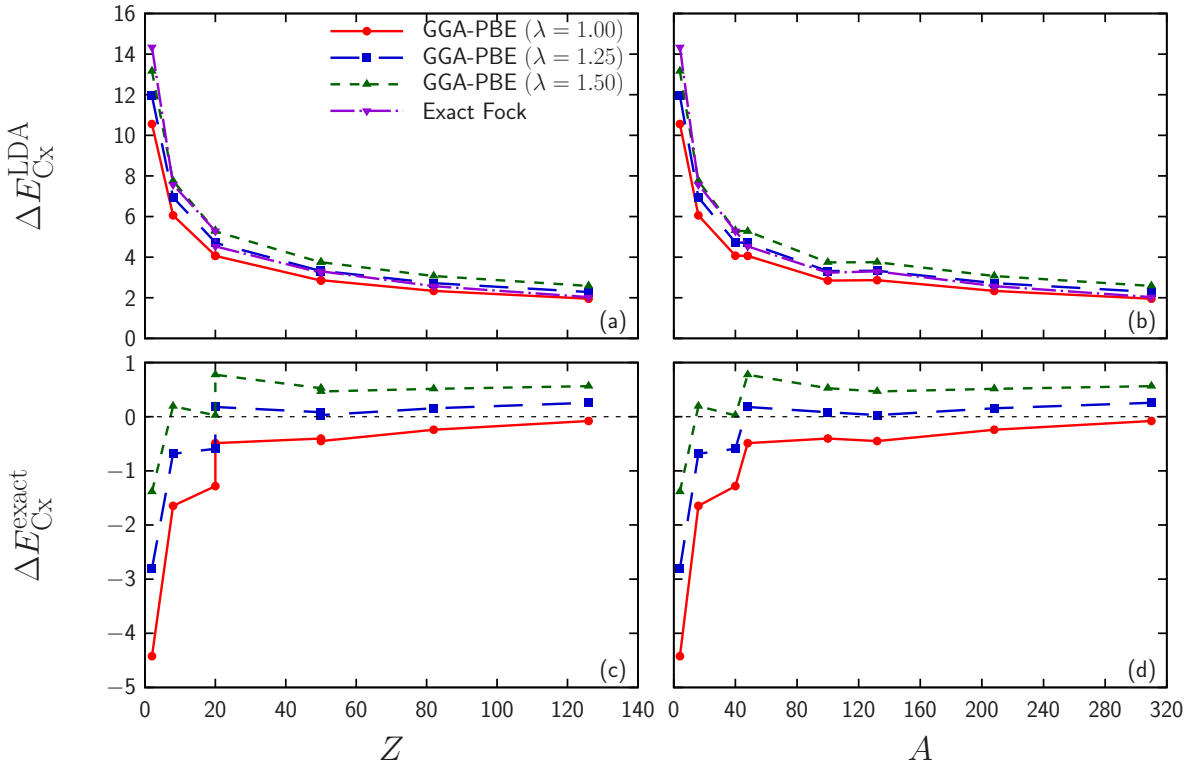

Figure 3.3.1: Relative difference between the exchange energy calculated by using the Coulomb LDA and that by the Coulomb GGA, $\Delta E_{\rm Cx}^{\rm LDA}$, as functions of (a) Z and (b) A, respectively. The same but for $\Delta E_{\rm Cx}^{\rm exact}$ are also shown in panels (c) and (d). This figure is taken from Ref. [A2].

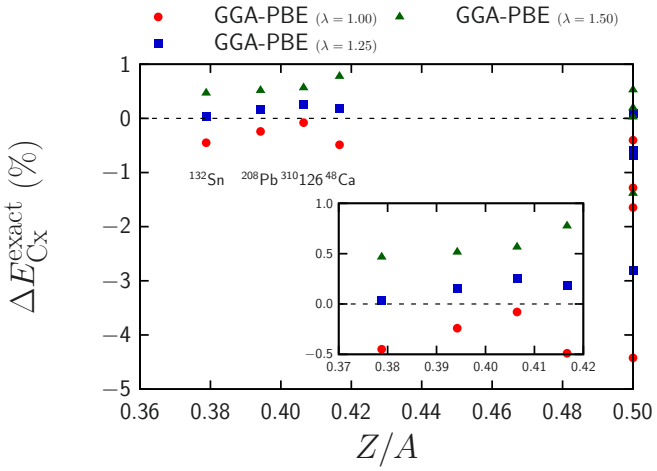

Figure 3.3.2: Relative difference between the exchange energy calculated by using the Coulomb LDA and that by the Coulomb GGA, $\Delta E_{\rm Cx}^{\rm exact}$, as functions of Z/A.

changes because of the change of ρ_p. Therefore, $\Delta\rho_n$ is approximately one order of magnitude smaller than $\Delta\rho_p$. Note that $\tau = p$ and n, respectively, indicate an equation for protons and that for neutrons.

In short, it is concluded that the Coulomb GGA-PBE exchange EDF gives more accurate Coulomb exchange energy, while it does not change single-particle energies or density distribution significantly.

Table 3.3.2: Single-particle energies for protons in ^{208}Pb calculated by using the LDA and PBE-GGA Coulomb exchange EDFs. Those from the exact-Fock calculation [85] are also shown. All the data are shown in MeV. This table is taken from Ref. [A2].

Orbital	Exact-Fock [85]	LDA	GGA-PBE ($\lambda = 1.25$)
$1s_{1/2}$	−45.501	−44.980	−44.983
$1p_{3/2}$	−39.863	−39.387	−39.390
$1p_{1/2}$	−39.574	−39.107	−39.111
$1d_{5/2}$	−32.903	−32.482	−32.485
$1d_{3/2}$	−32.209	−31.815	−31.817
$2s_{1/2}$	−28.899	−28.509	−28.507
$1f_{7/2}$	−25.045	−24.692	−24.693
$1f_{5/2}$	−23.648	−23.353	−23.353
$2p_{3/2}$	−19.702	−19.411	−19.406
$2p_{1/2}$	−18.906	−18.626	−18.621
$1g_{9/2}$	−16.605	−16.338	−16.336
$1g_{7/2}$	−14.175	−14.019	−14.017
$2d_{5/2}$	−10.411	−10.255	−10.246
$2d_{3/2}$	−8.897	−8.846	−8.837
$3s_{1/2}$	−7.813	−7.673	−7.660
$1h_{11/2}$	−7.802	−7.663	−7.658

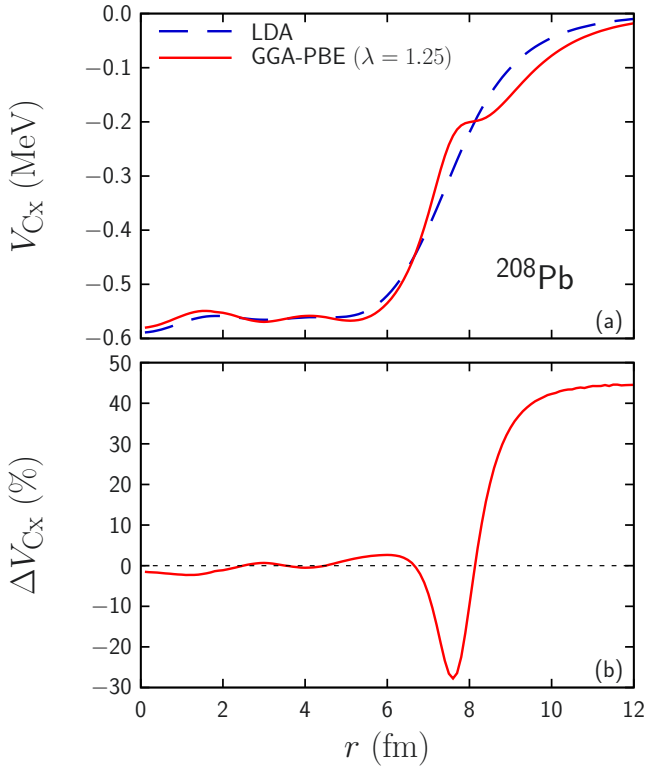

Figure 3.3.3: (a) Coulomb exchange potentials V_{Cx} for ^{208}Pb calculated by using the LDA and GGA-PBE ($\lambda = 1.25$) EDFs as functions of r. (b) Relative difference between the Coulomb exchange potential for ^{208}Pb calculated by using the GGA-PBE EDF and that by using the LDA EDF, ΔV_{Cx}, as a function of r. This figure is taken from Ref. [A2].

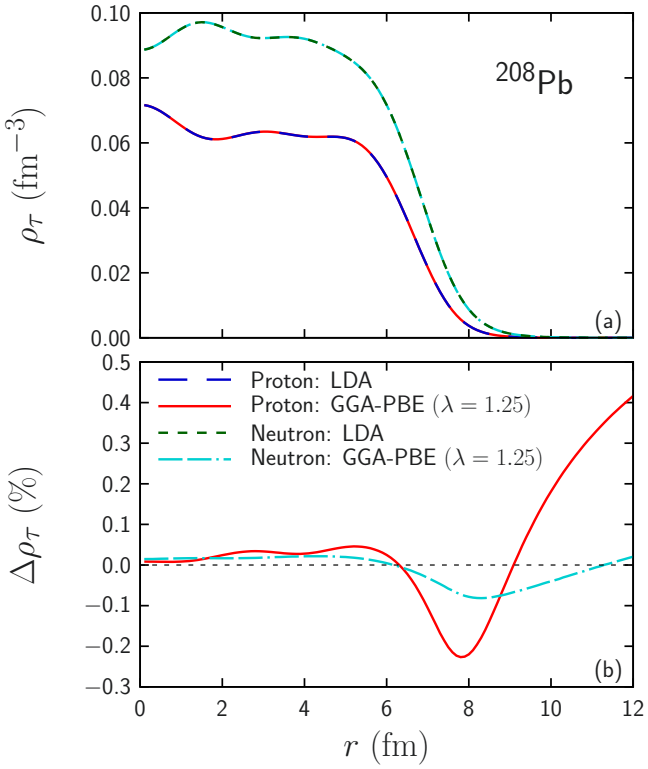

Figure 3.3.4: (a) Proton and neutron density distributions for ^{208}Pb calculated by using the LDA and GGA-PBE ($\lambda = 1.25$) EDFs as functions of r. (b) Relative difference between proton and neutron density distributions for ^{208}Pb calculated by using the GGA-PBE EDF and that by using the LDA EDF, $\Delta\rho_\tau$, as functions of r. This figure is taken from Ref. [A2].

3.4 Finite-Size Effects of Nucleons and Vacuum Polarization

In the previous section, the Coulomb GGA-PBE exchange EDF with $\lambda = 1.25$ reproduces the exact-Fock energy within a relatively small difference, under the point-particle approximation, i.e., assumption of $\rho_{\rm ch} \equiv \rho_p$. On top of this, the finite-size effects of nucleons, i.e., the difference between $\rho_{\rm ch}$ and ρ_p, are taken into account for the self-consistent calculation of the nuclear DFT. The vacuum polarization, i.e., electron-positron pair creation in the photon-exchange process between two protons, is also taken into account, where the Feynman diagram of the vacuum polarization is shown in Fig. 3.4.1. Although it is the higher-order correction to the Coulomb interaction, and the Coulomb interaction itself has just a small contribution to the total energy, it was shown in Refs. [191, 410] that the vacuum polarization may not be neglected to the total energy. Because of the vacuum polarization, the electromagnetic EDF $E_{\rm EM}$ now reads

$$E_{\rm EM}\left[\rho_{\rm ch}\right] = E_{\rm CH}\left[\rho_{\rm ch}\right] + E_{\rm Cx}\left[\rho_{\rm ch}\right] + E_{\rm VP}\left[\rho_{\rm ch}\right], \tag{3.4.1}$$

where $E_{\rm VP}$ is the EDF for the vacuum polarization.

Electromagnetic spin-orbit interaction is also considered. This is due to the magnetic interaction between nucleon spins and the Coulomb mean-field. More precisely, a nucleon moves in the charge density distribution, i.e., Coulomb mean-field. On the frame of a moving nucleon, this charge density distribution moves and generates a magnetic field. The spin of the nucleon interacts with this magnetic field, which can be regarded as the spin-orbit interaction. This effect can also be understood as an effect of the magnetic form factors of nucleons. This effect is approximately 100 keV or less, and thus it will be considered perturbatively.

3.4.1 Theoretical Framework

Finite-Size Effects of Nucleons

Since both protons and neutrons have finite charge density distribution as shown in Fig. 1.4.2, the charge density distribution of an atomic nucleus $\rho_{\rm ch}$ is expressed by using Eq. (1.4.4). Nonetheless, in usual nuclear DFT, $\rho_{\rm ch}$ is approximated to ρ_p throughout the self-consistent calculation. In some works, such as Ref. [411], this difference has been partly considered, but it is not complete.

In order to take into account the finite-size effects properly, first, Eq. (1.4.4) is written in the real space. Using the definition of convolution

$$\left(f * g\right)\left(\boldsymbol{r}\right) = \int f\left(\boldsymbol{r}'\right) g\left(\boldsymbol{r} - \boldsymbol{r}'\right)\, d\boldsymbol{r}' \tag{3.4.2}$$

and a useful relation

$$\tilde{f}\left(\boldsymbol{q}\right) \tilde{g}\left(\boldsymbol{q}\right) = \int \left(f * g\right)\left(\boldsymbol{r}\right) e^{-i\boldsymbol{q}\cdot\boldsymbol{r}}\, d\boldsymbol{r} \tag{3.4.3}$$

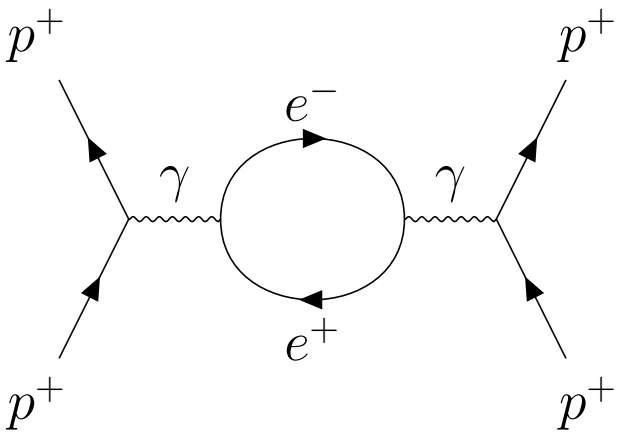

Figure 3.4.1: Feynman diagram of vacuum polarization.

from Eq. (1.4.4), one obtains

$$\begin{aligned}\rho_{\mathrm{ch}}(r) &= (\rho_p * G_{\mathrm{E}p})(r) + (\rho_n * G_{\mathrm{E}n})(r) \\ &= \int \rho_p(r')\, G_{\mathrm{E}p}(|\boldsymbol{r}-\boldsymbol{r}'|)\, d\boldsymbol{r}' + \int \rho_n(r')\, G_{\mathrm{E}n}(|\boldsymbol{r}-\boldsymbol{r}'|)\, d\boldsymbol{r}',\end{aligned} \tag{3.4.4}$$

where $G_{\mathrm{E}\tau}$ is the inverse Fourier transform of a nucleon electric form factor $\tilde{G}_{\mathrm{E}\tau}$, which corresponds to the charge density distribution of a single nucleon.

Equation (2.2.27) gives the Kohn-Sham effective potential. In the case of nuclear physics, substituting $E_{\mathrm{int}}[\rho_p,\rho_n] = E_{\mathrm{nucl}}[\rho_p,\rho_n] + E_{\mathrm{EM}}[\rho_{\mathrm{ch}}]$ into Eq. (2.2.27), one obtains

$$V_{\mathrm{eff}\tau}(\boldsymbol{r}) = \frac{\delta E_{\mathrm{nucl}}[\rho_p,\rho_n]}{\delta\rho_\tau(\boldsymbol{r})} + \frac{\delta E_{\mathrm{EM}}[\rho_{\mathrm{ch}}]}{\delta\rho_\tau(\boldsymbol{r})}. \tag{3.4.5}$$

The electric form factor does not play any role in the first term, effective potential due to nuclear EDF. The chain rule of the functional derivative

$$\frac{\delta}{\delta f(\boldsymbol{r})} = \int \frac{\delta g(\boldsymbol{r}')}{\delta f(\boldsymbol{r})} \frac{\delta}{\delta g(\boldsymbol{r}')}\, d\boldsymbol{r}' \tag{3.4.6}$$

must be considered to the second term of Eq. (3.4.5). Combining Eqs. (3.4.4) and (3.4.6), one gets

$$\begin{aligned}V_{\mathrm{EM}\tau}(\boldsymbol{r}) &= \frac{\delta E_{\mathrm{EM}}[\rho_{\mathrm{ch}}]}{\delta\rho_\tau(\boldsymbol{r})} \\ &= \int \frac{\delta E_{\mathrm{EM}}[\rho_{\mathrm{ch}}]}{\delta\rho_{\mathrm{ch}}(\boldsymbol{r}')} \frac{\delta\rho_{\mathrm{ch}}(\boldsymbol{r}')}{\delta\rho_\tau(\boldsymbol{r})}\, d\boldsymbol{r}' \\ &= \int \frac{\delta E_{\mathrm{EM}}[\rho_{\mathrm{ch}}]}{\delta\rho_{\mathrm{ch}}(\boldsymbol{r}')} G_{\mathrm{E}\tau}(|\boldsymbol{r}'-\boldsymbol{r}|)\, d\boldsymbol{r}' \\ &= \int \frac{\delta E_{\mathrm{EM}}[\rho_{\mathrm{ch}}]}{\delta\rho_{\mathrm{ch}}(\boldsymbol{r}')} G_{\mathrm{E}\tau}(|\boldsymbol{r}-\boldsymbol{r}'|)\, d\boldsymbol{r}'.\end{aligned} \tag{3.4.7}$$

For convenience, $\mathcal{V}_{\mathrm{EM}}$ is defined by

$$\mathcal{V}_{\mathrm{EM}}[\rho](\boldsymbol{r}) = \frac{\delta E_{\mathrm{EM}}[\rho]}{\delta\rho(\boldsymbol{r})}. \tag{3.4.8}$$

Under the point-particle approximation $\rho_{\mathrm{ch}} \equiv \rho_p$, i.e., normal treatment, the effective Coulomb potential reads

$$V_{\mathrm{EM}p}(\boldsymbol{r}) = \mathcal{V}_{\mathrm{EM}}[\rho_p](\boldsymbol{r}), \tag{3.4.9}$$

$$V_{\mathrm{EM}n}(\boldsymbol{r}) = 0. \tag{3.4.10}$$

If the finite-size effects are taken into account fully, the effective Coulomb potential now reads

$$\begin{aligned}V_{\mathrm{EM}\tau}(\boldsymbol{r}) &= \int \mathcal{V}_{\mathrm{EM}}[\rho_{\mathrm{ch}}](\boldsymbol{r}')\, G_{\mathrm{E}\tau}(|\boldsymbol{r}-\boldsymbol{r}'|)\, d\boldsymbol{r}' \\ &= (\mathcal{V}_{\mathrm{EM}}[\rho_{\mathrm{ch}}] * G_{\mathrm{E}\tau})(\boldsymbol{r}).\end{aligned} \tag{3.4.11}$$

It should be emphasized that, because of $G_{\mathrm{E}n} \not\equiv 0$, neutrons are also affected by the effective Coulomb potential. This is because a neutron has its internal charge distribution, which interacts with the Coulomb interaction. The finite-size effects treated with this formula will be referred to as "self-consistent finite-size effects". Note that the effective Coulomb potential with finite-size effects which were used in several previous works, such as in Ref. [411], reads

$$V_{\mathrm{EM}p}(\boldsymbol{r}) = \mathcal{V}_{\mathrm{EM}}[\rho_{\mathrm{ch}}](\boldsymbol{r}), \tag{3.4.12}$$

$$V_{\mathrm{EM}n}(\boldsymbol{r}) = 0. \tag{3.4.13}$$

This finite-size effects will be referred to as "conventional finite-size effects".

In order to understand the finite-size effects on the Coulomb effective potential, the Coulomb Hartree EDF with assuming the spherical symmetry is taken as an example:

$$\begin{aligned}E_{\mathrm{EM}}[\rho_{\mathrm{ch}}] &= \frac{e^2}{2} \iint \frac{\rho_{\mathrm{ch}}(r)\,\rho_{\mathrm{ch}}(r')}{|\boldsymbol{r}-\boldsymbol{r}'|}\, d\boldsymbol{r}\, d\boldsymbol{r}' \\ &= \frac{e^2}{2} \sum_{\tau,\tau'} \iiiint \frac{\rho_\tau(r'')\,\rho_{\tau'}(r''')}{|\boldsymbol{r}-\boldsymbol{r}'|} G_{\mathrm{E}\tau}(|\boldsymbol{r}-\boldsymbol{r}''|)\, G_{\mathrm{E}\tau'}(|\boldsymbol{r}'-\boldsymbol{r}'''|)\, d\boldsymbol{r}\, d\boldsymbol{r}'\, d\boldsymbol{r}''\, d\boldsymbol{r}'''.\end{aligned} \tag{3.4.14}$$

Under the point-particle approximation $\rho_{\rm ch} \equiv \rho_p$ the effective Coulomb potential reads

$$V_{{\rm EM}p}\left(r\right) = e^2 \int \frac{\rho_p\left(r'\right)}{\left|\boldsymbol{r}-\boldsymbol{r}'\right|}\, d\boldsymbol{r}', \tag{3.4.15}$$

$$V_{{\rm EM}n}\left(r\right) = 0. \tag{3.4.16}$$

The effective Coulomb potential with conventional finite-size effects reads

$$\begin{aligned} V_{{\rm EM}p}\left(r\right) &= e^2 \int \frac{\rho_{\rm ch}\left(r'\right)}{\left|\boldsymbol{r}-\boldsymbol{r}'\right|}\, d\boldsymbol{r}' \\ &= e^2 \sum_\tau \iint \frac{\rho_\tau\left(r''\right)}{\left|\boldsymbol{r}-\boldsymbol{r}'\right|} G_{{\rm E}\tau}\left(\left|\boldsymbol{r}-\boldsymbol{r}''\right|\right)\, d\boldsymbol{r}'\, d\boldsymbol{r}'', \end{aligned} \tag{3.4.17}$$

$$V_{{\rm EM}n}\left(r\right) = 0. \tag{3.4.18}$$

The effective Coulomb potential with self-consistent finite-size effects reads

$$\begin{aligned} V_{{\rm EM}\tau}\left(r\right) &= e^2 \iint \frac{\rho_{\rm ch}\left(r'\right)}{\left|\boldsymbol{r}''-\boldsymbol{r}'\right|} G_{{\rm E}\tau}\left(\left|\boldsymbol{r}-\boldsymbol{r}''\right|\right)\, d\boldsymbol{r}'\, d\boldsymbol{r}'' \\ &= e^2 \sum_{\tau'} \iiint \frac{\rho_{\tau'}\left(r'''\right)}{\left|\boldsymbol{r}''-\boldsymbol{r}'\right|} G_{{\rm E}\tau}\left(\left|\boldsymbol{r}-\boldsymbol{r}''\right|\right) G_{{\rm E}\tau}\left(\left|\boldsymbol{r}'-\boldsymbol{r}'''\right|\right)\, d\boldsymbol{r}'\, d\boldsymbol{r}''\, d\boldsymbol{r}'''. \end{aligned} \tag{3.4.19}$$

Two $G_{{\rm E}\tau}$ appear in Eqs. (3.4.14) and (3.4.19), which is because two particles take part in the interaction. In the potential with conventional finite-size effects [Eq. (3.4.17)], it is assumed that one nucleon has a finite size, while the other is a point particle.

In principle, the exchange interaction appears between two protons and between two neutrons only, and it does not appear between a proton and a neutron. If Eq. (3.4.4) is directly substituted into $\rho_{\rm ch}$ appearing in the Coulomb exchange EDF, such as Eq. (2.2.43), the proton-neutron Coulomb exchange interaction may be taken into account. However, the neutron finite-size effect is tiny and its dominant contribution is to the Coulomb Hartree energy. Indeed, the absolute value of the neutron finite-size effect on the Coulomb exchange energy in ^{208}Pb is just 0.09 keV, while it on the Coulomb Hartree one is more than 1 MeV. Therefore, for the sake of simplicity, Eq. (3.4.4) is used for both the Coulomb Hartree and exchange EDFs.

Vacuum Polarization

The effective potential for the vacuum polarization is known as the Uehling potential [412], which was originally adopted for electronic structures of atoms. This effective potential describes the electron-positron pair creation between an electron and the Coulomb potential caused by the charge density distribution $\rho_{\rm ch}$. Since the charge of a proton is the opposite sign of that of an electron, the Uehling potential used in this work also has the opposite sign to the original one, which reads [412]

$$V_{\rm VP}\left(\boldsymbol{r}\right) = \frac{2}{3}\frac{\alpha e^2}{\pi} \int \frac{\rho_{\rm ch}\left(\boldsymbol{r}'\right)}{\left|\boldsymbol{r}-\boldsymbol{r}'\right|} \mathcal{K}_1\left(\frac{2}{\lambda\!\!\!^{-}_e}\left|\boldsymbol{r}-\boldsymbol{r}'\right|\right) d\boldsymbol{r}', \tag{3.4.20}$$

where

$$\mathcal{K}_1\left(x\right) = \int_1^\infty e^{-xt}\left(\frac{1}{t^2}+\frac{1}{2t^4}\right)\sqrt{t^2-1}\, dt, \tag{3.4.21}$$

$\alpha \approx 1/137$ is the fine-structure constant, and $\lambda\!\!\!^{-}_e = \hbar/\left(m_e c\right) \approx 386.2\,{\rm fm}$ is the reduced Compton wavelength of electrons. Accordingly, the EDF for the vacuum polarization, $E_{\rm VP}$, is

$$E_{\rm VP}\left[\rho_{\rm ch}\right] = \frac{1}{2}\int \rho_{\rm ch}\left(\boldsymbol{r}\right) V_{\rm VP}\left(\boldsymbol{r}\right)\, d\boldsymbol{r}. \tag{3.4.22}$$

Under the spherical symmetry, Eq. (3.4.20) becomes [413]

$$V_{\rm VP}\left(r\right) = \frac{2\alpha e^2 \lambda\!\!\!^{-}_e}{3r}\int_0^\infty \left[\mathcal{K}_0\left(\frac{2}{\lambda\!\!\!^{-}_e}\left|r-r'\right|\right) - \mathcal{K}_0\left(\frac{2}{\lambda\!\!\!^{-}_e}\left|r+r'\right|\right)\right]\rho_{\rm ch}\left(r'\right)\, r'\, dr', \tag{3.4.23}$$

where

$$\begin{aligned}\mathcal{K}_0(x) &= -\int_{-\infty}^{x} \mathcal{K}_1(x')\,dx' \\ &= \int_1^{\infty} e^{-xt}\left(\frac{1}{t^3}+\frac{1}{2t^5}\right)\sqrt{t^2-1}\,dt.\end{aligned} \tag{3.4.24}$$

As the self-consistent finite-size effects on the effective Coulomb potential, in principle, those for the Uehling potential should also be considered. However, this Uehling potential is just a tiny correction for V_{EM}, and the finite-size effects on the Uehling potential is expected to be further tiny. Hence, V_{VP} [Eq. (3.4.23)] is directly applied only to protons, which corresponds to the conventional finite-size effects.

Electromagnetic Spin-Orbit Interaction

The electromagnetic spin-orbit interaction is taken into account by using the first-order perturbation theory. The correction is [414]

$$\begin{aligned}\Delta\varepsilon_i &= \frac{\hbar^2c^2}{2m^2c^4}x_i\left\langle\hat{\boldsymbol{l}}_i\cdot\hat{\boldsymbol{s}}_i\right\rangle\int_0^{\infty}\frac{[u_i(r)]^2}{r}\frac{d\mathcal{V}_{\mathrm{C}}(r)}{dr}\,dr \\ &= \frac{\hbar^2c^2}{2m^2c^4}x_i\left[j_i(j_i+1)-l_i(l_i+1)-\frac{3}{4}\right]\int_0^{\infty}\frac{[u_i(r)]^2}{r}\frac{d\mathcal{V}_{\mathrm{C}}(r)}{dr}\,dr,\end{aligned} \tag{3.4.25}$$

where $\mathcal{V}_{\mathrm{C}}$ is the Coulomb potential derived by using Eq. (3.4.8), $ru_i(r)$ is the radial part of a single-particle orbital, $\hat{\boldsymbol{l}}_i$ and $\hat{\boldsymbol{s}}_i$ are, respectively, its orbital and spin angular-momentum operators, and l_i and j_i are, respectively, the azimuthal quantum number and total angular momentum. The quantity x_i is the g factor minus charges as

$$x_i = \begin{cases} g_p - 1 & \text{for protons,} \\ g_n & \text{for neutrons,}\end{cases} \tag{3.4.26}$$

where -1 appears due to the charge. Here, for simplicity, $\mathcal{V}_{\mathrm{C}} \equiv \mathcal{V}_{\mathrm{C}}[\rho_p]$ is used.

3.4.2 Simple Estimations of Systematic Behaviours

In order to understand the systematic behaviours, these corrections to the total energy are estimated by using a simple ansatz. The proton density distribution is assumed to be a hard sphere:

$$\rho_p(r) = \begin{cases}\rho_0^p & r < R_p, \\ 0 & r > R_p,\end{cases} \tag{3.4.27}$$

where ρ_0^p is the saturation density of protons,

$$\rho_0^p = \frac{1}{2}\rho_0 \approx 0.08\,\mathrm{fm}^{-3}. \tag{3.4.28}$$

The radius of the proton distribution R_p is determined to satisfy

$$\rho_0^p = \frac{3Z}{4\pi R_p^3}, \tag{3.4.29}$$

which leads to

$$R_p = \left(\frac{3Z}{4\pi\rho_0^p}\right)^{1/3}. \tag{3.4.30}$$

This is just a simple estimation; hence the point-particle approximation is used unless we consider the finite-size effect.

The Coulomb Hartree potential is

$$\begin{aligned}V_{\mathrm{CH}}^{\mathrm{point}}(r) &= e^2\int\frac{\rho_p(r')}{|\boldsymbol{r}-\boldsymbol{r}'|}\,d\boldsymbol{r}' \\ &= \begin{cases}\frac{Ze^2}{2R_p}\left(3-\frac{r^2}{R_p^2}\right) & r < R_p, \\ \frac{Ze^2}{r} & r > R_p,\end{cases}\end{aligned} \tag{3.4.31}$$

and thus the Coulomb Hartree energy is

$$\begin{aligned} E_{\mathrm{CH}}^{\mathrm{point}} &= \frac{1}{2}\int \rho_p(r)\, V_{\mathrm{CH}}^{\mathrm{point}}(r)\, d\boldsymbol{r} \\ &= \frac{3e^2}{5}\frac{Z^2}{R_p} \\ &= \frac{3e^2}{5}\left(\frac{4\pi\rho_0^p}{3}\right)^{1/3} Z^{5/3} \\ &\simeq 0.60 Z^{5/3}\,\mathrm{MeV}. \end{aligned} \tag{3.4.32}$$

The Coulomb exchange energy is

$$\begin{aligned} E_{\mathrm{Cx}}^{\mathrm{point}} &= -\frac{3e^2}{4}\left(\frac{3}{\pi}\right)^{1/3}\int [\rho_p(r)]^{4/3}\, d\boldsymbol{r} \\ &= -\frac{3e^2}{4}\left(\frac{9}{4\pi^2}\right)^{1/3}\frac{Z^{4/3}}{R_p} \\ &= -\frac{3e^2}{4}\left(\frac{3\rho_0^p}{\pi}\right)^{1/3} Z \\ &\simeq -0.46 Z\,\mathrm{MeV}. \end{aligned} \tag{3.4.33}$$

Next, the finite-size effects on the Coulomb energy are considered. The superscript "point" means energies calculated without any finite-size effect (the point-particle approximation); "p-fin" means those only with the proton finite-size effect; "pn-fin" means those with the proton and neutron finite-size effects. Since the finite-size effects are just tiny corrections, those for the Coulomb Hartree energy are only discussed here. The charge radius of an atomic nucleus can be calculated as [98]

$$R_{\mathrm{ch}}^2 \simeq R_p^2 + \left\langle r_p^2 \right\rangle + \frac{N}{Z}\left\langle r_n^2 \right\rangle, \tag{3.4.34}$$

where R_{ch} and R_p are, respectively, the charge and proton radii of the nucleus, and $\left\langle r_\tau^2 \right\rangle$ is the mean square radius of a nucleon τ. The relativistic corrections for R_{ch} is neglected here. The Coulomb Hartree energy with the finite-size effects reads

$$E_{\mathrm{CH}}^{\mathrm{finite}} = \frac{3e^2}{5}\frac{Z^2}{R_{\mathrm{ch}}}. \tag{3.4.35}$$

If one estimates the proton finite-size effect on the total energy, which corresponds to neglecting $\left\langle r_n^2 \right\rangle$ in Eq. (3.4.34), one obtains

$$\begin{aligned} E_{\mathrm{C}}^{p\text{-fin}} - E_{\mathrm{C}}^{\mathrm{point}} &\simeq E_{\mathrm{CH}}^{p\text{-fin}} - E_{\mathrm{CH}}^{\mathrm{point}} \\ &= \frac{3e^2}{5} Z^2 \left(\frac{1}{R_{\mathrm{ch}}^{p\text{-fin}}} - \frac{1}{R_p}\right) \\ &= \frac{3e^2}{5} Z^2 \left[\frac{1}{\sqrt{R_p^2 + \left\langle r_p^2 \right\rangle}} - \frac{1}{R_p}\right] \\ &\simeq -\frac{3e^2\left\langle r_p^2 \right\rangle}{10}\frac{Z^2}{R_p^3} \\ &= -\frac{2\pi e^2 \rho_0^p \left\langle r_p^2 \right\rangle}{5} Z \\ &\simeq -0.11 Z\,\mathrm{MeV}, \end{aligned} \tag{3.4.36}$$

where $E_{\rm C}$ is the total Coulomb energy. The contribution of the neutron finite-size effect is

$$\begin{aligned}
E_{\rm C}^{pn\text{-fin}} - E_{\rm C}^{p\text{-fin}} &\simeq E_{\rm CH}^{pn\text{-fin}} - E_{\rm CH}^{p\text{-fin}} \\
&= \frac{3e^2}{5} Z^2 \left(\frac{1}{R_{\rm ch}^{pn\text{-fin}}} - \frac{1}{R_{\rm ch}^{p\text{-fin}}} \right) \\
&= \frac{3e^2}{5} Z^2 \left[\frac{1}{\sqrt{R_p^2 + \langle r_p^2 \rangle + \frac{N}{Z} \langle r_n^2 \rangle}} - \frac{1}{\sqrt{R_p^2 + \langle r_p^2 \rangle}} \right] \\
&\simeq -\frac{3e^2 \langle r_n^2 \rangle}{10} \frac{NZ}{\left(R_p^2 + \langle r_p^2 \rangle \right)^{3/2}} \\
&\simeq -\frac{3e^2 \langle r_n^2 \rangle}{10} \frac{NZ}{R_p^3} \\
&= -\frac{2\pi e^2 \rho_0^p \langle r_n^2 \rangle}{5} N \\
&\simeq 0.010 N \,\text{MeV}.
\end{aligned} \tag{3.4.37}$$

Here, $\langle r_p^2 \rangle = 0.73666\,\text{fm}^2$ and $\langle r_n^2 \rangle = -0.07222\,\text{fm}^2$ obtained by Ref. [148] are used. Note that $\langle r_n^2 \rangle < 0$ means that neutrons have negative effective charge.

The contribution of the vacuum polarization to the total energy reads

$$\begin{aligned}
E_{\rm VP} &= \frac{1}{2} \int \rho_{\rm ch}(r)\, V_{\rm VP}(r)\, d\boldsymbol{r} \\
&\simeq 2\pi \int_0^\infty \rho_p(r)\, V_{\rm VP}(r)\, r^2\, dr \\
&= 2\pi \rho_0^p \int_0^{R_p} V_{\rm VP}(r)\, r^2\, dr \\
&= 2\pi \rho_0^p \frac{2\alpha e^2 \lambda\!\!\!^{-}_e}{3} \int_0^{R_p} \int_0^\infty \left[\mathcal{K}_0\left(\frac{2}{\lambda\!\!\!^{-}_e} |r - r'| \right) - \mathcal{K}_0\left(\frac{2}{\lambda\!\!\!^{-}_e} |r + r'| \right) \right] \rho_{\rm ch}(r')\, r'\, dr'\, r\, dr \\
&\simeq 2\pi \left(\rho_0^p \right)^2 \frac{2\alpha e^2 \lambda\!\!\!^{-}_e}{3} \int_0^{R_p} \int_0^{R_p} \left[\mathcal{K}_0\left(\frac{2}{\lambda\!\!\!^{-}_e} |r - r'| \right) - \mathcal{K}_0\left(\frac{2}{\lambda\!\!\!^{-}_e} |r + r'| \right) \right] r'\, dr'\, r\, dr.
\end{aligned} \tag{3.4.38}$$

The first term of the integral in Eq. (3.4.38) is estimated as

$$\begin{aligned}
&\int_0^{R_p} \int_0^{R_p} \mathcal{K}_0\left(\frac{2}{\lambda\!\!\!^{-}_e} |r - r'| \right) r'\, dr'\, r\, dr \\
&= \int_0^{R_p} \int_0^{R_p} \int_1^\infty e^{-2\tilde{t}|r-r'|} \left(\frac{1}{t^3} + \frac{1}{2t^5} \right) \sqrt{t^2 - 1}\, dt\, r'\, dr'\, r\, dr \\
&= \int_1^\infty \int_0^{R_p} \left[\int_0^r e^{-2\tilde{t}(r-r')} r'\, dr' + \int_r^{R_p} e^{2\tilde{t}(r-r')} r'\, dr' \right] r\, dr \left(\frac{1}{t^3} + \frac{1}{2t^5} \right) \sqrt{t^2 - 1}\, dt \\
&= \int_1^\infty \int_0^{R_p} \frac{r}{4\tilde{t}^2} \left[4\tilde{t} r + e^{-2\tilde{t}r} - e^{2\tilde{t}(r-R_p)} \left(1 + 2\tilde{t} R_p \right) \right] dr \left(\frac{1}{t^3} + \frac{1}{2t^5} \right) \sqrt{t^2 - 1}\, dt \\
&= \int_1^\infty \frac{3 - 6\tilde{t}^2 R_p^2 + 8\tilde{t}^3 R_p^3 - 3e^{-2\tilde{t}R_p} \left(1 + 2\tilde{t} R_p \right)}{24\tilde{t}^4} \left(\frac{1}{t^3} + \frac{1}{2t^5} \right) \sqrt{t^2 - 1}\, dt;
\end{aligned} \tag{3.4.39}$$

the second term reads

$$\begin{aligned}
\int_0^{R_p} \int_0^{R_p} \mathcal{K}_0\left(\frac{2}{\lambda\!\!\!^{-}_e} |r + r'| \right) r'\, dr'\, r\, dr &= \int_0^{R_p} \int_0^{R_p} \int_1^\infty e^{-2\tilde{t}|r+r'|} \left(\frac{1}{t^3} + \frac{1}{2t^5} \right) \sqrt{t^2 - 1}\, dt\, r'\, dr'\, r\, dr \\
&= \int_1^\infty \int_0^{R_p} \int_0^{R_p} e^{-2\tilde{t}(r+r')} r'\, dr'\, r\, dr \left(\frac{1}{t^3} + \frac{1}{2t^5} \right) \sqrt{t^2 - 1}\, dt \\
&= \int_1^\infty \frac{e^{-4\tilde{t}R_p} \left(1 - e^{2\tilde{t}R_p} + 2\tilde{t} R_p \right)^2}{16\tilde{t}^4} \left(\frac{1}{t^3} + \frac{1}{2t^5} \right) \sqrt{t^2 - 1}\, dt,
\end{aligned} \tag{3.4.40}$$

where $\tilde{t} = t/\lambda\!\!\!^{-}_e$. Combining Eqs. (3.4.38)–(3.4.40),

$$\begin{aligned}
&\int_0^{R_p}\int_0^{R_p}\left[\mathcal{K}_0\left(\frac{2}{\lambda\!\!\!^{-}_e}\left|r-r'\right|\right)-\mathcal{K}_0\left(\frac{2}{\lambda\!\!\!^{-}_e}\left|r+r'\right|\right)\right]r'\,dr'\,r\,dr \\
&=\int_1^{\infty}\left[\frac{3-6\tilde{t}^2R_p^2+8\tilde{t}^3R_p^3-3e^{-2\tilde{t}R_p}\left(1+2\tilde{t}R_p\right)}{24\tilde{t}^4}-\frac{e^{-4\tilde{t}R_p}\left(1-e^{2\tilde{t}R_p}+2\tilde{t}R_p\right)^2}{16\tilde{t}^4}\right]\left(\frac{1}{t^3}+\frac{1}{2t^5}\right)\sqrt{t^2-1}\,dt \\
&\simeq 0.0070R_p^5\,\mathrm{MeV}. \qquad (3.4.41)
\end{aligned}$$

is obtained. Finally, Eq. (3.4.38) is estimated as

$$\begin{aligned}
E_{\mathrm{VP}} &\simeq 2\pi\left(\rho_0^p\right)^2\frac{2\alpha e^2\lambda\!\!\!^{-}_e}{3}\times 0.0070R_p^5\,\mathrm{MeV} \\
&\simeq 0.0047Z^{5/3}\,\mathrm{MeV}. \qquad (3.4.42)
\end{aligned}$$

These simple estimations are consistent with Refs. [191, 410], while $A^{-1/3}$, which is related to the radius, is now replaced by $Z^{-1/3}$ since the hard sphere distributions of protons and neutrons are assumed to be identical and accordingly, the radius is proportional to $Z^{-1/3}$ as well.

3.4.3 Systematic Analysis

Next, the systematic calculation is performed. The numerical conditions are the same as in Sec. 3.3. As proposed in Sec. 3.3, the GGA-PBE Coulomb exchange EDF with $\lambda = 1.25$ is used for E_{Cx} other than it is specified that the Coulomb LDA EDF is used.

First of all, total binding energies, proton radii, and neutron radii of the selected doubly-magic nuclei are shown in Tables 3.4.2, 3.4.3, and 3.4.4, respectively. The columns labelled "LDA" and "GGA" refer to the results calculated without the finite-size effects; the columns labelled "p-fin" and "pn-fin", respectively, refer to the results calculated with the proton and proton-neutron finite-size effects on top of the GGA; the column labelled "All" refers to the results calculated with the vacuum polarization on top of the proton-neutron finite-size effects; the column labelled "All + EMSO" refers to the results calculated with the electromagnetic spin-orbit interaction on top of the proton-neutron finite-size effects and the vacuum polarization. For comparison, results calculated with the SAMi-ISB EDF [183], which includes the isospin symmetry breaking effects of the nuclear interaction, on top of "All + EMSO", calculation are also shown. The detail of the SAMi-ISB EDF will be discussed in the next chapter. These labels are summarized in Table 3.4.1.

Figure 3.4.2 shows the ratio of the Coulomb total energy calculated with and without nucleon finite-size effects. The proton finite-size effect decreases the Coulomb energy, while the neutron finite-size effect slightly increases the Coulomb energy. This is because the proton finite-size effect makes ρ_{ch} dilute and broadened, while the neutron finite-size effect makes ρ_{ch} dense and shrunken, as can be seen in Eq. (3.4.34). As seen in Table 3.4.2, the proton finite-size effect contributes to the total energy in $-0.584\,\mathrm{MeV}$, $-1.803\,\mathrm{MeV}$, and $-8.224\,\mathrm{MeV}$ for ^{16}O, ^{48}Ca, and ^{208}Pb, respectively, and the neutron finite-size effect does in $+0.065\,\mathrm{MeV}$, $+0.245\,\mathrm{MeV}$, and $+1.232\,\mathrm{MeV}$, respectively. The desired accuracy of the nuclear EDF is around 100 keV or even less, especially for the application to the calculation of nucleosynthesis in the universe [216, 220]. Hence, even the neutron finite-size effect is non-negligible in heavy nuclei compared to the desired accuracy. Tables 3.4.3 and 3.4.4 show that the proton finite-size effect makes proton radii smaller approximately in 0.005 fm and the neutron finite-size effect makes them larger approximately in 0.0005 fm in medium-heavy and heavy nuclei. The importance of these changes will be discussed in Chap. 4.

The vacuum polarization contributes to the total energy in $+0.087\,\mathrm{MeV}$, $+0.396\,\mathrm{MeV}$, and $+3.694\,\mathrm{MeV}$ for ^{16}O, ^{48}Ca, and ^{208}Pb, respectively. Although the vacuum polarization is the higher-order contribution to the Coulomb interaction, it is not negligible in heavy nuclei. In contrast to the total energy, it is seen in Tables 3.4.3 and 3.4.4 that proton radii change by the order of 0.001 fm and neutron radii change by less than 0.0001 fm.

The electromagnetic spin-orbit interaction does not contribute to the total energy in the spin-saturated nuclei, i.e., nuclei with all the $j_>$ and $j_<$ orbitals pairs are occupied, while in the spin-unsaturated nuclei, such as ^{208}Pb, a few dozen of keV. The electromagnetic spin-orbit interaction does not show any systematic behaviour, since it depends on shell structures.

Table 3.4.1: Abbreviation of the methods used in this thesis.

	LDA	GGA	p-fin	pn-fin	All	All + EMSO	ISB
Coulomb exchange	LDA	GGA	GGA	GGA	GGA	GGA	GGA
Finite-size effects	None	None	p	pn	pn	pn	pn
Vacuum polarization	None	None	None	None	Yes	Yes	Yes
EM spin-orbit	None	None	None	None	None	Yes	Yes
$E_{\rm nucl}$	SAMi	SAMi	SAMi	SAMi	SAMi	SAMi	SAMi-ISB

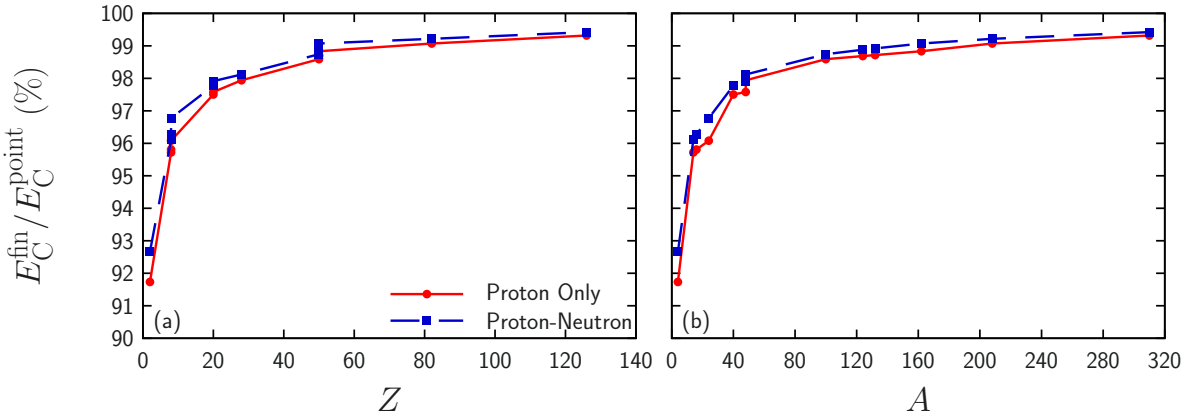

Figure 3.4.2: Ratios of the Coulomb energy calculated with and without finite-size effects as functions of (a) Z and (b) A, respectively. This figure is taken from Ref. [A3].

Before closing this section, the systematic behaviours discussed in the previous section are numerically confirmed. The contributions of these corrections are fitted to

$$E = aZ^b, \tag{3.4.43}$$

where only the neutron finite-size effect is fitted to

$$E = aN^b. \tag{3.4.44}$$

Here, the Coulomb Hartree energies calculated by using "LDA" in Table 3.4.1 are used for fitting. Contributions of the finite-size effects and the vacuum polarization are defined by the difference between the total energy calculated with and that without these effects; in other words, the contribution of the proton finite-size effect corresponds to the difference between the total energy obtained by "GGA" and that by "p-fin", that of the neutron finite-size effect corresponds to the difference between the total energy obtained by "p-fin" and that by "pn-fin", and that of the vacuum polarization corresponds to the difference between the total energy obtained by "pn-fin" and that by "All".

The fitted values are shown in Table 3.4.5. As can be seen, the values of a and b are compatible with those obtained in the previous section. In short, the proton finite-size effect is approximately five times smaller than the Coulomb exchange energy; the neutron finite-size effect is approximately one-order magnitude smaller than the proton finite-size effect with the opposite sign. The vacuum polarization is proportional to $Z^{5/3}$, while the Coulomb exchange energy and the proton finite-size effect are proportional to Z; hence, in the light nuclei, the vacuum polarization is much smaller than the proton finite-size effect, while it becomes larger in heavy nuclei.

As seen in Table 3.4.2, the ISB terms of the nuclear interaction give a larger contribution to the total energy than the precise treatments of the Coulomb interaction in light nuclei. The precise treatments of the Coulomb interaction, such as the proton finite-size effects and the vacuum polarization, give a larger contribution than the ISB terms of the nuclear interaction in heavy nuclei. The detail will be discussed in Chap. 4.

Table 3.4.2: Total energies for the selected doubly-magic nuclei. The treatment of the Coulomb interaction is precisified step by step, as shown in Table 3.4.1. For more detail, see the text. All the data are shown in MeV. This table is taken from Ref. [A3].

Nucleus	LDA	GGA	p-fin	pn-fin	All	All + EMSO	ISB
^{4}He	−27.526	−27.612	−27.675	−27.668	−27.660	−27.660	−29.386
^{16}O	−130.480	−130.693	−131.277	−131.212	−131.125	−131.125	−135.035
^{40}Ca	−347.085	−347.458	−349.363	−349.158	−348.754	−348.754	−354.618
^{48}Ca	−415.615	−415.981	−417.784	−417.539	−417.143	−417.004	−418.648
^{48}Ni	−352.639	−353.115	−356.085	−355.836	−355.124	−355.331	−351.046
^{100}Sn	−811.664	−812.338	−817.924	−817.332	−815.536	−815.590	−812.031
^{132}Sn	−1103.088	−1103.733	−1108.462	−1107.719	−1106.044	−1105.993	−1105.103
^{208}Pb	−1636.615	−1637.485	−1645.709	−1644.477	−1640.783	−1640.725	−1639.780
^{310}126	−2131.415	−2132.537	−2145.544	−2143.665	−2136.400	−2136.340	−2134.405

Table 3.4.3: Proton radii for the selected doubly-magic nuclei. The treatment of the Coulomb interaction is precisified step by step, as shown in Table 3.4.1. Since the electromagnetic spin-orbit interaction is considered perturbatively and thus it does not change radii, "All + EMSO" is not shown. For more detail, see the text. All the data are shown in fm.

Nucleus	LDA	GGA	p-fin	pn-fin	All	ISB
^{4}He	1.9213	1.9222	1.9205	1.9206	1.9207	1.9008
^{16}O	2.6483	2.6481	2.6447	2.6449	2.6451	2.6334
^{40}Ca	3.3895	3.3890	3.3842	3.3845	3.3850	3.3763
^{48}Ca	3.4359	3.4354	3.4313	3.4316	3.4320	3.4030
^{48}Ni	3.7022	3.7015	3.6944	3.6948	3.6956	3.7417
^{100}Sn	4.4351	4.4343	4.4278	4.4283	4.4292	4.4344
^{132}Sn	4.6782	4.6775	4.6726	4.6731	4.6739	4.6638
^{208}Pb	5.4616	5.4609	5.4549	5.4555	5.4567	5.4452
^{310}126	6.2859	6.2851	6.2781	6.2788	6.2806	6.2685

Table 3.4.4: Same as Table 3.4.4 but for neutron radii.

Nucleus	LDA	GGA	p-fin	pn-fin	All	ISB
^{4}He	1.9149	1.9151	1.9148	1.9149	1.9149	1.8774
^{16}O	2.6250	2.6249	2.6241	2.6243	2.6244	2.5904
^{40}Ca	3.3424	3.3422	3.3408	3.3411	3.3413	3.3091
^{48}Ca	3.6111	3.6109	3.6096	3.6100	3.6101	3.6190
^{48}Ni	3.4118	3.4114	3.4092	3.4096	3.4098	3.3689
^{100}Sn	4.3522	4.3518	4.3491	4.3495	4.3499	4.3385
^{132}Sn	4.8890	4.8887	4.8867	4.8872	4.8875	4.8833
^{208}Pb	5.6083	5.6079	5.6052	5.6059	5.6064	5.5986
^{310}126	6.3631	6.3627	6.3593	6.3600	6.3608	6.3522

Table 3.4.5: Parameters a and b for Eq. (3.4.43). For the neutron finite-size effect, Eq. (3.4.44) is used instead of Eq. (3.4.43). This table is taken from Ref. [A3].

	a (MeV)	b
Direct Coulomb (LDA)	0.528757	1.6692
Exchange Coulomb (LDA)	−0.390342	1.0009
Exchange Coulomb (GGA)	−0.368013	1.0103
Proton Finite Size	−0.0757012	1.0640
Neutron Finite Size	0.00706328	1.0620
Vacuum Polarization	0.00354808	1.5765

3.4.4 Detailed Analysis of ^{208}Pb

We shall perform a detailed analysis of ^{208}Pb. The proton and neutron single-particle energies are shown in Table 3.4.6. The proton finite-size effect, the neutron finite-size effect, and the vacuum polarization change the proton single-particle energies approximately -250–$-150\,\mathrm{keV}$, $+10$–$+30\,\mathrm{keV}$, and $+80$–$+100\,\mathrm{keV}$, respectively, while even with this change, the order of the single-particle energies does not change. Since the neutron has no charge, these corrections to the Coulomb energy are not expected to change the neutron single-particle energies. Indeed, even the neutron finite-size effect changes these energies only a few or dozen keV, while its order is the same as the proton finite-size effect on proton single-particle energies. In contrast, the spin-orbit interaction changes proton $j_>$ orbitals and neutron $j_<$ orbitals bound deeper, while proton $j_<$ orbitals and neutron $j_>$ orbitals bound shallower. Although its effect is less than 100 keV, it changes the order of single-particle energies, especially near the Fermi energy.

The Coulomb potential for protons and neutrons, $V_{\mathrm{C}p}$ and $V_{\mathrm{C}n}$, and the vacuum polarization potential for protons are shown in Fig. 3.4.3(a). It can be seen the vacuum polarization correction for protons V_{VP} is also repulsive as $V_{\mathrm{C}p}$, while their strengths are two orders of magnitude or more smaller than $V_{\mathrm{C}p}$. The Coulomb potential for neutrons $V_{\mathrm{C}n}$ is rather complicated that it is repulsive in the internal region, whereas it is attractive in the surface region, although it is much weaker than even V_{VP}. In order to understand how the finite-size effects and the vacuum polarization affect the Coulomb potential, the relative difference between the Coulomb potential for protons obtained by the precise treatments of the Coulomb interaction, $V_{\mathrm{C}p}^{\mathrm{precise}}$, and that by the Coulomb LDA, $V_{\mathrm{C}p}^{\mathrm{LDA}}$,

$$\Delta V_{\mathrm{C}p} = \frac{V_{\mathrm{C}p}^{\mathrm{precise}} - V_{\mathrm{C}p}^{\mathrm{LDA}}}{V_{\mathrm{C}p}^{\mathrm{precise}}}, \tag{3.4.45}$$

is also shown in Fig. 3.4.3(b). It is seen that the Coulomb potential obtained by the GGA-PBE shows the significant difference at the surface region, while the finite-size effects shows the significant difference at the central region. This may be because $\rho_{\mathrm{ch}}(r) < \rho_p(r)$ holds at the central region, and accordingly, the absolute value of the Coulomb Hartree potential, which dominates in $V_{\mathrm{C}p}$, also gives smaller at the central region. The effective potential of the vacuum polarization, i.e., the Uehling potential given in Eq. (3.4.23), is short-range interaction due to $\mathcal{K}_1$. Therefore, its effect is appreciable in the central region. Since the finite-size effects and the vacuum polarization change $V_{\mathrm{C}p}$ in the central region, they also change the single-particle energies more than the GGA. However, $V_{\mathrm{C}p}$ is small compared to the nuclear effective potential, and hence it does not change the single-particle energies or density drastically. Indeed, Fig. 3.4.4 shows the change of the proton density distribution $\Delta\rho_p$ defined by Eq. (3.3.7). Because of the change of $V_{\mathrm{C}p}$ at the central region, the finite-size effects and the vacuum polarization gives non-zero $\Delta\rho_p$ at the central region, while its value is less than 0.5 %. In the surface region, $|\Delta\rho_p|$ is enhanced while ρ_p itself is quite small, and thus it does not give a significant difference.

In short, it is concluded that the nucleon finite-size effects and the vacuum polarization are non-negligible for the total energy, especially in the heavy nuclei, and sometimes for the single-particle energies, while it does not change density distributions significantly.

3.4.5 Mass Difference of Mirror Nuclei

Before closing this section, the method proposed in this section is applied to calculate the mass difference of a mirror nuclei pair. In principle, since the finite-size effects and the vacuum polarization give, in total, a contribution to the total energy in more than 1 MeV, the parameters of E_{nucl} should be refitted. Therefore, the total energies given above cannot be used for comparison with experimental data, while it is still useful to understand how such effects contribute to total energies and densities. Nonetheless, the mass difference of mirror nuclei can be used for comparison with experimental data, since, in principle, the contribution of E_{nucl} vanishes.

The mirror nuclei are the pair of two atomic nuclei, one of which is composed of Z protons and N neutrons, while the other is composed of N protons and Z neutrons, for instance, ^{48}Ca (20 protons and 28 neutrons) and ^{48}Ni (28 protons and 20 neutrons). If neither the Coulomb interaction nor the ISB terms of the nuclear interaction exist, the masses of these two nuclei must be identical. However, in reality, both the Coulomb interaction and the ISB terms of the nuclear interaction exist, and accordingly, the masses of two nuclei are

Table 3.4.6: Single-particle energies of ^{208}Pb. The treatment of the Coulomb interaction is precisified step by step, as shown in Table 3.4.1. For more detail, see the text. All the data are shown in MeV.

Orbital	LDA	GGA	p-fin	pn-fin	All	All + EMSO	ISB
$\pi 1s_{1/2}$	−44.980	−44.983	−45.253	−45.229	−45.123	−45.123	−42.870
$\pi 1p_{3/2}$	−39.387	−39.390	−39.640	−39.618	−39.519	−39.537	−37.737
$\pi 1p_{1/2}$	−39.107	−39.111	−39.360	−39.338	−39.239	−39.202	−37.243
$\pi 1d_{5/2}$	−32.482	−32.485	−32.711	−32.692	−32.598	−32.635	−31.392
$\pi 1d_{3/2}$	−31.815	−31.818	−32.042	−32.023	−31.930	−31.875	−30.361
$\pi 2s_{1/2}$	−28.509	−28.507	−28.724	−28.707	−28.610	−28.610	−27.576
$\pi 1f_{7/2}$	−24.692	−24.693	−24.893	−24.877	−24.789	−24.842	−24.180
$\pi 1f_{5/2}$	−23.353	−23.353	−23.550	−23.535	−23.448	−23.376	−22.380
$\pi 2p_{3/2}$	−19.411	−19.406	−19.597	−19.582	−19.492	−19.509	−19.055
$\pi 2p_{1/2}$	−18.626	−18.621	−18.809	−18.795	−18.705	−18.670	−18.195
$\pi 1g_{9/2}$	−16.338	−16.336	−16.511	−16.498	−16.415	−16.483	−16.357
$\pi 1d_{7/2}$	−14.019	−14.017	−14.184	−14.172	−14.091	−14.004	−13.557
$\pi 2d_{5/2}$	−10.255	−10.246	−10.413	−10.401	−10.316	−10.350	−10.374
$\pi 2d_{3/2}$	−8.846	−8.837	−8.999	−8.988	−8.904	−8.854	−8.841
$\pi 3s_{1/2}$	−7.673	−7.660	−7.822	−7.811	−7.726	−7.726	−7.824
$\pi 1h_{11/2}$	−7.662	−7.658	−7.808	−7.797	−7.719	−7.800	−8.121
$\nu 1s_{1/2}$	−59.291	−59.298	−59.364	−59.343	−59.328	−59.328	−54.587
$\nu 1p_{3/2}$	−52.953	−52.960	−53.011	−52.992	−52.982	−52.966	−48.798
$\nu 1p_{1/2}$	−52.656	−52.662	−52.712	−52.693	−52.683	−52.715	−48.808
$\nu 1d_{5/2}$	−45.375	−45.380	−45.416	−45.399	−45.392	−45.362	−41.843
$\nu 1d_{3/2}$	−44.744	−44.749	−44.781	−44.765	−44.759	−44.805	−41.755
$\nu 2s_{1/2}$	−41.962	−41.965	−41.993	−41.978	−41.971	−41.971	−38.918
$\nu 1f_{7/2}$	−36.904	−36.907	−36.927	−36.913	−36.910	−36.865	−34.035
$\nu 1f_{5/2}$	−35.702	−35.704	−35.716	−35.704	−35.702	−35.763	−33.673
$\nu 2p_{3/2}$	−32.094	−32.094	−32.105	−32.093	−32.090	−32.076	−29.930
$\nu 2p_{1/2}$	−31.344	−31.344	−31.352	−31.341	−31.339	−31.368	−29.612
$\nu 1g_{9/2}$	−27.863	−27.863	−27.867	−27.857	−27.856	−27.799	−25.636
$\nu 1g_{7/2}$	−25.791	−25.790	−25.783	−25.774	−25.776	−25.849	−24.798
$\nu 2d_{5/2}$	−22.277	−22.275	−22.271	−22.262	−22.263	−22.235	−20.861
$\nu 3s_{1/2}$	−19.959	−19.957	−19.948	−19.940	−19.941	−19.941	−18.992
$\nu 2d_{3/2}$	−20.843	−20.841	−20.831	−20.823	−20.825	−20.867	−20.244
$\nu 1h_{11/2}$	−18.533	−18.532	−18.521	−18.514	−18.516	−18.447	−16.871
$\nu 1h_{9/2}$	−15.306	−15.303	−15.277	−15.271	−15.276	−15.361	−15.377
$\nu 2f_{7/2}$	−12.672	−12.668	−12.651	−12.645	−12.648	−12.609	−11.844
$\nu 2f_{5/2}$	−10.622	−10.618	−10.594	−10.590	−10.594	−10.647	−10.971
$\nu 3p_{3/2}$	−9.859	−9.855	−9.835	−9.830	−9.833	−9.820	−9.509
$\nu 1i_{13/2}$	−9.150	−9.147	−9.124	−9.120	−9.124	−9.046	−7.922
$\nu 3p_{1/2}$	−9.063	−9.059	−9.037	−9.032	−9.036	−9.061	−9.165

different from each other. This difference is called the mass difference of mirror nuclei. It was pointed out in the 1960s [189,190] that the Coulomb interaction is not enough for explaining this difference, which is called "Okamoto-Nolen-Schiffer anomaly", or sometimes called "Nolen-Schiffer anomaly" simply. This anomaly has been a long-standing problem.

Here, we shall study the mass difference between ^{48}Ca and ^{48}Ni. It has been pointed out that the ISB terms of the nuclear interaction is indispensable for explaining this anomaly, and thus, here the SAMi-ISB EDF [183] is adopted [3]. The detailed discussion of the ISB interaction will be given in the next chapter, while in this section, the interaction is just used. Table 3.4.7 shows the total energies of ^{48}Ca and ^{48}Ni

[3]Note that the original parameter set of the SAMi-ISB EDF shown in Ref. [183] was used in the original paper [A3], while the "precise" parameter set shown in Sec. 4.3 is used in this thesis. The detail of the difference between two parameter sets is shown in Ref. [A6].

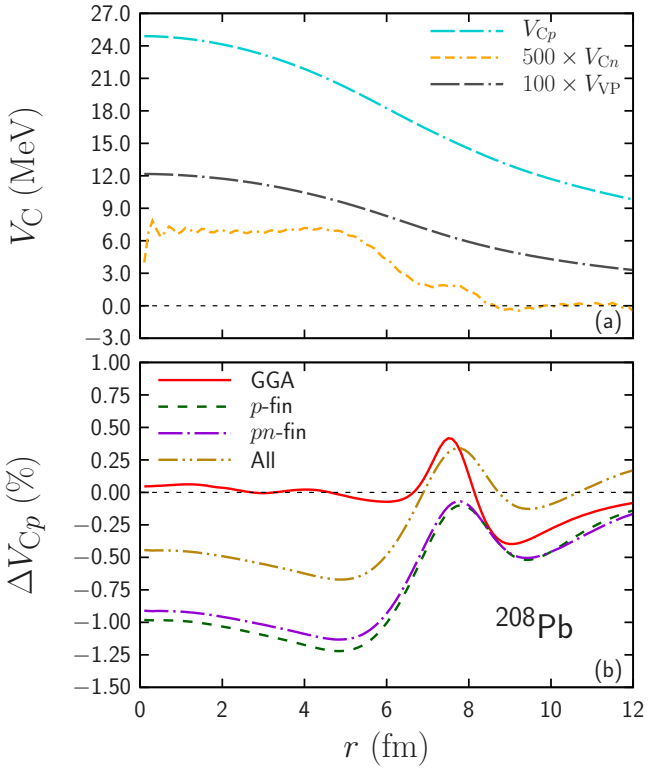

Figure 3.4.3: (a) Coulomb potential for protons and neutrons and vacuum polarization potential for protons as functions of r. To enhance visibility, the Coulomb potential for neutrons and the vacuum polarization potential for protons are scaled by 500 and 100, respectively. (b) Relative difference between the Coulomb potential for protons in ^{208}Pb calculated by the precise treatments and that by the LDA EDF, ΔV_{Cp}, as functions of r.

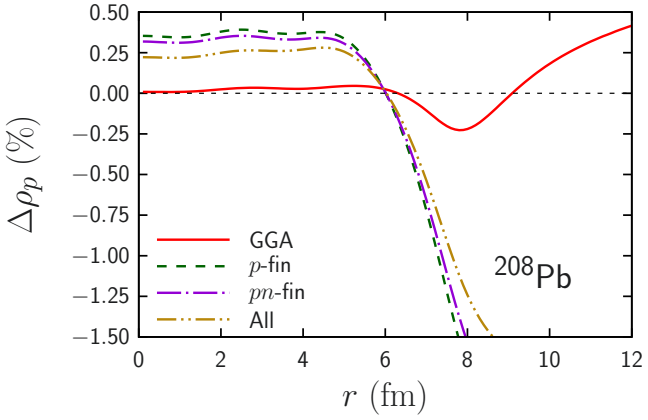

Figure 3.4.4: Relative difference between the proton density distributions for ^{208}Pb calculated by the precise treatments and that by the LDA EDF, $\Delta\rho_p$, as functions of r.

calculated with the Coulomb LDA or the precise Coulomb treatment (All + EMSO) and with the original SAMi EDF or the SAMi-ISB one. For comparison, calculations with all the corrections but the conventional finite-size effects are also shown as "(All)". The experimental data given by Atomic Mass Evaluation (AME) in 2003 [415], in 2016 [416, 417], and in 2020 [418, 419] are also shown. It is shown that the conventional treatment, i.e., calculation without ISB terms or any corrections to the Coulomb interaction (SAMi & LDA), gives approximately 4.5 MeV difference compared with AME2016 data, and the ISB terms of the nuclear interaction (SAMi-ISB & LDA) reduces the difference to 1.5 MeV. The precise treatment (SAMi-ISB &

Table 3.4.7: Mass difference of the mirror nuclei pair ^{48}Ca and ^{48}Ni calculated with the Coulomb LDA or all the corrections to the Coulomb interaction (All + EMSO) for the Coulomb interaction and the SAMi or SAMi-ISB EDF for the nuclear interaction. Here, "(All) + EMSO" and "All + EMSO" show the results by the conventional finite-size effects and the present self-consistent finite-size effects, respectively. For "[All] + EMSO", see the text. All units are in MeV. This table is taken from Ref. [A3].

EDF	^{48}Ca	^{48}Ni	Difference
SAMi & LDA	−415.6148	−352.6388	62.9760
SAMi & (All) + EMSO	−416.2855	−354.0639	62.2216
SAMi & [All] + EMSO	−417.0038	−355.3334	61.6703
SAMi & All + EMSO	−417.0041	−355.3307	61.6734
SAMi-ISB & LDA	−417.2186	−348.4383	68.7803
SAMi-ISB & (All) + EMSO	−417.9084	−349.8219	68.0865
SAMi-ISB & [All] + EMSO	−418.6604	−351.0761	67.5844
SAMi-ISB & All + EMSO	−418.6476	−351.0464	67.6012
AME2003 [415]	−415.991	−347.1	68.9
AME2016 [416, 417]	−416.0009	−348.7	67.3
AME2020 [418, 419]	−416.0012	−347.3	68.7

All + EMSO) further reduces the difference to 0.3 MeV. Therefore, once both the precise treatment of the Coulomb interaction and the ISB terms of the nuclear interaction are considered at the same time, the Okamoto-Nohlen-Schiffer anomaly for the ^{48}Ca-^{48}Ni pair is overcome, while the ISB terms of the nuclear interaction are not enough to solve it. Note that ^{48}Ni is not used for the fitting of the parameters of the SAMi nor the SAMi-ISB EDF.

Compared with the results obtained by the conventional finite-size effects (SAMi-ISB & (All) + EMSO), two different finite-size effects gives a difference of 0.5 MeV. Hence, in order to discuss quantities related to isospin symmetry breaking, the self-consistent treatment of the finite-size effects is indispensable, as well as the GGA, the vacuum polarization, the electromagnetic spin-orbit interaction, and the ISB terms of the nuclear interaction. It should be noted that the experimental data was updated to AME2020 data, and AME2020 data is close to the "SAMi-ISB & LDA" data rather than the "SAMi-ISB & All + EMSO" data. However, the SAMi and SAMi-ISB were originally fitted to the AME2003 and AME2016, respectively. Hence, once the nuclear part of EDF is refitted to AME2020 data, this difference may be remedied. If one uses other EDFs, such as the SLy4 EDF [58], instead of the SAMi or the SAMi-ISB EDF, its tendency that the ISB terms and the precise treatments of the Coulomb interaction reduce the deviation from the experimental data, while raw values of $\Delta E_{\rm tot}$ are different [4].

Table 3.4.7 also shows results with "[All]", in which the self-consistent calculation to obtain the single-particle orbitals and densities is performed under the conventional finite-size effects, while the total energies are calculated with $E_{\rm C}\,[\rho_{\rm ch}]$. In other words, calculation without any finite-size effect, the conventional finite-size effects shown as "(All)" in the table, the intermediate treatment shown as "[All]", and the self-consistent

[4] For example, $\Delta E_{\rm tot}$ of "SLy4 & LDA", "SLy4 & All + EMSO", "SLy4-ISB & LDA", and "SLy4-ISB & All + EMSO" are, respectively, 63.4171, 62.0848, 71.4169, and 70.1398 MeV, where, in the SLy4-ISB, the SLy4 EDF is used for the $\mathcal{E}_{\rm IS}$, while the SAMi-ISB EDF is used for the ISB part $\mathcal{E}_{\rm CIB} + \mathcal{E}_{\rm CSB}$, which is not, although, guaranteed to reproduce any experimental properties.

finite-size effects shown as "All" are summarized as follows:

No finite-size effect

$$\begin{cases} V_{\mathrm{CH}p}\left(\boldsymbol{r}\right) = \displaystyle\int \frac{\rho_p\left(\boldsymbol{r}'\right)}{\left|\boldsymbol{r}-\boldsymbol{r}'\right|}\, d\boldsymbol{r}', \qquad V_{\mathrm{CH}n}\left(\boldsymbol{r}\right) = 0, \\ E_{\mathrm{CH}} = \dfrac{1}{2}\displaystyle\int V_{\mathrm{CH}p}\left(\boldsymbol{r}\right)\rho_p\left(\boldsymbol{r}\right)\, d\boldsymbol{r} = \frac{1}{2}\iint \frac{\rho_p\left(\boldsymbol{r}\right)\rho_p\left(\boldsymbol{r}'\right)}{\left|\boldsymbol{r}-\boldsymbol{r}'\right|}\, d\boldsymbol{r}\, d\boldsymbol{r}', \end{cases}$$

Conventional finite-size effects "(All)"

$$\begin{cases} V_{\mathrm{CH}p}\left(\boldsymbol{r}\right) = \displaystyle\int \frac{\rho_{\mathrm{ch}}\left(\boldsymbol{r}'\right)}{\left|\boldsymbol{r}-\boldsymbol{r}'\right|}\, d\boldsymbol{r}', \qquad V_{\mathrm{CH}n}\left(\boldsymbol{r}\right) = 0, \\ E_{\mathrm{CH}} = \dfrac{1}{2}\displaystyle\int V_{\mathrm{CH}p}\left(\boldsymbol{r}\right)\rho_p\left(\boldsymbol{r}\right)\, d\boldsymbol{r} = \frac{1}{2}\iint \frac{\rho_{\mathrm{ch}}\left(\boldsymbol{r}\right)\rho_p\left(\boldsymbol{r}'\right)}{\left|\boldsymbol{r}-\boldsymbol{r}'\right|}\, d\boldsymbol{r}\, d\boldsymbol{r}', \end{cases}$$

Intermediate treatment "[All]"

$$\begin{cases} V_{\mathrm{CH}p}\left(\boldsymbol{r}\right) = \displaystyle\int \frac{\rho_{\mathrm{ch}}\left(\boldsymbol{r}'\right)}{\left|\boldsymbol{r}-\boldsymbol{r}'\right|}\, d\boldsymbol{r}', \qquad V_{\mathrm{CH}n}\left(\boldsymbol{r}\right) = 0, \\ E_{\mathrm{CH}} = \dfrac{1}{2}\displaystyle\iint \frac{\rho_{\mathrm{ch}}\left(\boldsymbol{r}\right)\rho_{\mathrm{ch}}\left(\boldsymbol{r}'\right)}{\left|\boldsymbol{r}-\boldsymbol{r}'\right|}\, d\boldsymbol{r}\, d\boldsymbol{r}', \end{cases}$$

Self-consistent finite-size effects "All"

$$\begin{cases} V_{\mathrm{CH}\tau}\left(\boldsymbol{r}\right) = \left[\displaystyle\int \frac{\rho_{\mathrm{ch}}\left(\boldsymbol{r}'\right)}{\left|\boldsymbol{r}-\boldsymbol{r}'\right|}\, d\boldsymbol{r}'\right] * G_{\mathrm{E}\tau}\left(r\right) = \iint \frac{\rho_{\mathrm{ch}}\left(\boldsymbol{r}'\right)}{\left|\boldsymbol{r}''-\boldsymbol{r}'\right|} G_{\mathrm{E}\tau}\left(\left|\boldsymbol{r}-\boldsymbol{r}''\right|\right)\, d\boldsymbol{r}'\, d\boldsymbol{r}'', \\ E_{\mathrm{CH}} = \displaystyle\sum_{\tau}\frac{1}{2}\int V_{\mathrm{CH}\tau}\left(\boldsymbol{r}\right)\rho_\tau\left(\boldsymbol{r}\right)\, d\boldsymbol{r} = \frac{1}{2}\iint \frac{\rho_{\mathrm{ch}}\left(\boldsymbol{r}\right)\rho_{\mathrm{ch}}\left(\boldsymbol{r}'\right)}{\left|\boldsymbol{r}-\boldsymbol{r}'\right|}\, d\boldsymbol{r}\, d\boldsymbol{r}', \end{cases}$$

where, for the sake of simplicity, the Coulomb Hartree potential $V_{\mathrm{H}\tau}$ and the Coulomb Hartree energy are shown as examples. In the conventional finite-size effects, the self-consistency between the Coulomb EDF $E_{\mathrm{C}}\left[\rho_{\mathrm{ch}}\right]$ and the Coulomb potential $V_{\mathrm{C}\tau}$ is broken, while the total energy is calculated straightforwardly from the potential; in the intermediate treatment, the total energy is not calculated straightforwardly as well. Comparing among results "(All)", "[All]", and "All", it is found that the effect of $G_{\mathrm{E}\tau}$ for the Coulomb potential is quite small, while the difference between ρ_p and ρ_{ch} for both V_{C} and E_{C} is significant. Although the intermediate treatment reproduces the total energy obtained by the self-consistent finite-size effects, the calculation procedure, in principle, breaks the self-consistency and indeed, because of this braking self-consistency, the calculation procedure, i.e., calculation code, becomes complicated. Hence, one is recommended to use the self-consistent finite-size effects.

At last, it should be noted that the experimental data shown in Table 3.4.7 are -1 times the binding energy. In principle, the mass difference should be calculated by using the difference of the mass excess, instead of the difference of the binding energy, where the mass excess and the binding energy of an atomic nucleus with Z protons and N neutrons, respectively, read

$$\Delta\left(Z,N\right) = M\left(Z,N\right) - \left(Z+N\right)u, \tag{3.4.46}$$

$$B\left(Z,N\right) = Zm_{\mathrm{H}} + Nm_n - M\left(Z,N\right) \tag{3.4.47}$$

with the atomic mass unit $u = M\left(6,6\right)/12$ and the masses of the nucleus $M\left(Z,N\right)$, hydrogen atoms m_{H}, and neutrons m_n. Nevertheless, here, the binding energy is used since the calculated total energy corresponds to -1 times the binding energy.

3.5 Finite-Light-Speed Correction to Coulomb Interaction

In the previous sections, apart from the vacuum polarization, the Coulomb interaction was used for the electromagnetic interaction, while its calculation accuracy was improved as much as possible. The Coulomb interaction, which is the lowest-order with respect to $1/c$ of the electromagnetic interaction, is instantaneous and the next-leading-order term is known as the Breit correction [402–405]. This correction is also referred to as the finite-light-speed correction or the relativistic correction. In the electronic structure of atoms, it is known that the Breit correction between electrons contributes more than the vacuum polarization between electrons and atomic nuclei [420].

In this section, the contribution of the Breit correction to nuclear properties is investigated. The LDA exchange EDF for the Breit correction has been known [421], and results with this EDF are compared with those with the Coulomb LDA EDF. The purpose of this section is to see whether the relativistic correction is larger than the vacuum polarization, and thus, the LDA exchange EDF is enough for this purpose. In atomic DFT, it is pointed out in Ref. [A13] that the contribution of the Breit correction to total energies is almost the same magnitude but opposite direction to effects of the density gradient in the heavy atoms. Therefore, it is interesting to see whether, in atomic nuclei, the contribution of density gradient to total energies is comparable to that of the Breit correction. Note that a relativistic extension of the GGA-B88 exchange EDF has been proposed [422], while the dependence on the density gradient was treated with the original form. It may be important to check the dependence on the density gradient for the Coulomb interaction is applicable to the Breit correction, especially in nuclear DFT. Moreover, in order to make a fair comparison to calculation only with the Coulomb interaction, first, parameters of the original B88 exchange EDF should be adjusted for atomic nuclei, as we did with the PBE exchange EDF. Hence, the relativistic LDA exchange EDF is used in this work, instead of the relativistic extension of the GGA-B88 exchange EDF.

3.5.1 Theoretical Framework

The next-leading-order interaction with respect to $1/c$ in the Coulomb gauge is the Breit correction

$$v_{\mathrm{Breit}}\left(\boldsymbol{r}_j, \boldsymbol{r}_k\right) = -\left[\frac{c\boldsymbol{\alpha}_j \cdot c\boldsymbol{\alpha}_k}{2c^2 r_{jk}} + \frac{\left(c\boldsymbol{\alpha}_j \cdot \boldsymbol{r}_{jk}\right)\left(c\boldsymbol{\alpha}_k \cdot \boldsymbol{r}_{jk}\right)}{2c^2 r_{jk}^3}\right], \tag{3.5.1}$$

where $\boldsymbol{\alpha}$ is 4×4 matrix defined by

$$\boldsymbol{\alpha} = \left(\begin{pmatrix} O_2 & \sigma_x \\ \sigma_x & O_2 \end{pmatrix}, \begin{pmatrix} O_2 & \sigma_y \\ \sigma_y & O_2 \end{pmatrix}, \begin{pmatrix} O_2 & \sigma_z \\ \sigma_z & O_2 \end{pmatrix}\right) \tag{3.5.2}$$

with the Pauli matrices σ_x, σ_y, and σ_z and the 2×2 zero matrix O_2. The Foldy-Wouthuysen-Tani transformation [423–426] of the Dirac Hamiltonian $H = T_{\mathrm{D}} + v_{\mathrm{Coul}} + v_{\mathrm{Breit}}$ leads to the Breit correction in the non-relativistic scheme $\tilde{v}_{\mathrm{Breit}}$, which reads [427, 428]

$$\begin{aligned}
&\tilde{v}_{\mathrm{Breit}}\left(\boldsymbol{r}_j, \boldsymbol{s}_j, \boldsymbol{r}_k, \boldsymbol{s}_k\right) \\
&= -\frac{\pi\hbar^2 e^2}{M^2c^2}\delta\left(\boldsymbol{r}_{jk}\right) - \frac{e^2}{2M^2c^2}\boldsymbol{p}_j \cdot \left[\frac{1}{r_{jk}} + \frac{\boldsymbol{r}_{jk}\boldsymbol{r}_{jk}}{r_{jk}^3}\right] \cdot \boldsymbol{p}_k \\
&\quad - \frac{8\pi\hbar^2 e^2}{3M^2c^2}\delta\left(\boldsymbol{r}_{jk}\right)\boldsymbol{s}_j \cdot \boldsymbol{s}_k - \frac{\hbar^2 e^2}{M^2c^2}\boldsymbol{s}_j \cdot \left[\frac{3\boldsymbol{r}_{jk}\boldsymbol{r}_{jk}}{r_{jk}^5} - \frac{1}{r_{jk}^3}\right] \cdot \boldsymbol{s}_k + \frac{\hbar^2 e^2}{M^2c^2}\frac{1}{r_{jk}^3}\boldsymbol{s}_j \cdot \left[\boldsymbol{r}_{jk} \times \left(2\boldsymbol{p}_k - \boldsymbol{p}_j\right)\right],
\end{aligned} \tag{3.5.3}$$

where T_{D} is the Dirac kinetic operator, M is the mass of particles, and $\boldsymbol{p}_j$ is the momentum of the particle j. The first term corresponds to the Darwin term for the Coulomb interaction, which is related to Zitterbewegung [399]; the second term corresponds to the retardation of the Coulomb interaction; the remaining terms are the spin-orbit and the spin-magnetic interactions [427–429]. In this section, the Coulomb interaction and the Breit correction are considered for proton-proton electromagnetic interaction, where the point-particle approximation is assumed. Hence, the electromagnetic EDF E_{EM} is the LDA Coulomb-Breit one, i.e., $E_{\mathrm{EM}}\left[\rho_p\right] = E_{\mathrm{CH}}\left[\rho_p\right] + E_{\mathrm{Cx}}\left[\rho_p\right] + E_{\mathrm{Breit}}^{\mathrm{tot}}\left[\rho_p\right]$. The argument of E_{EM} is ρ_p, instead of ρ_{ch}, since the point-particle approximation is used, i.e., the finite spatial charge distributions of nucleons are neglected.

The Breit Hartree and exchange EDFs are [421, A13]

$$E_{\mathrm{Breit}}^{\mathrm{H}}\left[\rho_p\right] = -\frac{\pi\hbar^2 e^2}{2M^2c^2}\int \left[\rho_p\left(\boldsymbol{r}\right)\right]^2 d\boldsymbol{r}, \tag{3.5.4}$$

$$E_{\mathrm{Breit}}^{\mathrm{x}}\left[\rho_p\right] = +\frac{3\pi\hbar^2 e^2}{2M^2c^2}\int \left[\rho_p\left(\boldsymbol{r}\right)\right]^2 d\boldsymbol{r}, \tag{3.5.5}$$

respectively. Accordingly, the total correction is

$$\begin{aligned}
E_{\mathrm{Breit}}^{\mathrm{tot}}\left[\rho_p\right] &= E_{\mathrm{Breit}}^{\mathrm{H}}\left[\rho_p\right] + E_{\mathrm{Breit}}^{\mathrm{x}}\left[\rho_p\right] \\
&= +\frac{\pi\hbar^2 e^2}{M^2c^2}\int \left[\rho_p\left(\boldsymbol{r}\right)\right]^2 d\boldsymbol{r}.
\end{aligned} \tag{3.5.6}$$

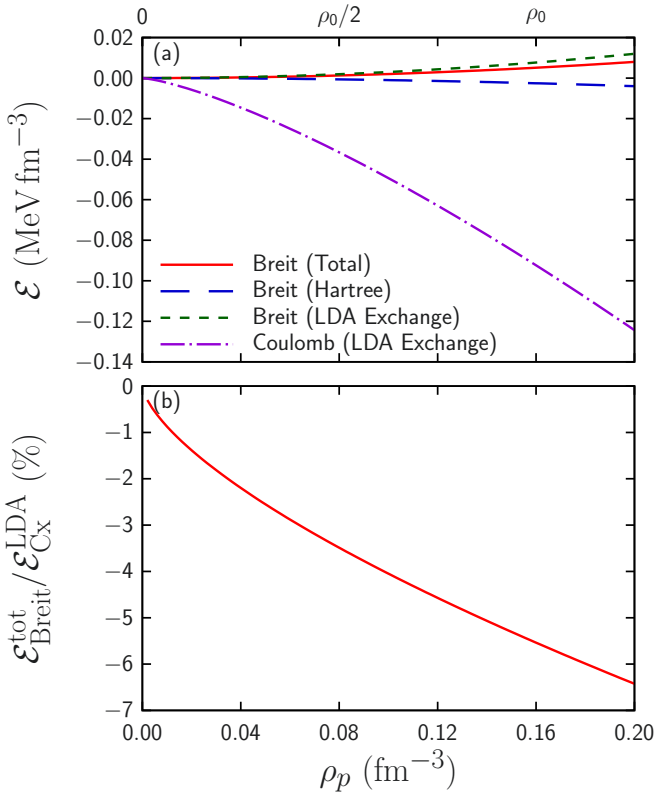

Figure 3.5.1: (a) Energy densities of $E^{\rm tot}_{\rm Breit}$, $E^{\rm H}_{\rm Breit}$, and $E^{\rm x}_{\rm Breit}$ as functions of the proton density ρ_p. Here, $\rho_0 = 0.16\,{\rm fm}^{-3}$ is the saturation density. For comparison, the Coulomb LDA exchange energy density is also plotted. (b) Ratio of $\mathcal{E}^{\rm tot}_{\rm Breit}$ to $\mathcal{E}^{\rm LDA}_{\rm Cx}$ as a function of ρ_p. This figure is taken from Ref. [A5].

Figure 3.5.1(a) shows the energy densities (energy per volume) of the Breit total EDF $E^{\rm tot}_{\rm Breit}$, the Breit Hartree EDF $E^{\rm H}_{\rm Breit}$, and the Breit exchange EDF $E^{\rm x}_{\rm Breit}$ as functions of ρ_p. For comparison, the Coulomb LDA exchange EDF $E^{\rm LDA}_{\rm Cx}$ is also plotted. Figure 3.5.1(b) shows the ratio $\mathcal{E}^{\rm tot}_{\rm Breit}/\mathcal{E}^{\rm LDA}_{\rm Cx}$ as a function of ρ_p. In $N = Z$ nuclei, the proton density distribution at the central region is approximately $\rho_p(r) \approx \rho_0/2 \approx 0.08\,{\rm fm}^{-3}$. Hence, the Breit correction to the total energy is expected to be approximately $-4\,\%$ of the Coulomb exchange energy, i.e., approximately 300 keV for ^{40}Ca.

3.5.2 Simple Estimations of Systematic Behaviours

In order to understand the systematic behaviours, these corrections to the total energy are estimated by using the simple ansatz, as Sec. 3.4.2. The proton density distribution is assumed to be the hard sphere [Eq. (3.4.28)]. Then, the Breit Hartree and exchange correlation energies read

$$\begin{aligned} E^{\rm H}_{\rm Breit} &= -\frac{\pi\,(\hbar c)^2\,e^2}{2\,(Mc^2)^2}\rho_0^p Z \\ &\simeq -0.0080Z\,{\rm MeV}, \end{aligned} \tag{3.5.7}$$

$$\begin{aligned} E^{\rm x}_{\rm Breit} &= +\frac{3\pi\,(\hbar c)^2\,e^2}{2\,(Mc^2)^2}\rho_0^p Z \\ &\simeq +0.024Z\,{\rm MeV}. \end{aligned} \tag{3.5.8}$$

Accordingly, the total correction is estimated as

$$\begin{aligned} E_{\mathrm{Breit}}^{\mathrm{tot}} &= E_{\mathrm{Breit}}^{\mathrm{H}} + E_{\mathrm{Breit}}^{\mathrm{x}} \\ &= +\frac{\pi \left(\hbar c\right)^2 e^2}{\left(Mc^2\right)^2} \rho_0^p Z \\ &\simeq +0.016 Z \,\mathrm{MeV}. \end{aligned} \tag{3.5.9}$$

Compared with the estimations for the Coulomb Hartree and exchange energies [Eqs. (3.4.32) and (3.4.33)], the absolute value of the Breit energy is 30 times smaller than the Coulomb exchange energy, which is consistent with the estimation shown in Fig. 3.5.1.

In atoms, the Breit correction between electrons is the leading order correction to the Hamiltonian; the vacuum polarization to the Coulomb potential is the next leading order to the Breit correction. On the contrary, in the nuclear structure of atomic nuclei, comparing Eqs. (3.4.42) and (3.5.9), one can conclude that the Breit correction between protons is comparable to the vacuum polarization between protons in light nuclei, while the former is approximately one order of magnitude smaller to the latter in heavy nuclei.

3.5.3 Systematic Analysis

Next, the systematic calculation is performed. The numerical conditions are the same as in Sec. 3.3.

Table 3.5.1 shows the ground-state energies of the selected nuclei calculated with the Breit correction. For comparison, those calculated only by using the Coulomb LDA exchange EDF and those with both the Breit correction and the vacuum polarization are also shown. It can be seen that contribution of the Breit correction to the total energy is 0.072 MeV, 0.195 MeV, and 0.813 MeV for ^{16}O, ^{48}Ca, and ^{208}Pb, respectively, while that of the vacuum polarization is 0.090 MeV, 0.401 MeV, and 3.711 MeV, respectively [5]. As expected in the previous section, in light nuclei, two contributions are the same order, while in heavy nuclei, the vacuum polarization dominates.

Figure 3.5.2 shows the relative difference between the exchange energy calculated by using the Coulomb or Coulomb-Breit LDA, $E_{\mathrm{Cx}}^{\mathrm{LDA}}$, and that by the Coulomb GGA, $E_{\mathrm{Cx}}^{\mathrm{GGA}}$,

$$\Delta E_{\mathrm{Cx}} = \frac{E_{\mathrm{Cx}}^{\mathrm{LDA}} - E_{\mathrm{Cx}}^{\mathrm{GGA}}}{E_{\mathrm{Cx}}^{\mathrm{GGA}}}, \tag{3.5.10}$$

as functions of A, where E_{Cx} includes the Coulomb interaction only for "Coulomb", while it include the both Coulomb interaction and the Breit correction for "Coulomb-Breit". It is shown that $|\Delta E_{\mathrm{Cx}}|$ of both the Coulomb interaction and the Coulomb-Breit one becomes smaller as A increases, and they reach the constant value at $A \approx 100$, while the difference between ΔE_{Cx} of the Coulomb interaction and that of the Coulomb-Breit one is almost independent of A. This behaviour is consistent with the same comparison in the relativistic Hartree-Fock calculation [430, 431], where the Coulomb GGA exchange energy, which is expected to reproduce the Coulomb exact-Fock energy, corresponds to Eq. (4) in Ref. [431]. The correction of the density gradient to the total energy, which are discussed in Sec. 3.4.3, is -0.212 MeV, -0.367 MeV, and -0.870 MeV for ^{16}O, ^{48}Ca, and ^{208}Pb, respectively. Therefore, it can also be concluded that the Breit correction and the density gradient effect are opposite to each other and the former is smaller in light nuclei, while its absolute value is comparable to the latter in heavy nuclei. It is pointed out in Ref. [A13] that, in heavy atoms, since the density of atoms gets larger, the density gradient effect on the total energy is comparable with the absolute value of the Breit correction. In the case of atomic nuclei, the profile of the proton density does not change much, while central density is proportional to Z/A, which decreases in heavy nuclei, in contrast to atoms. Nevertheless, two effects become of comparable order. This may be because the density gradient effect decreases rapidly as Z or A increases, as shown in Fig. 3.3.1, while Z/A does not decrease rapidly, e.g., it is still approximately 0.4 in ^{208}Pb. Hence, the ratio $\left|\mathcal{E}_{\mathrm{Breit}}^{\mathrm{tot}}/\mathcal{E}_{\mathrm{Cx}}^{\mathrm{LDA}}\right|$ does not change drastically. Therefore, the mechanism of this behaviour in atomic nuclei is different from that in atoms. Meanwhile, in both cases, as Z increases, the Breit correction and the density gradient effect become of comparable order. Thus, it is indispensable to consider both effects on the Coulomb EDF, i.e., construct the Coulomb-Breit GGA exchange EDF without empirical fitting.

[5] The tiny difference between vacuum polarization contributions shown in Sec. 3.4.3 and those shown here is due to the tiny difference between ρ_p calculated with "the Coulomb GGA, the finite-size effects, and the vacuum polarization" and "the Coulomb LDA, the Breit correction, and the vacuum polarization". The tiny difference will not affect the discussion.

At last the Breit correction is fitted to aZ^b as in Sec. 3.4.3. We obtain

$$E_{\rm Breit}^{\rm tot} \simeq 0.0115 Z^{0.972}\,{\rm MeV}, \tag{3.5.11}$$

which is compatible with the simple analysis [Eq. (3.5.9)].

3.5.4 Detailed Analysis of ^{208}Pb

We shall perform a detailed analysis of ^{208}Pb. The proton single-particle energies are shown in Table 3.5.2. The Breit correction changes them by proton single-particle energies merely by 10–25 keV, while the vacuum polarization changes approximately 100 keV. The Breit correction itself makes the Coulomb repulsion weaker. The effective mean-field (Kohn-Sham) potential of the Breit correction is, nonetheless, repulsive-like potential. This is because the retardation (the second term of Eq. (3.5.3)) does not contribute to the Hartree potential, and eventually, the exchange potential, which makes the original interaction weaker effectively, is stronger than the Hartree potential.

At last, the relative difference between the proton density distributions of ^{208}Pb and that calculated by using the LDA, $\Delta\rho_p$ defined by Eq. (3.3.7), are shown in Fig. 3.5.3. It is seen that at the central region ($r \lesssim 6\,{\rm fm}$), the Breit correction does not change the density, while it changes slightly at the surface region ($6 \lesssim r \lesssim 8\,{\rm fm}$). However, the change is less than that of the vacuum polarization, even which changes ρ_p just slightly, compared to the finite-size effects discussed in Fig. 3.4.4. Thus, it can be safely concluded that neither the Breit correction nor the vacuum polarization changes significantly ρ_p.

3.6 Short Summary

In this chapter, we introduced the precise treatment of the Coulomb interaction to nuclear DFT. In Sec. 3.2, four types of the Coulomb GGA exchange EDFs, B88, PW92, PBE, and PBEsol, were used to calculate Coulomb exchange energies with the experimental charge density distribution. We found that the Coulomb GGA exchange EDF reduces the error of the Coulomb exchange energy compared to the exact-Fock energy, while these four EDFs do not give a significant difference.

In Sec. 3.3, the Coulomb GGA-PBE exchange EDF was taken as an example and was applied to the self-consistent calculation of nuclear DFT. We found that once the parameter of the GGA-PBE exchange EDF, μ, is multiplied by 1.25, it reproduces the Coulomb exact-Fock energy within 100 keV error. It was also found that the Coulomb GGA-PBE exchange EDF gives almost the same single-particle energies and densities as the Coulomb LDA one since the Coulomb GGA-PBE exchange EDF changes the Coulomb potential only in the surface region.

In Sec. 3.4, on top of the Coulomb GGA exchange EDF, the finite-size effects of nucleons, i.e., the non-zero spatial charge distribution of nucleons, and the vacuum polarization were taken into account for nuclear DFT. In addition, the electromagnetic spin-orbit interaction was also considered perturbatively. It was found that neutrons are also affected by the Coulomb interaction once the finite-size effects of nucleons are taken into account, which was missing in the finite-size effects in the previous works. The proton and neutron finite-size effects and the vacuum polarization contribute to the total energy of ^{208}Pb in -8.2 MeV, $+1.2$ MeV, and $+3.7$ MeV, respectively, which are non-negligible compared to the desired accuracy (0.1 MeV). By using all these treatments together with the isospin symmetry breaking terms of the nuclear interaction, the mass difference of the mirror nuclei pair ^{48}Ca and ^{48}Ni can be described within 300 keV difference.

In Sec. 3.5, the finite-light-speed correction to the Coulomb interaction, called Breit correction, was considered in the LDA. It was found that its contribution to the total energy reaches approximately 0.8 MeV in ^{208}Pb, which is less than the vacuum polarization, while it may not be negligible compared to the desired accuracy. Its correction is almost the same absolute value but the opposite sign to the correction due to the density gradient.

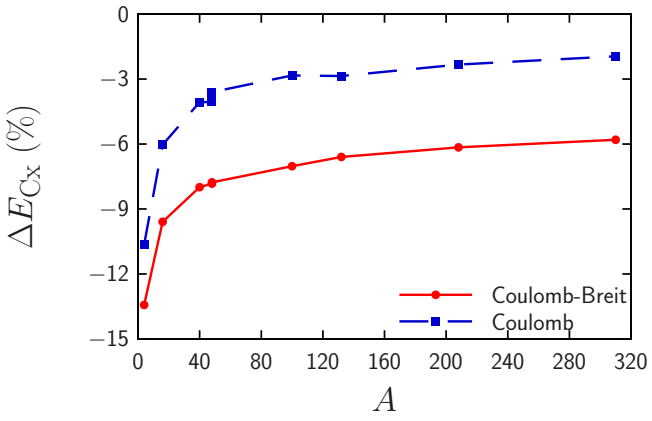

Figure 3.5.2: Relative difference between the exchange energy calculated by using the Coulomb or Coulomb-Breit LDA and that by the Coulomb GGA EDF as functions of A. This figure is taken from Ref. [A5].

Table 3.5.1: Ground-state energies calculated with the Breit correction ("Coulomb-Breit"). For comparison, those calculated with the Coulomb LDA ("Coulomb") and with both the Breit correction and the vacuum polarization ("C.-B. & Vacuum Pol.") are also shown. All units are in MeV. This table is taken from Ref. [A5].

Nuclei	Coulomb	Coulomb-Breit	C.-B. & Vacuum Pol.
^{4}He	−27.5263	−27.5134	−27.5050
^{16}O	−130.4800	−130.4084	−130.3188
^{40}Ca	−347.0848	−346.8798	−346.4702
^{48}Ca	−415.6148	−415.4201	−415.0190
^{48}Ni	−352.6388	−352.3274	−351.6077
^{100}Sn	−811.6641	−811.0990	−809.2893
^{132}Sn	−1103.0881	−1102.6076	−1100.9215
^{208}Pb	−1636.6149	−1635.8023	−1632.0911
^{310}126	−2131.4146	−2130.1539	−2122.8658

Table 3.5.2: Single-particle energies of ^{208}Pb calculated with the Breit correction ("Coulomb-Breit"). For comparison, those calculated with the Coulomb LDA ("Coulomb") and with both the Breit correction and the vacuum polarization ("C.-B. & Vacuum Pol.") are also shown. For more detail, see the text. All the data are shown in MeV. This table is taken from Ref. [A5].

Orbital	Coulomb	Coulomb-Breit	C.-B. & Vacuum Pol.
$\pi 1s_{1/2}$	−44.980	−44.955	−44.849
$\pi 1p_{3/2}$	−39.387	−39.363	−39.263
$\pi 1p_{1/2}$	−39.107	−39.084	−38.984
$\pi 1d_{5/2}$	−32.482	−32.460	−32.366
$\pi 1d_{3/2}$	−31.815	−31.793	−31.700
$\pi 2s_{1/2}$	−28.509	−28.489	−28.392
$\pi 1f_{7/2}$	−24.692	−24.672	−24.584
$\pi 1f_{5/2}$	−23.353	−23.333	−23.246
$\pi 2p_{3/2}$	−19.411	−19.393	−19.302
$\pi 2p_{1/2}$	−18.626	−18.608	−18.518
$\pi 1g_{9/2}$	−16.338	−16.320	−16.237
$\pi 1g_{7/2}$	−14.019	−14.002	−13.920
$\pi 2d_{5/2}$	−10.255	−10.240	−10.155
$\pi 2d_{3/2}$	−8.846	−8.832	−8.748
$\pi 3s_{1/2}$	−7.673	−7.658	−7.574
$\pi 1h_{11/2}$	−7.663	−7.648	−7.569

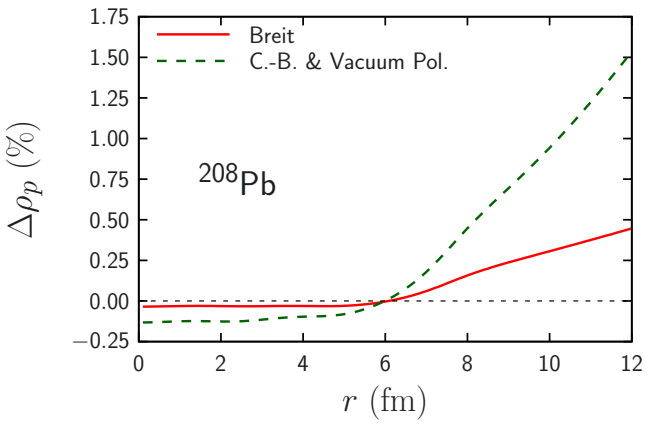

Figure 3.5.3: Relative difference between proton density distributions for ^{208}Pb calculated by the precise treatments and that by the LDA EDF, $\Delta\rho_p$, as functions of r.

Chapter 4

Isospin Symmetry Breaking on Ground-State Properties

In this chapter, the ISB terms of the nuclear interaction are introduced in the nuclear DFT. First, effects of the ISB terms of the nuclear interaction on the nuclear EoS are discussed. Then, effects of the electromagnetic interaction and that of the ISB terms of the nuclear interaction on nuclear properties are discussed. At last, a novel method to determine the CSB strength of a nuclear EDF is proposed.

4.1 Current Status of Isospin Symmetry Breaking Terms of Nuclear Interaction in Nuclear Density Functional Theory

In Sec. 1.5, it was explained that the isospin symmetry of the nuclear interaction is slightly broken. Since both the electromagnetic interaction and the ISB terms of the nuclear interaction break the isospin symmetry of atomic nuclei, experimentally measured isospin symmetry breaking originates from both. In the previous section, the electromagnetic interaction is treated in nuclear DFT as accurately as possible. In this chapter, the effects of the ISB terms of the nuclear interaction and the electromagnetic interaction on nuclear properties, i.e., sensitivity studies, are discussed.

The ISB terms of the nuclear interaction have been neglected in nuclear DFT. It was proposed in Ref. [175] that neglecting the Coulomb exchange EDF reduces the chi-square deviation from experimental values, which is mainly caused by the binding energy of ^{48}Ni. According to Ref. [177], this is because the Coulomb exchange energy and contribution of the CSB terms to the total energy cancel with each other, while it is an accidental consequence with no microscopic reason for that. Following Refs. [175,177], one of the mass formulae, named HFB-15 [432], also neglects the Coulomb exchange term to expect the cancellation between the Coulomb exchange energy and the CSB energy.

Recently, the ISB terms have been considered explicitly on top of the Skyrme density functional theory by Roca-Maza *et al.* [183, 433–436], by Bączyk *et al.* [185, 187, 188], and by Dong *et al.* [184, 186, 437, 438], while in most of these works, the Coulomb exchange EDF is still treated in the LDA, and the fundamental study on comparison with the electromagnetic and ISB interactions has not been done yet. Thus, in this thesis, such fundamental studies will be focused on.

In this chapter, the Skyrme-like CSB and CIB interactions are considered. If one considers the power counting proposed in Ref. [162], the CSB interaction is the next-leading order of the CIB interaction. If one only considers the fact that the scattering lengths of the proton-proton interaction v_{pp}, the neutron-neutron interaction v_{nn}, and the $T = 1$ channel of the proton-neutron interaction $v_{pn}^{T=1}$ are different [167], the CIB and CSB interactions are, respectively, defined simply as

$$v_{\mathrm{CIB}} \equiv \frac{v_{pp} + v_{nn}}{2} - v_{pn}^{T=1}, \tag{4.1.1}$$

$$v_{\mathrm{CSB}} \equiv v_{nn} - v_{pp}. \tag{4.1.2}$$

In this chapter, we take the latter definition, and thus the CIB and CSB interactions are in the same order.

In Sec. 4.2, the general form of the Skyrme-like CIB and CSB interactions are considered, which are extensions of the original (isospin symmetric) Skyrme interaction given in Eq. (2.3.3). In Secs. 4.3 and 4.4, only the s-wave of the Skyrme-like CIB and CSB interactions are considered, which corresponds to the t_0 term in Eq. (2.3.3). In Sec. 4.3, their effects on nuclear properties are compared with the effects of the Coulomb interaction. The parameters u_0, s_0, z_0, and y_0 determined in Ref. [183] is used, where the definitions of these parameters will be given later; in Sec. 4.4, the way to pin down the CSB strength s_0 with using *ab initio* calculation will be proposed.

Note that Secs. 4.2 and 4.3 are based on Ref. [A6] and Sec. 4.4 is based on Ref. [A4]. Not to make confusion, the isospin symmetric part of the nuclear EDF and its energy density will be referred to as $E_{\rm IS}$ and $\mathcal{E}_{\rm IS}$, respectively, which were simply referred to with the subscript "nucl" in the previous section.

4.2 Isospin Symmetry Breaking Energy Density Functional

In order to construct the ISB EDF on top of the Skyrme EDF, first, the Skyrme-like ISB interactions are considered. As discussed in Sec. 1.5, the class IV nuclear interaction is known to be much weaker than the whole nuclear interaction; hence, it will not be considered. The classes II and III nuclear interactions, i.e., CIB and CSB, respectively, are considered here. The CIB and CSB operators shown in Sec. 1.5 are denoted by $T_{12} = 3\tau_{z1}\tau_{z2} - \boldsymbol{\tau}_1 \cdot \boldsymbol{\tau}_2$ and $\tau_{z1} + \tau_{z2}$, respectively. The second term of T_{12} is, indeed, the isoscalar and does not break any isospin symmetry, while the first term of T_{12} breaks charge independence. Actually, some papers use T_{12}, while some papers use $\tau_{z1}\tau_{z2}$ simply. Hence, here, the CIB operator is denoted in the general form by $a\boldsymbol{\tau}_1\boldsymbol{\tau}_2 + b\tau_{z1}\tau_{z2}$. Then, the expectation values of the CIB and CSB operators are

$$\langle ij|a\boldsymbol{\tau}_1\boldsymbol{\tau}_2 + b\tau_{z1}\tau_{z2}|ij\rangle = \begin{cases} -3a - b & T = 0, \\ a + b & T = 1,\ pp \text{ or } nn, \\ a - b & T = 1,\ pn, \end{cases} \tag{4.2.1}$$

$$\langle ij|a\boldsymbol{\tau}_1\boldsymbol{\tau}_2 + b\tau_{z1}\tau_{z2}|ji\rangle = \begin{cases} a + b & T = 1,\ pp \text{ or } nn, \\ 0 & \text{otherwise}, \end{cases} \tag{4.2.2}$$

$$\langle ij|\tau_{z1} + \tau_{z2}|ij\rangle = \langle ij|\tau_{z1} + \tau_{z2}|ji\rangle = \begin{cases} -2 & i = p,\ j = p, \\ +2 & i = n,\ j = n, \\ 0 & \text{otherwise}, \end{cases} \tag{4.2.3}$$

respectively.

Section 4.2.1 is devoted to the derivation of the Skyrme-like ISB EDF. In Sec. 4.2.2, it will be shown that there is no criterion nor advantage to choose the specific form of the CIB operator, in the point of view of the pion exchange and the nuclear EoS.

4.2.1 Skyrme Isospin Symmetry Breaking Energy Density Functional

The Skyrme interaction is the leading and the next-leading orders of the effective interaction with respect to the momentum expansion. Hence, extending the Skyrme interaction to the ISB terms is not only just the extension of the Skyrme formalism but also the general idea to extend the effective interaction to the ISB terms. The Skyrme-like two-body ISB interactions are proposed as follows [183, 185, 188, A6]:

$$\begin{aligned} v_{\rm Sky}^{\rm CIB}(\boldsymbol{r}_1, \boldsymbol{r}_2) = \Big\{ & u_0 (1 + z_0 P_\sigma) \delta(\boldsymbol{r}_1 - \boldsymbol{r}_2) \\ & + \frac{u_1}{2} (1 + z_1 P_\sigma) \left[\boldsymbol{k}^{\dagger 2} \delta(\boldsymbol{r}_1 - \boldsymbol{r}_2) + \delta(\boldsymbol{r}_1 - \boldsymbol{r}_2) \boldsymbol{k}^2 \right] + u_2 (1 + z_2 P_\sigma) \boldsymbol{k}^\dagger \cdot \delta(\boldsymbol{r}_1 - \boldsymbol{r}_2) \boldsymbol{k} \Big\} \\ & \times (a\boldsymbol{\tau}_1 \cdot \boldsymbol{\tau}_2 + b\tau_{z1}\tau_{z2}), \end{aligned} \tag{4.2.4}$$

$$\begin{aligned} v_{\rm Sky}^{\rm CSB}(\boldsymbol{r}_1, \boldsymbol{r}_2) = \Big\{ & s_0 (1 + y_0 P_\sigma) \delta(\boldsymbol{r}_1 - \boldsymbol{r}_2) \\ & + \frac{s_1}{2} (1 + y_1 P_\sigma) \left[\boldsymbol{k}^{\dagger 2} \delta(\boldsymbol{r}_1 - \boldsymbol{r}_2) + \delta(\boldsymbol{r}_1 - \boldsymbol{r}_2) \boldsymbol{k}^2 \right] + s_2 (1 + y_2 P_\sigma) \boldsymbol{k}^\dagger \cdot \delta(\boldsymbol{r}_1 - \boldsymbol{r}_2) \boldsymbol{k} \Big\} \\ & \times \frac{\tau_{z1} + \tau_{z2}}{4}, \end{aligned} \tag{4.2.5}$$

which are analogues of the isospin-symmetric Skyrme interaction [Eq. (2.3.3)]. The spin-orbit term (an analogue of W_0 term in Eq. (2.3.3)) is not considered since the ISB terms are just corrections to the two-body interaction, while the spin-orbit term gives just a small contribution compared to the other terms. In addition, the three-body term (an analogue of t_3 term in Eq. (2.3.3)) is not considered since the three-body ISB interaction is not discussed yet even in the bare interaction. Accordingly, referring to the Skyrme energy density for the isospin symmetric case [Eqs. (2.3.4) and (2.3.5)], the Skyrme ISB energy density reads

$$\begin{aligned}
\mathcal{E}^{\mathrm{H}}_{\mathrm{CIB}}(\boldsymbol{r}) &= \frac{u_0}{2}\left(1+\frac{z_0}{2}\right)(a+b)(\rho_n-\rho_p)^2 + \frac{1}{4}\left[u_1\left(1+\frac{z_1}{2}\right)+u_2\left(1+\frac{z_2}{2}\right)\right](a+b)(\rho_n-\rho_p)(t_n-t_p) \\
&\quad - \frac{1}{16}\left[3u_1\left(1+\frac{z_1}{2}\right)-u_2\left(1+\frac{z_2}{2}\right)\right](a+b)(\rho_n-\rho_p)(\Delta\rho_n-\Delta\rho_p) \\
&\quad - \frac{1}{16}(u_1z_1+u_2z_2)(a+b)(\boldsymbol{J}_n-\boldsymbol{J}_p)^2, \qquad (4.2.6) \\
\mathcal{E}^{\mathrm{x}}_{\mathrm{CIB}}(\boldsymbol{r}) &= -\frac{u_0}{2}\left(\frac{1}{2}+z_0\right)(a+b)(\rho_n^2+\rho_p^2) - \frac{1}{4}\left[u_1\left(\frac{1}{2}+z_1\right)-u_2\left(\frac{1}{2}+z_2\right)\right](a+b)(\rho_n t_n+\rho_p t_p) \\
&\quad + \frac{1}{16}\left[3u_1\left(\frac{1}{2}+z_1\right)+u_2\left(\frac{1}{2}+z_2\right)\right](a+b)(\rho_n\Delta\rho_n+\rho_p\Delta\rho_p) \\
&\quad + \frac{1}{16}(u_1-u_2)(a+b)\left(\boldsymbol{J}_n^2+\boldsymbol{J}_p^2\right), \qquad (4.2.7) \\
\mathcal{E}^{\mathrm{H}}_{\mathrm{CSB}}(\boldsymbol{r}) &= \frac{s_0}{4}\left(1+\frac{y_0}{2}\right)(\rho_n^2-\rho_p^2) + \frac{1}{8}\left[s_1\left(1+\frac{y_1}{2}\right)+s_2\left(1+\frac{y_2}{2}\right)\right](\rho_n t_n-\rho_p t_p) \\
&\quad - \frac{1}{32}\left[3s_1\left(1+\frac{y_1}{2}\right)-s_2\left(1+\frac{y_2}{2}\right)\right](\rho_n\Delta\rho_n-\rho_p\Delta\rho_p) - \frac{1}{32}(s_1y_1+s_2y_2)\left(\boldsymbol{J}_n^2-\boldsymbol{J}_p^2\right), \qquad (4.2.8) \\
\mathcal{E}^{\mathrm{x}}_{\mathrm{CSB}}(\boldsymbol{r}) &= -\frac{s_0}{4}\left(\frac{1}{2}+y_0\right)(\rho_n^2-\rho_p^2) - \frac{1}{8}\left[s_1\left(\frac{1}{2}+y_1\right)-s_2\left(\frac{1}{2}+y_2\right)\right](\rho_n t_n-\rho_p t_p) \\
&\quad + \frac{1}{32}\left[3s_1\left(\frac{1}{2}+y_1\right)+s_2\left(\frac{1}{2}+y_2\right)\right](\rho_n\Delta\rho_n-\rho_p\Delta\rho_p) + \frac{1}{32}(s_1-s_2)\left(\boldsymbol{J}_n^2-\boldsymbol{J}_p^2\right). \qquad (4.2.9)
\end{aligned}$$

Accordingly, the nuclear EoS [Eq. (2.3.11)] becomes

$$
\begin{aligned}
&\frac{E_{\text{Skyrme}}}{A}(\rho,\beta)\\
&=\frac{E^{\text{IS}}_{\text{Skyrme}}}{A}(\rho,\beta)\\
&\quad+\frac{u_0}{2}\left(1+\frac{z_0}{2}\right)(a+b)\,\beta^2\rho\\
&\quad+\frac{1}{4}\frac{3}{5}\left(\frac{3\pi^2}{2}\right)^{2/3}\left[u_1\left(1+\frac{z_1}{2}\right)+u_2\left(1+\frac{z_2}{2}\right)\right](a+b)\,\beta\frac{(1+\beta)^{5/3}-(1-\beta)^{5/3}}{2}\rho^{5/3}\\
&\quad-\frac{u_0}{2}\left(\frac{1}{2}+z_0\right)(a+b)\,\frac{1+\beta^2}{2}\rho\\
&\quad-\frac{1}{4}\frac{3}{10}\left(\frac{3\pi^2}{2}\right)^{2/3}\left[u_1\left(\frac{1}{2}+z_1\right)-u_2\left(\frac{1}{2}+z_2\right)\right](a+b)\,\frac{(1+\beta)^{8/3}+(1-\beta)^{8/3}}{2}\rho^{5/3}\\
&\quad+\frac{s_0}{4}\left(1+\frac{y_0}{2}\right)\beta\rho+\frac{1}{8}\frac{3}{10}\left(\frac{3\pi^2}{2}\right)^{2/3}\left[s_1\left(1+\frac{y_1}{2}\right)+s_2\left(1+\frac{y_2}{2}\right)\right]\frac{(1+\beta)^{8/3}-(1-\beta)^{8/3}}{2}\rho^{5/3}\\
&\quad-\frac{s_0}{4}\left(\frac{1}{2}+y_0\right)\beta\rho-\frac{1}{8}\frac{3}{10}\left(\frac{3\pi^2}{2}\right)^{2/3}\left[s_1\left(\frac{1}{2}+y_1\right)-s_2\left(\frac{1}{2}+y_2\right)\right]\frac{(1+\beta)^{8/3}-(1-\beta)^{8/3}}{2}\rho^{5/3}\\
&\simeq\left\{\frac{3}{5}\frac{\hbar^2}{2m}\left(\frac{3\pi^2}{2}\right)^{2/3}\rho^{2/3}+\frac{1}{8}\left[3t_0-(a+b)\,u_0\,(1+2z_0)\right]\rho\right.\\
&\qquad\left.+\frac{3}{80}\left(\frac{3\pi^2}{2}\right)^{2/3}\left[3t_1+t_2\,(5+4x_2)-(a+b)\,(u_1\,(1+2z_1)-u_2\,(1+2z_2))\right]\rho^{5/3}+\frac{t_3}{16}\rho^{\alpha+1}\right\}\\
&\quad+\left\{\frac{1}{8}s_0\,(1-y_0)\,\rho+\frac{1}{20}\left(\frac{3\pi^2}{2}\right)^{2/3}\left(s_1\,(1-y_1)+3s_2\,(1+y_2)\right)\rho^{5/3}\right\}\beta\\
&\quad+\left\{\frac{1}{3}\frac{\hbar^2}{2m}\left(\frac{3\pi^2}{2}\right)^{2/3}\rho^{2/3}-\frac{1}{8}\left[t_0\,(1+2x_0)-3\,(a+b)\,u_0\right]\rho\right.\\
&\qquad-\frac{1}{24}\left(\frac{3\pi^2}{2}\right)^{2/3}\left[3t_1x_1-t_2\,(4+5x_2)-(a+b)\,(u_1\,(4-z_1)+u_2\,(8+7z_2))\right]\rho^{5/3}\\
&\qquad\left.-\frac{1}{48}t_3\,(1+2x_3)\,\rho^{\alpha+1}\right\}\beta^2,
\end{aligned}
\tag{4.2.10}
$$

where $E^{\rm IS}_{\rm Skyrme}/A$ is the EoS given in Eq. (2.3.11). Consequently, EoS parameters J, L, $K_{\rm sym}$, and K_∞ read

$$\begin{aligned}
J = &\frac{1}{3}\frac{\hbar^2}{2m}\left(\frac{3\pi^2}{2}\right)^{2/3}\rho_0^{2/3} - \frac{1}{8}\left[t_0\left(1+2x_0\right) - 3\left(a+b\right)u_0\right]\rho_0 \\
&- \frac{1}{24}\left(\frac{3\pi^2}{2}\right)^{2/3}\left[3t_1x_1 - t_2\left(4+5x_2\right) - \left(a+b\right)\left(u_1\left(4-z_1\right) + u_2\left(8+7z_2\right)\right)\right]\rho_0^{5/3} \\
&- \frac{1}{48}t_3\left(1+2x_3\right)\rho_0^{\alpha+1}, \qquad (4.2.11)\\
L = &\frac{2}{3}\frac{\hbar^2}{2m}\left(\frac{3\pi^2}{2}\right)^{2/3}\rho_0^{2/3} - \frac{3}{8}\left[t_0\left(1+2x_0\right) - 3\left(a+b\right)u_0\right]\rho_0 \\
&- \frac{5}{24}\left(\frac{3\pi^2}{2}\right)^{2/3}\left[3t_1x_1 - t_2\left(4+5x_2\right) - \left(a+b\right)\left(u_1\left(4-z_1\right) + u_2\left(8+7z_2\right)\right)\right]\rho_0^{5/3} \\
&- \frac{1}{16}t_3\left(1+2x_3\right)\left(\alpha+1\right)\rho_0^{\alpha+1}, \qquad (4.2.12)\\
K_{\rm sym} = &-\frac{2}{3}\frac{\hbar^2}{2m}\left(\frac{3\pi^2}{2}\right)^{2/3}\rho_0^{2/3} \\
&- \frac{5}{12}\left(\frac{3\pi^2}{2}\right)^{2/3}\left[3t_1x_1 - t_2\left(4+5x_2\right) - \left(a+b\right)\left(u_1\left(4-z_1\right) + u_2\left(8+7z_2\right)\right)\right]\rho_0^{5/3} \\
&- \frac{3}{16}t_3\left(1+2x_3\right)\alpha\left(\alpha+1\right)\rho_0^{\alpha+1}, \qquad (4.2.13)\\
K_\infty = &-\frac{6}{5}\frac{\hbar^2}{2m}\left(\frac{3\pi^2}{2}\right)^{2/3}\rho_0^{2/3} \\
&+ \frac{3}{8}\left(\frac{3\pi^2}{2}\right)^{2/3}\left[3t_1 + t_2\left(5+4x_2\right) - \left(a+b\right)\left(u_1\left(1+2z_1\right) - u_2\left(1+2z_2\right)\right)\right]\rho_0^{5/3} \\
&+ \frac{9}{16}t_3\alpha\left(\alpha+1\right)\rho_0^{\alpha+1}, \qquad (4.2.14)
\end{aligned}$$

respectively. The pressure of nuclear matter is

$$\begin{aligned}
P\left(\rho,\beta\right) \simeq &\left\{\frac{2}{5}\frac{\hbar^2}{2m}\left(\frac{3\pi^2}{2}\right)^{2/3}\rho^{5/3} + \frac{1}{8}\left[3t_0 - \left(a+b\right)u_0\left(1+2z_0\right)\right]\rho^2\right. \\
&+\frac{1}{16}\left(\frac{3\pi^2}{2}\right)^{2/3}\left[3t_1 + t_2\left(5+4x_2\right) - \left(a+b\right)\left(u_1\left(1+2z_1\right) - u_2\left(1+2z_2\right)\right)\right]\rho^{8/3} \\
&\left.+\frac{t_3}{16}\left(\alpha+1\right)\rho^{\alpha+2}\right\} \\
&+\left\{\frac{1}{8}s_0\left(1-y_0\right)\rho^2 + \frac{1}{12}\left(\frac{3\pi^2}{2}\right)^{2/3}\left(s_1\left(1-y_1\right) + 3s_2\left(1+y_2\right)\right)\rho^{8/3}\right\}\beta \\
&+\left\{\frac{2}{9}\frac{\hbar^2}{2m}\left(\frac{3\pi^2}{2}\right)^{2/3}\rho^{5/3} - \frac{1}{8}\left[t_0\left(1+2x_0\right) - 3\left(a+b\right)u_0\right]\rho^2\right. \\
&-\frac{5}{72}\left(\frac{3\pi^2}{2}\right)^{2/3}\left[3t_1x_1 - t_2\left(4+5x_2\right) - \left(a+b\right)\left(u_1\left(4-z_1\right) + u_2\left(8+7z_2\right)\right)\right]\rho^{8/3} \\
&\left.-\frac{1}{48}\left(\alpha+1\right)t_3\left(1+2x_3\right)\rho^{\alpha+2}\right\}\beta^2. \qquad (4.2.15)
\end{aligned}$$

The equation which the saturation density ρ_0 satisfies [Eq. (2.3.17)] also changes as

$$\begin{aligned}
&\frac{2}{5}\frac{\hbar^2}{2m}\left(\frac{3\pi^2}{2}\right)^{2/3}\rho_0^{5/3} + \frac{1}{8}\left[3t_0 - \left(a+b\right)u_0\left(1+2z_0\right)\right]\rho_0^2 \\
&+\frac{1}{16}\left(\frac{3\pi^2}{2}\right)^{2/3}\left[3t_1 + t_2\left(5+4x_2\right) - \left(a+b\right)\left(u_1\left(1+2z_1\right) - u_2\left(1+2z_2\right)\right)\right]\rho_0^{8/3} + \frac{t_3}{16}\left(\alpha+1\right)\rho_0^{\alpha+2} = 0. \qquad (4.2.16)
\end{aligned}$$

4.2.2 Isospin Symmetry Breaking Contribution to Nuclear Equation of State

This section is devoted to the ISB contribution to the nuclear EoS. Before going the discussion of the nuclear EoS, three forms of CIB operator—the simple form $\tau_{z1}\tau_{z2}$, the isotensor form $T_{12} = \boldsymbol{\tau}_1 \cdot \boldsymbol{\tau}_2 - 3\tau_{z1}\tau_{z2}$, and the general form $a\boldsymbol{\tau}_1 \cdot \boldsymbol{\tau}_2 - b\tau_{z1}\tau_{z2}$—are compared. These three forms are widely used [153,165,174,183,185]. The CIB term originates from the mass difference between neutral pions π^0 and charged ones $\pi^\pm$, whose masses are denoted by m_{π^0} and $m_{\pi^\pm}$, respectively. The one-pion exchange potential reads [28,29]

$$v_{\mathrm{OPEP}}\left(m_\pi, \boldsymbol{q}\right) \sim -\frac{\left(\boldsymbol{\sigma}_1 \cdot \boldsymbol{q}\right)\left(\boldsymbol{\sigma}_2 \cdot \boldsymbol{q}\right)}{m_\pi^2 + q^2}\boldsymbol{\tau}_1 \cdot \boldsymbol{\tau}_2, \tag{4.2.17}$$

where m_π is the averaged pion mass. If the mass difference between neutral pions and charged ones is explicitly considered, the difference between the one-pion exchange potential propagated by the neutral pion π^0 and that by the charged pion $\pi^\pm$ reads

$$\begin{aligned}
&v_{\mathrm{OPEP}}\left(m_{\pi^0}, \boldsymbol{q}\right) - v_{\mathrm{OPEP}}\left(m_{\pi^\pm}, \boldsymbol{q}\right) \\
&\sim -\frac{\left(\boldsymbol{\sigma}_1 \cdot \boldsymbol{q}\right)\left(\boldsymbol{\sigma}_2 \cdot \boldsymbol{q}\right)}{m_{\pi^0}^2 + q^2}\tau_{z1}\tau_{z2} + \frac{\left(\boldsymbol{\sigma}_1 \cdot \boldsymbol{q}\right)\left(\boldsymbol{\sigma}_2 \cdot \boldsymbol{q}\right)}{m_{\pi^\pm}^2 + q^2}\frac{\tau_1^+\tau_2^- + \tau_1^-\tau_2^+}{2} \\
&= -\frac{\left(\boldsymbol{\sigma}_1 \cdot \boldsymbol{q}\right)\left(\boldsymbol{\sigma}_2 \cdot \boldsymbol{q}\right)}{m_{\pi^0}^2 + q^2}\tau_{z1}\tau_{z2} + \frac{\left(\boldsymbol{\sigma}_1 \cdot \boldsymbol{q}\right)\left(\boldsymbol{\sigma}_2 \cdot \boldsymbol{q}\right)}{m_{\pi^0}^2 - \Delta m_\pi^2 + q^2}\frac{\tau_1^+\tau_2^- + \tau_1^-\tau_2^+}{2} \\
&= -\frac{\left(\boldsymbol{\sigma}_1 \cdot \boldsymbol{q}\right)\left(\boldsymbol{\sigma}_2 \cdot \boldsymbol{q}\right)}{m_{\pi^0}^2 + q^2}\tau_{z1}\tau_{z2} + \frac{\left(\boldsymbol{\sigma}_1 \cdot \boldsymbol{q}\right)\left(\boldsymbol{\sigma}_2 \cdot \boldsymbol{q}\right)}{m_{\pi^0}^2 + q^2}\frac{m_{\pi^0}^2 + q^2}{m_{\pi^0}^2 - \Delta m_\pi^2 + q^2}\frac{\tau_1^+\tau_2^- + \tau_1^-\tau_2^+}{2} \\
&= -\frac{\left(\boldsymbol{\sigma}_1 \cdot \boldsymbol{q}\right)\left(\boldsymbol{\sigma}_2 \cdot \boldsymbol{q}\right)}{m_{\pi^0}^2 + q^2}\tau_{z1}\tau_{z2} + \frac{\left(\boldsymbol{\sigma}_1 \cdot \boldsymbol{q}\right)\left(\boldsymbol{\sigma}_2 \cdot \boldsymbol{q}\right)}{m_{\pi^0}^2 + q^2}\left(1 + \frac{\Delta m_\pi^2}{m_{\pi^0}^2 - \Delta m_\pi^2 + q^2}\right)\frac{\tau_1^+\tau_2^- + \tau_1^-\tau_2^+}{2} \\
&= -\frac{\left(\boldsymbol{\sigma}_1 \cdot \boldsymbol{q}\right)\left(\boldsymbol{\sigma}_2 \cdot \boldsymbol{q}\right)}{m_{\pi^0}^2 + q^2}\boldsymbol{\tau}_1 \cdot \boldsymbol{\tau}_2 + \frac{\left(\boldsymbol{\sigma}_1 \cdot \boldsymbol{q}\right)\left(\boldsymbol{\sigma}_2 \cdot \boldsymbol{q}\right)}{m_{\pi^0}^2 + q^2}\frac{\Delta m_\pi^2}{m_{\pi^0}^2 - \Delta m_\pi^2 + q^2}\frac{\tau_1^+\tau_2^- + \tau_1^-\tau_2^+}{2} \\
&= -\frac{\left(\boldsymbol{\sigma}_1 \cdot \boldsymbol{q}\right)\left(\boldsymbol{\sigma}_2 \cdot \boldsymbol{q}\right)}{m_{\pi^0}^2 + q^2}\boldsymbol{\tau}_1 \cdot \boldsymbol{\tau}_2 + \frac{\left(\boldsymbol{\sigma}_1 \cdot \boldsymbol{q}\right)\left(\boldsymbol{\sigma}_2 \cdot \boldsymbol{q}\right)}{m_{\pi^0}^2 + q^2}\frac{\Delta m_\pi^2}{m_{\pi^0}^2 - \Delta m_\pi^2 + q^2}\left(\boldsymbol{\tau}_1 \cdot \boldsymbol{\tau}_2 - \tau_{z1}\tau_{z2}\right),
\end{aligned} \tag{4.2.18}$$

where $\Delta m_\pi^2 = m_{\pi^0}^2 - m_{\pi^\pm}^2$. The second term corresponds to the CIB term. Therefore, $a = 1$ and $b = -1$ is derived from the one-pion exchange potential.

Since the ISB contributions to nuclear EoS in the case of the zero-range interaction are shown before, here, the ISB contributions to nuclear EoS in the case of a finite-range interaction are considered with referring to the nuclear EoS for isospin symmetric finite-range interactions [439]. The Gogny interaction [376] is taken as an example. The original Gogny interaction contains only the isospin symmetric part $v_{\mathrm{G}}^{\mathrm{IS}}$, whose form is [376]

$$\begin{aligned}
v_{\mathrm{G}}^{\mathrm{IS}}\left(\boldsymbol{r}_1, \boldsymbol{r}_2\right) = &\sum_{j=1}^{2}\left(W_j^{\mathrm{IS}} + B_j^{\mathrm{IS}}P_\sigma - H_j^{\mathrm{IS}}P_\tau - M_j^{\mathrm{IS}}P_\sigma P_\tau\right)\exp\left(-\frac{r_{12}^2}{\mu_j^{\mathrm{IS2}}}\right) \\
&+ t\left(1 + xP_\sigma\right)\delta\left(\boldsymbol{r}_{12}\right)\left[\rho\left(\frac{\boldsymbol{r}_1 + \boldsymbol{r}_2}{2}\right)\right]^\alpha + iW_0\boldsymbol{\sigma} \cdot \boldsymbol{k}^\dagger \times \delta\left(\boldsymbol{r}_{12}\right)\boldsymbol{k},
\end{aligned} \tag{4.2.19}$$

where $\boldsymbol{r}_{12} = \boldsymbol{r}_1 - \boldsymbol{r}_2$ and $r_{12} = |\boldsymbol{r}_{12}|$. The Gogny interaction is extended to the ISB terms as follows:

$$v_{\mathrm{G}}^{\mathrm{CIB}}\left(\boldsymbol{r}_1, \boldsymbol{r}_2\right) = \sum_{j=1}^{2}\left(W_j^{\mathrm{CIB}} + B_j^{\mathrm{CIB}}P_\sigma\right)\exp\left(-\frac{r_{12}^2}{\mu_j^{\mathrm{CIB2}}}\right)\left(a\boldsymbol{\tau}_1 \cdot \boldsymbol{\tau}_2 + b\tau_{z1}\tau_{z2}\right), \tag{4.2.20}$$

$$v_{\mathrm{G}}^{\mathrm{CSB}}\left(\boldsymbol{r}_1, \boldsymbol{r}_2\right) = \sum_{j=1}^{2}\left(W_j^{\mathrm{CSB}} + B_j^{\mathrm{CSB}}P_\sigma\right)\exp\left(-\frac{r_{12}^2}{\mu_j^{\mathrm{CSB2}}}\right)\frac{\tau_{z1} + \tau_{z2}}{4}. \tag{4.2.21}$$

Here, Heisenberg (P_τ) and Majorana ($P_\sigma P_\tau$) terms are neglected since the isospin exchange in the ISB terms

is rather complicated. Accordingly, the CIB and CSB contributions to the nuclear EoS are, respectively,

$$\frac{E_{\rm CIB}}{A} = \frac{a+b}{2\pi^{1/2}} \sum_{j=1}^{2} \frac{1}{p_{{\rm F}p}^2 + p_{{\rm F}n}^2} \times \left\{ \frac{2W_j^{\rm CIB} + B_j^{\rm CIB}}{6} \mu_j^{\rm CIB3} \left(p_{{\rm F}p}^3 - p_{{\rm F}n}^3 \right)^2 - \frac{W_j^{\rm CIB} + 2B_j^{\rm CIB}}{\mu_j^{\rm CIB3}} \left[F\left(p_{{\rm F}p} \mu_j^{\rm CIB} \right) + F\left(p_{{\rm F}n} \mu_j^{\rm CIB} \right) \right] \right\}, \tag{4.2.22}$$

$$\frac{E_{\rm CSB}}{A} = \frac{1}{4\pi^{1/2}} \sum_{j=1}^{2} \frac{1}{p_{{\rm F}p}^2 + p_{{\rm F}n}^2} \times \left\{ \frac{2W_j^{\rm CSB} + B_j^{\rm CSB}}{6} \mu_j^{\rm CSB3} \left(p_{{\rm F}n}^6 - p_{{\rm F}p}^6 \right) - \frac{W_j^{\rm CSB} + 2B_j^{\rm CSB}}{\mu_j^{\rm CSB3}} \left[F\left(p_{{\rm F}n} \mu_j^{\rm CSB} \right) - F\left(p_{{\rm F}p} \mu_j^{\rm CSB} \right) \right] \right\}, \tag{4.2.23}$$

where

$$F(x) = \frac{1}{x^3} \left[e^{-x^2} \left(x^2 - 2 \right) + 2 - 3a^2 + \sqrt{\pi} x^3 \, {\rm erf}\,(x) \right] \tag{4.2.24}$$

and erf is the error function

$${\rm erf}\,(x) = \frac{2}{\sqrt{\pi}} \int_0^x e^{-t^2} \, dt. \tag{4.2.25}$$

The isotensor operator has an advantage in that its eigenvalue for $T = 0$ state is zero. The operator $\boldsymbol{\tau}_1 \cdot \boldsymbol{\tau}_2 - \tau_{z1}\tau_{z2}$, i.e., $a = 1$ and $b = -1$, has an advantage that it originates from the pion-exchange formalism, while it also has a disadvantage that all the CIB contribution vanishes.

Therefore, in general, any form of the CIB operator does not have a strong advantage, while the difference of these operators is absorbed in the isospin symmetric part. Thus, whichever form is chosen, nothing changes, in principle. Hereinafter, the simple form $\tau_{z1}\tau_{z2}/2$, i.e., $a = 0$ and $b = 1/2$, will be used for the CIB operator.

4.3 Sensitivity Studies on Coulomb and Isospin Symmetry Breaking Terms of Nuclear Interactions

4.3.1 Numerical Setup

As in Chap. 3, the self-consistent Skyrme Hartree-Fock calculation is performed by using the code SKYRME_RPA [408]. The pairing interaction is not considered and the spherical symmetry is assumed, since we shall calculate only doubly-magic nuclei. In order to calculate the radial wave function, a mesh with an interval 0.1 fm in $0 \le r \le 15$ fm is used.

Electromagnetic Part

For the electromagnetic part $E_{\rm EM}$, we start from the Hartree-Fock-Slater approximation of the Coulomb interaction, i.e., the Coulomb LDA exchange EDF for $E_{\rm Cx}$ with $E_{\rm VP} \equiv 0$ and $E_{\rm EMSO} \equiv 0$, together with the point-particle approximation $\rho_{\rm ch} \equiv \rho_p$. On top of this, the precise treatments of the Coulomb interaction proposed in Chap. 3, i.e., the GGA, the proton finite-size effect, the neutron finite-size effect, and the vacuum polarization, are introduced step by step. The abbreviations "NoEx", "LDA", "GGA", "p-fin", "pn-fin", and "All" are used for

$$E_{\rm EM}^{\rm NoEx} = E_{\rm CH}\left[\rho_p\right], \tag{4.3.1}$$

$$E_{\rm EM}^{\rm LDA} = E_{\rm CH}\left[\rho_p\right] + E_{\rm Cx}^{\rm LDA}\left[\rho_p\right], \tag{4.3.2}$$

$$E_{\rm EM}^{\rm GGA} = E_{\rm CH}\left[\rho_p\right] + E_{\rm Cx}^{\rm GGA}\left[\rho_p\right], \tag{4.3.3}$$

$$E_{\rm EM}^{p\text{-fin}} = E_{\rm CH}\left[\rho_{\rm ch}^{p\text{-fin}}\right] + E_{\rm Cx}^{\rm GGA}\left[\rho_{\rm ch}^{p\text{-fin}}\right], \tag{4.3.4}$$

$$E_{\rm EM}^{pn\text{-fin}} = E_{\rm CH}\left[\rho_{\rm ch}^{pn\text{-fin}}\right] + E_{\rm Cx}^{\rm GGA}\left[\rho_{\rm ch}^{pn\text{-fin}}\right], \tag{4.3.5}$$

$$E_{\rm EM}^{\rm All} = E_{\rm CH}\left[\rho_{\rm ch}^{pn\text{-fin}}\right] + E_{\rm Cx}^{\rm GGA}\left[\rho_{\rm ch}^{pn\text{-fin}}\right] + E_{\rm VP}\left[\rho_{\rm ch}^{pn\text{-fin}}\right], \tag{4.3.6}$$

respectively, as denoted in Table 3.4.1. Here, $E_{\rm CH}$, $E_{\rm Cx}^{\rm LDA}$, $E_{\rm Cx}^{\rm GGA}$, and $E_{\rm VP}$ denote the Coulomb Hartree, the Coulomb LDA exchange, the Coulomb GGA exchange, and the vacuum polarization EDFs, respectively. Here, the Coulomb GGA-PBE exchange EDF with $\lambda = 1.25$ is used for $E_{\rm Cx}^{\rm GGA}$. The charge densities $\rho_{\rm ch}^{p\text{-fin}}$ and $\rho_{\rm ch}^{pn\text{-fin}}$ are defined by

$$\tilde{\rho}_{\rm ch}^{p\text{-fin}}(q) = \tilde{G}_{{\rm E}p}\left(q^2\right)\tilde{\rho}_p(q), \tag{4.3.7}$$

$$\begin{aligned}\tilde{\rho}_{\rm ch}^{pn\text{-fin}}(q) &= \tilde{G}_{{\rm E}p}\left(q^2\right)\tilde{\rho}_p(q) + \tilde{G}_{{\rm E}n}\left(q^2\right)\tilde{\rho}_n(q) \\ &= \tilde{\rho}_{\rm ch}(q),\end{aligned} \tag{4.3.8}$$

the former and the latter of which, respectively, correspond to the charge density with only proton finite-size and both proton and neutron finite-size effects. On top of "All", we consider the electromagnetic spin-orbit term $E_{\rm EMSO}$ perturbatively, which is abbreviated as "All + EMSO".

Nuclear Part

As for the nuclear interaction, when the ISB terms are not considered, the SAMi EDF [409] or the SAMi-J EDF family [80] is adopted, while the SAMi-ISB EDF [183] is adopted when we consider the ISB terms. The SAMi EDF is a Skyrme EDF without ISB terms, whose parameters are determined to reproduce:

1. the binding energies of ^{40}Ca, ^{48}Ca, ^{90}Zr, ^{132}Sn, and ^{208}Pb;
2. the charge radii of ^{40}Ca, ^{48}Ca, ^{90}Zr, and ^{208}Pb;
3. the spin-orbit splittings of proton $1g$ and $2f$ levels in ^{90}Zr and ^{208}Pb;
4. the Landau-Migdal parameters at saturation density are fixed to $G_0 = 0.15$ and $G_0' = 0.35$.

Here, the Landau-Migdal parameters are related to the particle-hole interaction derived by the second functional derivative of the Hamiltonian density with respect to the density, whose definitions are left for Ref. [440].

It is known that the SAMi EDF gives a better description of spin-isospin properties, such as the isobaric analogue resonance. The SAMi-J EDF family is constructed to the same criteria as the SAMi EDF, while its symmetry energy J is changed by hand to study the symmetry energy dependence of nuclear properties. The parameters of the SAMi-J family are shown in Table 4.3.1. Accordingly, the symmetry parameter L is also changed. The values of J and L for the SAMi EDF and the SAMi-J EDF family are shown in Table 4.3.2.

The SAMi-ISB EDF is a similar EDF with the SAMi EDF, while all the parameters, including the CIB and the CSB parameters u_0 and s_0, are fitted altogether. Only the lowest-order (s-wave) ISB terms are considered, i.e.,

$$v_{\rm Sky}^{\rm CIB}(\boldsymbol{r}_1, \boldsymbol{r}_2) = u_0\left(1 + z_0 P_\sigma\right)\delta\left(\boldsymbol{r}_1 - \boldsymbol{r}_2\right)\frac{\tau_{z1}\tau_{z2}}{2}, \tag{4.3.9}$$

$$v_{\rm Sky}^{\rm CSB}(\boldsymbol{r}_1, \boldsymbol{r}_2) = s_0\left(1 + y_0 P_\sigma\right)\delta\left(\boldsymbol{r}_1 - \boldsymbol{r}_2\right)\frac{\tau_{z1} + \tau_{z2}}{4}. \tag{4.3.10}$$

Accordingly, the EDFs for CIB and CSB terms, respectively, reads

$$E_{\rm CIB}[\rho_p, \rho_n] = \frac{u_0\left(1 - z_0\right)}{8}\int\left\{\left[\rho_n(\boldsymbol{r})\right]^2 + \left[\rho_p(\boldsymbol{r})\right]^2\right\}d\boldsymbol{r} - \frac{u_0\left(2 + z_0\right)}{4}\int\rho_n(\boldsymbol{r})\,\rho_p(\boldsymbol{r})\,d\boldsymbol{r}, \tag{4.3.11}$$

$$E_{\rm CSB}[\rho_p, \rho_n] = \frac{s_0\left(1 - y_0\right)}{8}\int\left\{\left[\rho_n(\boldsymbol{r})\right]^2 - \left[\rho_p(\boldsymbol{r})\right]^2\right\}d\boldsymbol{r}, \tag{4.3.12}$$

where y_0 and z_0 are fixed to -1 in order to choose the spin-singlet ($S = 0$) channel. On top of the criteria of the SAMi EDF, these parameters are determined to reproduce:

5. the difference between EoS of symmetric nuclear matter calculated by using the Brueckner-Hartree-Fock calculation with AV18 (with all the ISB) and that with AV14 (without any ISB);
6. the isobaric analog energy of ^{208}Pb, i.e., the difference between the energy of $T_+\left|{\rm GS}\ (^{208}{\rm Pb})\right\rangle$ and that of $\left|{\rm GS}\ (^{208}{\rm Pb})\right\rangle$.

Table 4.3.1: Parameters of nuclear EDFs used in this thesis. The column labelled "$\boldsymbol{J}^2$ term" shows whether an EDF includes terms proportional to $\boldsymbol{J}^2$ (or $\boldsymbol{J}_\tau^2$) terms in Eqs. (2.3.4) and (2.3.5). It is shown in Ref. [A6] that inclusion of higher order digits sometimes changes total energies in several hundred keV or even several MeV; hence, higher order digits are shown for SAMi, SAMi-J family, and SAMi-ISB EDFs.

EDF	Ref.	t_0 (MeV fm^3)	t_1 (MeV fm^5)	t_2 (MeV fm^5)	t_3 (MeV fm$^{3+3\alpha}$)
SAMi	[409, A6]	−1877.746	475.5856	−85.20021	10219.58
SAMi-ISB	[183, A6]	−2098.25926057	394.74785380	−136.42542569	11995.53445425
SAMi-J27	[80]	−1876.09248747	481.08696436	−75.70694486	10184.55799817
SAMi-J28	[80]	−1870.30493361	476.24730879	−84.16554935	10177.74833404
SAMi-J29	[80]	−1862.57379772	471.27736305	−92.75732183	10161.14697600
SAMi-J30	[80]	−1853.89031724	466.11918413	−101.44789804	10139.48620155
SAMi-J31	[80]	−1844.27720624	460.72707670	−110.20019054	10112.38573844
SAMi-J32	[80]	−1833.82867579	455.05556386	−118.96632705	10079.73609044
SAMi-J33	[80]	−1822.72219560	449.07889064	−127.70223044	10041.98183482
SAMi-J34	[80]	−1811.23828845	442.79531241	−136.37494217	10000.27971787
SAMi-J35	[80]	−1799.52785064	436.22855422	−144.97201879	9955.44893745
SLy4	[58]	−2488.91	486.82	−546.39	13777.0
SLy5	[58]	−2484.88	483.13	−549.40	13763.0
SkM*	[441]	−2645.0	410.0	−135.0	15595.0

EDF	x_0	x_1	x_2	x_3	α
SAMi	0.3197176	−0.5319419	−0.0137857	0.6883226	0.2561388
SAMi-ISB	0.24191448	−0.17115663	−0.47023944	0.32083902	0.22330040
SAMi-J27	0.48223516	−0.55796747	0.21306627	1.00219029	0.25463434
SAMi-J28	0.37750965	−0.53458574	0.00738936	0.79593525	0.25756335
SAMi-J29	0.23683612	−0.51022743	−0.16371407	0.52396994	0.26095431
SAMi-J30	0.10253195	−0.48490711	−0.30801242	0.26024444	0.26456747
SAMi-J31	−0.02370875	−0.45860777	−0.43125103	0.00764843	0.26837237
SAMi-J32	−0.14068697	−0.43132816	−0.53761676	−0.23166347	0.27231589
SAMi-J33	−0.24900560	−0.40306823	−0.63028346	−0.45865169	0.27633327
SAMi-J34	−0.34917314	−0.37382403	−0.71170996	−0.67399136	0.28034532
SAMi-J35	−0.44390823	−0.34355719	−0.78386127	−0.88242707	0.28432299
SLy4	0.834	−0.344	−1.000	1.354	0.16666667
SLy5	0.778	−0.328	−1.000	1.267	0.16666667
SkM*	0.09	0.0	0.0	0.0	0.16666667

EDF	W_0 (MeV fm^5)	W_0' (MeV fm^5)	s_0 (MeV fm^3)	u_0 (MeV fm^3)	y_0	z_0	$\boldsymbol{J}^2$ term
SAMi	137.0603	42.32571	0.0	0.0	0	0	Yes
SAMi-ISB	294.78455088	−367.38585650	−26.3	25.8	−1	−1	Yes
SAMi-J27	81.93712451	180.37249880	0.0	0.0	0	0	Yes
SAMi-J28	114.40184753	105.18198737	0.0	0.0	0	0	Yes
SAMi-J29	150.86952848	20.19905357	0.0	0.0	0	0	Yes
SAMi-J30	185.74392820	−60.95480119	0.0	0.0	0	0	Yes
SAMi-J31	216.87450141	−133.57040757	0.0	0.0	0	0	Yes
SAMi-J32	241.82278955	−192.32693655	0.0	0.0	0	0	Yes
SAMi-J33	259.33599380	−234.96445838	0.0	0.0	0	0	Yes
SAMi-J34	269.45212910	−261.61292885	0.0	0.0	0	0	Yes
SAMi-J35	273.60818500	−275.62529456	0.0	0.0	0	0	Yes
SLy4	123.0	123.0	0.0	0.0	0	0	No
SLy5	126.0	126.0	0.0	0.0	0	0	No
SkM*	130.0	130.0	0.0	0.0	0	0	No

Table 4.3.2: The saturation density ρ_0, the symmetry energy J, and its slope L of the SAMi EDF and the SAMi-J EDF family. This table is taken from Ref. [A6].

EDF	ρ_0 (fm^{-3})	J (MeV)	L (MeV)
SAMi-J27	0.1595	27.000	30.000
SAMi-J28	0.1587	28.000	39.742
SAMi-J29	0.1579	29.000	51.604
SAMi-J30	0.1571	30.000	63.178
SAMi-J31	0.1563	31.000	74.368
SAMi-J32	0.1555	32.000	85.101
SAMi-J33	0.1548	33.000	95.407
SAMi-J34	0.1542	34.000	105.307
SAMi-J35	0.1537	35.000	114.954
SAMi	0.1587	28.126	43.558
SAMi-noISB	0.1613	30.827	50.095
SAMi-ISB	0.1597	31.434	52.362

Table 4.3.3: List of nuclear EDFs used in this thesis. Here, the SAMi-noISB refers $E_{\rm IS}$ of the SAMi-ISB EDF. The parameters of the all EDFs shown here are summarized in Table 4.3.1. As for the SAMi-J family, x refers to 27, 28, ..., 35.

EDF	$E_{\rm IS}$	$E_{\rm CIB}$	$E_{\rm CSB}$
SAMi	SAMi	None	None
SAMi-noISB	SAMi-noISB	None	None
SAMi-CIB	SAMi-noISB	$u_0 = 26.3\,\text{MeV fm}^3$	None
SAMi-CSB	SAMi-noISB	None	$s_0 = -25.8\,\text{MeV fm}^3$
SAMi-ISB	SAMi-noISB	$u_0 = 26.3\,\text{MeV fm}^3$	$s_0 = -25.8\,\text{MeV fm}^3$
SAMi-Jx	SAMi-Jx	None	None
SLy4	SLy4	None	None
SLy5	SLy5	None	None
SkM*	SkM*	None	None

Criterion 5 constrains u_0. Eventually, the parameters of the SAMi-ISB EDF are given in Table 4.3.1. Because all the parameters are fitted altogether, the parameters for $E_{\rm IS}$ in the SAMi-ISB EDF are different from those in the SAMi EDF, as one can see in Table 4.3.1. Not to make any confusion, $E_{\rm IS}$ for the SAMi-ISB EDF is called the SAMi-noISB EDF. These abbreviations are summarized in Table 4.3.3.

In this chapter, in order to see how the CIB term affects nuclear properties, on top of the SAMi-noISB EDF, the CIB strength u_0 is gradually changed from $0\,\text{MeV fm}^3$ to $50\,\text{MeV fm}^3$ with keeping the CSB strength $s_0 = 0\,\text{MeV fm}^3$. Also, to see the effects of the CSB term, on top of the SAMi-noISB EDF, the CSB strength $-s_0$ is gradually changed from $0\,\text{MeV fm}^3$ to $50\,\text{MeV fm}^3$ with keeping the CIB strength $u_0 = 0\,\text{MeV fm}^3$.

Before closing this section, let me discuss the parameters y_0 and z_0. There are two Skyrme ISB EDF other than the SAMi-ISB EDF: One is by Bączyk *et al.* [185, 187] and the other is by Dong *et al.* [184, 437, 438]. Both works consider only the s-wave interaction similar to the SAMi-ISB EDF. The former uses $y_0 = z_0 = 0$ and the isotensor operator ($a = 1$ and $b = 3$) for the CIB operator with the Hartree approximation; the latter uses $y_0 = z_0 = 1$, while the Wigner interaction is not considered, i.e., $v_{\rm ISB} \sim P_\sigma$. In the case of the CSB interaction, whichever approximation is used, the Hartree approximation or the Hartree-Fock one, y_0 only gives a scaling of s_0 since the density dependence of $\mathcal{E}^{\rm H}_{\rm CSB}$ and that of $\mathcal{E}^{\rm x}_{\rm CSB}$ are identical. In the case of the CIB interaction, if one uses the Hartree approximation, z_0 gives a scaling of u_0 and does not change any results; if one uses the Hartree-Fock approximation, z_0 gives a difference. The CIB Fock energy density, $\mathcal{E}^{\rm x}_{\rm CIB}$, is the isospin symmetric, and thus this difference can be absorbed fully in the IS Fock energy density $\mathcal{E}^{\rm x}_{\rm IS}$.

4.3.2 Neutron-Skin Thickness

The neutron-skin thickness ΔR_{np} is defined by the difference between the neutron radius R_n and the proton one R_p,

$$\Delta R_{np} := R_n - R_p, \tag{4.3.13}$$

where R_τ ($\tau = n$, p) is the root-mean-square radius

$$R_\tau^2 = \int \rho_\tau(\boldsymbol{r})\, r^2\, d\boldsymbol{r}. \tag{4.3.14}$$

It is known that neutron-skin thickness predicted by EDFs are strongly correlated to the symmetry parameter L associated with the EDFs [59, 442, 443]. This is because R_p obtained by EDFs are almost identical because of fitting protocols, while R_n are not; hence, different EDF gives different R_n. As shown in Eq. (1.3.4), the pressure is proportional to L in the lowest order, and larger pressure makes neutron distribution extend more. Accordingly, larger L gives larger R_n and therefore ΔR_{np}. Indeed, Ref. [59] shows that ΔR_{np} has a strong linear correlation with L.

Coulomb Effects on Neutron-Skin Thickness

First, we shall show how the different treatment of the Coulomb interaction affects the neutron-skin thickness. In order to see the L dependence of ΔR_{np}, the SAMi EDF and the SAMi-J EDF family are used to calculate ΔR_{np} of ^{16}O, ^{40}Ca, ^{48}Ca, ^{48}Ni, and ^{208}Pb. The different Coulomb treatments shown in Eqs. (4.3.1)–(4.3.6) are used, and the ISB terms are not considered. The obtained ΔR_{np} are fitted to

$$\Delta R_{np} = a + bL, \tag{4.3.15}$$

where fitting parameters are shown in Table 4.3.4. Panels (a) of Figs. 4.3.1–4.3.5 show the ΔR_{np} as functions of L, and panels (b) show deviations from ΔR_{np} calculated with the Coulomb LDA. In Figs. 4.3.3 and 4.3.5, experimental data and their error for ^{48}Ca ($0.168^{+0.025}_{-0.028}$ fm [444]) and ^{208}Pb ($\Delta R_{np} = 0.211^{+0.054}_{-0.063}$ fm [73], 0.283 ± 0.071 fm [92], and the reanalyzed data of PREX-II experiment $\Delta R_{np} = 0.190 \pm 0.020$ fm [94]) are shown as vertical arrows. The experimental value of ΔR_{np} for ^{40}Ca is $\Delta R_{np} = -0.010^{+0.022}_{-0.023}$ fm [444], which is not shown in Fig. 4.3.2 due to the range.

In $N = Z$ nuclei, if neither the Coulomb interaction nor the ISB terms of the nuclear interaction are considered, $\rho_n \equiv \rho_p$ and $R_n = R_p$, i.e., $\Delta R_{np} = 0$, holds for whatever value of L due to the isospin symmetry. Once the Coulomb interaction is considered, because of the Coulomb repulsion, the proton density distribution extends. Accordingly, ΔR_{np} becomes negative, which means $N = Z$ nuclei have proton skins. Since non-zero ΔR_{np} in $N = Z$ nuclei originates from the Coulomb interaction, ΔR_{np} hardly depends on L, and the order of b is, indeed, $10^{-5}\,\mathrm{MeV\,fm^{-1}}$, which is two orders of magnitude smaller than $N > Z$ nuclei.

In $N > Z$ nuclei, even if only the isospin symmetric nuclear interaction is considered, i.e., neither the Coulomb interaction nor the ISB terms of the nuclear interaction are considered, R_n can be larger than R_p, for instance, $R_n = 3.594$ fm and $R_p = 3.380$ fm for ^{48}Ca, and ΔR_{np} depends on properties of the nuclear interaction, such as L. If one sees the mirror nuclei pair, such as ^{48}Ca and ^{48}Ni, ρ_p (ρ_n) of an atomic nucleus is identical to ρ_n (ρ_p) of its mirror nucleus. Hence, the neutron-skin thickness has the same absolute value but with the opposite signs. Once the Coulomb interaction is considered, ρ_p extends slightly, while ρ_n hardly changes. As a result, ΔR_{np}, i.e., a and b, for ^{48}Ni deviates from $-\Delta R_{np}$, i.e., $-a$ and $-b$, for ^{48}Ca slightly.

It can also be found that different treatments of the Coulomb interaction give almost the same L dependence, i.e., b, while the absolute value of a changes slightly. As discussed in Chap. 3, different treatments of the Coulomb interaction gives the similar ρ_p and ρ_n, and gross structures of ρ_p and ρ_n are mainly determined by E_{IS}. Therefore, the absolute value of R_p, and consequently ΔR_{np}, change by less than 0.01 fm due to the different treatment of the Coulomb interaction, while ρ_n, i.e., R_n, does not change, and accordingly a changes. In addition, different treatment of the Coulomb interaction mainly changes the surface region of ρ_p. It was shown in Ref. [445] that the surface structure of the density hardly changes the L dependence of ΔR_{np}. Consequently, b does not change.

Next, we focus on the change of a in more detail. The Coulomb exchange interaction effectively makes the Coulomb repulsion weaker. Therefore, once the Coulomb exchange interaction is neglected (see NoEx),

Table 4.3.4: Parameters a and b in Eq. (4.3.15). See the text for more detail. This table is taken from Ref. [A6].

Nuclei	Coulomb	a (fm)	b (MeV fm^{-1})
^{16}O	NoEx	−0.029353	0.00001469
	LDA	−0.023886	0.00001274
	GGA	−0.023782	0.00001283
	p-fin	−0.021061	0.00001097
	pn-fin	−0.021098	0.00001192
	All	−0.021278	0.00001192
^{40}Ca	NoEx	−0.053942	0.00003132
	LDA	−0.048232	0.00002847
	GGA	−0.048001	0.00002903
	p-fin	−0.044467	0.00002712
	pn-fin	−0.044467	0.00002712
	All	−0.044879	0.00002843
^{48}Ca	NoEx	0.104330	0.00144605
	LDA	0.108463	0.00144801
	GGA	0.108747	0.00144866
	p-fin	0.111525	0.00144897
	pn-fin	0.111554	0.00144857
	All	0.111254	0.00144857
^{48}Ni	NoEx	−0.238189	−0.00129505
	LDA	−0.229357	−0.00130689
	GGA	−0.229163	−0.00130595
	p-fin	−0.223682	−0.00131776
	pn-fin	−0.223767	−0.00131670
	All	−0.224293	−0.00131690
^{208}Pb	NoEx	0.069984	0.00167210
	LDA	0.073847	0.00168003
	GGA	0.074152	0.00168124
	p-fin	0.077225	0.00168631
	pn-fin	0.077268	0.00168528
	All	0.076585	0.00168461

the Coulomb repulsion becomes effectively stronger and thus ρ_p extends. Accordingly, R_p becomes larger; that is, ΔR_{np} becomes smaller. Even if the Coulomb exchange EDF is changed from LDA to GGA, both R_p and R_n change in a similar order, as discussed in Chap. 3. Hence, ΔR_{np} hardly changes. The proton finite-size effect makes the Coulomb repulsion weaker. Thus, ρ_p shrinks, and accordingly, R_p becomes smaller. In contrast, the vacuum polarization makes the Coulomb repulsion stronger. Thus, ρ_p extends, and accordingly, R_p becomes larger. As discussed in Chap. 3, the proton finite-size effect and the vacuum polarization change R_n less than R_p. Hence, they change ΔR_{np} larger and smaller, respectively.

The neutron finite-size effect is quite small. Thus, it does not matter for discussion of ΔR_{np}, while its behaviour can be understood as follows: Once the neutron finite-size effect is considered, neutrons are also affected by the Coulomb interaction. In order to discuss the effect of the neutron finite size on ΔR_{np}, the effective charge formalism is introduced to implement the finite-size effect simply. Here, the effective charge of protons and neutrons are denoted by $e_{\mathrm{eff}p} > 0$ and $e_{\mathrm{eff}n} < 0$, respectively, where the negative effective charge of neutrons comes from the fact that the mean-square radius of neutron charge distribution is negative. Since the neutron effective charge is negative, proton-neutron attractive interaction is induced. Therefore, it seems that ΔR_{np} can become smaller. However, at the same time, ρ_{ch} shrinks, and accordingly, $V_{\mathrm{C}p}$ becomes larger, i.e., the Coulomb potential for protons becomes more repulsive than only with the proton finite-size effect, as shown in Fig. 3.4.3. The Coulomb potential for neutron $V_{\mathrm{C}n}$ is also repulsive in the internal region, while it is attractive in the surface region, as seen in Fig. 3.4.3(a). Eventually, the Coulomb potential for

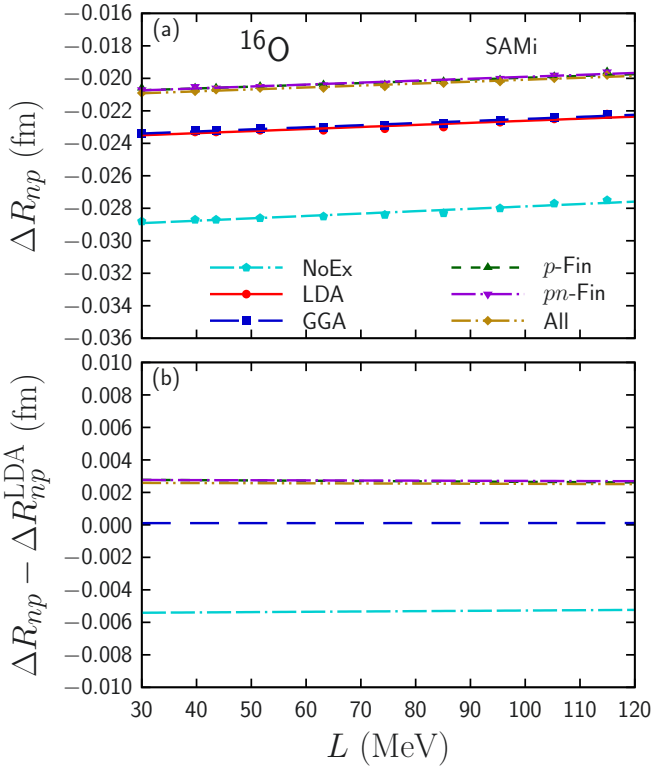

Figure 4.3.1: (a) Neutron-skin thickness ΔR_{np} of ^{16}O as functions of L calculated by using different treatments of the Coulomb interaction. (b) Difference between neutron-skin thickness and that calculated with the Coulomb LDA. This figure is taken from Ref. [A6].

neutron makes ρ_n extended and R_n larger. Therefore, the neutron-finite size effects on ΔR_{np} is complicated, while, in total, the change of ΔR_{np} due to the neutron finite-size effect is invisible.

At last, we shall estimate how large different treatments of the Coulomb interaction affect the estimation of L value by using ΔR_{np} in ^{208}Pb. Since the linear correlation is almost perfect ($r \approx 1.000$), uncertainty due to the fitting is neglected. The PREX-II value of $\Delta R_{np} = 0.283 \pm 0.071$ fm [92] is taken as an example. If one uses the Coulomb LDA exchange EDF, the estimated value of L is $L = 124 \pm 42$ MeV by using Eq. (4.3.13) and Table 4.3.4, while if one considers all the corrections to the Coulomb interaction, the estimated value of L is $L = 123 \pm 42$ MeV. Therefore, the treatment of the Coulomb interaction does not matter for the estimation of L.

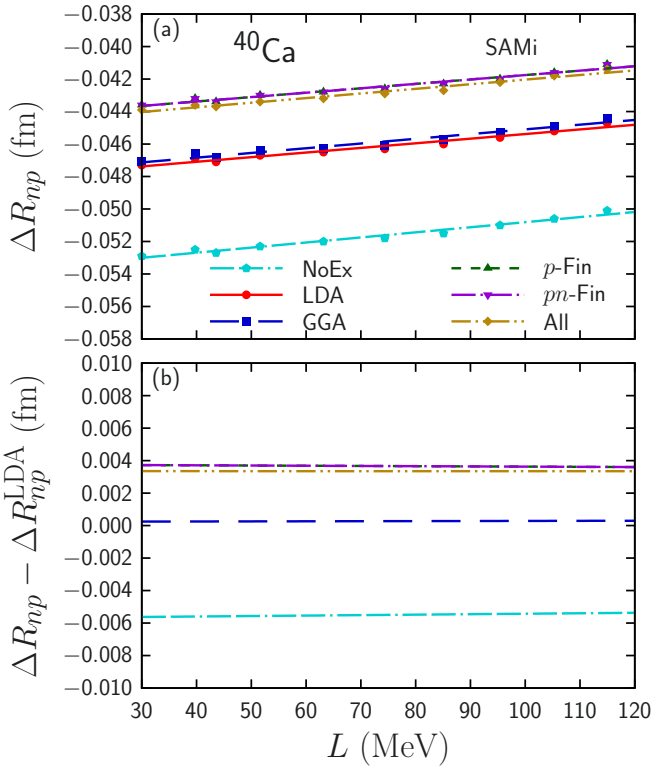

Figure 4.3.2: Same as Fig. 4.3.1 but for ^{40}Ca.

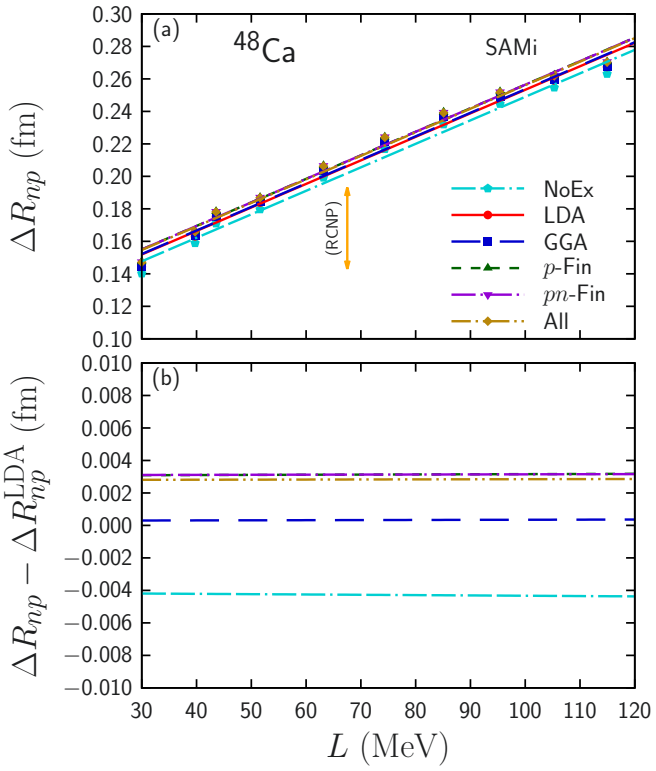

Figure 4.3.3: Same as Fig. 4.3.1 but for ^{48}Ca. The experimental data of ΔR_{np} ($0.168^{+0.025}_{-0.028}$ fm [444]) is also shown as a vertical arrow.

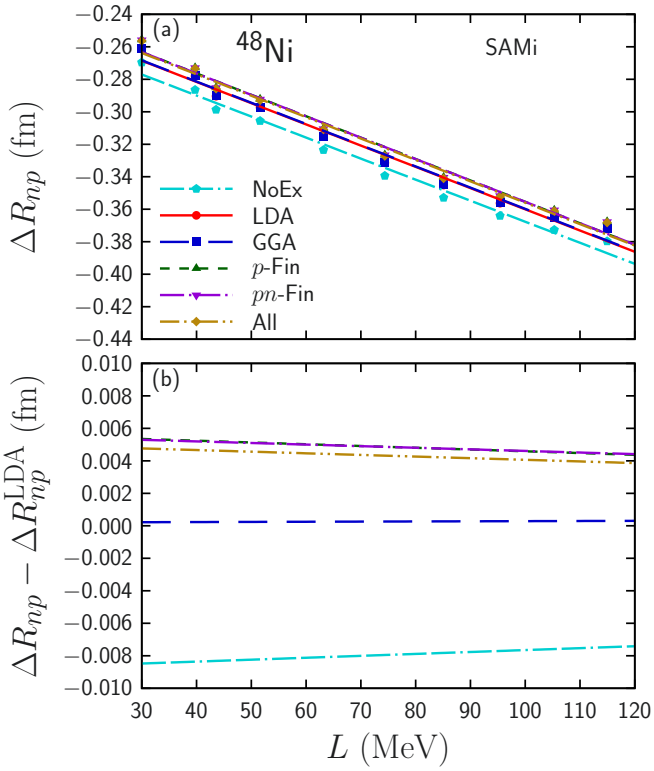

Figure 4.3.4: Same as Fig. 4.3.1 but for ^{48}Ni.

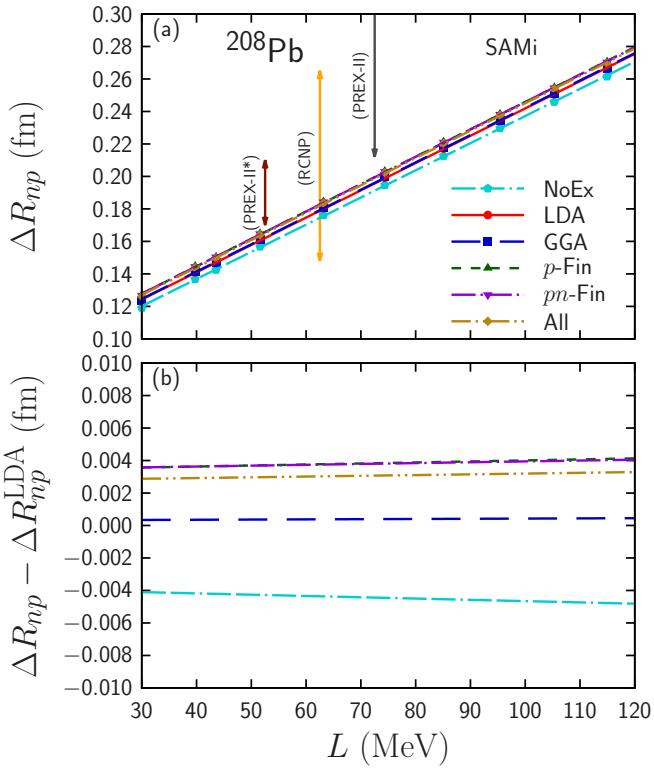

Figure 4.3.5: Same as Fig. 4.3.1 but for ^{208}Pb. The experimental data of ΔR_{np} ($\Delta R_{np} = 0.211^{+0.054}_{-0.063}$ fm [73], 0.283 ± 0.071 fm [92], and the reanalyzed data of PREX-II experiment $\Delta R_{np} = 0.190 \pm 0.020$ fm [94]) are also shown as vertical arrows.

Comparison between Coulomb and Isospin Symmetry Breaking Interactions

Next, two isospin symmetry breaking effects—the Coulomb interaction and the ISB terms of the nuclear interaction—are compared. Figures 4.3.6–4.3.10 show ΔR_{np} of the selected nuclei calculated with the SAMi, SAMi-noISB, SAMi-CIB, SAMi-CSB, and SAMi-ISB EDFs and with the proposed treatment of the Coulomb interaction. In order to see results more effectively, ΔR_{np} of ^{40}Ca, ^{48}Ca, and ^{208}Pb calculated without the Coulomb exchange (NoCx), with the Coulomb LDA (LDA), and with all the precise treatments of the Coulomb interaction (All) are also shown in Table 4.3.5.

In $N = Z$ nuclei, the SAMi-noISB and SAMi EDFs give almost the same ΔR_{np}, while the SAMi-ISB EDF gives different values. Since EoS properties of SAMi-noISB are different from those of SAMi. As a result, ρ_n and ρ_p given by the SAMi can be different from those given by the SAMi-noISB. However, as discussed in the previous section, in $N = Z$ nuclei, ΔR_{np} is mainly formed by the Coulomb interaction and does not depend on L. Therefore, the SAMi-noISB and SAMi EDFs give almost the same ΔR_{np}. In contrast, the SAMi-ISB EDF gives smaller ΔR_{np} in $N = Z$ nuclei, because of the existence of the ISB terms, which forms ΔR_{np} due to the same mechanism as the Coulomb interaction. Its effect is approximately 0.02 fm, which is mainly due to the CSB term. The CIB contribution to ΔR_{np} in ^{40}Ca is 0.0002 fm, which is one order of magnitude smaller than the dependence on the treatment of the Coulomb interaction.

In $N > Z$ nuclei, the SAMi-noISB EDF gives a larger ΔR_{np} than the SAMi EDF. This may be because the SAMi-noISB EDF gives a larger L than the SAMi EDF. The difference of L is approximately 6.5 MeV, and the corresponding differences of ΔR_{np} are approximately 0.01 fm in ^{48}Ca and ^{208}Pb, which is much smaller than the difference between ΔR_{np} obtained by the SAMi EDF and that by the SAMi-noISB EDF. The further difference may be due to other EoS (or EDF) properties, such as J, which can also be different due to the *indirect* effect of the ISB terms. In ^{48}Ni, the behaviour is opposite to ^{48}Ca, which is also discussed above.

Comparing results obtained by the SAMi-noISB and SAMi-ISB EDFs, in both $N > Z$ and $N < Z$ nuclei, one can find that the ISB terms decrease ΔR_{np} by 0.02–0.05 fm, where both the CSB and CIB terms contribute to ΔR_{np}. In $N > Z$ nuclei, the CIB contribution makes ΔR_{np} larger, while the CSB one makes it smaller; in $N < Z$ nuclei, both the CIB contribution and CSB one make it smaller. The CIB contributions to ΔR_{np} in ^{48}Ca and ^{208}Pb are approximately 0.005 fm, which are the same order of magnitude but slightly larger than the dependence on the treatment of the Coulomb interaction. In contrast, the CSB contributions to ΔR_{np} in ^{48}Ca and ^{208}Pb are approximately -0.03 fm, which are much larger than the dependence on the treatment of the Coulomb interaction. A more detailed discussion of ISB terms will be given later.

In ^{16}O, ^{40}Ca, ^{48}Ca, and ^{48}Ni, dependences on the treatment of the Coulomb interaction, even the existence of the Coulomb exchange term, of ΔR_{np} are much smaller than that of the ISB terms. Only the exception is ^{208}Pb: ΔR_{np} obtained by the SAMi-ISB EDF without the Coulomb exchange term (NoEx) has almost the same value as that by the SAMi EDF with the Coulomb LDA exchange term (LDA); ΔR_{np} obtained by the SAMi-ISB EDF with the Coulomb LDA or GGA exchange term (LDA or GGA) without finite-size effect is almost the same value as that by the SAMi EDF with finite-size effects (p-fin or pn-fin). In Refs. [175, 177, 432], it was claimed that the Coulomb exchange term is mainly cancelled with the CSB term of the nuclear interaction (or further correction of the Coulomb interaction). According to Figs. 4.3.6–4.3.10, this cancellation sometimes holds, such as in ^{208}Pb, while usually does not hold. Therefore, such treatment with expecting such cancellation is not appropriate for general calculation.

Isospin Symmetry Breaking Terms and Neutron-Skin Thickness

At the last of this subsection, dependences on the ISB terms of ΔR_{np} are discussed. Figures 4.3.11–4.3.15 show dependences on the CSB strength $-s_0$ and CIB one u_0 on the neutron-skin thickness ΔR_{np} for the selected nuclei, where the SAMi-noISB EDF is used for $E_{\rm IS}$ and the Coulomb LDA EDF is used for the Coulomb interaction. For comparison, ΔR_{np} calculated with the SAMi is shown as an empty arrow; that with the SAMi-ISB, i.e., the SAMi-noISB with $s_0 = -26.3\,\mathrm{MeV\,fm^3}$ and $u_0 = 25.8\,\mathrm{MeV\,fm^3}$, is shown as a filled arrow. The CSB and CIB dependences of ΔR_{np} are fitted to

$$\Delta R_{np} = c + d\,(-s_0)\,, \tag{4.3.16}$$

$$\Delta R_{np} = e + f u_0, \tag{4.3.17}$$

Table 4.3.5: Neutron-skin thickness ΔR_{np} of ^{40}Ca, ^{48}Ca, and ^{208}Pb and mass difference of the mirror nuclei pair ^{48}Ca and ^{48}Ni, $\Delta E_{\rm tot}$, calculated by using SAMi-ISB EDF without Coulomb exchange term (NoCx), with Coulomb LDA (LDA), or with full Coulomb treatment (All) without ISB term, only with CSB term, only with CIB term, and with all ISB terms. For comparison, ΔR_{np} and $\Delta E_{\rm tot}$ calculated with the SAMi EDF are also shown. This table is taken from Ref. [A6].

	$E_{\rm IS}$		SAMi	SAMi-noISB			
	$E_{\rm ISB}$		No ISB	No ISB	CIB	CSB	All ISB
^{40}Ca	R_p (fm)	NoCx	3.3971	3.3644	3.3762	3.3770	3.3886
		LDA	3.3895	3.3568	3.3686	3.3694	3.3810
		All	3.3850	3.3522	3.3639	3.3648	3.3763
	R_p (fm)	NoCx	3.3444	3.3130	3.3250	3.3003	3.3126
		LDA	3.3424	3.3108	3.3228	3.2982	3.3104
		All	3.3413	3.3096	3.3215	3.2970	3.3091
	ΔR_{np} (fm)	NoCx	−0.0527	−0.0514	−0.0512	−0.0767	−0.0760
		LDA	−0.0471	−0.0460	−0.0458	−0.0712	−0.0706
		All	−0.0437	−0.0426	−0.0424	−0.0678	−0.0672
^{48}Ca	R_p (fm)	NoCx	3.4421	3.3945	3.4067	3.4014	3.4134
		LDA	3.4359	3.3881	3.4003	3.3951	3.4070
		All	3.4320	3.3840	3.3962	3.3910	3.4030
	R_n (fm)	NoCx	3.6131	3.6244	3.6399	3.6071	3.6226
		LDA	3.6111	3.6221	3.6376	3.6050	3.6203
		All	3.6101	3.6209	3.6363	3.6037	3.6190
	ΔR_{np} (fm)	NoCx	0.1710	0.2299	0.2332	0.2057	0.2092
		LDA	0.1752	0.2340	0.2373	0.2099	0.2133
		All	0.1781	0.2369	0.2401	0.2127	0.2160
^{208}Pb	R_p (fm)	NoCx	5.4692	5.4396	5.4591	5.4386	5.4578
		LDA	5.4616	5.4318	5.4512	5.4309	5.4500
		All	5.4567	5.4269	5.4463	5.4260	5.4452
	R_n (fm)	NoCx	5.6117	5.6059	5.6330	5.5776	5.6046
		LDA	5.6083	5.6021	5.6291	5.5739	5.6008
		All	5.6064	5.6000	5.6269	5.5718	5.5986
	ΔR_{np} (fm)	NoCx	0.1425	0.1663	0.1739	0.1390	0.1468
		LDA	0.1467	0.1703	0.1779	0.1430	0.1508
		All	0.1497	0.1731	0.1806	0.1458	0.1534
^{48}Ca-^{48}Ni	^{48}Ca $E_{\rm tot}$ (MeV)	NoCx	−408.1636	−414.3409	−405.5041	−418.6020	−409.7030
		LDA	−415.6148	−421.8979	−413.0343	−426.1437	−417.2186
		All	−417.0041	−423.3531	−414.4749	−427.5868	−418.6476
	^{48}Ni $E_{\rm tot}$ (MeV)	NoCx	−341.7722	−349.4207	−340.8851	−346.1802	−337.6926
		LDA	−352.6388	−360.2735	−351.6879	−356.9761	−348.4383
		All	−355.3307	−362.9521	−354.3332	−359.6170	−351.0464
	$\Delta E_{\rm tot}$ (MeV)	NoCx	66.3915	64.9202	64.6190	72.4218	72.0104
		LDA	62.9760	61.6243	61.3465	69.1677	68.7803
		All	61.6734	60.4010	60.1418	67.9699	67.6012

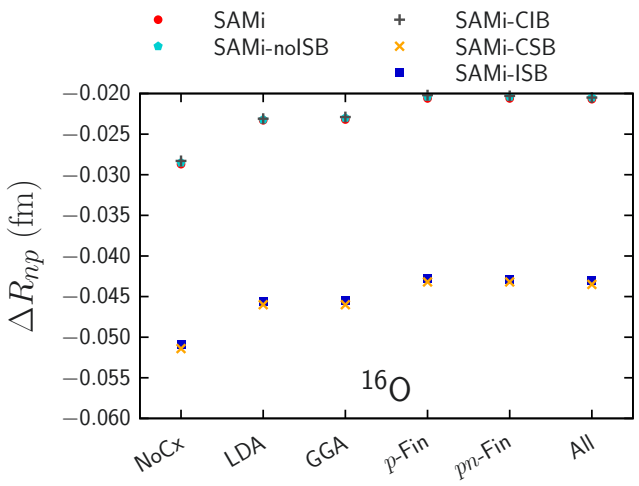

Figure 4.3.6: Comparison of ΔR_{np} for ^{16}O calculated by using the SAMi, SAMi-noISB, SAMi-CIB, SAMi-CSB, and SAMi-ISB EDFs and with several treatments of the Coulomb interaction. This figure is taken from Ref. [A6].

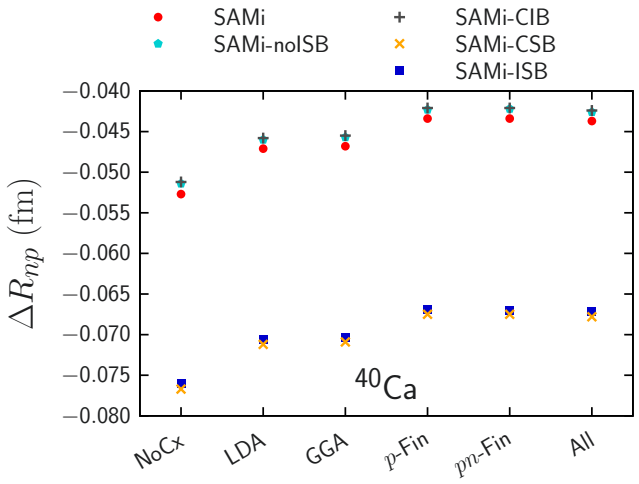

Figure 4.3.7: Same Fig. 4.3.6 but for ^{40}Ca.

respectively. The parameters c, d, e, and f are shown in Table 4.3.6. Since their correlations are almost perfect ($r \approx 1.000$) and their uncertainties are quite small, we do not show their uncertainties.

In $N = Z$ nuclei, the CIB term of the nuclear interaction does not change ΔR_{np}, while it increases ΔR_{np} in $N > Z$ nuclei. The change of ΔR_{np}, i.e., f, in ^{48}Ni has almost the same absolute value but the opposite sign to that in its mirror nuclei ^{48}Ca. In contrast, the CSB term decreases ΔR_{np} in all the selected nuclei, and the values of d are quite similar among the selected nuclei. In addition, d is 100 times (in $N = Z$ nuclei) or 5–10 times (in $N \neq Z$ nuclei) larger than the change due to the CIB term, f.

In order to understand this behaviour, first, the CSB two-body interaction is considered. The CSB two-body interaction for proton-proton (pp), proton-neutron (pn), and neutron-neutron (nn) are

$$v_{\mathrm{CSB}}^{pp}(\boldsymbol{r}) = +\frac{|s_0|}{2}(1 - P_\sigma)\,\delta(\boldsymbol{r}), \tag{4.3.18}$$

$$v_{\mathrm{CSB}}^{pn}(\boldsymbol{r}) = 0, \tag{4.3.19}$$

$$v_{\mathrm{CSB}}^{nn}(\boldsymbol{r}) = -\frac{|s_0|}{2}(1 - P_\sigma)\,\delta(\boldsymbol{r}), \tag{4.3.20}$$

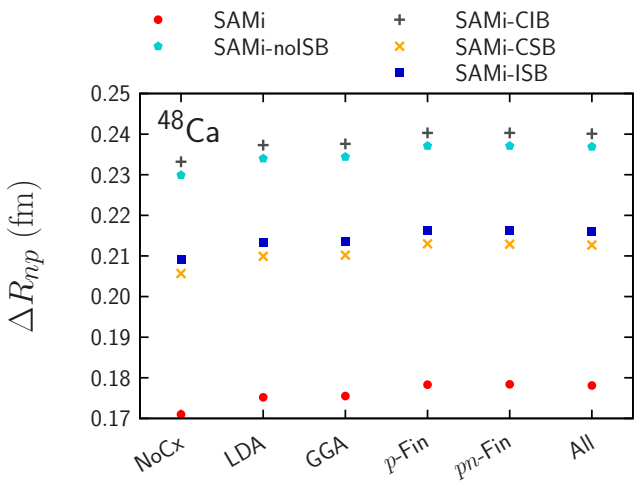

Figure 4.3.8: Same Fig. 4.3.6 but for ^{48}Ca.

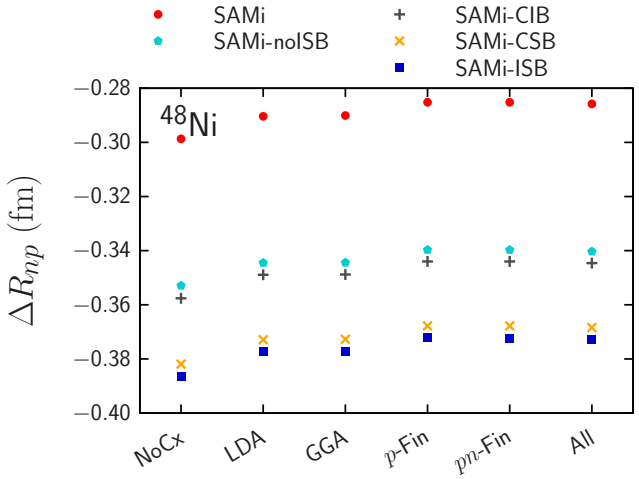

Figure 4.3.9: Same Fig. 4.3.6 but for ^{48}Ni.

respectively ($s_0 < 0$). As $|s_0|$ becomes larger, the repulsive $v^{pp}_{\rm CSB}$ and attractive $v^{nn}_{\rm CSB}$ become stronger. Hence, ρ_p extends and ρ_n shrinks more, i.e., R_p and R_n become, respectively, larger and smaller. Consequently, ΔR_{np} becomes smaller.

The pp, pn, and nn CIB two-body interactions are

$$v^{pp}_{\rm CIB}(\boldsymbol{r}) = +\frac{u_0}{2}(1-P_\sigma)\,\delta(\boldsymbol{r}), \tag{4.3.21}$$

$$v^{pn}_{\rm CIB}(\boldsymbol{r}) = -\frac{u_0}{2}(1-P_\sigma)\,\delta(\boldsymbol{r}), \tag{4.3.22}$$

$$v^{nn}_{\rm CIB}(\boldsymbol{r}) = +\frac{u_0}{2}(1-P_\sigma)\,\delta(\boldsymbol{r}), \tag{4.3.23}$$

respectively ($u_0 > 0$). As u_0 becomes larger, the repulsive $v^{pp}_{\rm CIB}$ and $v^{nn}_{\rm CIB}$ and attractive $v^{pn}_{\rm CIB}$ become stronger. Thus, it is rather difficult to understand the behaviour by using the two-body interaction. Instead, here, the effective potential of the CIB interaction is considered. The effective CIB potentials for protons and neutrons

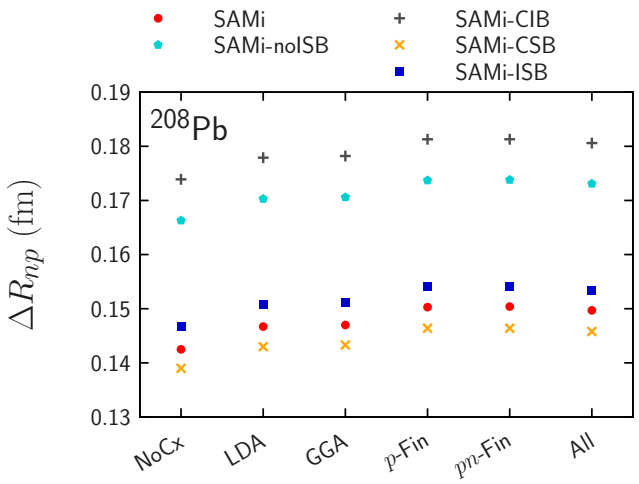

Figure 4.3.10: Same Fig. 4.3.6 but for ^{208}Pb.

read

$$V_{\mathrm{CIB}p}(\boldsymbol{r}) = \frac{\delta E_{\mathrm{CIB}}[\rho_p, \rho_n]}{\delta \rho_p(\boldsymbol{r})} = \frac{u_0}{2}\rho_p(\boldsymbol{r}) - \frac{u_0}{4}\rho_n(\boldsymbol{r}), \tag{4.3.24}$$

$$V_{\mathrm{CIB}n}(\boldsymbol{r}) = \frac{\delta E_{\mathrm{CIB}}[\rho_p, \rho_n]}{\delta \rho_n(\boldsymbol{r})} = \frac{u_0}{2}\rho_n(\boldsymbol{r}) - \frac{u_0}{4}\rho_p(\boldsymbol{r}), \tag{4.3.25}$$

respectively. In the case of $N = Z$ nuclei, $\rho_p \equiv \rho_n$ approximately holds; hence, $V_{\mathrm{CIB}p} \equiv V_{\mathrm{CIB}n} \equiv u_0\rho_p/4$ also approximately holds. This fact leads to that as u_0 becomes larger, both ρ_p and ρ_n extend and accordingly both R_p and R_n become larger. Their changes are almost the same, and accordingly, its difference, i.e., ΔR_{np}, hardly changes. In contrast, in the case of $N > Z$ nuclei, in general $\rho_p(\boldsymbol{r}) < \rho_n(\boldsymbol{r})$ holds, and consequently,

$$V_{\mathrm{CIB}n}(\boldsymbol{r}) - V_{\mathrm{CIB}p}(\boldsymbol{r}) = \frac{3u_0}{4}[\rho_n(\boldsymbol{r}) - \rho_p(\boldsymbol{r})] > 0 \tag{4.3.26}$$

holds. This means that the repulsive CIB potential for neutron is stronger than the CIB potential for protons, or the CIB potential for proton can be even attractive. Therefore, as u_0 becomes larger, ρ_n extends more and R_n becomes larger, while ρ_p extends less than ρ_n, or even shrinks, and R_n becomes larger but less than R_p, or even smaller. As a result, ΔR_{np} becomes larger as u_0 becomes larger. In the case of ^{48}Ni, all the discussion for ^{48}Ca holds but with opposite direction.

As shown in Table 4.3.5, the difference between ΔR_{np} calculated without ISB and that only with CSB is almost the same as the difference between ΔR_{np} calculated only with CIB and that with all ISB. This means that the CIB and CSB interactions are not entangled with each other on ΔR_{np}.

At last, we shall estimate how large ISB terms of the nuclear interaction affects the estimation of L value using ΔR_{np} in ^{208}Pb. Since the linear correlation is almost complete ($r \approx 1.000$), uncertainty due to the fitting is not considered. If $-s_0$ or u_0 independently changes by 10 MeV fm^3, ΔR_{np} changes by -0.010 fm and $+0.003$ fm, which corresponds to -6.1 MeV and $+1.7$ MeV in L, respectively. If the SAMi-ISB strengths for s_0 and u_0, $s_0 = -26.3$ MeV fm^3 and $u_0 = +25.8$ MeV fm^3, are taken as examples, ΔR_{np} changes by -0.0195 fm in total, and accordingly, L changes by -11.6 MeV if one uses Eq. (4.3.15) and values shown in Table 4.3.4. Indeed, Eq. (4.3.15) and its parameters shown in Table 4.3.4 do not include any effects of the ISB terms. Once effects of the ISB terms are considered for the fitting, Table 4.3.4, especially the parameter a, may change. In addition, the L parameter itself also includes the effect of the CIB term, while it does not include the effects of the CSB term. Hence, it is indispensable to find a simple quantity that can characterize EoS properties and include both CIB and CSB terms, and find such a correlation. This remains for a future perspective.

Table 4.3.6: Parameters c, d, e, and f in Eqs. (4.3.16) and (4.3.17). This table is taken from Ref. [A6].

Nuclei	ISB	c or e (fm)	d or f (MeV^{-1} fm^{-2})
^{16}O	CSB	−0.023145	−0.00087127
	CIB	−0.023168	0.00000455
^{40}Ca	CSB	−0.045923	−0.00096055
	CIB	−0.045986	0.00000927
^{48}Ca	CSB	0.233945	−0.00091309
	CIB	0.233977	0.00012818
^{48}Ni	CSB	−0.344227	−0.00109382
	CIB	−0.344459	−0.00017291
^{208}Pb	CSB	0.170209	−0.00103236
	CIB	0.170300	0.00029200

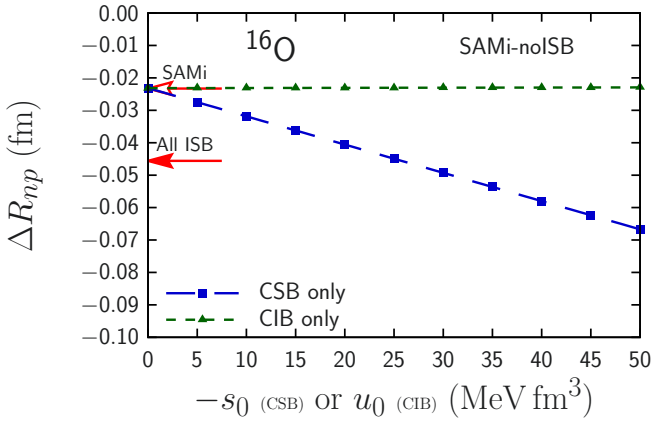

Figure 4.3.11: Dependences on CSB and CIB strength, $-s_0$ and u_0, of ΔR_{np} of ^{16}O on top of the SAMi-noISB EDF and the Coulomb LDA exchange EDF. The neutron-skin thickness ΔR_{np} calculated with the SAMi and SAMi-ISB EDFs are shown in empty and filled arrows, respectively. This figure is taken from Ref. [A6].

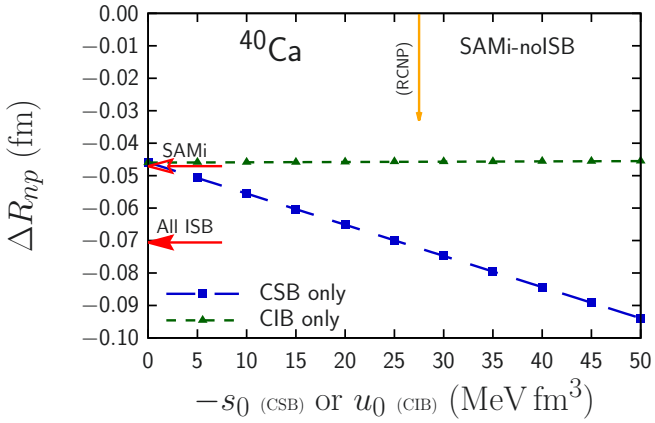

Figure 4.3.12: Same as Fig. 4.3.11 but for ^{40}Ca. The experimental data of ΔR_{np} ($-0.010^{+0.022}_{-0.023}$ fm [444]) is also shown as a vertical arrow.

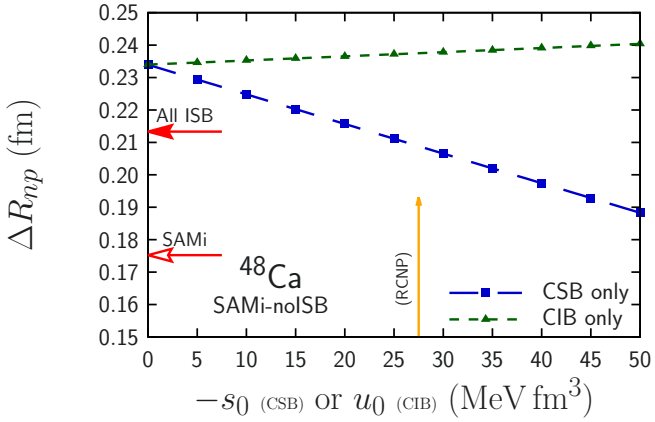

Figure 4.3.13: Same as Fig. 4.3.11 but for ^{48}Ca. The experimental data of ΔR_{np} ($0.168^{+0.025}_{-0.028}$ fm [444]) is also shown as a vertical arrow.

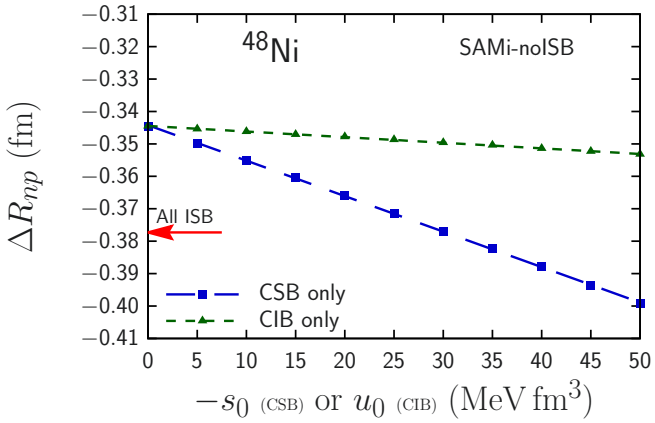

Figure 4.3.14: Same as Fig. 4.3.11 but for ^{48}Ni.

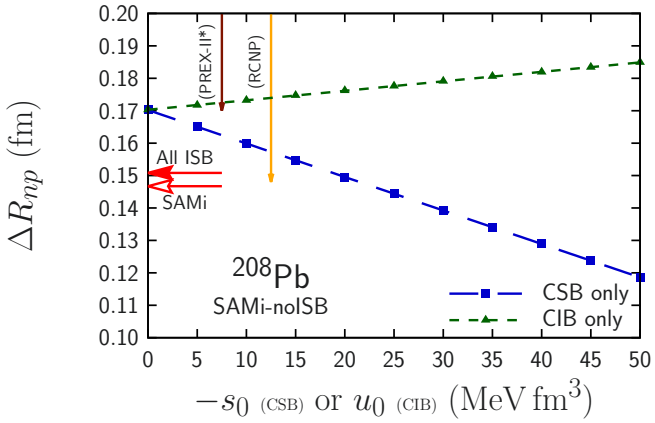

Figure 4.3.15: Same as Fig. 4.3.11 but for ^{208}Pb. The experimental data of ΔR_{np} ($\Delta R_{np} = 0.211^{+0.054}_{-0.063}$ fm [73] and the reanalyzed data of PREX-II experiment $\Delta R_{np} = 0.190 \pm 0.020$ fm [94]) are also shown as vertical arrows.

4.3.3 Masses of Mirror Nuclei

In this subsection, we shall discuss the mass difference of a mirror nuclei pair. Here, the ^{48}Ca-^{48}Ni pair is taken as an example, and $\Delta E_{\rm tot}$ is defined by $\Delta E_{\rm tot} = E_{\rm tot}^{\text{Ca-48}} - E_{\rm tot}^{\text{Ni-48}}$. Figure 4.3.16 shows the dependences of $\Delta E_{\rm tot}$ on treatments of the Coulomb interaction calculated with the SAMi, SAMi-noISB, SAMi-CIB, SAMi-CSB, and SAMi-ISB EDFs. For comparison, the experimental data taken from AME2020 [418, 419] is also shown, where it is calculated by using the binding energies as discussed in Sec. 3.4.5. In order to see results more effectively, $\Delta E_{\rm tot}$ calculated without the Coulomb exchange (NoCx), with the Coulomb LDA (LDA), and with all the precise treatments of the Coulomb interaction (All) are also shown in Table 4.3.5.

Apart from the existence of the Coulomb exchange term, the dependence on the treatment of the Coulomb interaction of $\Delta E_{\rm tot}$ ranges approximately 1 MeV, while that of the ISB terms is approximately 7.2 MeV derived from results obtained by the SAMi-noISB and that by the SAMi-ISB. The difference between $\Delta E_{\rm tot}$ obtained by the SAMi and that by the SAMi-ISB is approximately 5.8 MeV. Therefore, the ISB effect on $\Delta E_{\rm tot}$ is larger than the Coulomb one, while its direction is opposite, and even the difference between $\Delta E_{\rm tot}$ obtained by the Coulomb LDA and that by the precise treatment of the Coulomb interaction is non-negligible compared to the desired accuracy. Among these contributions, as shown in Table 4.3.5, the CSB contribution is the most dominant and approximately 7 MeV, whereas the CIB one is approximately 0.3 MeV, which is a quarter of the dependence on the treatment of the Coulomb interaction. In addition, by comparing the result obtained by the SAMi-noISB and that by the SAMi, it is concluded that the refitting effect is also non-negligible.

References [175,177,432] claimed that the Coulomb exchange term is mainly cancelled with the CSB term of the nuclear interaction (or further correction of the Coulomb interaction). Comparing $\Delta E_{\rm tot}$ obtained with the SAMi or SAMi-noISB without the Coulomb LDA with that with the SAMi-ISB with the Coulomb LDA, one can find that such cancellation does not hold, and their differences are more than 1 MeV. For example, $\Delta E_{\rm tot}$ calculated by using the SAMi-ISB with the Coulomb LDA and by using the SAMi-ISB with all the Coulomb terms are, respectively, 68.7803 MeV and 67.6012 MeV, while those by using the SAMi without the Coulomb exchange EDF and by using the SAMi-noISB without the Coulomb exchange EDF are, respectively, 66.3915 MeV and 64.9202 MeV. Such difference is larger than the target accuracy, and therefore, such treatment with expecting such cancellation is not proper for general calculation.

Next, to see how the ISB terms affect $\Delta E_{\rm tot}$, on top of the SAMi-noISB EDF, the CIB strength u_0 is gradually changed from 0 MeV fm^3 to 50 MeV fm^3 with the CSB strength s_0 fixed to 0 MeV fm^3, or the CSB strength $-s_0$ is gradually changed from 0 MeV fm^3 to 50 MeV fm^3 with the CIB strength u_0 fixed to 0 MeV fm^3. The result is shown in Fig. 4.3.17: Their results are fitted to the linear function, which are, respectively,

$$\Delta E_{\rm tot} = -61.625 + 0.01083 u_0, \tag{4.3.27}$$

$$\Delta E_{\rm tot} = -61.625 - 0.28677\,(-s_0)\,. \tag{4.3.28}$$

It can be seen that $\Delta E_{\rm tot}$ depends on the CSB strength $-s_0$, while scarcely depends on the CIB strength u_0. To explain this behaviour, proton and neutron density distributions of mirror nuclei are considered. If neither the Coulomb interaction nor the ISB terms of the nuclear interaction are considered, $\rho_p^{\text{Ca-48}} \equiv \rho_n^{\text{Ni-48}}$ and $\rho_n^{\text{Ca-48}} \equiv \rho_p^{\text{Ni-48}}$ hold. Substituting them into Eqs. (4.3.11) and (4.3.11), one obtains

$$\begin{aligned}
E_{\rm CSB}^{\text{Ca-48}} &= E_{\rm CSB}\left[\rho_p^{\text{Ca-48}}, \rho_n^{\text{Ca-48}}\right] \\
&= \frac{s_0\,(1-y_0)}{8} \int \left\{ \left[\rho_n^{\text{Ca-48}}(\boldsymbol{r})\right]^2 - \left[\rho_p^{\text{Ca-48}}(\boldsymbol{r})\right]^2 \right\} d\boldsymbol{r} \\
&= -\frac{s_0\,(1-y_0)}{8} \int \left\{ \left[\rho_p^{\text{Ni-48}}(\boldsymbol{r})\right]^2 - \left[\rho_n^{\text{Ni-48}}(\boldsymbol{r})\right]^2 \right\} d\boldsymbol{r} \\
&= -E_{\rm CSB}^{\text{Ni-48}},
\end{aligned} \tag{4.3.29}$$

$$\begin{aligned}
E_{\rm CIB}^{\text{Ca-48}} &= E_{\rm CIB}\left[\rho_p^{\text{Ca-48}}, \rho_n^{\text{Ca-48}}\right] \\
&= \frac{u_0\,(1-z_0)}{8} \int \left\{ \left[\rho_n^{\text{Ca-48}}(\boldsymbol{r})\right]^2 + \left[\rho_p^{\text{Ca-48}}(\boldsymbol{r})\right]^2 \right\} d\boldsymbol{r} - \frac{u_0\,(2+z_0)}{4} \int \rho_n^{\text{Ca-48}}(\boldsymbol{r})\,\rho_p^{\text{Ca-48}}(\boldsymbol{r})\,d\boldsymbol{r} \\
&= \frac{u_0\,(1-z_0)}{8} \int \left\{ \left[\rho_n^{\text{Ni-48}}(\boldsymbol{r})\right]^2 + \left[\rho_p^{\text{Ni-48}}(\boldsymbol{r})\right]^2 \right\} d\boldsymbol{r} - \frac{u_0\,(2+z_0)}{4} \int \rho_n^{\text{Ni-48}}(\boldsymbol{r})\,\rho_p^{\text{Ni-48}}(\boldsymbol{r})\,d\boldsymbol{r} \\
&= E_{\rm CIB}^{\text{Ni-48}}.
\end{aligned} \tag{4.3.30}$$

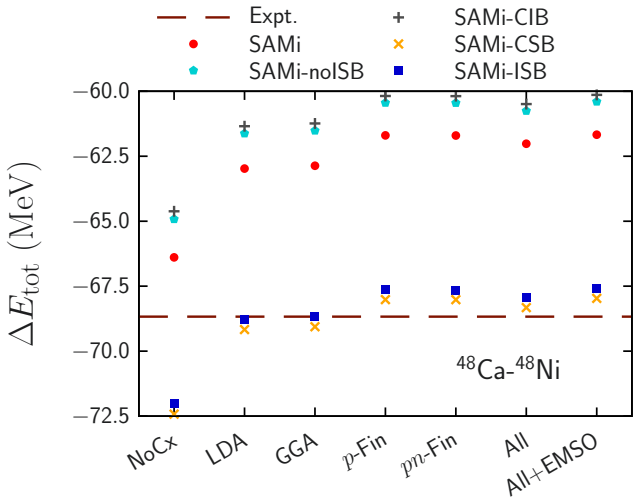

Figure 4.3.16: Comparison of the mass difference of the mirror nuclei pair ^{48}Ca and ^{48}Ni calculated with the SAMi, SAMi-noISB, SAMi-CIB, SAMi-CSB, and SAMi-ISB EDFs and with several treatments of the Coulomb interaction. The experimental data taken from AME2020 [418, 419] is also shown. This figure is taken from Ref. [A6].

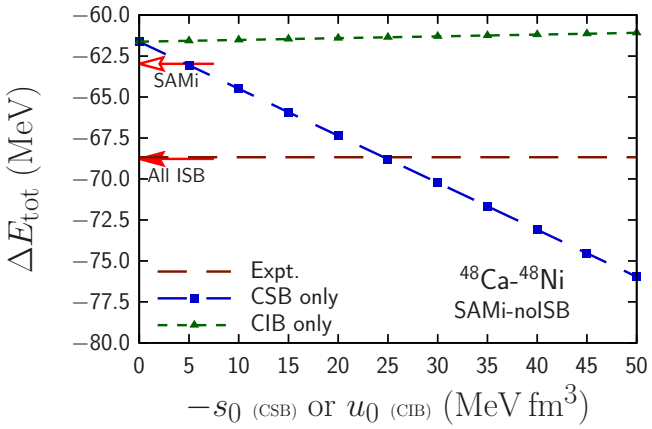

Figure 4.3.17: CSB and CIB strength, $-s_0$ and u_0, dependences of of the mirror nuclei pair ^{48}Ca and ^{48}Ni on top of the SAMi-noISB EDF and the Coulomb LDA exchange EDF. The mass difference calculated with the SAMi and SAMi-ISB EDFs are shown in empty and filled arrows, respectively. The experimental data taken from AME2020 [418, 419] is also shown. This figure is taken from Ref. [A6].

Consequently,

$$E_{\rm CSB}^{\text{Ca-48}} - E_{\rm CSB}^{\text{Ni-48}} = \frac{s_0\,(1-y_0)}{4} \int \left\{ \left[\rho_n^{\text{Ca-48}}(\boldsymbol{r})\right]^2 - \left[\rho_p^{\text{Ca-48}}(\boldsymbol{r})\right]^2 \right\} d\boldsymbol{r}$$
$$= \frac{s_0\,(1-y_0)\,C}{4}, \tag{4.3.31}$$
$$E_{\rm CIB}^{\text{Ca-48}} - E_{\rm CIB}^{\text{Ni-48}} = 0, \tag{4.3.32}$$

with a constant number $C > 0$. Therefore, the CSB contributes to $\Delta E_{\rm tot}$, and its effect is proportional to $-s_0$, while the CIB does not contribute to $\Delta E_{\rm tot}$. In reality, due to the existence of the Coulomb interaction and the ISB terms of the nuclear interaction, $\rho_p^{\text{Ca-48}}$ ($\rho_n^{\text{Ca-48}}$) is slightly different from $\rho_n^{\text{Ni-48}}$ ($\rho_p^{\text{Ni-48}}$), and hence, $\Delta E_{\rm tot}$ slightly depends on u_0.

4.4 *Ab Initio* Determination of Isospin Symmetry Breaking Terms of Skyrme Energy Density Functional

As discussed in Chap. 1, *ab initio* determination of the strength of the Skyrme EDF has been highly desired for a long time. Here, an *ab initio* EDF means that all the parameters of an EDF, as well as its EDF form, are determined only by referring to the theoretical (*ab initio*) calculation, while parameters of all the EDFs have been determined by referring to experimental data, as well as *ab initio* calculation of nuclear matter EoS.

A possible method to pin down the parameters of EDFs is using microscopic methods discussed in Sec. 2.2.4, while it is still difficult to apply these methods to nuclear systems, especially, for pinning down tiny parts. A method to pin down parameters of EDFs proposed here is, instead, combining *ab initio* calculations and phenomenological EDFs. As discussed in Sec. 4.3, the coupling constant of the CIB term of the SAMi-ISB EDF, u_0, was determined by referring to the Brueckner-Hartree-Fock calculation, one of the *ab initio* calculation methods, of symmetric nuclear matter with and without the CIB term of the nuclear interaction. In contrast, the coupling constant of the CSB term of the SAMi-ISB EDF, s_0, was not determined theoretically, but instead, with referring to the experimental data on the isobaric analogue energy of ^{208}Pb. In this section, we shall propose a way to pin down s_0 by using the *ab initio* calculation.

In order to pin down s_0, it is important to find observables that are sensitive to s_0. The *ab initio* calculation is difficult to calculate the isobaric analogue energy of ^{208}Pb because the numerical cost is too heavy and both the CSB and CIB terms may affect it. In the previous section, we have shown that the neutron-skin thickness ΔR_{np} and the mass difference of the mirror nuclei pair $\Delta E_{\rm tot}$ strongly depend on the strength of the CSB term of the nuclear interaction. In contrast, ΔR_{np} of $N = Z$ nuclei and $\Delta E_{\rm tot}$ are insensitive to the CIB term of the nuclear interaction, and ΔR_{np} of $N \neq Z$ nuclei depend on the CIB term, but weaker than the CSB term. Thus, instead of the isobaric analogue energy, we propose a method to pin down s_0 using ΔR_{np} and $\Delta E_{\rm tot}$. Here, ^{48}Ca and ^{208}Pb are taken as examples for ΔR_{np} and the ^{48}Ca-^{48}Ni pair is taken for $\Delta E_{\rm tot}$. At this moment, the coupled-cluster method with the bare nuclear interaction obtained by the chiral effective interaction has been applied to ^{48}Ca [446] and even ^{100}Sn [447] and the self-consistent Green's function method has been applied to Xe ($Z = 54$) isotopes [353]. Thus, ^{48}Ca and ^{48}Ni can be calculated by using some *ab initio* methods. Moreover, ^{208}Pb has not been able to be calculated by using any *ab initio* method at this moment, while it is desired to be calculated in the near future since it is a doubly-magic nucleus. Results for ^{16}O, ^{40}Ca, and ^{48}Ni are shown in Appendix A.

In order to see whether the s_0 dependence is affected by an EDF for $E_{\rm IS}$, the SAMi [409], SLy4 [58], SLy5 [58], and SkM* [441] EDFs are used for $E_{\rm IS}$. The CIB term is not considered to keep their EDF properties at most. Also, the SAMi-noISB EDF without CIB term (referred to as "SAMi-noISB") and with CIB term (referred to as "SAMi-CIB") are used. On top of these EDFs, the CSB term is gradually introduced with $-s_0 = 0\,\mathrm{MeV\,fm^3}$ to $50\,\mathrm{MeV\,fm^3}$. For the electromagnetic part $E_{\rm EM}$, the most general treatment is used, which corresponds to "LDA" in the previous section. Therefore, $E_{\rm EM}[\rho_p] = E_{\rm CH}[\rho_p] + E_{\rm Cx}[\rho_p]$, where $E_{\rm Cx}$ is the Coulomb LDA exchange EDF.

Figures 4.4.1 and 4.4.2 show the neutron-skin thickness for ^{48}Ca and ^{208}Pb, respectively. Their data are fitted to $\Delta R_{np} = a - bs_0$, where these fitting parameters are shown in Table 4.4.1. It is seen that all the EDFs show almost the same s_0 dependences, b, although their absolute values a are different. The average values of b and their standard deviations, $\bar{b}$ and Δb, are shown in Table 4.4.2. It is seen that b deviates less than 4 % around the average value $\bar{b}$. Therefore, once ΔR_{np} calculated with and without the CSB term of the nuclear interaction, denoted, respectively, as $\Delta R_{np}^{\text{w/ CSB}}$ and $\Delta R_{np}^{\text{w/o CSB}}$, are obtained by using the *ab initio* calculation, the CSB strength in the Skyrme interaction, s_0, can be obtained as

$$s_0 = -\frac{\Delta R_{np}^{\text{w/ CSB}} - \Delta R_{np}^{\text{w/o CSB}}}{\bar{b}} \tag{4.4.1}$$

within 4 % uncertainty.

Figure 4.4.3 shows the mass difference of mirror nuclei pair ^{48}Ca and ^{48}Ni. Their data are also fitted to $\Delta E_{\rm tot} = a - bs_0$, where these parameters are also shown in Table 4.4.1. It is seen that all the EDFs show almost the same s_0 dependences, b, although their absolute values a are different, as ΔR_{np}. As shown in Table 4.4.2, it is seen that b deviates with less than 6 % uncertainty around the average value $\bar{b}$. Therefore, once $\Delta E_{\rm tot}^{\text{w/ CSB}}$ and $\Delta E_{\rm tot}^{\text{w/o CSB}}$ are obtained by using the *ab initio* calculation, the CSB strength in the

Table 4.4.1: Fitting parameters of $\Delta R_{np} = a - bs_0$ for ^{48}Ca and ^{208}Pb and $\Delta E_{\rm tot} = a - bs_0$ for the ^{48}Ca-^{48}Ni pair. This table is taken from Ref. [A4].

EDF	^{48}Ca		^{208}Pb		$\Delta E_{\rm tot}$	
	a (fm)	b ($\times 10^{-3}$ MeV fm^4)	a (fm)	b ($\times 10^{-3}$ MeV fm^4)	a (MeV)	b (fm^{-3})
SLy4	+0.1535	−0.9807	+0.1595	−1.0525	−63.4143	−0.3234
SLy5	+0.1605	−0.9907	+0.1622	−1.0591	−63.1975	−0.3192
SkM*	+0.1551	−1.0002	+0.1686	−1.1138	−63.4399	−0.3220
SAMi	+0.1752	−0.9615	+0.1466	−1.0800	−62.9755	−0.3133
SAMi-noISB	+0.2339	−0.9131	+0.1702	−1.0324	−61.6251	−0.2868
SAMi-CIB	+0.2372	−0.9075	+0.1778	−1.0255	−61.3474	−0.2826

Table 4.4.2: Averaged values of the fitting parameter b for $\Delta E_{\rm tot}$ and ΔR_{np}. Standard deviations of $\bar{b}$ are also shown as $\Delta\bar{b}$. Columns entitled "only with four EDFs" show $\bar{b}$ and Δb calculated only with SAMi, SLy4, SLy5, and SkM* EDFs. This table is taken from Ref. [A4].

		with All EDFs			only with four EDFs		
		$\bar{b}$	$\Delta\bar{b}$	$\Delta\bar{b}/\lvert\bar{b}\rvert$ (%)	$\bar{b}$	$\Delta\bar{b}$	$\Delta\bar{b}/\lvert\bar{b}\rvert$ (%)
$\Delta E_{\rm tot}$	(fm^{-3})	−0.3079	0.0167	5.437	−0.3195	0.0039	1.216
ΔR_{np} (^{48}Ca)	(10^{-3} MeV^{-1} fm^4)	−0.9589	0.0364	3.795	−0.9833	0.0144	1.460
ΔR_{np} (^{208}Pb)	(10^{-3} MeV^{-1} fm^4)	−1.0605	0.0297	2.805	−1.0764	0.0239	2.219

Table 4.4.3: Same as Table 4.4.2 but calculated without the Coulomb interaction.

		with All EDFs			only with four EDFs		
		$\bar{b}$	$\Delta\bar{b}$	$\Delta\bar{b}/\lvert\bar{b}\rvert$ (%)	$\bar{b}$	$\Delta\bar{b}$	$\Delta\bar{b}/\lvert\bar{b}\rvert$ (%)
$\Delta E_{\rm tot}$	(fm^{-3})	−0.3272	0.0184	5.619	−0.3399	0.0046	1.359
ΔR_{np} (^{48}Ca)	(10^{-3} MeV^{-1} fm^4)	−0.9704	0.0361	3.718	−0.9945	0.0141	1.417
ΔR_{np} (^{208}Pb)	(10^{-3} MeV^{-1} fm^4)	−1.1454	0.0340	2.972	−1.1623	0.0297	2.552

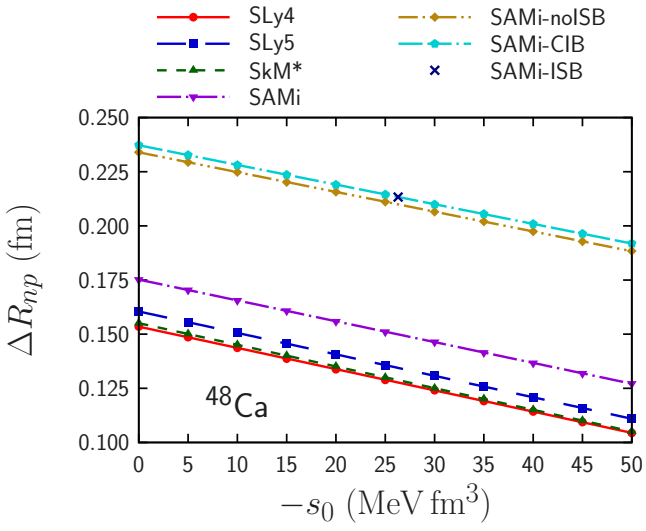

Figure 4.4.1: CSB strength $-s_0$ dependence of the neutron-skin thickness ΔR_{np} of ^{48}Ca calculated with several EDFs. The value obtained by the SAMi-ISB EDF is shown as cross symbol. This figure is taken from Ref. [A4].

Skyrme interaction, s_0, can be obtained as

$$s_0 = -\frac{\Delta E_{\rm tot}^{\rm w/\ CSB} - \Delta E_{\rm tot}^{\rm w/o\ CSB}}{\bar{b}} \tag{4.4.2}$$

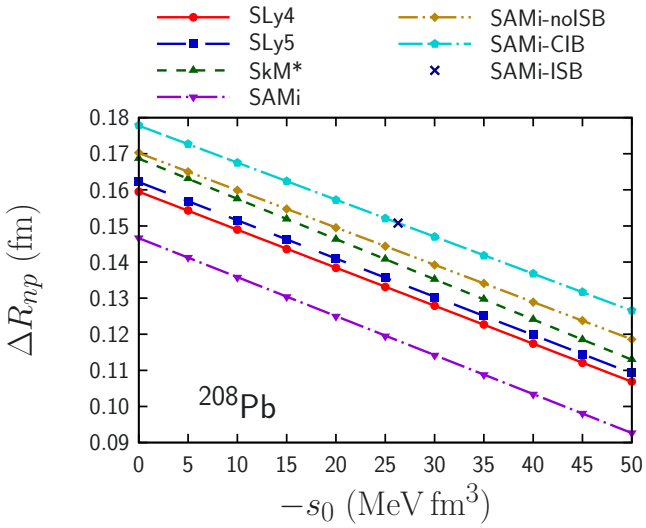

Figure 4.4.2: Same as Fig. 4.4.1 but of ^{208}Pb.

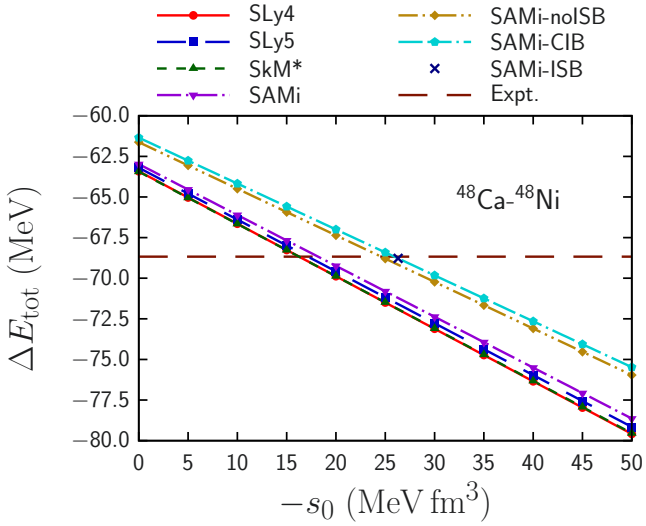

Figure 4.4.3: CSB strength $-s_0$ dependence of the mass difference of the mirror nuclei pair ^{48}Ca and ^{48}Ni calculated with several EDFs. The value obtained by the SAMi-ISB EDF is shown as cross symbol. The experimental data taken from AME2020 [418,419] is shown as the horizontal dashed line. This figure is taken from Ref. [A4].

within 6 % uncertainty.

The existence of the Coulomb interaction does not alter the conclusion. The Coulomb interaction breaks the isospin symmetry of atomic nuclei; hence it can make a deviation from the linear correlation. However, even if the Coulomb interaction is considered, as shown in Figs. 4.4.1–4.4.3, the linear correlation is good enough ($r \approx 1.000$). In addition, even if the Coulomb interaction is neglected, $\bar{b}$ and Δb change only slightly, as shown in Table 4.4.3.

As seen in Table 4.4.2 and Figs. 4.4.1–4.4.3, the SAMi-noISB and the SAMi-CIB give slightly different results to the other normal Skyrme EDFs. In the SAMi-ISB EDF, all the parameters of $E_{\rm IS}$, $E_{\rm CIB}$, and $E_{\rm CSB}$ are fitted altogether. Hence, properties of $E_{\rm IS}$ of the SAMi-ISB EDF, i.e., the SAMi-noISB EDF, are affected by the ISB terms of the nuclear interaction, although $E_{\rm IS}$ itself does not break the isospin symmetry. For instance, the symmetry energy of $E_{\rm IS}$ is affected as discussed in Sec. 4.2.1. Consequently, properties of the SAMi-noISB EDF may differ from the other normal EDFs, such as the SAMi, SLy4, SLy5, and SkM* EDFs. Hence, b obtained by the SAMi-noISB EDF is slightly different.

Comparing results obtained by the SAMi-noISB, SAMi-CIB, and the other EDFs, one can discuss whether

the ISB effect can be considered perturbatively. Since the fitting criteria of the SAMi-ISB and the SAMi are the same except for the existence of the ISB terms, the difference of b obtained by these EDFs originates from the existence of the ISB terms. Here, b obtained by the SAMi, SAMi-noISB, and SAMi-CIB are denoted by b^{SAMi}, $b^{\text{SAMi-noISB}}$, and $b^{\text{SAMi-CIB}}$, respectively. The parameter b^{SAMi} corresponds to the CSB strength determined perturbatively, while $b^{\text{SAMi-noISB}}$ and $b^{\text{SAMi-CIB}}$ correspond to the CSB strength determined by refitting. Since $b^{\text{SAMi-CIB}}/b^{\text{SAMi}}$ ranges from 0.90 to 0.95, perturbative consideration of the CSB strength may change s_0 by 5–10 %. Comparing $b^{\text{SAMi-noISB}}$ and $b^{\text{SAMi-CIB}}$, one can see the effect of the order of the refitting; the former corresponds to that the CSB term is fitted first, and the latter corresponds to that the CIB term is fitted first. Since $b^{\text{SAMi-CIB}}/b^{\text{SAMi-noISB}}$ is 0.99, the order of the determination of s_0 and u_0 does not affect their parameters.

At last, it should be noted that if *ab initio* calculation with various CSB strength gives results deviating from the linear correlation, it may indicate that higher-order terms of the Skyrme CSB interaction, i.e., s_1 and s_2 terms, are not negligible, or even the three-body term is not negligible. If s_0 obtained by ΔR_{np} differs substantially from that by ΔE_{tot}, it may also be evident that this model is not proper.

4.5 Short Summary

In this chapter, it was compared that the effects of the isospin symmetry breaking (ISB) terms of the nuclear interaction on the neutron-skin thickness, ΔR_{np}, and the mass difference of mirror nuclei, ΔE_{tot}, with those of the Coulomb interaction. The ISB terms of the nuclear interaction can be further divided into two parts: the charge independence breaking (CIB) and the charge symmetry breaking (CSB).

It was found that the CSB contributes to ΔR_{np} and ΔE_{tot} significantly. In contrast, the CIB does not contribute to ΔR_{np} for $N = Z$ nuclei or ΔE_{tot}; it contributes to ΔR_{np} for $N < Z$ nuclei in the same direction as the CSB contribution, while that for $N > Z$ nuclei in the opposite direction. The absolute value of the contribution of the CIB term to ΔR_{np} for $N \neq Z$ nuclei is smaller than that of the CSB, and it is comparable to the difference between ΔR_{np} obtained by the Coulomb LDA exchange EDF and that by the precise treatment of the Coulomb interaction. For instance, the CSB contribution to ΔE_{tot} of the ^{48}Ca-^{48}Ni pair is approximately 7.5 MeV, while the difference between ΔE_{tot} obtained by the Coulomb LDA exchange EDF and that by the precise treatment of the Coulomb interaction is approximately 1 MeV, and the CIB contribution to ΔE_{tot} is approximately 0.3 MeV. In addition, once the ISB terms of the nuclear interaction are considered, the estimation of an EoS parameter L using ΔR_{np} of ^{208}Pb changes approximately 10 MeV.

It should be noted that the CSB contributions to ΔR_{np} and ΔE_{tot} are much larger than the CIB ones, while the bare CIB interaction is much stronger than the CSB one. Therefore, it is important to find quantities that are sensitive to the CIB interaction.

Using the fact that ΔR_{np} and ΔE_{tot} are sensitive to the CSB strength, we also proposed the novel method to pin down the CSB strength combined with the *ab initio* calculations with and without the CSB term.

Chapter 5

Conclusion and Perspectives

This thesis consists of two parts: A precise treatment of the Coulomb interaction is developed in the context of the nuclear density functional theory (DFT), especially the Skyrme DFT; effects of the Coulomb interaction and the isospin symmetry breaking (ISB) terms of the nuclear interaction on the neutron-skin thickness and the mass difference of a mirror nuclei pair are compared. The spherical symmetry is assumed and the pairing correlation is not considered; thus, doubly-magic nuclei are chosen to study their effects. The nuclear interaction is known to have almost perfect isospin symmetry. Consequently, the atomic nuclei also have perfect isospin symmetry if neither the Coulomb interaction nor the ISB terms of the nuclear interaction are considered; however, the Coulomb interaction and the ISB terms of the nuclear interaction break the isospin symmetry of the atomic nuclei. In order to discuss the ISB terms of the nuclear interaction properly, the Coulomb interaction has to be treated precisely.

If protons are assumed to be point particles, the Coulomb exchange energy density functional (EDF) is expected to reproduce the Fock energy [Eq. (2.2.39)], which will be referred to as the exact-Fock energy. However, in nuclear DFT, the local density approximation (LDA), whose energy density is approximated to that for homogeneous systems, has been used in most works. The effect of the density gradient is taken into account for the Coulomb exchange EDF by using the generalized gradient approximation (GGA), which is widely used in condensed matter physics. Modifying one of the parameters of the Perdew-Burke-Ernzerhof parametrization of the Coulomb GGA exchange EDF, one can reproduce the Coulomb exchange energy calculated with the exact-Fock energy within an error of 100 keV.

Since protons and neutrons have finite spatial charge distribution, the charge density distribution $\rho_{\rm ch}$ is different from the proton density distribution ρ_p. Because the Coulomb interaction is the interaction between charges of particles, not protons themselves, the Coulomb EDF should be written in terms of $\rho_{\rm ch}$ instead of ρ_p. This difference, so-called finite-size effects of nucleons, is considered on top of the Coulomb GGA exchange EDF. Using the chain rule of the functional derivative, it is found that the Coulomb potential for neutrons does not vanish. It should be noted that the finite-size effects on the Coulomb effective potential were taken into account in several works, e.g., in Ref. [411], while it is found that this is incomplete: The electric form factors of nucleons are missing in the effective Coulomb potential, and consequently, neutrons are not affected by the Coulomb interaction. As a result, the mass difference of the mirror nuclei shows still a difference from the experimental data of more than 500 keV. On top of the finite-size effects, the vacuum polarization for the Coulomb potential, i.e., an electron-positron creation through the virtual photon exchange, is considered by using the Uehling effective potential, and the electromagnetic spin-orbit interaction is also considered perturbatively.

It is found that the proton finite-size effect, the neutron finite-size effect, and the vacuum polarization affect the total energy, respectively, by -580 keV, $+60$ keV, and $+90$ keV in ^{16}O, by -1800 keV, $+240$ keV, and $+400$ keV in ^{48}Ca, and by -8220 keV, $+1230$ keV, and $+3690$ keV in ^{208}Pb. The proton and neutron finite-size effects are proportional to Z and N, respectively, while the vacuum polarization is proportional to $Z^{5/3}$, and hence, in the light nuclei, the vacuum polarization is negligible, while it is non-negligible in the heavy nuclei, compared to the desired accuracy (100 keV).

The finite-light-speed effect of the Coulomb interaction, the Breit correction, is also considered in the LDA on top of the Coulomb LDA exchange EDF. In atomic systems, the Breit correction of the electron-electron Coulomb interaction is the leading order of the relativistic correction and is more dominant than the

vacuum polarization of the Coulomb potential formed by the atomic nucleus. In contrast, in nuclear systems, it is found that the vacuum polarization of proton-proton Coulomb interaction is more dominant than the Breit correction of the proton-proton Coulomb interaction. It is also fond that its difference is a comparable absolute value to but the opposite sign with the difference between the Coulomb exchange energy obtained by the LDA and that by the GGA, which is the same as in atomic systems.

Physical quantities related to the isospin symmetry breaking are discussed with the precise treatment of the Coulomb interaction—the GGA, the nucleon finite-size effects, the vacuum polarization, and the electromagnetic spin-orbit interaction—and the ISB terms of the nuclear interaction. The Skyrme-type ISB terms are used for the latter, and their parameters were determined in Ref. [183]. The ISB terms are further divided into two parts, the charge independence breaking (CIB) and the charge symmetry breaking (CSB). In principle, once the Coulomb interaction is taken into account precisely, the parameters of the nuclear EDF should be refitted. However, if one focuses on properties related to the isospin symmetry breaking, most part of the isospin symmetric part of the nuclear interaction is cancelled out, and hence it can be discussed properly even without refitting. In this thesis, the mass difference $\Delta E_{\rm tot}$ of the mirror nuclei and the neutron-skin thickness ΔR_{np} are taken as examples. Here, $\Delta E_{\rm tot}$ and ΔR_{np} for $N = Z$ nuclei are zero if neither the Coulomb interaction nor the ISB terms of the nuclear interaction are considered, and hence they are suitable to discuss the isospin symmetry breaking; ΔR_{np} for $N > Z$ nuclei is widely used to discuss the symmetry energy, especially its parameter L, and thus it is good to see whether such discussion is affected by the Coulomb interaction and the ISB terms of the nuclear interaction.

It is found that the Coulomb interaction does not change the L dependence of ΔR_{np} and changes the absolute value of ΔR_{np} less than 0.01 fm. This may be because different treatment of the Coulomb interaction changes the surface region of the density distribution, while it has been known in Ref. [445] that properties of the surface region do not change the L dependence of ΔR_{np}. The CSB term of the nuclear interaction affects ΔR_{np} significantly. The CIB term affects ΔR_{np} of only $N \neq Z$ nuclei, whose amount is less than the effect of the CSB term and is comparable with the difference between ΔR_{np} obtained by the Coulomb LDA exchange EDF and that by the precise treatment of the Coulomb interaction. In contrast, in the $N = Z$ nuclei, the effect of the CIB term is one order of the magnitude smaller than the difference between ΔR_{np} obtained by the Coulomb LDA exchange EDF and that by the precise treatment of the Coulomb interaction. In addition, if the CSB or CIB strengths change 10 MeV fm^3, estimation of L using ^{208}Pb changes approximately -6.1 MeV and 1.7 MeV, respectively. If one assumes the CSB and CIB strengths obtained by the SAMi-ISB EDF, the estimated value of L changes, in total, in 11.6 MeV.

The ISB terms of the nuclear interaction change $\Delta E_{\rm tot}$ of the ^{48}Ca-^{48}Ni pair more than 5 MeV, but there is still more than 1 MeV difference. The precise treatment of the Coulomb interaction further reduces the difference to 0.3 MeV. It should be noted here that the conventional finite-size effects on the Coulomb interaction have still missed part, and if the conventional one is used, the difference is reduced to 0.8 MeV only. The CSB term affects $\Delta E_{\rm tot}$, while the effect of the CIB term affects $\Delta E_{\rm tot}$ is even less than the difference between $\Delta E_{\rm tot}$ obtained by the Coulomb LDA exchange EDF and that by the precise treatment of the Coulomb interaction.

References [175, 177, 432] claimed the cancellation between the CSB energy and the Coulomb exchange energy. In this thesis, it is found that this cancellation does not hold in the neutron-skin thickness ΔR_{np} or the mass difference of the mirror nuclei $\Delta E_{\rm tot}$, in general. Therefore, both the CSB term and the Coulomb exchange term (and even further precise treatments) must be treated properly.

Using the fact that ΔR_{np} and $\Delta E_{\rm tot}$ are sensitive to the CSB strength while its dependence hardly depends on the choice of the isospin symmetric part of the nuclear EDF, we propose the way to determine the CSB strength of the Skyrme-like ISB effective interaction. Once ΔR_{np} or $\Delta E_{\rm tot}$ with and without the CSB interaction are calculated by using *ab initio* methods, using the linear correlation between the CSB strength of the Skyrme-like effective interaction and ΔR_{np} or $\Delta E_{\rm tot}$, one can determine the CSB strength. Another possible method to pin down the ISB strengths may be using the knowledge of the covariant density functional theory (CDFT), which starts from the QCD Lagrangian, while the ISB effects have not been taken into account for CDFT yet and thus it is not available up to now.

The CIB interaction is approximately ten times stronger than the CSB interaction in vacuum. In contrast, in this thesis, it is found that $\Delta E_{\rm tot}$ and ΔR_{np} are sensitive to the CSB interaction, while they are insensitive to the CIB interaction. In order to discuss the contribution of the CIB interaction to nuclear properties, it is important to find nuclear properties which are sensitive to the CIB interaction.

In this thesis, the spherical symmetry is assumed and the pairing correlation is not considered. Hence, only doubly-magic nuclei are used for discussion, while most nuclei are not doubly-magic nuclei. In order to discuss effects of the Coulomb interaction and the ISB terms of the nuclear interaction on properties of other atomic nuclei, these two should be implemented to numerical codes of the Hartree-Fock-Bogoliubov calculation without assuming the spherical symmetry. Especially, it is known that the Coulomb interaction enhances the nuclear deformation [448, A10]; hence, it is interesting to see whether the precise treatment changes nuclear shapes. However, to discuss such small effects, other corrections should also be considered carefully; for instance, it is known that the pairing correlation changes charge radii and the spin-orbit contribution non-negligibly [449, A18].

So far, only the leading term (s-wave) is considered for the ISB terms of the Skyrme-like interaction, since the ISB terms are just correction terms to the nuclear interaction. Once *ab initio* calculations with gradually changed ISB strengths are available, it will be able to discuss whether this assumption is proper. Not only to determine the CSB strength of the Skyrme-like interaction but also to discuss the validity of the assumption, *ab initio* calculation with the various ISB strength is indispensable, while it has not been available yet.

To see effects of the precise treatment of the Coulomb interaction and the ISB terms of the nuclear interaction on other nuclear properties, first of all, the isospin symmetric term of the nuclear EDF should be refitted, since even the finite-size effects on the Coulomb interaction is non-negligible in heavy nuclei. Once the nuclear EDF is refitted, it should be interesting to calculate properties of excited states in order to see the isobaric multiplet mass equation and isobaric analogue states. Calculation of the half-lives of β decays, including decays with $0^+ \to 0^+$ called the superallowed one, is also interesting [182,201–205] since it has been used to estimate a matrix element of the Cabibbo-Kobayashi-Maskawa matrix related to the standard model and the flavour symmetry of the quarks. To perform such calculation precisely, restoration of the symmetry which is broken due to the independent-particle (mean-field) approximation [450] should also be considered, which introduces fictitious isospin impurity [202, 203, 451–453, A20].

It is also discussed how large the ISB terms of the nuclear interaction affect the estimation of the L parameter of the nuclear equation of state using ΔR_{np}. In this thesis, it was simply estimated that first how large ΔR_{np} is changed once the ISB terms are introduced, and then how large L changes due to the change of ΔR_{np}. However, in principle, L itself also includes the effect of the CIB term, and hence the L dependence of ΔR_{np} may change once ISB terms are introduced. In addition, the strength of the CSB term affects ΔR_{np}, but L does not include the effect of the CSB term. Therefore, a quantity that includes effects of both the CSB and CIB strength and their sensitivity to ΔR_{np}, should be found in order to discuss effects of the ISB terms on ΔR_{np} properly. It should also be mentioned that the analysis to obtain ΔR_{np} from the parity-violating asymmetry did not consider the ISB terms [92], while the ISB terms may affect such analysis.

The proposed method to pin down the CSB strength of the nuclear EDF is a method that uses a quantity sensitive to a specific channel (or symmetry). Thus, this method may be applicable to other terms of the nuclear EDF or even EDFs for electronic systems.

Effects of the Coulomb correlation on the total energy is also an interesting topic. The correlation energy is defined by the difference between the exact total energy and the Hartree-Fock one. In electronic systems, since there is only the Coulomb interaction, which is known exactly, the correlation energy EDFs have been derived theoretically, as discussed in Chap. 1. In contrast, in nuclear systems, there are both the Coulomb and nuclear interactions, and consequently, the correlation energy originates from both interactions; hence the correlation energy originating from the Coulomb interaction, in short, the "Coulomb correlation energy", is not well-defined. In addition, the nuclear EDF is obtained by fitting to the experimental data, and thus the Coulomb correlation energy may be implicitly included in the nuclear EDF. Indeed, the Coulomb correlation energy discussed in Refs. [454, 455] is even the opposite sign to that calculated by using the Coulomb correlation EDF widely used in electronic systems [A1]. To achieve more accurate calculations related to the isospin symmetry breaking, construction and even the definition of the Coulomb correlation energy in nuclear physics are indispensable.

Appendix A

Supplemental Data for Sec. 4.4

In this appendix, first, the CSB strength $-s_0$ dependence of the neutron-skin thickness ΔR_{np} of ^{16}O, ^{40}Ca, and ^{48}Ni with several EDFs are shown in Figs. A.1.1, A.1.2, and A.1.3, respectively, to show the discussion in Sec. 4.4 holds for other nuclei. The fitting parameters of a and b in Eq. (4.3.15) are shown in Table A.1.1.

As seen in the figures, it is shown that s_0 dependence of the neutron-skin thickness ΔR_{np} is still universal among these tested EDFs also in ^{16}O, ^{40}Ca, and ^{48}Ni. Therefore, the discussion given in Sec. 4.4 holds not only in ^{48}Ca and ^{208}Pb but also other doubly-magic nuclei.

Tables A.1.2 and A.1.3 shows the same results but calculation without the Coulomb interaction. The neutron-skin thickness, ΔR_{np}, of $N = Z$ nuclei and the mass difference of the mirror nuclei, $\Delta E_{\rm tot}$, are exactly zero if the Coulomb interaction is not considered. Therefore, ΔR_{np} of ^{16}O and ^{40}Ca and $\Delta E_{\rm tot}$ are, respectively, fitted to $\Delta R_{np} = -bs_0$ and $\Delta E_{\rm tot} = -bs_0$, instead. These averaged values are shown in Tables A.1.4 and A.1.5.

Table A.1.1: Same as Table 4.4.1 but for ^{16}O, ^{40}Ca, and ^{48}Ni.

EDF	^{16}O		^{40}Ca		^{48}Ni	
	a	b	a	b	a	b
SLy4	−0.0248	−0.8884	−0.0475	−0.9604	−0.2675	−1.1005
SLy5	−0.0251	−0.9000	−0.0480	−0.9700	−0.2769	−1.1225
SkM*	−0.0251	−0.8842	−0.0493	−0.9893	−0.2710	−1.1125
SAMi	−0.0233	−0.8542	−0.0470	−0.9640	−0.2901	−1.1165
SAMi-noISB	−0.0231	−0.8713	−0.0459	−0.9605	−0.3442	−1.0938
SAMi-CIB	−0.0230	−0.8585	−0.0457	−0.9475	−0.3486	−1.0987

Table A.1.2: Same as Tables 4.4.1 and A.1.1 but calculated without the Coulomb interaction. In $N = Z$ nuclei, the results are fitted to $\Delta R_{np} = -bs_0$, instead.

EDF	^{16}O	^{40}Ca	^{48}Ca		^{48}Ni		^{208}Pb	
	b	b	a	b	a	b	a	b
SLy4	−0.8823	−0.9483	+0.1917	−0.9913	−0.1917	−1.0071	+0.2679	−1.1351
SLy5	−0.8944	−0.9594	+0.1994	−1.0035	−0.1994	−1.0185	+0.2717	−1.1411
SkM*	−0.8743	−0.9715	+0.1942	−1.0102	−0.1941	−1.0249	+0.2839	−1.2105
SAMi	−0.8438	−0.9458	+0.2141	−0.9731	−0.2140	−0.9956	+0.2608	−1.1624
SAMi-noISB	−0.8629	−0.9454	+0.2718	−0.9255	−0.2717	−0.9538	+0.2781	−1.1145
SAMi-CIB	−0.8498	−0.9307	+0.2747	−0.9187	−0.2747	−0.9469	+0.2853	−1.1087

Table A.1.3: Fitting parameters of $\Delta E_{\rm tot} = a - bs_0$ for the results with the Coulomb interaction and those of $\Delta E_{\rm tot} = -bs_0$ for the results without the Coulomb interaction. This table is taken from Ref. [A4].

EDF	Coulomb LDA		No Coulomb
	a (MeV)	b (fm^{-3})	b (fm^{-3})
SLy4	−63.4143	−0.3234	−0.3440
SLy5	−63.1975	−0.3192	−0.3397
SkM*	−63.4399	−0.3220	−0.3435
SAMi	−62.9755	−0.3133	−0.3325
SAMi-noISB	−61.6251	−0.2868	−0.3039
SAMi-CIB	−61.3474	−0.2826	−0.2998

Table A.1.4: Same as Table 4.4.2 but for ΔR_{np} of ^{16}O, ^{40}Ca, and ^{48}Ni calculated with the Coulomb LDA EDF.

		with All EDFs			only with four EDFs		
		$\bar{b}$	$\Delta\bar{b}$	$\Delta\bar{b}/\lvert\bar{b}\rvert$ (%)	$\bar{b}$	$\Delta\bar{b}$	$\Delta\bar{b}/\lvert\bar{b}\rvert$ (%)
ΔR_{np} (^{16}O)	(10^{-3} MeV^{-1} fm^4)	−0.8761	0.0163	1.863	−0.8817	0.0169	1.917
ΔR_{np} (^{40}Ca)	(10^{-3} MeV^{-1} fm^4)	−0.9653	0.0127	1.313	−0.9709	0.0111	1.148
ΔR_{np} (^{48}Ni)	(10^{-3} MeV^{-1} fm^4)	−1.1075	0.0104	0.937	−1.1130	0.0080	0.723

Table A.1.5: Same as Table A.1.4 but calculated without the Coulomb interaction.

		with All EDFs			only with four EDFs		
		$\bar{b}$	$\Delta\bar{b}$	$\Delta\bar{b}/\lvert\bar{b}\rvert$ (%)	$\bar{b}$	$\Delta\bar{b}$	$\Delta\bar{b}/\lvert\bar{b}\rvert$ (%)
ΔR_{np} (^{16}O)	(10^{-3} MeV^{-1} fm^4)	−0.8679	0.0177	2.040	−0.8737	0.0187	2.136
ΔR_{np} (^{40}Ca)	(10^{-3} MeV^{-1} fm^4)	−0.9502	0.0127	1.334	−0.9562	0.0102	1.064
ΔR_{np} (^{48}Ni)	(10^{-3} MeV^{-1} fm^4)	−0.9912	0.0303	3.059	−1.0115	0.0112	1.106

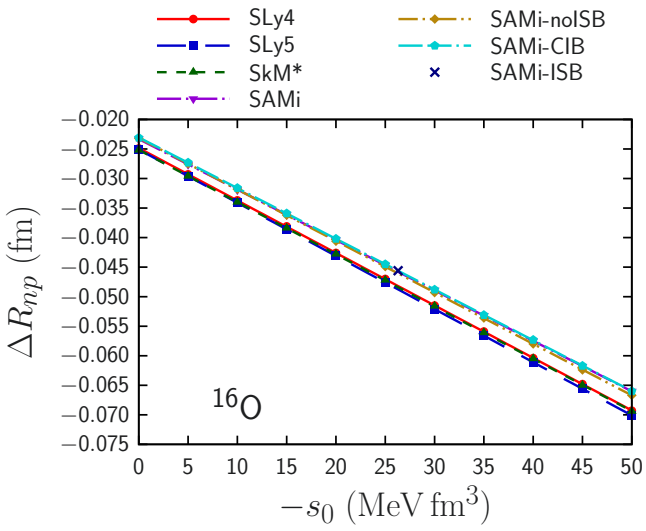

Figure A.1.1: Same as Fig. 4.4.1 but of ^{16}O.

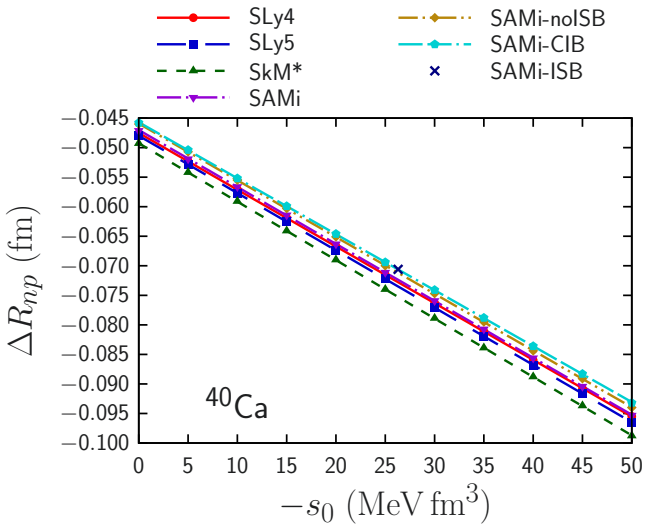

Figure A.1.2: Same as Fig. 4.4.1 but of ^{40}Ca.

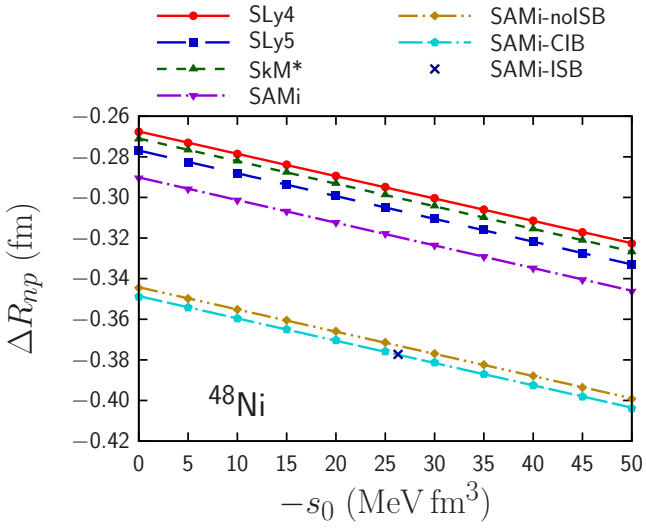

Figure A.1.3: Same as Fig. 4.4.1 but of ^{48}Ni.

Appendix B

Abbreviation List

Abbreviations used in this thesis are shown in Table B.1.1.

Table B.1.1: Abbreviations used in this thesis.

Abbreviation	Meaning
AME	Atomic mass evaluation
AV14 / AV18	Argonne v 14 or 18 interactions
CDFT	Covariant density functional theory
ChEFT	Chiral effective field theory
CIB	Charge independence breaking
CKM	Cabibbo-Kobayashi-Maskawa
CSB	Charge symmetry breaking
DFPT	Density functional perturbation theory
DFT	Density functional theory
EDF	Energy density functional
EM	Electromagnetic
EMSO	Electromagnetic spin-orbit interaction
EoS	Equation of state
Exp	Experimental data
ext	External potential
FRG-DFT	Functional-renormalization-group aided density functional theory
GGA	Generalized gradient approximation
GS	Ground state
HF	Hartree-Fock
HK	Hohenberg-Kohn
Hxc	Hartree-exchange-correlation
IKS	Inverse Kohn-Sham
int	Interaction
IS	Isospin symmetry or isospin symmetric
ISB	Isospin symmetry breaking
KS	Kohn-Sham
LDA	Local density approximation
LQCD	Lattice QCD
p-fin	Proton finite-size effect
pn-fin	Proton-neutron (all) finite-size effect
PBE	Perdew-Bruke-Ernzerhof
QCD	Quantum chromodynamics
QED	Quantum electrodynamics
xc	Exchange-correlation

Appendix C

Symbol List

Symbols used in this thesis are shown in Tables C.1.1 and C.1.2.

Table C.1.1: Symbols used in this thesis (1).

Symbols	Meaning	Definition
A	Mass number	
$E[\rho]$	Total EDF	Eq. (2.2.19)
E_{Breit}	Breit EDF	Eq. (3.5.6)
$E^{\mathrm{H}}_{\mathrm{Breit}}$	Breit Hartree EDF	Eq. (3.5.4)
$E^{\mathrm{x}}_{\mathrm{Breit}}$	Breit exchange EDF	Eq. (3.5.5)
E_{c}	Correlation eneregy (or EDF)	
E_{C}	Coulomb EDF	
E_{CH}	Coulomb Hartree EDF	
E_{Cx}	Coulomb exchange EDF	Eq. (3.2.1)
E_{EM}	Electromagnetic EDF	
E_{ext}	External potential energy	Eq. (2.1.8)
E_{F}	Exact-Fock energy	Eq. (2.2.39)
E_{gs}	Ground-state energy	Eq. (2.1.2)
E_{H}	Hartree energy (or EDF)	Eq. (2.1.9)
E_{Hxc}	Hartree-Exchange-correlation EDF	
E_{nucl}	Nuclear EDF	
E_{rea}	Rearrangement energy	Eq. (2.2.33)
E_{sym}	Symmetry energy	Eq. (1.3.1)
E_{VP}	Vacuum polarization EDF	Eq. (3.4.22)
E_{x}	Exchange energy (or EDF)	
$E^{\mathrm{LDA}}_{\mathrm{x}}$	Exchange EDF in LDA	Eq. (2.2.43)
E_{xc}	Exchange-correlation EDF	
$\mathcal{E}_{\mathrm{H}} = \mathcal{E}^{\mathrm{H}}_{\mathrm{IS}}$	Skyrme Hartree energy density	Eq. (2.3.4)
$\mathcal{E}_{\mathrm{x}} = \mathcal{E}^{\mathrm{x}}_{\mathrm{IS}}$	Skyrme exchange energy density	Eq. (2.3.5)
$\mathcal{E}^{\mathrm{H}}_{\mathrm{CIB}}$	Skyrme CIB Hartree energy density	Eq. (4.2.6)
$\mathcal{E}^{\mathrm{x}}_{\mathrm{CIB}}$	Skyrme CIB exchange energy density	Eq. (4.2.7)
$\mathcal{E}^{\mathrm{H}}_{\mathrm{CSB}}$	Skyrme CSB Hartree energy density	Eq. (4.2.8)
$\mathcal{E}^{\mathrm{x}}_{\mathrm{CSB}}$	Skyrme CSB exchange energy density	Eq. (4.2.9)
F	GGA enhancement factor	E.g. Eq. (3.3.1)
F	Kohn-Sham universal functional	Eq. (2.2.9)
$\tilde{f}$	Fourier transform of f	Eq. (1.4.5)
$\tilde{G}_{\mathrm{E}\tau}$	Electric form factor ($\tau = p$ for protons, n for neutrons)	
H	Hamiltonian	
J, L, K_{sym}, E_0, K_∞	EoS parameters	Eqs. (1.3.2) & (1.3.3)
N	Neutron number	

Table C.1.2: Symbols used in this thesis (2).

Symbols	Meaning	Definition
P_σ	Spin exchange operator	Eq. (1.2.6)
P_τ	Isospin exchange operator	Eq. (1.2.7)
r_s	Wigner-Seitz radius	Eq. (2.2.45)
s	Dimensionless density gradient	Eq. (2.2.59)
S_{jk}	Tensor operator	Eq. (1.2.2)
$\boldsymbol{T}$	Total isospin	
$\boldsymbol{t}$	Isospin	Eq. (1.1.1)
$T_\pm$	Isospin ladder operator	
T_{jk}	Isotensor operator	Eq. (1.5.5)
T_KS	Kohn-Sham kinetic energy	Eq. (2.2.18)
t_τ	Kinetic energy density	Eq. (2.3.8)
V_C	Coulomb effective potential	
V_eff^τ	Effective potential for nucleon τ	Eq. (3.4.5)
V_ext	External potential	
V_EM	Electromagnetic effective potential	See Sec. 3.4.1
V_Hxc	Hartree-exchange-correlation potential	Eq. (2.2.27)
V_KS	Kohn-Sham effective potential	Eq. (2.2.24)
V_VP	Vacuum polarization effective potential	Eq. (3.4.23)
V_xc	Exchange-correlation potential	Eq. (2.2.25)
v_Breit	Breit correction	Eq. (3.5.1)
$\tilde{v}_\mathrm{Breit}$	Non-relativistic reduction of v_Breit	Eq. (3.5.3)
v_CIB	CIB term of nuclear interaction	Eq. (4.1.1)
v_CSB	CSB term of nuclear interaction	Eq. (4.1.2)
v_int	Interaction (general)	
v_nucl	Nuclear interaction	
v_{nn}	Neutron-neutron interaction	
$v_{pn}^{T=t}$	Proton-neutron interaction ($T = t$ channel)	
v_{pp}	Proton-proton interaction	
v_Sky	Skyrme interaction	
$v_\mathrm{Sky}^\mathrm{CIB}$	CIB term of Skyrme nuclear interaction	Eq. (4.2.4)
$v_\mathrm{Sky}^\mathrm{CSB}$	CSB term of Skyrme nuclear interaction	Eq. (4.2.5)
$\mathcal{V}_\mathrm{EM}$	Electromagnetic effective potential	See Sec. 3.4.1
Z	Proton number	
β	Isospin asymmetry	
ΔE_tot	Mass difference of the mirror nuclei pair ^{48}Ca and ^{48}Ni	
ΔR_{np}	Neutron-skin thickness	
$\Delta\varepsilon_j$	Correction of EMSO for ε_j	Eq. (3.4.25)
ε_c	Correlation energy density	
ε_j	(Kohn-Sham) Single-particle energy	Eq. (2.2.23)
ε_x	Exchange energy density	
ρ_0	Saturation density	Eq. (1.3.5)
ρ_ch	Charge density	Eq. (1.4.4)
ρ_gs	Ground-state density	Eq. (2.1.3) or (2.2.15)
ρ_n	Neutron density	
ρ_p	Proton density	
$\boldsymbol{\sigma} = (\sigma_x, \sigma_y, \sigma_z)$	Pauli matrices for spin	
$\boldsymbol{\tau} = (\tau_x, \tau_y, \tau_z)$	Pauli matrices for isospin	
Φ_0	Slater determinant	
φ_j	(Kohn-Sham) Single-particle orbital	Eq. (2.2.23)
Ψ_gs	Ground-state wave function	Eq. (2.1.2)

Appendix D

Experimental Techniques Related to This Thesis

In this chapter, experimental techniques referred to in this thesis will be explained briefly: masses, charge radii or densities, and neutron-skin thickness.

Data obtained by the Atomic Mass Evaluation (AME) [415–419] are used for experimental values of binding energies in this thesis. Some experimental techniques provide absolute values of masses, while some provide relative values, i.e., mass differences from a neighbouring nucleus. Combining these all data, the AME provides absolute values of masses of all the measured nuclei [214, 456]. The methods which provide absolute values of masses are, for instance, using time-of-flight [457,458], storage rings [459–462], and penning traps [463]. All these methods are based on the fact that the cyclotron frequency is proportional to $1/M$, where M is the mass of an atomic nucleus [214, 464]. In these methods, $\Delta M/M$ is expected to be 10^{-5} or smaller, where ΔM is an experimental error [214]. In contrast, in the indirect measurements, Q-values of decays, i.e., energies of emitted particles in nuclear decays, are used.

The charge density distribution $\rho_{\rm ch}$ of an atomic nucleus is obtained by using the elastic scattering of an electron [141–143, 145, 146, 465, 466]. Under the one-photon exchange approximation, in the case of the doubly-magic nuclei, the ratio of the experimental cross section to that of the point charge corresponds to the form factor, i.e., the Fourier transform of $\rho_{\rm ch}$. In the case of the open-shell nuclei, the magnetic form factors of nucleons also contribute. Indeed, higher-order corrections to the one-photon exchange also contribute to the cross section, while these effects are extracted [400, 401]. Calculating the root-mean-square radius of $\rho_{\rm ch}$, one can obtain the charge radius $R_{\rm ch}$. Charge radii can also be measured by using the laser spectroscopy of atoms [467–474]. In laser spectroscopy, only isotope shifts, i.e., differences of the charge radii from a neighbouring nucleus, are obtained, while isotope shifts of many unstable nuclei have also been obtained [475], in contrast to the electron scattering. In both methods, obtained $R_{\rm ch}$ are so accurate; experimental error is the order of 0.001 fm in the stable nuclei, which is 0.1 % error or less.

Once $R_{\rm ch}$ is obtained, using Eq. (3.4.34) [1], one can obtain the root-mean-square radius of the proton distribution R_p. Since the charge radius of protons is also known precisely [10] and contributions of the charge radius of neutrons and the magnetic radii of nucleons to $R_{\rm ch}$ are quite small [476, A18], R_p can also be obtained quite precisely.

In order to calculate the neutron-skin thickness ΔR_{np}, the neutron root-mean-square radius R_n is also needed. In contrast to R_p, it cannot be measured by using the electromagnetic probe. Instead, hadronic probes, for instance, polarized-proton scattering [73, 444, 477], have been used. However, the nuclear interaction induces the model dependence in the analysis. Accordingly, experimental errors and uncertainty of R_n are large.

Another method to measure R_n is the parity-violating electron scattering [78, 92, 93]. In this method, the spin-polarized electron beam is used, and the ratio of the cross section of an up-spin electron to that of a down-spin electron, $(\sigma_\uparrow - \sigma_\downarrow)\,/\,(\sigma_\uparrow + \sigma_\downarrow)$, is measured. It is known that this parity-violating asymmetry is related to the weak charge density of an atomic nucleus. Since the weak charge of neutrons is approximately

[1] Equation (3.4.34) considers $\tilde{G}_{{\rm E}\tau}$ only, while effects of $\tilde{G}_{{\rm M}\tau}$ on $R_{\rm ch}$ are discussed in Refs. [476, A18]. Effects of $\tilde{G}_{{\rm M}\tau}$ is so small that it does not affect the conclusion in this thesis, unless one compares $R_{\rm ch}$ of spin unsaturated nuclei to experimental data.

-1 whereas that of protons is almost zero [478], the weak charge density $\rho_{\rm wk}$ is almost the same as $-\rho_n$. In principle, the parity-violating asymmetry does not include model dependence. However, in order to obtain enough accuracy, a longer beam time is required. Accordingly, $\tilde{\rho}_{\rm wk}$ of only a few points of the momentum transfer q can be obtained [78,92]. Therefore, $\rho_{\rm wk}$ itself has not been able to be obtained. Consequently, to get $R_{\rm wk}$, R_n, and ΔR_{np}, the model-dependent analysis is needed to be introduced [78,92]. Reference [92] claimed that the experimental error was small enough that $\Delta R_{np} = 0.283 \pm 0.071\,{\rm fm}$. However, a reanalysis done by another group using the same data of the parity-violating asymmetry gave $\Delta R_{np} = 0.19 \pm 0.02\,{\rm fm}$ [94]. Therefore, the systematic error induced by theoretical models seems to be quite large. Also, it should be mentioned that as mentioned in Chap. 5, the ISB terms may affect the analysis to obtain $R_{\rm wk}$, R_n, or ΔR_{np} from the parity-violating asymmetry, while they have not been considered yet.

Considering these situations discussed above, masses M and charge radii $R_{\rm ch}$, and accordingly proton radii R_p, are assumed to be accurate enough and their experimental errors are expected to be smaller than the theoretical uncertainties. Hence, experimental errors are not considered in this thesis. In contrast, experimental errors of neutron radii R_n, and accordingly the neutron-skin thickness ΔR_{np}, may be larger than theoretical uncertainties. Accordingly, these errors are considered in this thesis.

Acknowledgements

First of all, I thank my supervisor Prof. Shinji Tsuneyuki (U. Tokyo) for his kind supervision during my five-year graduate study. He has been so kind that he allows me to research whatever I like, while he has always given me suggestive comments during discussions. Especially, during my PhD study, approximately 70 % of my works have been in nuclear physics, although I belong to a group focusing on condensed matter physics. Since he is kind enough to allow me to work in nuclear physics, I was able to start this work, which was motivated by a knowledge of DFT for condensed matter physics.

Next, I also thank Prof. Gianluca Colò (U. Milan/INFN Milano), Prof. Haozhao Liang (U. Tokyo/RIKEN), and Prof. Xavier Roca-Maza (U. Milan/INFN Milano) for a long-term collaboration, where most of this thesis is based on collaboration with them. Haozhao has allowed me to join activities in his group even unofficially since I was a fourth-year student of the bachelor course. This has enabled me to work on nuclear physics, while I have belonged to the condensed matter theory group. Thanks to this opportunity, I found that knowledge of DFT for condensed matter physics may be applicable to nuclear DFT. During a workshop on interdisciplinary DFT at RIKEN, I had a chance to discuss with Gianluca, a friend of Haozhao. I visited Gianluca and Xavi and started collaborating when I was in the first year of the master's course in February 2018; after that, I visited them several times to continue our collaboration. I learnt topics related to the isospin symmetry breaking and the neutron-skin thickness in detail then, which were interesting for me and really motivated me to continue research in nuclear physics. Finally, the number of papers with them is reaching five; they have always taught me many things related not only to nuclear physics itself but also to writing research papers. Their kind hospitality, profound knowledge, and suggestive comments are really indispensable for my research activity and have helped me to understand nuclear physics deeper.

I cannot forget to thank Prof. Hiroyuki Sagawa (U. Aizu/RIKEN). Although I just started to collaborate with him in 2020, I have discussed with him since I was an undergraduate student. He has given me so many opportunities to learn cutting-edge nuclear physics. Thanks to his broad knowledge of nuclear physics and such opportunities, I have learnt from him numerous things. In addition, he has always taught me how to research physics and given me numerous suggestions for calculation, sometimes with drinking.

I am indebted to Prof. Kouichi Hagino (Kyoto U.) for giving me many suggestions and comments. He does not only have a deeper knowledge of nuclear physics but also has a knowledge of atomic physics. He gave me much information related to super-heavy elements, including their chemical study, and accordingly, I started to study the chemical properties of super-heavy elements, although its work is not directly related to this thesis. Owing to discussion with him, we were also able to discuss the origin of nuclear deformation by comparing it with atomic structure.

I am also indebted to Dr. Ryosuke Akashi (U. Tokyo) for stimulating comments during the Tsuneyuki group seminars and daily discussion, as well as for the collaboration. He has a deeper knowledge of condensed matter DFT, and his knowledge is really helpful to understand DFT for both electronic systems and nuclear systems well. He is also really open-minded for physics, not only for condensed matter physics; he has always given me very valuable comments, even for my works in nuclear physics.

I am grateful for the daily discussion and valuable comments on this thesis by Dr. Hiroyuki Tajima (U. Tokyo) and Dr. Tomohiro Oishi (U. Zagreb). I have known Dr. Tajima for five years since he was a postdoc researcher in RIKEN, and his research was really stimulating for me. After he joined the Liang Group in U. Tokyo as an assistant professor, we started regularly discussions, which has been even more stimulating for me. I have known Dr. Oishi for three years and started to discuss when I visited U. Zagreb. He has a deeper knowledge of covariant density functional theory in nuclear physics, and we eventually started a collaboration. I am also grateful for valuable comments on this thesis by Prof. Koichi Yazaki

(RIKEN/U. Tokyo). Although I have not discussed any detailed topic with him yet, he has always kindly given suggestive advice and encouraged me.

My special thanks go to Dr. Tetsuo Hatsuda (RIKEN), Dr. Masahiko Iwasaki (RIKEN), Prof. Hiroyoshi Sakurai (RIKEN/U. Tokyo), and Dr. Tsukasa Tada (RIKEN) for their warmful hospitality at my visiting position ("student trainee") at the RIKEN Nishina Center. My special thanks also go to Prof. Yasuhiro Sakemi (U. Tokyo) for his kind hospitality at regular seminar series in his group. Other special thanks go to all my collaborators: Mr. Giacomo Accorto (U. Zagreb), Ms. Maureen Ciccarelli (U. Lille), Dr. Shimpei Endo (Tohoku U.), Dr. Yuichi Hirata (Private Company), Prof. Naoyuki Itagaki (Kyoto U.), Prof. Yoshikazu Ito (U. Tsukuba), Dr. Yoshihiko Kobayashi (Oita U.), Prof. Mikito Koshino (Osaka U.), Prof. Wen Hui Long (Lanzhou U.), Dr. Futoshi Minato (JAEA), Prof. Tamara Nikšić (U. Zagreb), Dr. Nobuya Nishimura (RIKEN), Mr. Daisuke Ohashi (Private Company), Dr. Hajime Sotani (RIKEN), Prof. Yoichi Tanabe (Okayama U. Science), Dr. Junki Tanaka (RIKEN), Dr. Yusuke Tanimura (Tohoku U.), Dr. Tomohiro Uesaka (RIKEN), Prof. Dario Vretenar (U. Zagreb), Dr. Zhiheng Wang (Lanzhou U.), Dr. Takeru Yokota (RIKEN), Prof. Satoshi Yoshida (Hosei U.), and Prof. Juzo Zenihiro (Kyoto U.). I also thank the referees of the defense for fruitful suggestion during the defense: Prof. Nobuaki Imai (chair, U. Tokyo), Prof. Takumi Doi (RIKEN/U. Tokyo), Prof. Kenji Fukushima (U. Tokyo), Prof. Kentaro Yako (U. Tokyo), and Prof. Hidetoshi Yamaguchi (U. Tokyo).

At last, but not least, I would like to appreciate discussions on various topics, even apart from topics related to this thesis, with many people, especially, Dr. Takashi Abe (RIKEN), Mr. Giancarlo Agnelli (Private Company), Dr. Kazuhiko Akiyama (Tokyo Metropolitan U.), Dr. Noboru Aoyagi (JAEA), Dr. Takeshi Aoyagi (AIST), Prof. Yoshihiro Aritomo (Kindai U.), Prof. Koichiro Asahi (RIKEN), Dr. Masato Asai (JAEA), Dr. Toshiyuki Azuma (RIKEN), Prof. Carlo Barbieri (U. Milan/INFN Milano), Prof. Aurel Bulgac (U. Washington), Dr. Yohei Chiba (Osaka City U.), Prof. Bhanu Pratap Das (TCG CREST), Dr. Keisuke Fujii (Kyoto U.), Dr. Junji Fujimoto (KITS, UCAS), Dr. Tokuro Fukui (RIKEN), Dr. Zhigang Ge (CIAE), Prof. Lisheng Geng (BUAA), Prof. Shin-ichi Goto (Niigata U.), Dr. Yukimi Goto (RIKEN), Mr. Yixin Guo (U. Tokyo), Dr. Hiromitsu Haba (RIKEN), Mr. Naoto Hasegawa (Tohoku U.), Dr. Yuichi Hatsukawa (QST), Dr. Tomohiro Hayamizu (RIKEN), Dr. Nobuo Hinohara (U. Tsukuba), Mr. Yuma Hizume (U. Tokyo), Dr. Masaru Hongo (U. Illinois Chicago/RIKEN), Dr. Shiqi Hu (IOP, CAS), Prof. Yuichi Ichikawa (Kyushu U.), Prof. Kei Iida (Kochi U.), Dr. Nobuki Inoue (RIKEN), Dr. Yuta Ito (JAEA), Dr. Jun-Ichi Iwata (Private Company), Prof. Yoshiko Kanada-En'yo (Kyoto U.), Dr. Masashi Kaneko (JAEA), Dr. Konstantinos Karakatsanis (U. Zagreb), Prof. Yoshitaka Kasamatsu (Osaka U.), Mr. Haruki Kasuya (Kyoto U.), Prof. Daiji Kato (NIFS), Prof. Takeo Kato (U. Tokyo), Dr. Yuichiro Kato (RIKEN), Prof. Hidetoshi Kikunaga (Tohoku U.), Prof. Masaaki Kimura (Hokkaido U./RIKEN), Prof. Masaaki Kitaguchi (Nagoya U.), Dr. Teppei Kitahara (Nagoya U.), Dr. Hiroki Kodama (Tohoku U./RIKEN), Dr. Hiroyuki Koura (JAEA), Dr. Bharat Kumar (NIT Rourkela), Prof. Teiji Kunihiro (Kyoto U.), Dr. Cristian Le Minh (U. Tokyo), Prof. Yang Lei (Southwest U. Sci. Tech.), Prof. Silvia Leoni (U. Milan/INFN Milano), Dr. Xinyue Li (Beijing Normal U.), Prof. Zhipan Li (Southwest U., China), Mr. Jia Liu (Lanzhou U.), Dr. Xinbao Liu (IOP, CAS), Prof. Zhong Liu (IMP, CAS), Dr. Diwen Luo (Peking U.), Mr. Yan Lyu (Peking U.), Prof. Peter Maksym (U. Tokyo/U. Leicester), Prof. Masakazu Matsumoto (Okayama U.), Ms. Moemi Matsumoto (Tohoku U.), Dr. Munehisa Matsumoto (KEK), Mr. Riku Matsumura (Saitama U.), Prof. Mamoru Matsuo (KITS, UCAS), Prof. Masayuki Matsuo (Niigata U.), Prof. Jie Meng (Peking U.), Dr. Keita Mikami (RIKEN), Ms. Midori Miwa (Saitama U.), Dr. Yutaka Miyamoto (JAEA), Prof. Hiroari Miyatake (KEK), Dr. Hiroyasu Miyazaki (RIKEN), Dr. Kazuhito Mizuyama (Duy Tan U.), Prof. Kosuke Morita (Kyushu U./RIKEN), Dr. Yuichiro Nagame (JAEA), Prof. Hitoshi Nakada (Chiba U.), Prof. Takashi Nakatsukasa (U. Tsukuba), Dr. Hiroki Nagahama (U. Tokyo), Prof. Hisashi Naito (Nagoya U.), Dr. Megumi Niikura (U. Tokyo), Prof. Kazuhiko Ninomiya (Osaka U.), Dr. Makiko Nio (RIKEN), Dr. Shunji Nishimura (RIKEN), Dr. Katsuhisa Nishio (JAEA), Prof. Yifei Niu (Lanzhou U.), Prof. Zhongming Niu (Anhui U.), Ms. Honoka Obata (QST), Dr. Tetsuya Ohnishi (RIKEN), Dr. Tatsuhiko Ohto (Osaka U.), Dr. Yuya Ominato (KITS, UCAS), Dr. Natalia S. Oreshkina (MPI), Mr. Daigo Oue (Imperial Colledge London), Prof. Taisuke Ozaki (U. Tokyo), Mr. Naoya Ozawa (U. Tokyo), Dr. Zhengxue Ren (Peking U.), Prof. Peter Ring (U. Munich), Mr. Riccardo Romano (Private Company), Ms. Yu-Ting Rong (UCAS), Mr. Takeshi Saito (U. Tokyo), Prof. Satoshi Sakaguchi (Kyushu U.), Dr. Koichi Sato (Kochi U.), Dr. Shunsuke A. Sato (U. Tsukuba), Dr. Tetsuya K. Sato (JAEA), Dr. Yukihiko Satou (JAEA), Prof. Kazuyuki Sekizawa (Tokyo Tech.), Dr. Shihang Shen (Forschungszentrum Jülich), Dr. Yudai Shigekawa (RIKEN), Dr. Hiroshi Shinaoka (Saitama U.), Prof. Hirohiko M. Shimizu

(Nagoya U.), Prof. Noritaka Shimizu (U. Tokyo), Prof. Susumu Shimoura (U. Tokyo), Prof. Toshimi Suda (Tohoku U.), Prof. Osamu Sugino (U. Tokyo), Dr. Ayaki Sunaga (Kyoto U.), Prof. Toshio Suzuki (Tohoku U.), Prof. Masaomi Tanaka (Tohoku U.), Dr. Minoru Tanaka (Osaka U.), Mr. Shoya Tanaka (Kindai U./JAEA), Prof. Hajime Tanuma (Tokyo Metropolitan U.), Prof. Tatsuya Tate (Tohoku U.), Prof. Akihiro Tohsaki (Osaka U.), Dr. Masaaki Tokieda (INRIA), Dr. Hui Tong (Tianjin Normal U.), Dr. Kazuaki Tsukada (JAEA), Prof. Kyo Tsukada (Kyoto U.), Ms. Rieko Tsunoda (U. Tokyo), Dr. Yutaka Utsuno (JAEA), Prof. Enrico Vigezzi (INFN Milano), Prof. Tomotsugu Wakasa (Kyushu U.), Mr. Chencan Wang (Nankai U.), Dr. Sibo Wang (Chongqing U.), Mr. Eisuke Watanabe (Osaka U.), Ms. Hikari Wauke (Tohoku U.), Prof. Cheng-Jun Xia (Zhejiang U.), Dr. Bingwu Xiong (Peking U.), Prof. Masayuki Yamagami (U. Aizu), Dr. Yasuhiro Yamamoto (NCTS), Dr. Nodoka Yamanaka (Nagoya U.), Dr. Kota Yanase (U. Tokyo), Dr. Di-Lun Yang (Academia Sinica), Dr. Lei Yang (CIAE), Dr. Zuxing Yang (RIKEN), Dr. Kenichiro Yasuda (JAEA), Prof. Nobutoshi Yasutake (Chiba Tech.), Dr. Kenichi Yoshida (Kyoto U.), Mr. Kaiyuan Zhang (Peking U.), Dr. Shengjie Zhang (IOP, CAS), Prof. Shuangquan Zhang (Peking U.), Mr. Tingyu Zhang (U. Tokyo), Dr. Yiming Zhang (IOP, CAS), Prof. Pengwei Zhao (Peking U.), Dr. Qiang Zhao (Peking U.), and Prof. Shan-Gui Zhou (ITP, CAS).

This work is supported by the JSPS Grant-in-Aid for JSPS Fellows under Grant No. 19J20543. The numerical calculations were performed on cluster computers at the RIKEN iTHEMS program. I am also grateful for kind hospitality at Yukawa Institute for Theoretical Physics, Kyoto University (Japan), School of Physics, Peking University (China), Institute of Theoretical Physics, Chinese Academy of Sciences (China), Kavli Institute for Theoretical Science, University of Chinese Academy of Sciences (China), School of Physics and Material Science, Anhui University (China), Department of Physics, University of Zagreb (Croatia), Dipartimento di Fisica “Aldo Pontremoli”, Università degli Studi di Milano (Italy), and Sezione di Milano, Istituto Nazionale di Fisica Nucleare (Italy).

Publication List

Original Papers Involved in This Thesis

[A1] Tomoya Naito, Ryosuke Akashi, and Haozhao Liang.
"Application of a Coulomb energy density functional for atomic nuclei: Case studies of local density approximation and generalized gradient approximation"
Phys. Rev. C **97**, 044319 (2018).

[A2] Tomoya Naito, Xavier Roca-Maza, Gianluca Colò, and Haozhao Liang.
"Coulomb exchange functional with generalized gradient approximation for self-consistent Skyrme Hartree-Fock calculations"
Phys. Rev. C **99**, 024309 (2019).

[A3] Tomoya Naito, Xavier Roca-Maza, Gianluca Colò, and Haozhao Liang.
"Effects of finite nucleon size, vacuum polarization, and electromagnetic spin-orbit interaction on nuclear binding energies and radii in spherical nuclei"
Phys. Rev. C **101**, 064311 (2020).

[A4] Tomoya Naito, Gianluca Colò, Haozhao Liang, Xavier Roca-Maza, and Hiroyuki Sagawa.
"Toward *ab initio* charge symmetry breaking in nuclear energy density functionals"
Phys. Rev. C **105**, L021304 (2022).

[A5] Tomoya Naito.
"Effects of finite-light-speed correction for the Coulomb interaction on nuclear binding energies and radii in spherical nuclei"
arXiv:2106.14270 [nucl-th].

[A6] Tomoya Naito, Gianluca Colò, Haozhao Liang, Xavier Roca-Maza, and Hiroyuki Sagawa.
"Effects of Coulomb and isospin symmetry breaking interactions on binding energies and neutron-skin thickness"
To Be Submitted.

Original Papers Involved Only in Introduction of This Thesis

[A7] Takeru Yokota and Tomoya Naito.
"Functional-renormalization-group aided density functional analysis for the correlation energy of the two-dimensional homogeneous electron gas"
Phys. Rev. B **99**, 115106 (2019).

[A8] Tomoya Naito, Daisuke Ohashi, and Haozhao Liang.
"Improvement of functionals in density functional theory by the inverse Kohn–Sham method and density functional perturbation theory"
J. Phys. B **52**, 245003 (2019).

[A9] Takeru Yokota and Tomoya Naito.
"*Ab initio* construction of the energy density functional for electron systems with the functional-renormalization-group-aided density functional theory"
Phys. Rev. Research **3**, L012015 (2021).

[A10] Tomoya Naito, Shimpei Endo, Kouichi Hagino, and Yusuke Tanimura.
"On the deformability of atoms—comparative study between atoms and atomic nuclei"
J. Phys. B **54**, 165201 (2021).

[A11] Takeru Yokota and Tomoya Naito.
"Construction of energy density functional for arbitrary spin polarization using functional renormalization group"
Phys. Rev. B **105**, 035105 (2022).

[A12] Hajime Sotani, Nobuya Nishimura, and Tomoya Naito.
"New constraints on the neutron-star mass and radius relation from the terrestrial nuclear experiments"
Submitted.

Original Papers Referred in This Thesis

[A13] Tomoya Naito, Ryosuke Akashi, Haozhao Liang, and Shinji Tsuneyuki.
"Relativistic density functional theory with finite-light-speed correction for the Coulomb interaction: a non-relativistic-reduction-based approach"
J. Phys. B **53**, 215002 (2020).

[A14] Naoyuki Itagaki and Tomoya Naito.
"Consistent description for cluster dynamics and single-particle correlation"
Phys. Rev. C **103**, 044303 (2021).

[A15] Giacomo Accorto, Tomoya Naito, Haozhao Liang, Tamara Nikšić, and Dario Vretenar.
"Nuclear energy density functionals from empirical ground-state densities"
Phys. Rev. C **103**, 044304 (2021).

[A16] Zhiheng Wang, Tomoya Naito, Haozhao Liang, and Wen Hui Long.
"Exploring effects of tensor force and its strength via neutron drops"
Chin. Phys. C **45**, 064103 (2021).

[A17] Zhiheng Wang, Tomoya Naito, and Haozhao Liang.
"Tensor-force effects on shell-structure evolution in $N = 82$ isotones and $Z = 50$ isotopes in the relativistic Hartree-Fock theory"
Phys. Rev. C **103**, 064326 (2021).

[A18] Tomoya Naito, Gianluca Colò, Haozhao Liang, and Xavier Roca-Maza.
"Second and fourth moments of the charge density and neutron-skin thickness of atomic nuclei"
Phys. Rev. C **104**, 024316 (2021).

[A19] Naoyuki Itagaki, Tomoya Naito, and Yuichi Hirata.
"Persistence of cluster structure in the ground state of ^{11}B"
Phys. Rev. C **105**, 024304 (2022).

[A20] Hiroyuki Sagawa, Satoshi Yoshida, Tomoya Naito, Tomohiro Uesaka, Juzo Zenihiro, and Junki Tanaka.
"Isovector density and isospin impurity in ^{40}Ca"
arXiv:2112.06169 [nucl-th].

Other Original Papers

[A21] Zhiheng Wang, Tomoya Naito, Haozhao Liang, and Wen Hui Long.
"Self-consistent random-phase approximation based on the relativistic Hartree-Fock theory: Role of ρ-tensor coupling"
Phys. Rev. C **101**, 064306 (2020).

[A22] Maureen Ciccarelli, Futoshi Minato, and Tomoya Naito.
"Theoretical study of Nb isotope productions by muon capture reaction on ^{100}Mo"
Phys. Rev. C **102**, 034306 (2020).

[A23] Yoichi Tanabe, Yoshikazu Ito, Katsuaki Sugawara, Mikito Koshino, Shojiro Kimura, Tomoya Naito, Isaac Johnson, Takashi Takahashi, and Mingwei Chen.
"Dirac Fermion Kinetics in 3D Curved Graphene"
Adv. Mater. **32**, 2005838 (2020).

Conference Proceedings

[B1] Tomoya Naito, Ryosuke Akashi, Gianluca Colò, Haozhao Liang, and Xavier Roca-Maza.
"Coulomb Energy Density Functionals for Nuclear Systems: Recent Studies of Coulomb Exchange and Correlation Functionals"
EPJ Web Conf. **223**, 01044 (2019).
IV International Conference on Nuclear Structure and Dynamics (NSD2019) (Venice, Italy)

[B2] Tomoya Naito, Daisuke Ohashi, and Haozhao Liang.
"How to Improve Functionals in Density Functional Theory? —Formalism and Benchmark Calculation—"
J. Phys. Conf. Ser. **1643**, 012149 (2020).
International Nuclear Physics Conference 2019 (INPC2019) (Glasgow, United Kingdom)

Others

[C1] Tomoya Naito, Kouichi Hagino, and Yoshihiko Kobayashi.
"History of Sign Convention of Isospin" (in Japanese, "アイソスピンの符号の慣習をめぐって")
Butsuri (日本物理学会誌) **77**, 99 (2022).

Bibliography

[1] B. Cassen and E. U. Condon, "On Nuclear Forces", *Phys. Rev.* **50**, 846 (1936).

[2] S.-i. Tomonaga, "On the Effect of the Field Reactions on the Interaction of Mesotrons and Nuclear Particles, I", *Prog. Theor. Phys.* **1**, 83 (1946).

[3] T. Nakano and K. Nishijima, "Charge Independence for V-particles", *Prog. Theor. Phys.* **10**, 581 (1953).

[4] M. Gell-Mann, "Isotopic Spin and New Unstable Particles", *Phys. Rev.* **92**, 833 (1953).

[5] K. Nishijima, "Charge Independence Theory of V Particles", *Prog. Theor. Phys.* **13**, 285 (1955).

[6] M. Gell-Mann, "The interpretation of the new particles as displaced charge multiplets", *Nuovo Cim.* **4**, 848 (1956).

[7] W. Heisenberg, "Über den Bau der Atomkerne. I", *Z. Phys.* **77**, 1 (1932).

[8] E. Wigner, "On the Consequences of the Symmetry of the Nuclear Hamiltonian on the Spectroscopy of Nuclei", *Phys. Rev.* **51**, 106 (1937).

[9] M. Gell-Mann, "A schematic model of baryons and mesons", *Phys. Lett.* **8**, 214 (1964).

[10] P. A. Zyla, R. M. Barnett, J. Beringer, O. Dahl, D. A. Dwyer, D. E. Groom, C.-J. Lin, K. S. Lugovsky, E. Pianori, D. J. Robinson, *et al.*, "Review of Particle Physics", *Prog. Theor. Exp. Phys.* **2020**, 083C01 (2020).

[11] A. Obertelli and H. Sagawa, *Modern Nuclear Physics* (Springer, Singapore, 2021).

[12] S. Weinberg, *The Quantum Theory of Fields* (Cambridge University Press, Cambridge, 1995).

[13] R. B. Wiringa, R. A. Smith, and T. L. Ainsworth, "Nucleon-nucleon potentials with and without $\Delta(1232)$ degrees of freedom", *Phys. Rev. C* **29**, 1207 (1984).

[14] E. Gerjuoy and J. Schwinger, "On Tensor Forces and the Theory of Light Nuclei", *Phys. Rev.* **61**, 138 (1942).

[15] T. E. O. Ericson and M. Rosa-Clot, "D-State Admixture and Tensor Forces in Light Nuclei", *Annu. Rev. Nucl. Part. Sci.* **35**, 271 (1985).

[16] K. Ikeda, T. Myo, K. Kato, and H. Toki, "Di-Neutron Clustering and Deuteron-like Tensor Correlation in Nuclear Structure Focusing on ^{11}Li", in *Clusters in Nuclei: Volume 1*, edited by C. Beck (Springer-Verlag, Berlin, Heidelberg, 2010).

[17] T. Otsuka, T. Suzuki, R. Fujimoto, H. Grawe, and Y. Akaishi, "Evolution of Nuclear Shells due to the Tensor Force", *Phys. Rev. Lett.* **95**, 232502 (2005).

[18] T. Otsuka, T. Matsuo, and D. Abe, "Mean Field with Tensor Force and Shell Structure of Exotic Nuclei", *Phys. Rev. Lett.* **97**, 162501 (2006).

[19] D. Tarpanov, H. Liang, N. V. Giai, and C. Stoyanov, "Mean-field study of single-particle spectra evolution in $Z = 14$ and $N = 28$ chains", *Phys. Rev. C* **77**, 054316 (2008).

[20] M. Moreno-Torres, M. Grasso, H. Liang, V. De Donno, M. Anguiano, and N. Van Giai, "Tensor effects in shell evolution at Z, $N = 8, 20$, and 28 using nonrelativistic and relativistic mean-field theory", *Phys. Rev. C* **81**, 064327 (2010).

[21] H. Sagawa and G. Colò, "Tensor interaction in mean-field and density functional theory approaches to nuclear structure", *Prog. Part. Nucl. Phys.* **76**, 76 (2014).

[22] K. Karakatsanis, G. A. Lalazissis, P. Ring, and E. Litvinova, "Spin-orbit splittings of neutron states in $N = 20$ isotones from covariant density functionals and their extensions", *Phys. Rev. C* **95**, 034318 (2017).

[23] Z. Wang, Q. Zhao, H. Liang, and W. H. Long, "Quantitative analysis of tensor effects in the relativistic Hartree-Fock theory", *Phys. Rev. C* **98**, 034313 (2018).

[24] R. B. Wiringa and S. C. Pieper, "Evolution of Nuclear Spectra with Nuclear Forces", *Phys. Rev. Lett.* **89**, 182501 (2002).

[25] E. Wigner, "On the Mass Defect of Helium", *Phys. Rev.* **43**, 252 (1933).

[26] J. H. Bartlett, "Exchange Forces and the Structure of the Nucleus", *Phys. Rev.* **49**, 102 (1936).

[27] E. Majorana, "Über die Kerntheorie", *Z. Phys.* **82**, 137 (1933).

[28] H. Yukawa, "On the Interaction of Elementary Particles. I", *Proc. Phys. Math. Soc. Jpn. Third* **17**, 48 (1935).

[29] R. Machleidt, K. Holinde, and C. Elster, "The Bonn meson-exchange model for the nucleon–nucleon interaction", *Phys. Rep.* **149**, 1 (1987).

[30] R. Machleidt, "The Meson Theory of Nuclear Forces and Nuclear Structure", in *Advances in Nuclear Physics: Volume 19*, edited by J. W. Negele and E. Vogt (Springer US, Boston, 1989).

[31] M. Taketani, S. Nakamura, and M. Sasaki, "On the Method of the Theory of Nuclear Forces", *Prog. Theor. Phys.* **6**, 581 (1951).

[32] N. Hoshizaki, S. Otsuki, W. Watari, and M. Yonezawa, "Nuclear Forces and Bosons: The Sakata Model and One-Boson-Exchange-Potentials", *Prog. Theor. Phys.* **27**, 1199 (1962).

[33] S. Sawada, T. Ueda, W. Watari, and M. Yonezawa, "One Boson Exchange Model in Proton-Proton Scattering: An Approach to the Strong Interaction", *Prog. Theor. Phys.* **28**, 991 (1962).

[34] M. Taketani, S. Machida, and S. O-numa, "The Meson Theory of Nuclear Forces, I: The Deuteron Ground State and Low Energy Neutron-Proton Scattering", *Prog. Theor. Phys.* **7**, 45 (1952).

[35] J.-i. Fujita and H. Miyazawa, "Pion Theory of Three-Body Forces", *Prog. Theor. Phys.* **17**, 360 (1957).

[36] T. Otsuka, T. Suzuki, J. D. Holt, A. Schwenk, and Y. Akaishi, "Three-Body Forces and the Limit of Oxygen Isotopes", *Phys. Rev. Lett.* **105**, 032501 (2010).

[37] H.-W. Hammer, A. Nogga, and A. Schwenk, "Colloquium: Three-body forces: From cold atoms to nuclei", *Rev. Mod. Phys.* **85**, 197 (2013).

[38] S. Goudarzi and H. R. Moshfegh, "Effects of three-body forces on the maximum mass of neutron stars in the lowest-order constrained variational formalism", *Phys. Rev. C* **91**, 054320 (2015).

[39] R. Machleidt and D. Entem, "Chiral effective field theory and nuclear forces", *Phys. Rep.* **503**, 1 (2011).

[40] E. Epelbaum, "Nuclear forces from chiral effective field theory", *Prog. Part. Nucl. Phys.* **67**, 343 (2012).

[41] N. Ishii, S. Aoki, and T. Hatsuda, "Nuclear Force from Lattice QCD", *Phys. Rev. Lett.* **99**, 022001 (2007).

[42] S. Aoki, T. Hatsuda, and N. Ishii, "Theoretical Foundation of the Nuclear Force in QCD and Its Application to Central and Tensor Forces in Quenched Lattice QCD Simulations", *Prog. Theor. Phys.* **123**, 89 (2010).

[43] T. Hatsuda, "Hadron interactions from lattice QCD", *Prog. Part. Nucl. Phys.* **67**, 122 (2012).

[44] P. Navrátil, V. G. Gueorguiev, J. P. Vary, W. E. Ormand, and A. Nogga, "Structure of $A = 10$–13 Nuclei with Two- Plus Three-Nucleon Interactions from Chiral Effective Field Theory", *Phys. Rev. Lett.* **99**, 042501 (2007).

[45] Y. Z. Ma, F. R. Xu, L. Coraggio, B. S. Hu, J. G. Li, T. Fukui, L. De Angelis, N. Itaco, and A. Gargano, "Chiral three-nucleon force and continuum for dripline nuclei and beyond", *Phys. Lett. B* **802**, 135257 (2020).

[46] V. Somà, P. Navrátil, F. Raimondi, C. Barbieri, and T. Duguet, "Novel chiral Hamiltonian and observables in light and medium-mass nuclei", *Phys. Rev. C* **101**, 014318 (2020).

[47] L. Coraggio, G. De Gregorio, A. Gargano, N. Itaco, T. Fukui, Y. Z. Ma, and F. R. Xu, "Shell-model study of calcium isotopes toward their drip line", *Phys. Rev. C* **102**, 054326 (2020).

[48] K. Hebeler, J. M. Lattimer, C. J. Pethick, and A. Schwenk, "Constraints on Neutron Star Radii Based on Chiral Effective Field Theory Interactions", *Phys. Rev. Lett.* **105**, 161102 (2010).

[49] T. Iritani, T. Doi, S. Aoki, S. Gongyo, T. Hatsuda, Y. Ikeda, T. Inoue, N. Ishii, K. Murano, H. Nemura, *et al.*, "Mirage in temporal correlation functions for baryon-baryon interactions in lattice QCD", *J. High Energy Phys.* **2016**, 101 (2016).

[50] T. Iritani, S. Aoki, T. Doi, T. Hatsuda, Y. Ikeda, T. Inoue, N. Ishii, H. Nemura, and K. Sasaki, "Are two nucleons bound in lattice QCD for heavy quark masses? Consistency check with Lüscher's finite volume formula", *Phys. Rev. D* **96**, 034521 (2017).

[51] T. Iritani, S. Aoki, T. Doi, F. Etminan, S. Gongyo, T. Hatsuda, Y. Ikeda, T. Inoue, N. Ishii, T. Miyamoto, *et al.*, "$N\Omega$ dibaryon from lattice QCD near the physical point", *Phys. Lett. B* **792**, 284 (2019).

[52] Y. Lyu, H. Tong, T. Sugiura, S. Aoki, T. Doi, T. Hatsuda, J. Meng, and T. Miyamoto, "Dibaryon with Highest Charm Number near Unitarity from Lattice QCD", *Phys. Rev. Lett.* **127**, 072003 (2021).

[53] G. Baym, T. Hatsuda, T. Kojo, P. D. Powell, Y. Song, and T. Takatsuka, "From hadrons to quarks in neutron stars: a review", *Rep. Prog. Phys.* **81**, 056902 (2018).

[54] R. C. Tolman, "Effect of Inhomogeneity on Cosmological Models", *Proc. Natl. Acad. Sci. USA* **20**, 169 (1934).

[55] R. C. Tolman, "Static Solutions of Einstein's Field Equations for Spheres of Fluid", *Phys. Rev.* **55**, 364 (1939).

[56] J. R. Oppenheimer and G. M. Volkoff, "On Massive Neutron Cores", *Phys. Rev.* **55**, 374 (1939).

[57] J.-M. Dong, W. Zuo, and J.-Z. Gu, "First-Order Symmetry Energy Induced by Neutron—Proton Mass Difference", *Chin. Phys. Lett.* **33**, 102101 (2016).

[58] E. Chabanat, P. Bonche, P. Haensel, J. Meyer, and R. Schaeffer, "A Skyrme parametrization from subnuclear to neutron star densities Part II. Nuclei far from stabilities", *Nucl. Phys. A* **635**, 231 (1998).

[59] X. Roca-Maza, M. Centelles, X. Viñas, and M. Warda, "Neutron Skin of ^{208}Pb, Nuclear Symmetry Energy, and the Parity Radius Experiment", *Phys. Rev. Lett.* **106**, 252501 (2011).

[60] A. Tamii, I. Poltoratska, P. von Neumann-Cosel, Y. Fujita, T. Adachi, C. A. Bertulani, J. Carter, M. Dozono, H. Fujita, K. Fujita, *et al.*, "Complete Electric Dipole Response and the Neutron Skin in ^{208}Pb", *Phys. Rev. Lett.* **107**, 062502 (2011).

[61] X. Roca-Maza, M. Brenna, G. Colò, M. Centelles, X. Viñas, B. K. Agrawal, N. Paar, D. Vretenar, and J. Piekarewicz, "Electric dipole polarizability in ^{208}Pb: Insights from the droplet model", *Phys. Rev. C* **88**, 024316 (2013).

[62] N. Paar, C. C. Moustakidis, T. Marketin, D. Vretenar, and G. A. Lalazissis, "Neutron star structure and collective excitations of finite nuclei", *Phys. Rev. C* **90**, 011304 (2014).

[63] X. Roca-Maza, X. Viñas, M. Centelles, B. K. Agrawal, G. Colò, N. Paar, J. Piekarewicz, and D. Vretenar, "Neutron skin thickness from the measured electric dipole polarizability in ^{68}Ni, ^{120}Sn, and ^{208}Pb", *Phys. Rev. C* **92**, 064304 (2015).

[64] P. Danielewicz, "Surface symmetry energy", *Nucl. Phys. A* **727**, 233 (2003).

[65] M. A. Famiano, T. Liu, W. G. Lynch, M. Mocko, A. M. Rogers, M. B. Tsang, M. S. Wallace, R. J. Charity, S. Komarov, D. G. Sarantites, *et al.*, "Neutron and Proton Transverse Emission Ratio Measurements and the Density Dependence of the Asymmetry Term of the Nuclear Equation of State", *Phys. Rev. Lett.* **97**, 052701 (2006).

[66] A. Klimkiewicz, N. Paar, P. Adrich, M. Fallot, K. Boretzky, T. Aumann, D. Cortina-Gil, U. D. Pramanik, T. W. Elze, H. Emling, *et al.*, "Nuclear symmetry energy and neutron skins derived from pygmy dipole resonances", *Phys. Rev. C* **76**, 051603 (2007).

[67] L. Trippa, G. Colò, and E. Vigezzi, "Giant dipole resonance as a quantitative constraint on the symmetry energy", *Phys. Rev. C* **77**, 061304 (2008).

[68] M. Warda, X. Viñas, X. Roca-Maza, and M. Centelles, "Neutron skin thickness in the droplet model with surface width dependence: Indications of softness of the nuclear symmetry energy", *Phys. Rev. C* **80**, 024316 (2009).

[69] M. Centelles, X. Roca-Maza, X. Viñas, and M. Warda, "Nuclear Symmetry Energy Probed by Neutron Skin Thickness of Nuclei", *Phys. Rev. Lett.* **102**, 122502 (2009).

[70] M. B. Tsang, Y. Zhang, P. Danielewicz, M. Famiano, Z. Li, W. G. Lynch, and A. W. Steiner, "Constraints on the Density Dependence of the Symmetry Energy", *Phys. Rev. Lett.* **102**, 122701 (2009).

[71] A. Carbone, G. Colò, A. Bracco, L.-G. Cao, P. F. Bortignon, F. Camera, and O. Wieland, "Constraints on the symmetry energy and neutron skins from pygmy resonances in ^{68}Ni and ^{132}Sn", *Phys. Rev. C* **81**, 041301 (2010).

[72] L.-W. Chen, C. M. Ko, B.-A. Li, and J. Xu, "Density slope of the nuclear symmetry energy from the neutron skin thickness of heavy nuclei", *Phys. Rev. C* **82**, 024321 (2010).

[73] J. Zenihiro, H. Sakaguchi, T. Murakami, M. Yosoi, Y. Yasuda, S. Terashima, Y. Iwao, H. Takeda, M. Itoh, H. P. Yoshida, *et al.*, "Neutron density distributions of ^{204,206,208}Pb deduced via proton elastic scattering at $E_p = 295$ MeV", *Phys. Rev. C* **82**, 044611 (2010).

[74] C. Xu, B.-A. Li, and L.-W. Chen, "Symmetry energy, its density slope, and neutron-proton effective mass splitting at normal density extracted from global nucleon optical potentials", *Phys. Rev. C* **82**, 054607 (2010).

[75] A. W. Steiner, J. M. Lattimer, and E. F. Brown, "The Equation of State from Observed Masses and Radii of Neutron Stars", *Astrophys. J.* **722**, 33 (2010).

[76] S. Gandolfi, J. Carlson, and S. Reddy, "Maximum mass and radius of neutron stars, and the nuclear symmetry energy", *Phys. Rev. C* **85**, 032801 (2012).

[77] P. Möller, W. D. Myers, H. Sagawa, and S. Yoshida, "New Finite-Range Droplet Mass Model and Equation-of-State Parameters", *Phys. Rev. Lett.* **108**, 052501 (2012).

[78] S. Abrahamyan, Z. Ahmed, H. Albataineh, K. Aniol, D. S. Armstrong, W. Armstrong, T. Averett, B. Babineau, A. Barbieri, V. Bellini, *et al.*, "Measurement of the Neutron Radius of ^{208}Pb through Parity Violation in Electron Scattering", *Phys. Rev. Lett.* **108**, 112502 (2012).

[79] B. K. Agrawal, J. N. De, and S. K. Samaddar, "Determining the Density Content of Symmetry Energy and Neutron Skin: An Empirical Approach", *Phys. Rev. Lett.* **109**, 262501 (2012).

[80] X. Roca-Maza, M. Brenna, B. K. Agrawal, P. F. Bortignon, G. Colò, L.-G. Cao, N. Paar, and D. Vretenar, "Giant quadrupole resonances in ^{208}Pb, the nuclear symmetry energy, and the neutron skin thickness", *Phys. Rev. C* **87**, 034301 (2013).

[81] B.-A. Li and X. Han, "Constraining the neutron-proton effective mass splitting using empirical constraints on the density dependence of nuclear symmetry energy around normal density", *Phys. Lett. B* **727**, 276 (2013).

[82] J. M. Lattimer and Y. Lim, "Constraining the Symmetry Parameters of the Nuclear Interaction", *Astrophys. J.* **771**, 51 (2013).

[83] C. M. Tarbert, D. P. Watts, D. I. Glazier, P. Aguar, J. Ahrens, J. R. M. Annand, H. J. Arends, R. Beck, V. Bekrenev, B. Boillat, *et al.*, "Neutron Skin of ^{208}Pb from Coherent Pion Photoproduction", *Phys. Rev. Lett.* **112**, 242502 (2014).

[84] P. Danielewicz and J. Lee, "Symmetry energy II: Isobaric analog states", *Nucl. Phys. A* **922**, 1 (2014).

[85] X. Roca-Maza, L.-G. Cao, G. Colò, and H. Sagawa, "Fully self-consistent study of charge-exchange resonances and the impact on the symmetry energy parameters", *Phys. Rev. C* **94**, 044313 (2016).

[86] M. Oertel, M. Hempel, T. Klähn, and S. Typel, "Equations of state for supernovae and compact stars", *Rev. Mod. Phys.* **89**, 015007 (2017).

[87] X. Roca-Maza and N. Paar, "Nuclear equation of state from ground and collective excited state properties of nuclei", *Prog. Part. Nucl. Phys.* **101**, 96 (2018).

[88] H. Sotani, K. Iida, and K. Oyamatsu, "Constraints on the nuclear equation of state and the neutron star structure from crustal torsional oscillations", *Mon. Not. R. Astron Soc.* **479**, 4735 (2018).

[89] H. Sotani, K. Iida, and K. Oyamatsu, "Astrophysical implications of double-layer torsional oscillations in a neutron star crust as a lasagna sandwich", *Mon. Not. R. Astron Soc.* **489**, 3022 (2019).

[90] S. Tagami, T. Wakasa, J. Matsui, M. Yahiro, and M. Takechi, "Neutron skin thickness of ^{208}Pb determined from the reaction cross section for proton scattering", *Phys. Rev. C* **104**, 024606 (2021).

[91] J. Estee, W. G. Lynch, C. Y. Tsang, J. Barney, G. Jhang, M. B. Tsang, R. Wang, M. Kaneko, J. W. Lee, T. Isobe, *et al.*, "Probing the Symmetry Energy with the Spectral Pion Ratio", *Phys. Rev. Lett.* **126**, 162701 (2021).

[92] D. Adhikari, H. Albataineh, D. Androic, K. Aniol, D. S. Armstrong, T. Averett, C. Ayerbe Gayoso, S. Barcus, V. Bellini, R. S. Beminiwattha, *et al.*, "Accurate Determination of the Neutron Skin Thickness of ^{208}Pb through Parity-Violation in Electron Scattering", *Phys. Rev. Lett.* **126**, 172502 (2021).

[93] B. T. Reed, F. J. Fattoyev, C. J. Horowitz, and J. Piekarewicz, "Implications of PREX-2 on the Equation of State of Neutron-Rich Matter", *Phys. Rev. Lett.* **126**, 172503 (2021).

[94] P.-G. Reinhard, X. Roca-Maza, and W. Nazarewicz, "Information Content of the Parity-Violating Asymmetry in ^{208}Pb", *Phys. Rev. Lett.* **127**, 232501 (2021).

[95] K. Oyamatsu, H. Sotani, and K. Iida, "Neutron Star Structure Explored with A Family of Unified Equations of State of Neutron Star Matter", *Proc. Sci.* **281**, 136 (2017).

[96] C. P. Lorenz, D. G. Ravenhall, and C. J. Pethick, "Neutron star crusts", *Phys. Rev. Lett.* **70**, 379 (1993).

[97] E. Chabanat, *Interactions effectivespour desconditions extrêmes d'isospin*, PhD Thesis (Université Claude Bernard Lyon 1, 1995).

[98] E. Chabanat, P. Bonche, P. Haensel, J. Meyer, and R. Schaeffer, "A Skyrme parametrization from subnuclear to neutron star densities", *Nucl. Phys. A* **627**, 710 (1997).

[99] H. Shen, H. Toki, K. Oyamatsu, and K. Sumiyoshi, "Relativistic equation of state of nuclear matter for supernova and neutron star", *Nucl. Phys. A* **637**, 435 (1998).

[100] H. T. Cromartie, E. Fonseca, S. M. Ransom, P. B. Demorest, Z. Arzoumanian, H. Blumer, P. R. Brook, M. E. DeCesar, T. Dolch, J. A. Ellis, *et al.*, "Relativistic Shapiro delay measurements of an extremely massive millisecond pulsar", *Nat. Astron.* **4**, 72 (2020).

[101] E. Fonseca, H. T. Cromartie, T. T. Pennucci, P. S. Ray, A. Y. Kirichenko, S. M. Ransom, P. B. Demorest, I. H. Stairs, Z. Arzoumanian, L. Guillemot, *et al.*, "Refined Mass and Geometric Measurements of the High-mass PSR J0740+6620", *Astrophys. J. Lett.* **915**, L12 (2021).

[102] E. Annala, T. Gorda, A. Kurkela, and A. Vuorinen, "Gravitational-wave constraints on the neutron-star-matter equation of state", *Phys. Rev. Lett.* **120**, 172703 (2018).

[103] T. E. Riley, A. L. Watts, S. Bogdanov, P. S. Ray, R. M. Ludlam, S. Guillot, Z. Arzoumanian, C. L. Baker, A. V. Bilous, D. Chakrabarty, *et al.*, "A NICER View of PSR J0030+0451: Millisecond Pulsar Parameter Estimation", *Astrophys. J. Lett.* **887**, L21 (2019).

[104] M. C. Miller, F. K. Lamb, A. J. Dittmann, S. Bogdanov, Z. Arzoumanian, K. C. Gendreau, S. Guillot, A. K. Harding, W. C. G. Ho, J. M. Lattimer, *et al.*, "PSR J0030+0451 Mass and Radius from NICER Data and Implications for the Properties of Neutron Star Matter", *Astrophys. J. Lett.* **887**, L24 (2019).

[105] D. Blaschke, A. Ayriyan, D. E. Alvarez-Castillo, and H. Grigorian, "Was GW170817 a Canonical Neutron Star Merger? Bayesian Analysis with a Third Family of Compact Stars", *Universe* **6**, 81 (2020).

[106] A. W. Steiner, J. M. Lattimer, and E. F. Brown, "The Neutron Star Mass-Radius Relation and The Equation of State of Dense Matter", *Astrophys. J. Lett.* **765**, L5 (2013).

[107] J. M. Lattimer, "The Nuclear Equation of State and Neutron Star Masses", *Annu. Rev. Nucl. Part. Sci.* **62**, 485 (2012).

[108] H. Sotani, K. Iida, K. Oyamatsu, and A. Ohnishi, "Mass and radius formulas for low-mass neutron stars", *Prog. Theor. Exp. Phys.* **2014**, 051E01 (2014).

[109] C. F. v. Weizsäcker, "Zur Theorie der Kernmassen", *Z. Phys.* **96**, 431 (1935).

[110] H. A. Bethe and R. F. Bacher, "Nuclear Physics A. Stationary States of Nuclei", *Rev. Mod. Phys.* **8**, 82 (1936).

[111] O. Haxel, J. H. D. Jensen, and H. E. Suess, "On the "Magic Numbers" in Nuclear Structure", *Phys. Rev.* **75**, 1766 (1949).

[112] M. G. Mayer, "Nuclear Configurations in the Spin-Orbit Coupling Model. I. Empirical Evidence", *Phys. Rev.* **78**, 16 (1950).

[113] M. G. Mayer, "Nuclear Configurations in the Spin-Orbit Coupling Model. II. Theoretical Considerations", *Phys. Rev.* **78**, 22 (1950).

[114] A. Bohr, B. R. Mottelson, and D. Pines, "Possible Analogy between the Excitation Spectra of Nuclei and Those of the Superconducting Metallic State", *Phys. Rev.* **110**, 936 (1958).

[115] P. Van Isacker and D. D. Warner, "$T = 0$ versus $T = 1$ Pairing in the Interacting Boson Model", *Phys. Rev. Lett.* **78**, 3266 (1997).

[116] R. R. Chasman, "*n*-*p*Pairing, Wigner Energy, and Shell Gaps", *Phys. Rev. Lett.* **99**, 082501 (2007).

[117] H. Sagawa, Y. Tanimura, and K. Hagino, "Competition between $T = 1$ and $T = 0$ pairing in pf-shell nuclei with $N = Z$", *Phys. Rev. C* **87**, 034310 (2013).

[118] I. Bentley and S. Frauendorf, "Relation between Wigner energy and proton-neutron pairing", *Phys. Rev. C* **88**, 014322 (2013).

[119] K. Yoshida, "Proton-neutron pairing vibrations in $N = Z$ nuclei: Precursory soft mode of isoscalar pairing condensation", *Phys. Rev. C* **90**, 031303 (2014).

[120] H. Sagawa, C. L. Bai, and G. Colò, "Isovector spin-singlet ($T = 1$, $S = 0$) and isoscalar spin-triplet ($T = 0$, $S = 1$) pairing interactions and spin-isospin response", *Phys. Scr.* **91**, 083011 (2016).

[121] A. Arima and H. Horie, "Configuration Mixing and Magnetic Moments of Nuclei", *Prog. Theor. Phys.* **11**, 509 (1954).

[122] H. Sagawa and B. A. Brown, "E2 core polarization for sd-shell single-particle states calculated with a skyrme-type interaction", *Nucl. Phys. A* **430**, 84 (1984).

[123] T. Minamisono, S. Fukuda, T. Ohtsubo, A. Kitagawa, Y. Nakayama, Y. Someda, S. Takeda, M. Fukuda, K. Matsuta, and Y. Nojiri, "Quadrupole moment of the doubly-closed-shell-plus-one-nucleon nucleus ^{41}Sc and its core deformation", *Nucl. Phys. A* **559**, 239 (1993).

[124] T. Minamisono, K. Matsuta, K. Minamisono, S. Kudo, M. Ogura, S. Fukuda, K. Sato, M. Mihara, and M. Fukuda, "Precise Quadrupole Moment of the Doubly Closed Shell Plus One Proton Nucleus ^{41}Sc", *Hyperfine Interact.* **136**, 225 (2001).

[125] T. Ohtsubo, N. J. Stone, J. R. Stone, I. S. Towner, C. R. Bingham, C. Gaulard, U. Köster, S. Muto, J. Nikolov, K. Nishimura, *et al.*, "Magnetic Dipole Moment of the Doubly-Closed-Shell Plus One Proton Nucleus ^{49}Sc", *Phys. Rev. Lett.* **109**, 032504 (2012).

[126] H. Morinaga, "Interpretation of Some of the Excited States of $4n$ Self-Conjugate Nuclei", *Phys. Rev.* **101**, 254 (1956).

[127] H. Morinaga, "On the spin of a broad state around 10 MeV in ^{12}C", *Phys. Lett.* **21**, 78 (1966).

[128] K. Ikeda, N. Takigawa, and H. Horiuchi, "The Systematic Structure-Change into the Molecule-like Structures in the Self-Conjugate $4n$ Nuclei", *Prog. Theor. Phys. Suppl.* **E68**, 464 (1968).

[129] N. Itagaki, T. Otsuka, K. Ikeda, and S. Okabe, "Equilateral-Triangular Shape in ^{14}C", *Phys. Rev. Lett.* **92**, 142501 (2004).

[130] W. von Oertzen, M. Freer, and Y. Kanada-En'yo, "Nuclear clusters and nuclear molecules", *Phys. Rep.* **432**, 43 (2006).

[131] M. Freer and H. O. U. Fynbo, "The Hoyle state in ^{12}C", *Prog. Part. Nucl. Phys.* **78**, 1 (2014).

[132] Y. Chiba, M. Kimura, and Y. Taniguchi, "Isoscalar dipole transition as a probe for asymmetric clustering", *Phys. Rev. C* **93**, 034319 (2016).

[133] R. Imai, T. Tada, and M. Kimura, "Real-time evolution method and its application to the 3α cluster system", *Phys. Rev. C* **99**, 064327 (2019).

[134] T. Baba and M. Kimura, "Variety of clustering in ^{18}O", *Phys. Rev. C* **100**, 064311 (2019).

[135] N. Tajima and N. Suzuki, "Prolate dominance of nuclear shape caused by a strong interference between the effects of spin-orbit and l^2 terms of the Nilsson potential", *Phys. Rev. C* **64**, 037301 (2001).

[136] I. Hamamoto and B. R. Mottelson, "Further examination of prolate-shape dominance in nuclear deformation", *Phys. Rev. C* **79**, 034317 (2009).

[137] S. Takahara, N. Onishi, Y. R. Shimizu, and N. Tajima, "The role of spin-orbit potential in nuclear prolate-shape dominance", *Phys. Lett. B* **702**, 429 (2011).

[138] K.-i. Arita, "Periodic-orbit approach to nuclear shell structures with power-law potential models: Bridge orbits and prolate-oblate asymmetry", *Phys. Rev. C* **86**, 034317 (2012).

[139] S. Takahara, N. Tajima, and Y. R. Shimizu, "Nuclear prolate-shape dominance with the Woods-Saxon potential", *Phys. Rev. C* **86**, 064323 (2012).

[140] J. Dobaczewski, W. Nazarewicz, J. Skalski, and T. Werner, "Nuclear Deformation: A Proton-Neutron Effect?", *Phys. Rev. Lett.* **60**, 2254 (1988).

[141] R. Hofstadter, H. R. Fechter, and J. A. McIntyre, "Scattering of High-Energy Electrons and the Method of Nuclear Recoil", *Phys. Rev.* **91**, 422 (1953).

[142] R. Hofstadter, H. R. Fechter, and J. A. McIntyre, "High-Energy Electron Scattering and Nuclear Structure Determinations", *Phys. Rev.* **92**, 978 (1953).

[143] R. Hofstadter, "Electron Scattering and Nuclear Structure", *Rev. Mod. Phys.* **28**, 214 (1956).

[144] H. De Vries, C. W. De Jager, and C. De Vries, "Nuclear charge-density-distribution parameters from elastic electron scattering", *At. Data Nucl. Data Tables* **36**, 495 (1987).

[145] T. Suda and H. Simon, "Prospects for electron scattering on unstable, exotic nuclei", *Prog. Part. Nucl. Phys.* **96**, 1 (2017).

[146] K. Tsukada, A. Enokizono, T. Ohnishi, K. Adachi, T. Fujita, M. Hara, M. Hori, T. Hori, S. Ichikawa, K. Kurita, *et al.*, "First Elastic Electron Scattering from ^{132}Xe at the SCRIT Facility", *Phys. Rev. Lett.* **118**, 262501 (2017).

[147] T. de Forest, Jr. and J. D. Walecka, "Electron scattering and nuclear structure", *Adv. Phys.* **15**, 1 (1966).

[148] J. Friedrich and T. Walcher, "A coherent interpretation of the form factors of the nucleon in terms of a pion cloud and constituent quarks", *Eur. Phys. J. A* **17**, 607 (2003).

[149] E. M. Henley, "Charge independece and charge symmetry of nuclear forces", in *Isospin in Nuclear Physics*, edited by D. H. Wilkinson (North-Holland, Amsterdam, 1969).

[150] E. M. Henley and G. A. Miller, "Meson theory of charge-dependent nuclear forces", in *Mesons in Nuclei: Volume I* edited by M. Rho and D. Wilkinson (North-Holland, Amsterdam, New York, Oxford, 1979).

[151] G. A. Miller, "Overview of charge symmetry", *AIP Conf. Proc.* **339**, 172 (1995).

[152] J. L. Friar and U. van Kolck, "Charge-independence breaking in the two-pion-exchange nucleon-nucleon force", *Phys. Rev. C* **60**, 034006 (1999).

[153] G. A. Miller, A. K. Opper, and E. J. Stephenson, "Charge Symmetry Breaking and QCD", *Annu. Rev. Nucl. Part. Sci.* **56**, 253 (2006).

[154] N. Kemmer, "The charge-dependence of nuclear forces", *Math. Proc. Camb. Philos. Soc.* **34**, 354 (1938).

[155] H. Yukawa, S. Sakata, M. Kobayasi, and M. Taketani, "On the Interaction of Elementary Particles. IV", *Proc. Phys. Math. Soc. Jpn. Third* **20**, 720 (1938).

[156] B. W. Downs and Y. Nogami, "Meson mixing and the charge asymmetry of the N-N interaction", *Nucl. Phys. B* **2**, 459 (1967).

[157] S. A. Coon, M. D. Scadron, and P. C. McNamee, "On the sign of the ρ-ω mixing charge asymmetric nn potential", *Nucl. Phys. A* **287**, 381 (1977).

[158] S. A. Coon and M. D. Scadron, "Role of $\pi^0\eta'$ mixing in nuclear charge asymmetry", *Phys. Rev. C* **26**, 562 (1982).

[159] S. A. Coon and M. D. Scadron, "Two-pion exchange contributions to charge asymmetric and charge dependent nuclear forces", *Phys. Rev. C* **26**, 2402 (1982).

[160] S. A. Coon and R. C. Barrett, "ρ-ω mixing in nuclear charge asymmetry", *Phys. Rev. C* **36**, 2189 (1987).

[161] J. A. Niskanen, "Charge symmetry breaking two-pion exchange", *Phys. Rev. C* **45**, 2648 (1992).

[162] U. van Kolck, "Isospin Violation in Low-energy Hadronic Physics", *Few-Body Syst. Suppl.* **9**, 444 (1995).

[163] E. Epelbaum and U.-G. Meißner, "Charge independence breaking and charge symmetry breaking in the nucleon-nucleon interaction from effective field theory", *Phys. Lett. B* **461**, 287 (1999).

[164] J. A. Niskanen, "Charge symmetry breaking in NN scattering with an interaction from effective field theory", *Phys. Rev. C* **65**, 037001 (2002).

[165] A. Gezerlis, I. Tews, E. Epelbaum, M. Freunek, S. Gandolfi, K. Hebeler, A. Nogga, and A. Schwenk, "Local chiral effective field theory interactions and quantum Monte Carlo applications", *Phys. Rev. C* **90**, 054323 (2014).

[166] A. Calle Cordón, M. Pavón Valderrama, and E. Ruiz Arriola, "Charge independence, charge symmetry breaking in the S-wave nucleon-nucleon interaction, and renormalization", *Phys. Rev. C* **85**, 024002 (2012).

[167] R. B. Wiringa, V. G. J. Stoks, and R. Schiavilla, "Accurate nucleon-nucleon potential with charge-independence breaking", *Phys. Rev. C* **51**, 38 (1995).

[168] N. Auerbach, "Coulomb effects in nuclear structure", *Phys. Rep.* **98**, 273 (1983).

[169] Y. Wu, S. Ishikawa, and T. Sasakawa, "Nuclear charge asymmetry and charge dependence and the ^{3}H-^{3}He binding-energy difference", *Phys. Rev. Lett.* **64**, 1875 (1990).

[170] T. Suzuki, H. Sagawa, and A. Arima, "Effects of valence nucleon orbits and charge symmetry breaking interaction on the Nolen-Schiffer anomally of mirror nuclei", *Nucl. Phys. A* **536**, 141 (1992).

[171] T. Suzuki, H. Sagawa, and N. Van Giai, "Charge independence and charge symmetry breaking interactions and the Coulomb energy anomaly in isobaric analog states", *Phys. Rev. C* **47**, R1360 (1993).

[172] K. Saito and A. W. Thomas, "The Nolen-Schiffer anomaly and isospin symmetry breaking in nuclear matter", *Phys. Lett. B* **335**, 17 (1994).

[173] M. H. Shahnas, "Nolen-Schiffer anomaly of mirror nuclei and charge symmetry breaking in nuclear interactions", *Phys. Rev. C* **50**, 2346 (1994).

[174] H. Sagawa, N. Van Giai, and T. Suzuki, "Isospin mixing and the sum rule of super-allowed fermi β decay", *Phys. Lett. B* **353**, 7 (1995).

[175] B. A. Brown, "New Skyrme interaction for normal and exotic nuclei", *Phys. Rev. C* **58**, 220 (1998).

[176] H. Müther, A. Polls, and R. Machleidt, "Isospin symmetry breaking nucleon-nucleon potentials and nuclear structure", *Phys. Lett. B* **445**, 259 (1999).

[177] B. A. Brown, W. A. Richter, and R. Lindsay, "Displacement energies with the Skyrme Hartree-Fock method", *Phys. Lett. B* **483**, 49 (2000).

[178] K. Kaneko, S. Tazaki, T. Mizusaki, Y. Sun, M. Hasegawa, and G. de Angelis, "Isospin symmetry breaking at high spins in the mirror pair ^{67}Se and ^{67}As", *Phys. Rev. C* **82**, 061301 (2010).

[179] K. Kaneko, T. Mizusaki, Y. Sun, S. Tazaki, and G. de Angelis, "Coulomb Energy Difference as a Probe of Isospin-Symmetry Breaking in the Upper fp-Shell Nuclei", *Phys. Rev. Lett.* **109**, 092504 (2012).

[180] K. Kaneko, Y. Sun, T. Mizusaki, and S. Tazaki, "Variation in Displacement Energies Due to Isospin-Nonconserving Forces", *Phys. Rev. Lett.* **110**, 172505 (2013).

[181] K. Kaneko, Y. Sun, T. Mizusaki, and S. Tazaki, "Isospin nonconserving interaction in the $T = 1$ analogue states of the mass-70 region", *Phys. Rev. C* **89**, 031302 (2014).

[182] K. Kaneko, Y. Sun, T. Mizusaki, S. Tazaki, and S. K. Ghorui, "Isospin-symmetry breaking in super-allowed Fermi β-decay due to isospin-nonconserving forces", *Phys. Lett. B* **773**, 521 (2017).

[183] X. Roca-Maza, G. Colò, and H. Sagawa, "Nuclear Symmetry Energy and the Breaking of the Isospin Symmetry: How Do They Reconcile with Each Other?", *Phys. Rev. Lett.* **120**, 202501 (2018).

[184] J. M. Dong, Y. H. Zhang, W. Zuo, J. Z. Gu, L. J. Wang, and Y. Sun, "Generalized isobaric multiplet mass equation and its application to the Nolen-Schiffer anomaly", *Phys. Rev. C* **97**, 021301 (2018).

[185] P. Bączyk, J. Dobaczewski, M. Konieczka, W. Satuła, T. Nakatsukasa, and K. Sato, "Isospin-symmetry breaking in masses of $N \simeq Z$ nuclei", *Phys. Lett. B* **778**, 178 (2018).

[186] J. M. Dong, X. L. Shang, W. Zuo, Y. F. Niu, and Y. Sun, "An effective Coulomb interaction in nuclear energy density functionals", *Nucl. Phys. A* **983**, 133 (2019).

[187] P. Bączyk, W. Satuła, J. Dobaczewski, and M. Konieczka, "Isobaric multiplet mass equation within nuclear density functional theory", *J. Phys. G* **46**, 03LT01 (2019).

[188] P. Bączyk and W. Satuła, "Mirror energy differences in $T = 1/2$ $f_{7/2}$-shell nuclei within isospin-dependent density functional theory", *Phys. Rev. C* **103**, 054320 (2021).

[189] K. Okamoto, "Coulomb energy of He^3 and possible charge asymmetry of nuclear forces", *Phys. Lett.* **11**, 150 (1964).

[190] J. A. Nolen, Jr. and J. P. Schiffer, "Coulomb Energies", *Annu. Rev. Nucl. Sci.* **19**, 471 (1969).

[191] N. Auerbach, J. Hüfner, A. K. Kerman, and C. M. Shakin, "A Theory of Isobaric Analog Resonances", *Rev. Mod. Phys.* **44**, 48 (1972).

[192] D. E. M. Hoff, A. M. Rogers, S. M. Wang, P. C. Bender, K. Brandenburg, K. Childers, J. A. Clark, A. C. Dombos, E. R. Doucet, S. Jin, *et al.*, "Mirror-symmetry violation in bound nuclear ground states", *Nature* **580**, 52 (2020).

[193] K. Wimmer, W. Korten, P. Doornenbal, T. Arici, P. Aguilera, A. Algora, T. Ando, H. Baba, B. Blank, A. Boso, *et al.*, "Shape Changes in the Mirror Nuclei ^{70}Kr and ^{70}Se", *Phys. Rev. Lett.* **126**, 072501 (2021).

[194] C. J. Horowitz, "Discussion after Misha's talk today", MITP Virtual Workshop on "Parity Violation and Related Topics" on July 27, 2020.

[195] J. Yasuda, M. Sasano, R. G. T. Zegers, H. Baba, D. Bazin, W. Chao, M. Dozono, N. Fukuda, N. Inabe, T. Isobe, *et al.*, "Extraction of the Landau-Migdal Parameter from the Gamow-Teller Giant Resonance in ^{132}Sn", *Phys. Rev. Lett.* **121**, 132501 (2018).

[196] J. Jänecke, "The quartic isobaric multiplet mass equation", *Nucl. Phys. A* **128**, 632 (1969).

[197] A. T. Gallant, M. Brodeur, C. Andreoiu, A. Bader, A. Chaudhuri, U. Chowdhury, A. Grossheim, R. Klawitter, A. A. Kwiatkowski, K. G. Leach, *et al.*, "Breakdown of the Isobaric Multiplet Mass Equation for the $A = 20$ and 21 Multiplets", *Phys. Rev. Lett.* **113**, 082501 (2014).

[198] M. B. Bennett, C. Wrede, B. A. Brown, S. N. Liddick, D. Pérez-Loureiro, D. W. Bardayan, A. A. Chen, K. A. Chipps, C. Fry, B. E. Glassman, *et al.*, "Isobaric multiplet mass equation in the $A = 31$, $T = 3/2$ quartets", *Phys. Rev. C* **93**, 064310 (2016).

[199] N. Cabibbo, "Unitary Symmetry and Leptonic Decays", *Phys. Rev. Lett.* **10**, 531 (1963).

[200] M. Kobayashi and T. Maskawa, "CP-Violation in the Renormalizable Theory of Weak Interaction", *Prog. Theor. Phys.* **49**, 652 (1973).

[201] H. Liang, N. Van Giai, and J. Meng, "Isospin corrections for superallowed Fermi β decay in self-consistent relativistic random-phase approximation approaches", *Phys. Rev. C* **79**, 064316 (2009).

[202] W. Satuła, J. Dobaczewski, W. Nazarewicz, and M. Rafalski, "Microscopic Calculations of Isospin-Breaking Corrections to Superallowed Beta Decay", *Phys. Rev. Lett.* **106**, 132502 (2011).

[203] W. Satuła, J. Dobaczewski, W. Nazarewicz, and T. R. Werner, "Isospin-breaking corrections to super-allowed Fermi β decay in isospin- and angular-momentum-projected nuclear density functional theory", *Phys. Rev. C* **86**, 054316 (2012).

[204] M. Rafalski and W. Satuła, "Microscopic calculations of isospin mixing in $N \approx Z$ nuclei and isospin-symmetry-breaking corrections to the superallowed β-decay", *Phys. Scr.* **T150**, 014032 (2012).

[205] J. C. Hardy and I. S. Towner, "Superallowed $0^+ \to 0^+$ nuclear β decays: 2020 critical survey, with implications for V_{ud} and CKM unitarity", *Phys. Rev. C* **102**, 045501 (2020).

[206] M. Bender, P.-H. Heenen, and P.-G. Reinhard, "Self-consistent mean-field models for nuclear structure", *Rev. Mod. Phys.* **75**, 121 (2003).

[207] J. Meng, H. Toki, S. G. Zhou, S. Q. Zhang, W. H. Long, and L. S. Geng, "Relativistic continuum Hartree Bogoliubov theory for ground-state properties of exotic nuclei", *Prog. Part. Nucl. Phys.* **57**, 470 (2006).

[208] T. Nikšić, D. Vretenar, and P. Ring, "Relativistic nuclear energy density functionals: Mean-field and beyond", *Prog. Part. Nucl. Phys.* **66**, 519 (2011).

[209] T. Nakatsukasa, K. Matsuyanagi, M. Matsuo, and K. Yabana, "Time-dependent density-functional description of nuclear dynamics", *Rev. Mod. Phys.* **88**, 045004 (2016).

[210] S. Bogner, A. Bulgac, J. Carlson, J. Engel, G. Fann, R. J. Furnstahl, S. Gandolfi, G. Hagen, M. Horoi, C. Johnson, *et al.*, "Computational nuclear quantum many-body problem: The UNEDF project", *Comput. Phys. Commun.* **184**, 2235 (2013).

[211] M. V. Stoitsov, J. Dobaczewski, W. Nazarewicz, S. Pittel, and D. J. Dean, "Systematic study of deformed nuclei at the drip lines and beyond", *Phys. Rev. C* **68**, 054312 (2003).

[212] M. Kortelainen, T. Lesinski, J. Moré, W. Nazarewicz, J. Sarich, N. Schunck, M. V. Stoitsov, and S. Wild, "Nuclear energy density optimization", *Phys. Rev. C* **82**, 024313 (2010).

[213] N. Wang, M. Liu, X. Wu, and J. Meng, "Surface diffuseness correction in global mass formula", *Phys. Lett. B* **734**, 215 (2014).

[214] T. Yamaguchi, H. Koura, Y. A. Litvinov, and M. Wang, "Masses of exotic nuclei", *Prog. Part. Nucl. Phys.* **120**, 103882 (2021).

[215] Z. M. Niu and H. Z. Liang, "Nuclear mass predictions based on Bayesian neural network approach with pairing and shell effects", *Phys. Lett. B* **778**, 48 (2018).

[216] Z. Niu, H. Liang, B. Sun, Y. Niu, J. Guo, and J. Meng, "High precision nuclear mass predictions towards a hundred kilo-electron-volt accuracy", *Sci. Bull.* **63**, 759 (2018).

[217] E. M. Burbidge, G. R. Burbidge, W. A. Fowler, and F. Hoyle, "Synthesis of the Elements in Stars", *Rev. Mod. Phys.* **29**, 547 (1957).

[218] Y.-Z. Qian and G. J. Wasserburg, "Where, oh where has the r-process gone?", *Phys. Rep.* **442**, 237 (2007).

[219] M. Arnould, S. Goriely, and K. Takahashi, "The r-process of stellar nucleosynthesis: Astrophysics and nuclear physics achievements and mysteries", *Phys. Rep.* **450**, 97 (2007).

[220] D. Lunney, J. M. Pearson, and C. Thibault, "Recent trends in the determination of nuclear masses", *Rev. Mod. Phys.* **75**, 1021 (2003).

[221] K. Hagino and Y. Maeno, "A nuclear periodic table", *Found. Chem.* **22**, 267 (2020).

[222] Y. Maeno, K. Hagino, and T. Ishiguro, "Three related topics on the periodic tables of elements", *Found. Chem.* **23**, 201 (2021).

[223] M. Born and R. Oppenheimer, "Zur Quantentheorie der Molekeln", *Ann. Phys.* **389**, 457 (1927).

[224] E. Schrödinger, "Quantisierung als Eigenwertproblem (Erste Mitteilung)", *Ann. Phys.* **384**, 361 (1926).

[225] E. Schrödinger, "Quantisierung als Eigenwertproblem (Zweite Mitteilung)", *Ann. Phys.* **384**, 489 (1926).

[226] E. Schrödinger, "Quantisierung als Eigenwertproblem (Dritte Mitteilung: Störungstheorie, mit Anwendung auf den Starkeffekt der Balmerlinien)", *Ann. Phys.* **385**, 437 (1926).

[227] E. Schrödinger, "Quantisierung als Eigenwertproblem (Vierte Mitteilung)", *Ann. Phys.* **386**, 109 (1926).

[228] E. Schrödinger, "An Undulatory Theory of the Mechanics of Atoms and Molecules", *Phys. Rev.* **28**, 1049 (1926).

[229] L. H. Thomas, "The calculation of atomic fields", *Math. Proc. Camb. Philos. Soc.* **23**, 542 (1927).

[230] E. Fermi, "Un Metodo Statistico per La Determinazione di Alcune Proprietà dell'Atomo", *Rend. Lincei* **6**, 602 (1927).

[231] D. R. Hartree, "The Wave Mechanics of an Atom with a Non-Coulomb Central Field. Part I. Theory and Methods", *Math. Proc. Camb. Philos. Soc.* **24**, 89 (1928).

[232] D. R. Hartree, "The Wave Mechanics of an Atom with a Non-Coulomb Central Field. Part II. Some Results and Discussion", *Math. Proc. Camb. Philos. Soc.* **24**, 111 (1928).

[233] J. A. Gaunt, "A Theory of Hartree's Atomic Fields", *Math. Proc. Camb. Philos. Soc.* **24**, 328 (1928).

[234] D. R. Hartree, "The Wave Mechanics of an Atom with a non-Coulomb Central Field. Part III. Term Values and Intensities in Series in Optical Spectra", *Math. Proc. Camb. Philos. Soc.* **24**, 426 (1928).

[235] J. C. Slater, "The Self Consistent Field and the Structure of Atoms", *Phys. Rev.* **32**, 339 (1928).

[236] V. Fock, "Näherungsmethode zur Lösung des quantenmechanischen Mehrkörperproblems", *Z. Phys.* **61**, 126 (1930).

[237] H. A. Bethe, "Thomas-Fermi Theory of Nuclei", *Phys. Rev.* **167**, 879 (1968).

[238] H. Togashi, K. Nakazato, Y. Takehara, S. Yamamuro, H. Suzuki, and M. Takano, "Nuclear equation of state for core-collapse supernova simulations with realistic nuclear forces", *Nucl. Phys. A* **961**, 78 (2017).

[239] M. Ghazanfari Mojarrad, N. S. Razavi, and S. Vaezzade, "Thomas-Fermi approximation for β-stable nuclear matter in the Landau Fermi-liquid theory", *Nucl. Phys. A* **980**, 51 (2018).

[240] H. Kanzawa, M. Takano, K. Oyamatsu, and K. Sumiyoshi, "Nonuniform Matter in Neutron Star Crusts Studied by the Variational Method with Thomas-Fermi Calculations", *Prog. Theor. Phys.* **122**, 673 (2009).

[241] H. Shen, H. Toki, K. Oyamatsu, and K. Sumiyoshi, "Relativistic Equation of State for Core-Collapse Supernova Simulations", *Astrophys. J. Suppl. Ser.* **197**, 20 (2011).

[242] M. Ghazanfari Mojarrad and N. S. Razavi, "Proto-neutron stars in the Thomas-Fermi theory", *Nucl. Phys. A* **986**, 133 (2019).

[243] E. H. Lieb and B. Simon, "Thomas-Fermi Theory Revisited", *Phys. Rev. Lett.* **31**, 681 (1973).

[244] E. H. Lieb, "Thomas-fermi and related theories of atoms and molecules", *Rev. Mod. Phys.* **53**, 603 (1981).

[245] E. Teller, "On the Stability of Molecules in the Thomas-Fermi Theory", *Rev. Mod. Phys.* **34**, 627 (1962).

[246] C. Zener, "Analytic Atomic Wave Functions", *Phys. Rev.* **36**, 51 (1930).

[247] D. R. Hartree and W. Hartree, "Self-consistent field, with exchange, for beryllium", *Proc. R. Soc. Lond. A* **150**, 9 (1935).

[248] P.-O. Löwdin, "Quantum Theory of Many-Particle Systems. III. Extension of the Hartree-Fock Scheme to Include Degenerate Systems and Correlation Effects", *Phys. Rev.* **97**, 1509 (1955).

[249] T. Kato, "On the eigenfunctions of many-particle systems in quantum mechanics", *Commun. Pure Appl. Math.* **10**, 151 (1957).

[250] O. Sinanoğlu, "Theory of electron correlation in atoms and molecules", *Proc. R. Soc. Lond. A* **260**, 379 (1961).

[251] N. R. Kestner and O. Sinanoğlu, "Study of Electron Correlation in Helium-Like Systems Using an Exactly Soluble Model", *Phys. Rev.* **128**, 2687 (1962).

[252] O. Sinanoğlu and I. Öksüz, "Theory of Atomic Structure Including Electron Correlation", *Phys. Rev. Lett.* **21**, 507 (1968).

[253] I. Öksüz and O. Sinanoğlu, "Theory of Atomic Structure Including Electron Correlation. I. Three Kinds of Correlation in Ground and Excited Configurations", *Phys. Rev.* **181**, 42 (1969).

[254] I. Öksüz and O. Sinanoğlu, "Theory of Atomic Structure Including Electron Correlation. II. All-External Pair Correlations in the Various States and Ions of B, C, N, O, F, Ne, and Na, and Prediction of Electron Affinities and Atomic Excitation Energies", *Phys. Rev.* **181**, 54 (1969).

[255] P. Westhaus and O. Sinanoğlu, "Theory of Atomic Structure Including Electron Correlation. III. Calculations of Multiplet Oscillator Strengths and Comparisons with Experiments for CII, NI, NII, NIII, OII, OIII, OIV, FII, NeII, and NaIII", *Phys. Rev.* **183**, 56 (1969).

[256] C. Nicolaides, O. Sinanoğlu, and P. Westhaus, "Theory of Atomic Structure Including Electron Correlation. IV. Method for Forbidden-Transition Probabilities with Results for [O I], [O II], [O III], [N I], [N II], and [C I].", *Phys. Rev. A* **4**, 1400 (1971).

[257] O. Sinanoğlu, "Theory of Electron Correlation in Ground and Excited States with Application to Atomic Properties", *J. Phys. Colloques* **31**, C4-83 (1970).

[258] J. A. Pople, J. S. Binkley, and R. Seeger, "Theoretical models incorporating electron correlation", *Int. J. Quantum Chem.* **10**, 1 (1976).

[259] J. A. Pople, R. Seeger, and K. Raghavachari, "Variational configuration interaction methods and comparison with perturbation theory", *Int. J. Quantum Chem.* **12**, 149 (1977).

[260] J. A. Pople, "Nobel Lecture: Quantum chemical models", *Rev. Mod. Phys.* **71**, 1267 (1999).

[261] J. Čížek, "On the Correlation Problem in Atomic and Molecular Systems. Calculation of Wavefunction Components in Ursell-Type Expansion Using Quantum-Field Theoretical Methods", *J. Chem. Phys.* **45**, 4256 (1966).

[262] J. Čížek and J. Paldus, "Correlation problems in atomic and molecular systems III. Rederivation of the coupled-pair many-electron theory using the traditional quantum chemical methodst", *Int. J. Quantum Chem.* **5**, 359 (1971).

[263] C. Møller and M. S. Plesset, "Note on an Approximation Treatment for Many-Electron Systems", *Phys. Rev.* **46**, 618 (1934).

[264] D. Ceperley, G. V. Chester, and M. H. Kalos, "Monte Carlo simulation of a many-fermion study", *Phys. Rev. B* **16**, 3081 (1977).

[265] R. E. Lowther and R. L. Coldwell, "Monte Carlo calculation of the Born-Oppenheimer potential between two helium atoms", *Phys. Rev. A* **22**, 14 (1980).

[266] P. Hohenberg and W. Kohn, "Inhomogeneous Electron Gas", *Phys. Rev.* **136**, B864 (1964).

[267] W. Kohn and L. J. Sham, "Self-Consistent Equations Including Exchange and Correlation Effects", *Phys. Rev.* **140**, A1133 (1965).

[268] W. Kohn, "Nobel Lecture: Electronic structure of matter—wave functions and density functionals", *Rev. Mod. Phys.* **71**, 1253 (1999).

[269] M. Levy, "Universal variational functionals of electron densities, first-order density matrices, and natural spin-orbitals and solution of the v-representability problem", *Proc. Natl. Acad. Sci. USA* **76**, 6062 (1979).

[270] M. Levy, "Electron densities in search of Hamiltonians", *Phys. Rev. A* **26**, 1200 (1982).

[271] E. H. Lieb, "Density Functionals for Coulomb Systems", *Int. J. Quantum Chem.* **24**, 243 (1983).

[272] E. Engel and R. M. Dreizler, *Density Functional Theory—An Advanced Course*, (Springer-Verlag, Berlin, Heiderberg, 2011).

[273] W. Kutzelnigg, "Density functional theory in terms of a Legendre transformation for beginners", *J. Mol. Struct.* **768**, 163 (2006).

[274] T. L. Gilbert, "Hohenberg-Kohn theorem for nonlocal external potentials", *Phys. Rev. B* **12**, 2111 (1975).

[275] H. Eschrig, *The Fundamentals of Density Functional Theory*, (B. G. Teubner Verlagsgesellschaft, Stuttgart, Leipzig, 1996).

[276] R. Stowasser and R. Hoffmann, "What Do the Kohn-Sham Orbitals and Eigenvalues Mean?", *J. Am. Chem. Soc.* **121**, 3414 (1999).

[277] J. F. Janak, "Proof that $\frac{\partial E}{\partial n_i} = \varepsilon$ in density-functional theory", *Phys. Rev. B* **18**, 7165 (1978).

[278] T. Koopmans, "Über die Zuordnung von Wellenfunktionen und Eigenwerten zu den Einzelnen Elektronen Eines Atoms", *Physica* **1**, 104 (1934).

[279] J. P. Perdew and K. Schmidt, "Jacob's ladder of density functional approximations for the exchange-correlation energy", *AIP Conf. Proc.* **577**, 1 (2001).

[280] M. Gell-Mann and K. A. Brueckner, "Correlation Energy of an Electron Gas at High Density", *Phys. Rev.* **106**, 364 (1957).

[281] E. Wigner, "Effects of the electron interaction on the energy levels of electrons in metals", *Trans. Faraday Soc.* **34**, 678 (1938).

[282] W. J. Carr, "Energy, Specific Heat, and Magnetic Properties of the Low-Density Electron Gas", *Phys. Rev.* **122**, 1437 (1961).

[283] D. M. Ceperley and B. J. Alder, "Ground State of the Electron Gas by a Stochastic Method", *Phys. Rev. Lett.* **45**, 566 (1980).

[284] S. H. Vosko, L. Wilk, and M. Nusair, "Accurate spin-dependent electron liquid correlation energies for local spin density calculations: a critical analysis", *Can. J. Phys.* **58**, 1200 (1980).

[285] J. P. Perdew and A. Zunger, "Self-interaction correction to density-functional approximations for many-electron systems", *Phys. Rev. B* **23**, 5048 (1981).

[286] J. P. Perdew and Y. Wang, "Accurate and simple analytic representation of the electron-gas correlation energy", *Phys. Rev. B* **45**, 13244 (1992).

[287] P.-F. Loos and P. M. W. Gill, "Leading-order behavior of the correlation energy in the uniform electron gas", *Int. J. Quantum Chem.* **112**, 1712 (2012).

[288] T. Yokota, K. Yoshida, and T. Kunihiro, "Functional renormalization-group calculation of the equation of state of one-dimensional uniform matter inspired by the Hohenberg-Kohn theorem", *Phys. Rev. C* **99**, 024302 (2019).

[289] T. Yokota, *Functional-renormalization-group aided density-functional theory—ab-inito description of ground and excited states of quantum many-body systems—*, PhD Thesis (Kyoto University, 2019).

[290] T. Chachiyo, "Communication: Simple and accurate uniform electron gas correlation energy for the full range of densities", *J. Chem. Phys.* **145**, 021101 (2016).

[291] V. V. Karasiev, "Comment on "Communication: Simple and accurate uniform electron gas correlation energy for the full range of densities" [J. Chem. Phys. 145, 021101 (2016)]", *J. Chem. Phys.* **145**, 157101 (2016).

[292] U. von Barth and L. Hedin, "A local exchange-correlation potential for the spin polarized case. I", *J. Phys. C* **5**, 1629 (1972).

[293] T. Asada and K. Terakura, "Cohesive properties of iron obtained by use of the generalized gradient approximation", *Phys. Rev. B* **46**, 13599 (1992).

[294] T. Asada and K. Terakura, "Generalized-gradient-approximation study of the magnetic and cohesive properties of bcc, fcc, and hcp Mn", *Phys. Rev. B* **47**, 15992 (1993).

[295] J. P. Perdew, K. Burke, and M. Ernzerhof, "Generalized Gradient Approximation Made Simple", *Phys. Rev. Lett.* **77**, 3865 (1996).

[296] J. P. Perdew, K. Burke, and Y. Wang, "Generalized gradient approximation for the exchange-correlation hole of a many-electron system", *Phys. Rev. B* **54**, 16533 (1996).

[297] Y. Wang and J. P. Perdew, "Spin scaling of the electron-gas correlation energy in the high-density limit", *Phys. Rev. B* **43**, 8911 (1991).

[298] M. Levy, "Asymptotic coordinate scaling bound for exchange-correlation energy in density-functional theory", *Int. J. Quantum Chem.* **36**, 617 (1989).

[299] M. Levy and J. P. Perdew, "Hellmann-Feynman, virial, and scaling requisites for the exact universal density functionals. Shape of the correlation potential and diamagnetic susceptibility for atoms", *Phys. Rev. A* **32**, 2010 (1985).

[300] E. H. Lieb, "A lower bound for Coulomb energies", *Phys. Lett. A* **70**, 444 (1979).

[301] E. H. Lieb and S. Oxford, "Improved lower bound on the indirect Coulomb energy", *Int. J. Quantum Chem.* **19**, 427 (1981).

[302] G. Kin-Lic Chan and N. C. Handy, "Optimized Lieb-Oxford bound for the exchange-correlation energy", *Phys. Rev. A* **59**, 3075 (1999).

[303] M. Slamet and V. Sahni, "Coulomb holes and correlation potentials in the helium atom", *Phys. Rev. A* **51**, 2815 (1995).

[304] T. Tsuneda, *Density Functional Theory in Quantum Chemistry*, (Springer Japan, Tokyo, 2014).

[305] R. M. Martin, *Electronic Structure* (Second edition), (Cambridge University Press, Cambridge, 2020).

[306] J. P. Perdew, A. Ruzsinszky, G. I. Csonka, O. A. Vydrov, G. E. Scuseria, L. A. Constantin, X. Zhou, and K. Burke, "Restoring the Density-Gradient Expansion for Exchange in Solids and Surfaces", *Phys. Rev. Lett.* **100**, 136406 (2008).

[307] P. R. Antoniewicz and L. Kleinman, "Kohn-Sham exchange potential exact to first order in $\rho(\boldsymbol{K})/\rho_0$", *Phys. Rev. B* **31**, 6779 (1985).

[308] A. D. Becke, "Density-functional exchange-energy approximation with correct asymptotic behavior", *Phys. Rev. A* **38**, 3098 (1988).

[309] J. P. Perdew, J. A. Chevary, S. H. Vosko, K. A. Jackson, M. R. Pederson, D. J. Singh, and C. Fiolhais, "Atoms, molecules, solids, and surfaces: Applications of the generalized gradient approximation for exchange and correlation", *Phys. Rev. B* **46**, 6671 (1992).

[310] M. Rasolt and D. J. W. Geldart, "Exchange and correlation energy in a nonuniform fermion fluid", *Phys. Rev. B* **34**, 1325 (1986).

[311] M. G. Medvedev, I. S. Bushmarinov, J. Sun, J. P. Perdew, and K. A. Lyssenko, "Density functional theory is straying from the path toward the exact functional", *Science* **355**, 49 (2017).

[312] K. P. Kepp, "Comment on "Density functional theory is straying from the path toward the exact functional"", *Science* **356**, 496 (2017).

[313] J. C. Snyder, M. Rupp, K. Hansen, K.-R. Müller, and K. Burke, "Finding Density Functionals with Machine Learning", *Phys. Rev. Lett.* **108**, 253002 (2012).

[314] F. Brockherde, L. Vogt, L. Li, M. E. Tuckerman, K. Burke, and K.-R. Müller, "Bypassing the Kohn-Sham equations with machine learning", *Nat. Commun.* **8**, 872 (2017).

[315] R. Nagai, R. Akashi, S. Sasaki, and S. Tsuneyuki, "Neural-network Kohn-Sham exchange-correlation potential and its out-of-training transferability", *J. Chem. Phys.* **148**, 241737 (2018).

[316] G. R. Schleder, A. C. M. Padilha, C. M. Acosta, M. Costa, and A. Fazzio, "From DFT to machine learning: recent approaches to materials science—a review", *J. Phys. Mater.* **2**, 032001 (2019).

[317] R. Nagai, R. Akashi, and O. Sugino, "Completing density functional theory by machine learning hidden messages from molecules", *Npj Comput. Mater.* **6**, 43 (2020).

[318] M. Bogojeski, L. Vogt-Maranto, M. E. Tuckerman, K.-R. Müller, and K. Burke, "Quantum chemical accuracy from densityfunctional approximations via machine learning", *Sci. Rep.* **11**, 5223 (2020).

[319] R. Meyer, M. Weichselbaum, and A. W. Hauser, "Machine Learning Approaches toward Orbital-free Density Functional Theory: Simultaneous Training on the Kinetic Energy Density Functional and Its Functional Derivative", *J. Chem. Theory Comput.* **16**, 5685 (2020).

[320] R. Nagai, R. Akashi, and O. Sugino, "Machine-Learning-Based Exchange-Correlation Functional with Physical Asymptotic Constraints", arXiv:2111.15593 [cond-mat.mtrl-sci] (2021).

[321] H. Verschelde and M. Coppens, "A variational approach to quantum field theory", *Phys. Lett. B* **287**, 133 (1992).

[322] R. Fukuda, T. Kotani, Y. Suzuki, and S. Yokojima, "Density Functional Theory through Legendre Transformation", *Prog. Theor. Phys.* **92**, 833 (1994).

[323] G. D. Mahan, *Many-Particle Physics* (Third edition), (Kluwer Academic/Plenum Publishers, New York, 2000).

[324] N. Dupuis, L. Canet, A. Eichhorn, W. Metzner, J. M. Pawlowski, M. Tissier, and N. Wschebor, "The nonperturbative functional renormalization group and its applications", *Phys. Rep.* **910**, 1 (2021).

[325] J. Polonyi and K. Sailer, "Effective action and density-functional theory", *Phys. Rev. B* **66**, 155113 (2002).

[326] S. Kemler and J. Braun, "Towards a renormalization group approach to density functional theory—general formalism and case studies", *J. Phys. G* **40**, 085105 (2013).

[327] S. Kemler, M. Pospiech, and J. Braun, "Formation of selfbound states in a one-dimensional nuclear model—a renormalization group based density functional study", *J. Phys. G* **44**, 015101 (2017).

[328] H. Liang, Y. Niu, and T. Hatsuda, "Functional renormalization group and Kohn-Sham scheme in density functional theory", *Phys. Lett. B* **779**, 436 (2018).

[329] T. Yokota, K. Yoshida, and T. Kunihiro, "*Ab initio* description of excited states of 1D uniform matter with the Hohenberg-Kohn-theorem-inspired functional-renormalization-group method", *Prog. Theor. Exp. Phys.* **2019**, 011D01 (2019).

[330] Y. Wang and R. G. Parr, "Construction of exact Kohn-Sham orbitals from a given electron density", *Phys. Rev. A* **47**, R1591 (1993).

[331] Q. Zhao and R. G. Parr, "Constrained-search method to determine electronic wave functions from electronic densities", *J. Chem. Phys.* **98**, 543 (1993).

[332] R. van Leeuwen and E. J. Baerends, "Exchange-correlation potential with correct asymptotic behavior", *Phys. Rev. A* **49**, 2421 (1994).

[333] Q. Zhao, R. C. Morrison, and R. G. Parr, "From electron densities to Kohn-Sham kinetic energies, orbital energies, exchange-correlation potentials, and exchange-correlation energies", *Phys. Rev. A* **50**, 2138 (1994).

[334] D. S. Jensen and A. Wasserman, "Numerical methods for the inverse problem of density functional theory", *Int. J. Quantum Chem.* **118**, e25425 (2018).

[335] G. Accorto, P. Brandolini, F. Marino, A. Porro, A. Scalesi, G. Colò, X. Roca-Maza, and E. Vigezzi, "First step in the nuclear inverse Kohn-Sham problem: From densities to potentials", *Phys. Rev. C* **101**, 024315 (2020).

[336] Y. Shi and A. Wasserman, "Inverse Kohn–Sham Density Functional Theory: Progress and Challenges", *J. Phys. Chem. Lett.* **12**, 5308 (2021).

[337] S. Baroni, S. de Gironcoli, A. Dal Corso, and P. Giannozzi, "Phonons and related crystal properties from density-functional perturbation theory", *Rev. Mod. Phys.* **73**, 515 (2001).

[338] J. Carlson, "Green's function Monte Carlo study of light nuclei", *Phys. Rev. C* **36**, 2026 (1987).

[339] B. S. Pudliner, V. R. Pandharipande, J. Carlson, and R. B. Wiringa, "Quantum Monte Carlo Calculations of $A \leq 6$ Nuclei", *Phys. Rev. Lett.* **74**, 4396 (1995).

[340] J. L. Forest, V. R. Pandharipande, S. C. Pieper, R. B. Wiringa, R. Schiavilla, and A. Arriaga, "Femtometer toroidal structures in nuclei", *Phys. Rev. C* **54**, 646 (1996).

[341] R. Schiavilla, R. B. Wiringa, S. C. Pieper, and J. Carlson, "Tensor Forces and the Ground-State Structure of Nuclei", *Phys. Rev. Lett.* **98**, 132501 (2007).

[342] J. Carlson, S. Gandolfi, F. Pederiva, S. C. Pieper, R. Schiavilla, K. E. Schmidt, and R. B. Wiringa, "Quantum Monte Carlo methods for nuclear physics", *Rev. Mod. Phys.* **87**, 1067 (2015).

[343] D. Lonardoni, S. Gandolfi, J. E. Lynn, C. Petrie, J. Carlson, K. E. Schmidt, and A. Schwenk, "Auxiliary field diffusion Monte Carlo calculations of light and medium-mass nuclei with local chiral interactions", *Phys. Rev. C* **97**, 044318 (2018).

[344] P. Navrátil, J. P. Vary, and B. R. Barrett, "Large-basis ab initio no-core shell model and its application to ^{12}**C**", *Phys. Rev. C* **62**, 054311 (2000).

[345] I. Stetcu, B. R. Barrett, and U. van Kolck, "No-core shell model in an effective-field-theory framework", *Phys. Lett. B* **653**, 358 (2007).

[346] B. R. Barrett, P. Navrátil, and J. P. Vary, "*Ab initio* no core shell model", *Prog. Part. Nucl. Phys.* **69**, 131 (2013).

[347] A. Calci, P. Navrátil, R. Roth, J. Dohet-Eraly, S. Quaglioni, and G. Hupin, "Can *Ab Initio* Theory Explain the Phenomenon of Parity Inversion in ^{11}Be?", *Phys. Rev. Lett.* **117**, 242501 (2016).

[348] E. Gebrerufael, K. Vobig, H. Hergert, and R. Roth, "*Ab Initio* Description of Open-Shell Nuclei: Merging No-Core Shell Model and In-Medium Similarity Renormalization Group", *Phys. Rev. Lett.* **118**, 152503 (2017).

[349] W. H. Dickhoff and C. Barbieri, "Self-consistent Green's function method for nuclei and nuclear matter", *Prog. Part. Nucl. Phys.* **52**, 377 (2004).

[350] A. Carbone, A. Cipollone, C. Barbieri, A. Rios, and A. Polls, "Self-consistent Green's functions formalism with three-body interactions", *Phys. Rev. C* **88**, 054326 (2013).

[351] A. Rios, A. Polls, and W. H. Dickhoff, "Density and isospin-asymmetry dependence of high-momentum components", *Phys. Rev. C* **89**, 044303 (2014).

[352] F. Raimondi and C. Barbieri, "Core-polarization effects and effective charges in O and Ni isotopes from chiral interactions", *Phys. Rev. C* **100**, 024317 (2019).

[353] P. Arthuis, C. Barbieri, M. Vorabbi, and P. Finelli, "*Ab Initio* Computation of Charge Densities for Sn and Xe Isotopes", *Phys. Rev. Lett.* **125**, 182501 (2020).

[354] V. Somà, "Self-Consistent Green's Function Theory for Atomic Nuclei", *Front. Phys.* **8**, 340 (2020).

[355] D. Lee, "Lattice simulations for few- and many-body systems", *Prog. Part. Nucl. Phys.* **63**, 117 (2009).

[356] E. Epelbaum, H. Krebs, D. Lee, and U.-G. Meißner, "Lattice Effective Field Theory Calculations for $A = 3$, 4, 6, 12 Nuclei", *Phys. Rev. Lett.* **104**, 142501 (2010).

[357] S. Elhatisari, D. Lee, G. Rupak, E. Epelbaum, H. Krebs, T. A. Lähde, T. Luu, and U.-G. Meißner, "*Ab initio* alpha–alpha scattering", *Nature* **528**, 111 (2015).

[358] T. A. Lähde and U.-G. Meißner, *Nuclear Lattice Effective Field Theory*, (Springer, Switzerland, 2019).

[359] D. Lee, "Recent Progress in Nuclear Lattice Simulations", *Front. Phys.* **8**, 174 (2020).

[360] S. Shen, T. A. Lähde, D. Lee, and U.-G. Meißner, "Wigner SU(4) symmetry, clustering, and the spectrum of ^{12}C", *Eur. Phys. J. A* **57**, 276 (2021).

[361] R. Brockmann and H. Toki, "Relativistic density-dependent Hartree approach for finite nuclei", *Phys. Rev. Lett.* **68**, 3408 (1992).

[362] M. Baldo, G. F. Burgio, H.-J. Schulze, and G. Taranto, "Nucleon effective masses within the Brueckner-Hartree-Fock theory: Impact on stellar neutrino emission", *Phys. Rev. C* **89**, 048801 (2014).

[363] B. S. Hu, F. R. Xu, Q. Wu, Y. Z. Ma, and Z. H. Sun, "Brueckner-Hartree-Fock calculations for finite nuclei with renormalized realistic forces", *Phys. Rev. C* **95**, 034321 (2017).

[364] S. Shen, H. Liang, W. H. Long, J. Meng, and P. Ring, "Towards an *ab initio* covariant density functional theory for nuclear structure", *Prog. Part. Nucl. Phys.* **109**, 103713 (2019).

[365] S. Wang, Q. Zhao, P. Ring, and J. Meng, "Nuclear matter in relativistic Brueckner-Hartree-Fock theory with Bonn potential in the full Dirac space", *Phys. Rev. C* **103**, 054319 (2021).

[366] B. A. Brown, "The nuclear shell model towards the drip lines", *Prog. Part. Nucl. Phys.* **47**, 517 (2001).

[367] T. Otsuka, A. Gade, O. Sorlin, T. Suzuki, and Y. Utsuno, "Evolution of shell structure in exotic nuclei", *Rev. Mod. Phys.* **92**, 015002 (2020).

[368] N. Tsunoda, T. Otsuka, N. Shimizu, M. Hjorth-Jensen, K. Takayanagi, and T. Suzuki, "Exotic neutron-rich medium-mass nuclei with realistic nuclear forces", *Phys. Rev. C* **95**, 021304 (2017).

[369] G. Colò, "Nuclear density functional theory", *Adv. Phys.:X* **5**, 1740061 (2020).

[370] J. Dobaczewski, H. Flocard, and J. Treiner, "Hartree-Fock-Bogolyubov description of nuclei near the neutron-drip line", *Nucl. Phys. A* **422**, 103 (1984).

[371] J. Engel, "Intrinsic-density functionals", *Phys. Rev. C* **75**, 014306 (2007).

[372] N. Barnea, "Density functional theory for self-bound systems", *Phys. Rev. C* **76**, 067302 (2007).

[373] B. G. Giraud, B. K. Jennings, and B. R. Barrett, "Existence of a density functional for an intrinsic state", *Phys. Rev. A* **78**, 032507 (2008).

[374] T. H. R. Skyrme, "The effective nuclear potential", *Nucl. Phys.* **9**, 615 (1958).

[375] D. Vautherin and D. M. Brink, "Hartree-Fock Calculations with Skyrme's Interaction. I. Spherical Nuclei", *Phys. Rev. C* **5**, 626 (1972).

[376] J. Dechargé and D. Gogny, "Hartree-Fock-Bogolyubov calculations with the $D1$ effective interaction on spherical nuclei", *Phys. Rev. C* **21**, 1568 (1980).

[377] G. Bertsch, J. Borysowicz, H. McManus, and W. G. Love, "Interactions for inelastic scattering derived from realistic potentials", *Nucl. Phys. A* **284**, 399 (1977).

[378] H. Nakada, "Hartree-Fock approach to nuclear matter and finite nuclei with M3Y-type nucleon-nucleon interactions", *Phys. Rev. C* **68**, 014316 (2003).

[379] N. Anantaraman, H. Toki, and G. F. Bertsch, "An effective interaction for inelastic scattering derived from the Paris potential", *Nucl. Phys. A* **398**, 269 (1983).

[380] B. D. Serot and J. D. Walecka, "The Relativistic Nuclear Many-Body Problem", in *Advances in Nuclear Physics: Volume 16*, edited by J. W. Negele and E. Vogt (Plenum Press, New York, 1986).

[381] W.-H. Long, N. Van Giai, and J. Meng, "Density-dependent relativistic Hartree-Fock approach", *Phys. Lett. B* **640**, 150 (2006).

[382] B.-A. Li, L.-W. Chen, and C. M. Ko, "Recent progress and new challenges in isospin physics with heavy-ion reactions", *Phys. Rep.* **464**, 113 (2008).

[383] J. E. Drut, R. J. Furnstahl, and L. Platter, "Toward *ab initio* density functional theory for nuclei", *Prog. Part. Nucl. Phys.* **64**, 120 (2010).

[384] J. Dobaczewski, "*Ab initio* derivation of model energy density functionals", *J. Phys. G* **43**, 04LT01 (2016).

[385] R. J. Furnstahl, "Turning the nuclear energy density functional method into a proper effective field theory: reflections", *Eur. Phys. J. A* **56**, 85 (2020).

[386] G. Salvioni, J. Dobaczewski, C. Barbieri, G. Carlsson, A. Idini, and A. Pastore, "Model nuclear energy density functionals derived from *ab initio* calculations", *J. Phys. G* **47**, 085107 (2020).

[387] F. Marino, C. Barbieri, A. Carbone, G. Colò, A. Lovato, F. Pederiva, X. Roca-Maza, and E. Vigezzi, "Nuclear energy density functionals grounded in *ab initio* calculations", *Phys. Rev. C* **104**, 024315 (2021).

[388] A. Akmal, V. R. Pandharipande, and D. G. Ravenhall, "Equation of state of nucleon matter and neutron star structure", *Phys. Rev. C* **58**, 1804 (1998).

[389] D. Vautherin and D. M. Brink, "Hartree-Fock calculations with Skyrme's interaction", *Phys. Lett. B* **32**, 149 (1970).

[390] D. Vautherin, M. Veneroni, and D. M. Brink, "A Hartree-Fock calculation for the stability of super-heavy nuclei", *Phys. Lett. B* **33**, 381 (1970).

[391] D. Vautherin, "Hartree-Fock Calculations with Skyrme's Interaction. II. Axially Deformed Nuclei", *Phys. Rev. C* **7**, 296 (1973).

[392] P.-G. Reinhard, D. J. Dean, W. Nazarewicz, J. Dobaczewski, J. A. Maruhn, and M. R. Strayer, "Shape coexistence and the effective nucleon-nucleon interaction", *Phys. Rev. C* **60**, 014316 (1999).

[393] P. Danielewicz and J. Lee, "Symmetry energy I: Semi-infinite matter", *Nucl. Phys. A* **818**, 36 (2009).

[394] P.-G. Reinhard and H. Flocard, "Nuclear effective forces and isotope shifts", *Nucl. Phys. A* **584**, 467 (1995).

[395] C. Mondal, B. K. Agrawal, J. N. De, and S. K. Samaddar, "Correlations among symmetry energy elements in Skyrme models", *Int. J. Mod. Phys. E* **27**, 1850078 (2018).

[396] Y. M. Engel, D. M. Brink, K. Goeke, S. J. Krieger, and D. Vautherin, "Time-dependent hartree-fock theory with Skyrme's interaction", *Nucl. Phys. A* **249**, 215 (1975).

[397] J. Dobaczewski and J. Dudek, "Time-odd components in the mean field of rotating superdeformed nuclei", *Phys. Rev. C* **52**, 1827 (1995).

[398] J. Dobaczewski and J. Dudek, "Solution of the Skyrme-Hartree-Fock equations in the Cartesian deformed harmonic oscillator basis I. The method", *Comput. Phys. Commun.* **102**, 166 (1997).

[399] J. J. Sakurai, *Advanced Quantum Mechanics*, (Addison Wesley, Boston, 1967).

[400] A. Afanasev, I. Akushevich, and N. Merenkov, "Model independent radiative corrections in processes of polarized electron-nucleon elastic scattering", *Phys. Rev. D* **64**, 113009 (2001).

[401] J. Arrington, K. de Jager, and C. F. Perdrisat, "Nucleon Form Factors—A Jefferson Lab Perspective", *J. Phys. Conf. Ser.* **299**, 012002 (2011).

[402] G. Breit, "The Effect of Retardation on the Interaction of Two Electrons", *Phys. Rev.* **34**, 553 (1929).

[403] G. Breit, "The Fine Structure of HE as a Test of the Spin Interactions of Two Electrons", *Phys. Rev.* **36**, 383 (1930).

[404] G. Breit, "Dirac's Equation and the Spin-Spin Interactions of Two Electrons", *Phys. Rev.* **39**, 616 (1932).

[405] T. Saue, "Relativistic Hamiltonians for Chemistry: A Primer", *ChemPhysChem* **12**, 3077 (2011).

[406] J. Le Bloas, M.-H. Koh, P. Quentin, L. Bonneau, and J. I. A. Ithnin, "Exact Coulomb exchange calculations in the Skyrme-Hartree-Fock-BCS framework and tests of the Slater approximation", *Phys. Rev. C* **84**, 014310 (2011).

[407] H. Kasuya and K. Yoshida, "Hartree–Fock–Bogoliubov theory for odd-mass nuclei with a time-odd constraint and application to deformed halo nuclei", *Prog. Theor. Exp. Phys.* **2021**, 013D01 (2020).

[408] G. Colò, L. Cao, N. Van Giai, and L. Capelli, "Self-consistent RPA calculations with Skyrme-type interactions: The skyrme_rpa program", *Comput. Phys. Commun.* **184**, 142 (2013).

[409] X. Roca-Maza, G. Colò, and H. Sagawa, "New Skyrme interaction with improved spin-isospin properties", *Phys. Rev. C* **86**, 031306 (2012).

[410] S. K. Samaddar, M. M. Majumdar, B. C. Samanta, and J. N. De, "Vacuum polarization and the nuclear mass formula", *Nucl. Phys. A* **451**, 160 (1986).

[411] N. Chamel, S. Goriely, and J. M. Pearson, "Further explorations of Skyrme-Hartree-Fock-Bogoliubov mass formulas. XI. Stabilizing neutron stars against a ferromagnetic collapse", *Phys. Rev. C* **80**, 065804 (2009).

[412] E. A. Uehling, "Polarization Effects in the Positron Theory", *Phys. Rev.* **48**, 55 (1935).

[413] L. Wayne Fullerton and G. A. Rinker, "Accurate and efficient methods for the evaluation of vacuum-polarization potentials of order $Z\alpha$ and $Z\alpha^2$", *Phys. Rev. A* **13**, 1283 (1976).

[414] X. Roca-Maza, G. Colò, and H. Sagawa, "The nuclear symmetry energy and the breaking of the isospin symmetry: how do they reconcile with each other?", *EPJ Web Conf.* **194**, 01002 (2018).

[415] G. Audi, A. H. Wapstra, and C. Thibault, "The AME2003 atomic mass evaluation", *Nucl. Phys. A* **729**, 337 (2003),

[416] W. J. Huang, G. Audi, M. Wang, F. G. Kondev, S. Naimi, and X. Xu, "The AME2016 atomic mass evaluation (I). Evaluation of input data; and adjustment procedures", *Chin. Phys. C* **41**, 030002 (2017).

[417] M. Wang, G. Audi, F. G. Kondev, W. J. Huang, S. Naimi, and X. Xu, "The AME2016 atomic mass evaluation (II). Tables, graphs and references", *Chin. Phys. C* **41**, 030003 (2017).

[418] W. J. Huang, M. Wang, F. G. Kondev, G. Audi, and S. Naimi, "The AME 2020 atomic mass evaluation (I). Evaluation of input data, and adjustment procedures", *Chin. Phys. C* **45**, 030002 (2021).

[419] M. Wang, W. J. Huang, F. G. Kondev, G. Audi, and S. Naimi, "The AME 2020 atomic mass evaluation (II). Tables, graphs and references", *Chin. Phys. C* **45**, 030003 (2021).

[420] M. I. Eides, H. Grotch, and V. A. Shelyuto, "Theory of Light Hydrogenlike Atoms", *Phys. Rep.* **342**, 63 (2001).

[421] A. H. MacDonald and S. H. Vosko, "A relativistic density functional formalism", *J. Phys. C* **12**, 2977 (1979).

[422] E. Engel, S. Keller, and R. M. Dreizler, "Generalized gradient approximation for the relativistic exchange-only energy functional", *Phys. Rev. A* **53**, 1367 (1996).

[423] M. H. L. Pryce, "The mass-centre in the restricted theory of relativity and its connexion with the quantum theory of elementary particles", *Proc. R. Soc. Lond. A* **195**, 62 (1948).

[424] L. L. Foldy and S. A. Wouthuysen, "On the Dirac Theory of Spin 1/2 Particles and Its Non-Relativistic Limit", *Phys. Rev.* **78**, 29 (1950).

[425] S. Tani, "Connection between Particle Models and Field Theories, I —The Case Spin 1/2—", *Prog. Theor. Phys.* **6**, 267 (1951).

[426] L. L. Foldy, "The Electromagnetic Properties of Dirac Particles", *Phys. Rev.* **87**, 688 (1952).

[427] T. Itoh, "Derivation of Nonrelativistic Hamiltonian for Electrons from Quantum Electrodynamics", *Rev. Mod. Phys.* **37**, 159 (1965).

[428] S. D. Kenny, G. Rajagopal, and R. J. Needs, "Relativistic corrections to atomic energies from quantum Monte Carlo calculations", *Phys. Rev. A* **51**, 1898 (1995).

[429] S. D. Kenny, G. Rajagopal, R. J. Needs, W.-K. Leung, M. J. Godfrey, A. J. Williamson, and W. M. C. Foulkes, "Quantum Monte Carlo Calculations of the Energy of the Relativistic Homogeneous Electron Gas", *Phys. Rev. Lett.* **77**, 1099 (1996).

[430] Z. M. Niu, Q. Liu, Y. F. Niu, W. H. Long, and J. Y. Guo, "Nuclear effective charge factor originating from covariant density functional theory", *Phys. Rev. C* **87**, 037301 (2013).

[431] H.-Q. Gu, H. Liang, W. H. Long, N. Van Giai, and J. Meng, "Slater approximation for Coulomb exchange effects in nuclear covariant density functional theory", *Phys. Rev. C* **87**, 041301 (2013).

[432] S. Goriely and J. M. Pearson, "Further explorations of Skyrme-Hartree-Fock-Bogoliubov mass formulas. VIII. Role of Coulomb exchange", *Phys. Rev. C* **77**, 031301 (2008).

[433] H. Sagawa, G. Colò, X. Roca-Maza, and Y. Niu, "Collective excitations involving spin and isospin degrees of freedom", *Eur. Phys. J. A* **55**, 227 (2019).

[434] X. Roca-Maza, H. Sagawa, and G. Colò, "Double charge-exchange phonon states", *Phys. Rev. C* **101**, 014320 (2020).

[435] X. Roca-Maza, H. Sagawa, and G. Colò, "Isobaric analog state energy in deformed nuclei: A toy model", *Phys. Rev. C* **102**, 064303 (2020).

[436] G. Selva, X. Roca-Maza, and G. Colò, "Isospin Symmetry Breaking Effects on the Mass-Radius Relation of a Neutron Star", *Symmetry* **13**, 144 (2021).

[437] J. M. Dong, L. J. Wang, W. Zuo, and J. Z. Gu, "Constraints on Coulomb energy, neutron skin thickness in ^{208}Pb, and symmetry energy", *Phys. Rev. C* **97**, 034318 (2018).

[438] J. M. Dong, J. Z. Gu, Y. H. Zhang, W. Zuo, L. J. Wang, Y. A. Litvinov, and Y. Sun, "Beyond Wigner's isobaric multiplet mass equation: Effect of charge-symmetry-breaking interaction and Coulomb polarization", *Phys. Rev. C* **99**, 014319 (2019).

[439] D. Davesne, P. Becker, A. Pastore, and J. Navarro, "Infinite matter properties and zero-range limit of non-relativistic finite-range interactions", *Ann. Phys.* **375**, 288 (2016).

[440] L.-G. Cao, G. Colò, and H. Sagawa, "Spin and spin-isospin instabilities and Landau parameters of Skyrme interactions with tensor correlations", *Phys. Rev. C* **81**, 044302 (2010).

[441] J. Bartel, P. Quentin, M. Brack, C. Guet, and H.-B. Håkansson, "Towards a better parametrisation of Skyrme-like effective forces: A critical study of the SkM force", *Nucl. Phys. A* **386**, 79 (1982).

[442] W. D. Myers and W. J. Swiatecki, "Average nuclear properties", *Ann. Phys.* **55**, 395 (1969).

[443] W. D. Myers and W. J. Swiatecki, "Droplet-model theory of the neutron skin", *Nucl. Phys. A* **336**, 267 (1980).

[444] J. Zenihiro, H. Sakaguchi, S. Terashima, T. Uesaka, G. Hagen, M. Itoh, T. Murakami, Y. Nakatsugawa, T. Ohnishi, H. Sagawa, *et al.*, "Direct determination of the neutron skin thicknesses in ^{40,48}Ca from proton elastic scattering at $E_p = 295$ MeV", arXiv:1810.11796 [nucl-ex] (2018).

[445] M. Centelles, X. Roca-Maza, X. Viñas, and M. Warda, "Origin of the neutron skin thickness of ^{208}Pb in nuclear mean-field models", *Phys. Rev. C* **82**, 054314 (2010).

[446] G. Hagen, A. Ekström, C. Forssén, G. R. Jansen, W. Nazarewicz, T. Papenbrock, S. Wendt, K. A.and Bacca, N. Barnea, B. Carlsson, C. Drischler, *et al.*, "Neutron and weak-charge distributions of the ^{48}Ca nucleus", *Nat. Phys.* **12**, 186 (2016).

[447] T. D. Morris, J. Simonis, S. R. Stroberg, C. Stumpf, G. Hagen, J. D. Holt, G. R. Jansen, T. Papenbrock, R. Roth, and A. Schwenk, "Structure of the Lightest Tin Isotopes", *Phys. Rev. Lett.* **120**, 152503 (2018).

[448] N. Bohr and J. A. Wheeler, "The Mechanism of Nuclear Fission", *Phys. Rev.* **56**, 426 (1939).

[449] P.-G. Reinhard and W. Nazarewicz, "Toward a global description of nuclear charge radii: Exploring the Fayans energy density functional", *Phys. Rev. C* **95**, 064328 (2017).

[450] H. A. Fertig and W. Kohn, "Symmetry of the atomic electron density in Hartree, Hartree-Fock, and density-functional theories", *Phys. Rev. A* **62**, 052511 (2000).

[451] W. Satuła, J. Dobaczewski, W. Nazarewicz, and M. Rafalski, "Isospin Mixing in Nuclei within the Nuclear Density Functional Theory", *Phys. Rev. Lett.* **103**, 012502 (2009).

[452] W. Satuła, J. Dobaczewski, W. Nazarewicz, and M. Rafalski, "Isospin-symmetry restoration within the nuclear density functional theory: Formalism and applications", *Phys. Rev. C* **81**, 054310 (2010).

[453] W. Satuła, J. Dobaczewski, W. Nazarewicz, M. Borucki, and M. Rafalski, "Isospin mixing in the Vicinity of the $N = Z$ line", *Int. J. Mod. Phys. E* **20**, 244 (2011).

[454] A. Bulgac and V. R. Shaginyan, "A systematic surface contribution to the ground-state binding energies", *Nucl. Phys. A* **601**, 103 (1996).

[455] A. Bulgac and V. R. Shaginyan, "Proton single-particle energy shifts due to Coulomb correlations", *Phys. Lett. B* **469**, 1 (1999).

[456] A. H. Wapstra, "Memories of Mass Determinations", *Hyperfine Interact.* **132**, 127 (2001).

[457] Y. Ito, P. Schury, M. Wada, S. Naimi, T. Sonoda, H. Mita, F. Arai, A. Takamine, K. Okada, A. Ozawa, *et al.*, "Single-reference high-precision mass measurement with a multireflection time-of-flight mass spectrograph", *Phys. Rev. C* **88**, 011306 (2013).

[458] P. Schury, T. Niwase, M. Wada, P. Brionnet, S. Chen, T. Hashimoto, H. Haba, Y. Hirayama, D. S. Hou, S. Iimura, *et al.*, "First high-precision direct determination of the atomic mass of a superheavy nuclide", *Phys. Rev. C* **104**, L021304 (2021).

[459] B. Franzke, "The heavy ion storage and cooler ring project ESR at GSI", *Nucl. Instrum. Methods Phys. Res., Sect. B* **24**, 18 (1987).

[460] J. W. Xia, W. L. Zhan, B. W. Wei, Y. J. Yuan, M. T. Song, W. Z. Zhang, X. D. Yang, P. Yuan, D. Q. Gao, H. W. Zhao, *et al.*, "The heavy ion cooler-storage-ring project (HIRFL-CSR) at Lanzhou", *Nucl. Instrum. Methods Phys. Res., Sect. A* **488**, 11 (2002).

[461] A. Ozawa, T. Uesaka, and M. Wakasugi, "The rare-RI ring", *Prog. Theor. Exp. Phys.* **2012**, 03C009 (2012).

[462] X. L. Tu, X. C. Chen, J. T. Zhang, P. Shuai, K. Yue, X. Xu, C. Y. Fu, Q. Zeng, X. Zhou, Y. M. Xing, *et al.*, "First application of combined isochronous and Schottky mass spectrometry: Half-lives of fully ionized $^{49}Cr^{24+}$ and $^{53}Fe^{26+}$ atoms", *Phys. Rev. C* **97**, 014321 (2018).

[463] M. Smith, M. Brodeur, T. Brunner, S. Ettenauer, A. Lapierre, R. Ringle, V. L. Ryjkov, F. Ames, P. Bricault, G. W. F. Drake, *et al.*, "First Penning-Trap Mass Measurement of the Exotic Halo Nucleus ^{11}Li", *Phys. Rev. Lett.* **101**, 202501 (2008).

[464] H. Wollnik, "High-resolving mass spectrographs and spectrometers", *Hyperfine Interact.* **235**, 61 (2015).

[465] A. N. Antonov, M. K. Gaidarov, M. V. Ivanov, D. N. Kadrev, M. Aïche, G. Barreau, S. Czajkowski, B. Jurado, G. Belier, A. Chatillon, *et al.*, "The electron–ion scattering experiment ELISe at the International Facility for Antiproton and Ion Research (FAIR)—conceptual design study", *Nucl. Instrum. Methods Phys. Res., Sect. A* **637**, 60 (2011).

[466] G. P. A. Berg, T. Adachi, M. N. Harakeh, N. Kalantar-Nayestanaki, H. J. Wörtche, H. Simon, I. A. Koop, M. Couder, and M. Fujiwara, "A novel spectrometer for studying exotic nuclei with the electron/ion collider ELISe", *Nucl. Instrum. Methods Phys. Res., Sect. A* **640**, 123 (2011).

[467] L. Aronberg, "Note on the Spectrum of the Isotopes of Lead", *Astrophys. J.* **47**, 96 (1918).

[468] T. R. Merton, "On the spectra of isotopes", *Proc. R. Soc. Lond. A* **96**, 388 (1920).

[469] R. Marrus and D. McColm, "Atomic-Beam Method for the Study of Isotope Shifts", *Phys. Rev. Lett.* **15**, 813 (1965).

[470] H. Hühnermann and H. Wagner, "Messung der isotopieverschiebung am ^{134}Cs", *Phys. Lett.* **21**, 303 (1966).

[471] P. Jacquinot and R. Klapisch, "Hyperfine spectroscopy of radioactive atoms", *Rep. Prog. Phys.* **42**, 773 (1979).

[472] H.-J. Kluge and W. Nörtershäuser, "Lasers for nuclear physics", *Spectrochim. Acta, Part B* **58**, 1031 (2003).

[473] P. Campbell, I. D. Moore, and M. R. Pearson, "Laser spectroscopy for nuclear structure physics", *Prog. Part. Nucl. Phys.* **86**, 127 (2016).

[474] V. V. Flambaum and V. A. Dzuba, "Sensitivity of the isotope shift to the distribution of nuclear charge density", *Phys. Rev. A* **100**, 032511 (2019).

[475] I. Angeli and K. P. Marinova, "Table of experimental nuclear ground state charge radii: An update", *At. Data Nucl. Data Tables* **99**, 69 (2013).

[476] C. J. Horowitz and J. Piekarewicz, "Impact of spin-orbit currents on the electroweak skin of neutron-rich nuclei", *Phys. Rev. C* **86**, 045503 (2012).

[477] H. Sakaguchi and J. Zenihiro, "Proton elastic scattering from stable and unstable nuclei—Extraction of nuclear densities", *Prog. Part. Nucl. Phys.* **97**, 1 (2017).

[478] C. J. Horowitz, "Weak radius of the proton", *Phys. Lett. B* **789**, 675 (2019).